



Eidgenössische Technische Hochschule Zürich
Swiss Federal Institute of Technology Zurich



Department of Information Technology
and Electrical Engineering

DISS. ETH NO. 22812

In vivo study of lung physiology with dynamic synchrotron-based tomographic microscopy

A thesis submitted to attain the degree of

DOCTOR OF SCIENCES of ETH ZURICH

(Dr. sc. ETH Zurich)

presented by

Goran Lovrić

MSc., Graz University of Technology

BSc., Graz University of Technology

born on 11.02.1986

citizen of the

Republic of Croatia

accepted on the recommendation of

Examiner: Prof. Dr. Marco Stampanoni

Co-examiner: Dr. Rajmund Mokso

Co-examiner: Prof. Dr. Johannes C. Schittny

Co-examiner: Dr. Matthias Roth-Kleiner

Co-examiner: Dr. Alberto Bravin

2015

ISBN: 978-3-906327-25-9
DOI: 10.3929/ethz-a-010587266

© Goran Lovrić, March 2016

Typesetting, layout and design with \LaTeX by Goran Lovrić.

Dedicated to my family and friends.

Abstract

Lungs represent the integrative part of the mammalian respiratory system, without which no molecular processes would be possible. However, lung failure still represents one of the leading causes of morbidity and mortality worldwide while the connection between macroscopic observations and the processes taking place at the microscopic and functional scale are still largely unexplored. In particular, in the study of lung inflation and deflation issues, little is known about the structural alterations taking place in the gas-exchange area at the alveolar and acinar scale. While the need for high-resolution imaging techniques remains fundamental in lung research, third-generation synchrotrons have established themselves as valuable experimental machines, providing fast acquisitions in the order of sub-seconds, high resolutions at the micrometer scale and highly coherent X-rays. However, their large capabilities in high-resolution imaging have not been fully explored yet in the field of lung physiology.

The underlying thesis is devoted to the development and realization of *in vivo* tomographic X-ray microscopy for the study of lung physiology at the micrometer scale. The aim of conceiving a fully performant *in vivo* endstation with its first successful application to micrometer-scale tomography is achieved by a wide combination of different aspects such as the development of the necessary beamline instrumentation (hardware, controls software), dosimetry considerations, novel approaches towards image processing and quantitative data analysis as well as a systematic optimization of various experimental parameters. A first realization of a prospective heartbeat-triggered acquisition scheme for performing *in vivo* lung tomography at the micrometer scale is reported and first indicative biological results are presented. In particular, a series of different aspects are reported which indicate that lungs exhibit highly heterogeneous inflation patterns reaching down to the micrometer scale.

Zusammenfassung

Die Lunge stellt den integrativen Teil des Atemapparats bei Säugetieren dar, ohne die keine molekularen Prozesse möglich wären. Lungenversagen stellt jedoch nach wie vor eine der führenden Ursachen für die hohe Erkrankungsrate und Sterblichkeit weltweit dar, wobei der Zusammenhang zwischen makroskopischen Beobachtungen und mikroskopischen Prozessen, die auf der funktionellen Ebene stattfinden, weitgehend unbekannt bleibt. Insbesondere in der näheren Erforschung der Ein- und Ausatmung ist sehr wenig über die strukturellen Veränderungen der Gasaustauschfläche bekannt, die sich auf der Ebene der Azini und Alveolen ereignen. Der Einsatz hochauflösender bildgebender Verfahren bleibt daher nach wie vor fundamental für die Lungenforschung. Gleichzeitig haben sich Synchrotrone der dritten Generation als sehr brauchbare experimentelle Instrumente etabliert, indem sie schnelle Bildaufnahmen mit unter einer Sekunde und hohe Auflösungsvermögen im Bereich von Mikrometern erzielen, noch dazu mit sehr kohärentem Röntgenlicht. Bis heute wurde aber ihr Potenzial bei hochauflösenden bildgebenden Verfahren auf dem Gebiet der Lungenphysiologie noch nicht völlig ausgeschöpft.

Die vorliegende Arbeit beschäftigt sich mit der Entwicklung und Realisierung von tomographischer *in vivo* Röntgenmikroskopie, um die Lungenphysiologie im Mikrometerbereich zu erforschen. Das Ziel, eine völlig leistungsfähige *in vivo* Endstation mit der ersten erfolgreichen Anwendung in der Mikrometer-Tomographie zu errichten, wird erreicht indem eine Vielzahl an verschiedenen Aspekten behandelt wird, wie etwa die Entwicklung der benötigten Beamline-Instrumentierung (Hardware und Kontrollsoftware), Überlegungen zur Dosimetrie, neuartige Behandlungen auf dem Gebiet der Bildverarbeitung und der quantitativen Datenanalyse sowie der systematischen Optimierung aller experimentellen Parameter. Die erste Realisierung einer sogenannten prospektiven Herz-getriggerten Bildaufnahme wird dargestellt, mit der *in vivo* Lungentomographie auf der Ebene von Mikrometern bewerkstelligt wird, und erste indikative biologische Resultate werden präsentiert. Im Speziellen wird eine Reihe an Aspekten behandelt, welche darauf hindeuten, dass die Lunge in hohem Maße heterogene Strukturen bei der Beatmung aufweist die bis zur Mikrometer-Skala herunterreicht.

Acknowledgments

First of all I would like to thank my dissertation advisor and main proposer of the project, Prof. Dr. Marco Stampanoni, for giving me the opportunity to conduct a PhD thesis in his group as well as for his excellent guidance as a group leader throughout the years. The constant encouragement towards new ideas, always striving for the highest criteria, as well as his ability to formulate science in a sharp and concise way are only a few things from which I have greatly benefited. Another aspect I am particularly thankful for is the constant support and trust I received from him, which has been a key motivating factor during all the years.

I am at least equally grateful to my day-to-day supervisor Dr. Rajmund Mokso, whom I still admire for his relentless optimism and trust towards myself, even when my results with data analysis were anything but promising. Without his exhaustive knowledge in physics, his diplomatic skills in explaining me the most basic questions as well as his holistic view on my whole project, this work wouldn't have been possible.

To the same extent I would also like to express my deepest acknowledgments to my collaborators Prof. Dr. Johannes Schittny and Dr. Matthias Roth-Kleiner, with whom it has been an exceptional and extraordinary pleasure to work. Both not only proved to be extremely tireless and devoted scientists, but also made substantial contribution towards creating a respectful and professional working environment. Their conscience and preciseness in approaching various scientific problems have made a lasting impression on me.

I would also like to thank my closest collaborators Filippo Arcadu and Yannis Vogiatzis Oikonomidis who were always at hand when I needed help and showed their relentless willingness in giving me support. In the same way I would also like to mention my office colleague Matias Kagias, who would always let stand his own work to help me solving various issues I experienced during data analysis. Likewise, my other office colleagues deserve special thanks: Silvia Peter with whom I had many nice discussions on physics; Carolina Arboleda for her constant helpfulness and friendliness and Anabelle Medebach for always providing me with all sorts of useful information.

From the scientific part, I would like to mention Dr. Peter Modregger, with whom it has always been a pleasure to discuss about various scientific aspects of my work but also any kind of controversial human topic; Dr. Sally Irvine and Dr. Zhentian Wang, who were always eager to help and share all their knowledge with me; Dr. Kevin Mader, Dr. David Haberthür, Matteo Abis and Dr. Federica Marone, for all the practical discussions and suggestions I used to get from them. Also, I would like to mention Dr. Julie Fife for all the nice discussions and Dr. Alberto Astolfo, whom it was always a pleasure to ask about all kinds of opinions.

Apart from the rest of the TOMCAT team, who all in their own way contributed in setting the bar very high in terms of an idealized working environment, I'd also like to thank the following individuals: Gordan Mikuljan, the best technician I've

ever met; Dr. Tine Celcer, equally the best controls guy; and finally Christophe Frieh (from the Phoenix beamline) and Alain Studer (from the Scientific Computing group), who were both exceptionally supportive whenever needed.

I am also thankful for having had the opportunity to work with Daniel Pelt and Dr. Alexander Kostenko during our experimental and computational sessions and for all the discussions we had. At the same time and in the same way I'd like to mention Martin Nyvlt.

Finally, thanks to Dr. Pablo Villanueva and Dr. Spyros Gkoumas, who gave me a lot of moral support during the hard period of finishing my PhD thesis.

Last but not least, I owe my deepest gratitude to Dr. Renate Belaj who despite the exhaustive task agreed to proofread the whole underlying thesis.

Contents

List of Figures	xv
List of Tables	xix
1 Introduction	1
1.1 Lead-in	1
1.2 Scientific aims and outline	2
2 Biological background	5
2.1 Pulmonary anatomy	5
2.2 Pulmonary physiology	7
2.2.1 The respiratory system	7
2.2.2 Ventilation	9
2.3 Lung development	10
2.4 Relevance for neonatology	13
2.5 Role of small animal imaging	13
3 X-ray imaging	15
3.1 X-ray sources	15
3.1.1 X-ray tube	15
3.1.2 Synchrotron-based X-ray sources	16
3.2 X-ray interaction with matter	20
3.2.1 Photoelectric absorption	21
3.2.2 Scattering	22
3.3 Phase-contrast imaging	25
3.4 Principles of X-ray tomography	32
3.5 Post-processing	37
4 X-ray instrumentation	41
4.1 Beam stability measurements	41

4.2	Coherence characterization	49
4.2.1	Abstract	49
4.2.2	Introduction	49
4.2.3	Methods	50
4.2.4	Results and discussion	60
4.2.5	Conclusion	63
4.2.6	Appendix	64
4.2.7	Acknowledgments	64
4.3	Dosimetry	65
4.3.1	Essentials	65
4.3.2	Dose calculations	66
4.3.3	Discussion	70
4.3.4	Conclusion	71
4.4	<i>In vivo</i> endstation	73
4.4.1	Rotation stage	75
4.4.2	Sample holders and alignment system	79
4.4.3	Small animal ventilator	82
4.4.4	ECG and oscilloscope	87
4.4.5	Animal preparation and anesthesia	91
5	Dose optimization approach to fast X-ray microtomography of the lung alveoli	93
5.1	Abstract	93
5.2	Introduction	93
5.3	Materials and methods	94
5.3.1	Image acquisition	94
5.3.2	Post-processing	95
5.3.3	Image analysis	96
5.3.4	Dose calculations	96
5.4	Results	98
5.5	Discussion	99
5.6	Conclusion	101
5.7	Acknowledgements	101
6	Quantitative analysis of intact lungs at the alveolar and acinar scale	103
6.1	Abstract	103
6.2	Introduction	103
6.3	Materials and methods	105

6.3.1	Image acquisition	105
6.3.2	Animal preparation	105
6.3.3	Post-processing	106
6.3.4	Local thickness analysis	109
6.3.5	Curvature analysis	110
6.4	Results	112
6.4.1	Image formation	112
6.4.2	Thickness maps results	114
6.4.3	Curvature results	117
6.5	Discussion	118
6.6	Conclusion	120
6.7	Acknowledgements	121
7	Tomographic <i>in vivo</i> study of lung physiology at the micrometer scale	123
7.1	Abstract	123
7.2	Introduction	123
7.3	Materials and methods	125
7.3.1	Animal preparation	125
7.3.2	Image acquisition and reconstruction	126
7.4	Results	129
7.4.1	Influence of heart-induced motion	129
7.4.2	Ventilation patterns at different pressures	132
7.5	Discussion	134
7.6	Conclusion	136
7.7	Acknowledgements	136
8	Summary	137
8.1	Conclusion	137
8.2	Perspectives	139
	Bibliography	143
	Curriculum vitae	163

List of Figures

Figure 2.1.	Schematic diagram of airway branching	6
Figure 2.2.	Sketch of the lungs branching tree	7
Figure 2.3.	Simplified diagram of the chest wall	8
Figure 2.4.	Sketch of the compliance curves	9
Figure 3.1.	Principle of X-ray creation in an X-ray tube	16
Figure 3.2.	TOMCAT white beam spectrum	19
Figure 3.3.	Total mass attenuation coefficient for carbon	22
Figure 3.4.	Demonstration of the Fourier slice theorem	33
Figure 3.5.	Reduction of the number of projections at $2.9 \mu\text{m}$ pixel size	36
Figure 3.6.	Reduction of the number of projections at $1.1 \mu\text{m}$ pixel size	36
Figure 3.7.	Demonstration of wavelet ring-removal	37
Figure 3.8.	Manual registration of lung volumes at different pressures	39
Figure 4.1.	Demonstration of a distorted flat-field correction	42
Figure 4.2.	Demonstration of the normlized cross-correlation	44
Figure 4.3.	Normalized cross-correlation result used for further processing	45
Figure 4.4.	Mean power spectral densities (PSD) of the mono-beam fluctuations	46
Figure 4.5.	Mean power spectral densities (PSD) of the white beam fluctuations	47
Figure 4.6.	Seismic vibration measurements at TOMCAT	48
Figure 4.7.	Experimental setup for measuring coherence	51
Figure 4.8.	SEM image of the 2D grating	52
Figure 4.9.	Flowchart for calculating the source size	56
Figure 4.10.	Demonstration of the fitting algorithm from Fig. 4.9	56
Figure 4.11.	Principal Fourier coefficients as functions of the propagation distance	61
Figure 4.12.	Principal Fourier coefficients for the [Ru/C] monochromator	62
Figure 4.13.	Principal Fourier coefficients for the for the V/B-C multilayer crystal	62
Figure 4.14.	Calculated source sizes for the [Ru/C] ₁₀₀ multilayer	64
Figure 4.15.	Derivation of the <i>entrance skin dose</i>	67

List of Figures

Figure 4.16.	Comparison between absorbed dose and skin entrance dose	68
Figure 4.17.	Absolute flux measurement system	72
Figure 4.18.	Inner workings of the PIPS diode	72
Figure 4.19.	<i>In vivo</i> endstation with its main components	74
Figure 4.20.	CAD drawings of the air bearing rotation axis system	76
Figure 4.21.	Sketch of the Aerotech EPICS driver implementation	77
Figure 4.22.	Control panel of the Aerotech EPICS driver implementation	78
Figure 4.23.	Original and final sample-holder alignment system	80
Figure 4.24.	Animal sample holders of various sizes	81
Figure 4.25.	Experimental setup at the Clinic of Neonatology (CHUV)	84
Figure 4.26.	Ventilation curve as a function of time	85
Figure 4.27.	Lung phantom with cannula	86
Figure 4.28.	Front and rear view of the ECG device	88
Figure 4.29.	Complete TTL triggering schematic for the <i>in vivo</i> setup	89
Figure 4.30.	Recorded oscilloscope signals with angular increments	90
Figure 4.31.	Isoflurane-influx/outflow system and final animal positioning	91
Figure 5.1.	Experimental setup at the X02DA TOMCAT beamline	94
Figure 5.2.	Flowchart of the post-processing pipeline	95
Figure 5.3.	A tomographic slice of a lung for the $2.9\ \mu\text{m}$ -pixel-size optics	97
Figure 5.4.	Dose and flux measuring setup	98
Figure 5.5.	Contrast-to-noise ratio (CNR) as a function of propagation distance	99
Figure 5.6.	Comparison of tomographic slices before and after thresholding	100
Figure 5.7.	CNR as a function of total scan time per tomographic scan	101
Figure 6.1.	Experimental setup at the X02DA TOMCAT beamline.	105
Figure 6.3.	Complete segmentation flowchart for 3D lung data	108
Figure 6.4.	Manual measurement of air thickness on a tomographic slice	109
Figure 6.5.	Interface shape distributions map	111
Figure 6.6.	Processing flowchart of the curvature analysis	112
Figure 6.7.	Comparison between the low-resolution and the high-resolution optics	113
Figure 6.8.	Structure diameters obtained by thickness map calculation	114
Figure 6.9.	Probability density functions (PDF) of the local thicknesses	115
Figure 6.10.	Visualization of the thickness maps in 3D	116
Figure 6.11.	Interface shape distribution results	117
Figure 6.12.	Probability density functions (PDF) of Gaussian and mean curvatures	118
Figure 6.13.	3D visualization of the four regions from the ISD-plot	119

Figure 6.14.	Sketch showing the identification of alveolar surface	120
Figure 6.15.	Alteration to alveolar surface shape due to overstretching	120
Figure 7.1.	Experimental setup at the TOMCAT beamline	126
Figure 7.2.	Trigger sketch and animal in sample holder	127
Figure 7.3.	<i>In vivo</i> tomographic slice and angles information	128
Figure 7.4.	Tomographic slice of a rat's lung without heartbeat gating	129
Figure 7.5.	Various ECG-trigger delays	130
Figure 7.6.	Comparison of <i>in vivo</i> and <i>ex vivo</i> tomographic slices (low-res.)	131
Figure 7.7.	Comparison of <i>in vivo</i> and <i>ex vivo</i> tomographic slices (high-res.)	131
Figure 7.8.	Rats lungs at different breath-hold peak-inspiratory pressures	132
Figure 7.9.	Small ROI-s for different pressures of animal A	133
Figure 7.10.	Small ROI-s for different pressures of animal B	133
Figure 8.1.	Monte Carlo dose distributions	140
Figure 8.2.	Application of NN-FBP with a reduced number of projections	140
Figure 8.3.	Application of NN-FBP in a noisy image	141

List of Tables

Table 2.1.	Stages of lung formation and major structural developments	11
Table 3.1.	TOMCAT beamline parameters	19
Table 4.1.	Beam vibrations measurement setups	43
Table 4.2.	Horizontal and vertical source sizes at the TOMCAT beamline	63
Table 4.3.	Scan parameters for comparing absorbed to entrance dose	68
Table 4.4.	Comparison between absorbed dose and entrance dose	69
Table 4.5.	Complete device list of the <i>in vivo</i> endstation	73
Table 4.6.	Optimal ventilation settings with favorable blood gas values	85
Table 6.1.	Volumetric distributions of the thicknesses	115

Introduction

1.1 LEAD-IN

The biggest challenge in all interdisciplinary projects seems to be to find a balance between two facets: on the one hand, devoting oneself to some highly specialized topics and thus losing the complete overview; on the other hand, expanding one's own interest to so many fields that the remainder becomes superficial.

To be even more complicated, one constantly deals with collaborators and colleagues coming from other fields, with different ideas and different understandings which, upon the first impression, in the best case seem peculiar. Sometimes this situation is even enhanced by the fact that at the very moment things get really interesting, one already has to move on to cover the next small field or scientific problem.

Obviously, this small preface tells only a fractional part of the truth by describing some of the pitfalls many people discover during their time as a PhD candidate, including the author of the underlying thesis. To complete the story, the point that actually makes an interdisciplinary project exceptionally interesting is the fact that it never gets repetitive, and one is constantly driven by new ideas and impulses, where actual achievements are only established through real collaborative work. As a consequence, one inevitably collaborates with other people and exchanges ideas, and each small accomplishment is doubled or tripled if more people have contributed to it. Also, one has the ultimate possibility to focus on some topics more and others less, which gives the researcher freedom and particular motivation to devote oneself fully to the project.

In this sense, with the present work the author hopes to prove that neither of the aforementioned pitfalls was the case in the underlying project. He particularly hopes to be able to provide a detailed description of the whole work, without omitting crucial details, but still maintaining the general overview.

1.2 SCIENTIFIC AIMS AND OUTLINE

The study of lung physiology has been driven by many aspects, but mainly by the fact that the lung represents the integrative part of the mammalian respiratory system, without which no molecular processes would be possible. However, lungs still are largely unexplored when it comes to drawing the link between macroscopic observations and the processes taking place at the microscopic and *functional* scale. Therefore, it is not by chance that lung failure still represents one of the leading causes of morbidity and mortality worldwide, while the connection between current lung diseases and microscopic disruptions in lung tissue is still far from being understood. That means that the need for high-resolution imaging techniques remains fundamental in present and future lung research. One of such applications is the study of lung dynamics, in particular lung inflation and deflation issues, where little is known about the structural alterations taking place in the gas-exchange area at the alveolar and acinar scale.

In parallel, third-generation synchrotrons have established themselves as valuable experimental machines in probing a huge variety of materials with unmatched spatial and temporal resolutions. Combined with tomography, they have fundamentally contributed to exploring some of the most remarkable physical and biological phenomena. It is only since recently that high-efficiency detectors can acquire Gigabytes of data in terms of seconds, and even brighter and more powerful synchrotron X-ray sources are being constructed which will push further the developments of accompanying techniques. Fast acquisitions in the order of sub-seconds, high resolutions at the micrometer scale and highly coherent X-rays are only obtainable at synchrotrons, and keeping in mind the aforementioned open topics in functional biology of lungs, the obvious question that arises is whether it is possible to combine these two cornerstones.

At synchrotrons, so far, the use of animals has been realized in several studies, but is still far from being an established standard. On the other hand, the large capabilities of high-resolution imaging have not been fully explored yet when it comes to the application to *in vivo* animal models, particularly in the study of lung physiology.

From this small preface, it is now possible to formulate the basic objectives addressed in the underlying work. While the quantitative description of alveolar and acinar dynamics during respiration is the main scientific case motivating the project, the primary focus consists of developing a platform for *in vivo* tomographic microscopy at the micrometer scale. As will be shown at various occasions within the thesis, this goal is only achieved by a wide combination of different aspects such as the development of the necessary beamline instrumentation (hardware, controls software), dosimetry considerations, novel approaches towards image processing and quantitative data analysis as well as a systematic optimization of various experimental parameters. The path towards the ultimate goal, namely to answer still open biological questions, is drawn, and first indicative results are discussed in the end.

The thesis is organized as follows:

In Chapter 2, an overview on the biological background is provided, playing the most crucial part for the motivation of the underlying project. The anatomy and physiology of mammalian lungs are discussed and the link is drawn to recent studies with small-animals.

In Chapter 3, the basics of coherent X-ray imaging are summarized, and the impact of establishing combined fast-imaging and high-resolution techniques is described.

In Chapter 4, we describe a big variety of aspects from different directions, mostly in terms of instrumentation, that were crucial for the underlying project. The chapter is rather descriptive, as most of the expertise has been built from the ground up. It can also be seen as some sort of manual about animal handling at the beamline.

In Chapter 5, the first study on high-resolution microtomography of mouse lungs is presented, indicating its feasibility for the *in vivo* case and discussing limits in dose and image acquisition.

In Chapter 6, a quantitative framework towards the analysis of high-resolution 3D lung image data is presented.

In Chapter 7, the results from first *in vivo* studies at the micrometer scale are described, showing the current limitations and possibilities of future improvements.

In Chapter 8, the thesis is concluded by summarizing all different aspects of the underlying work.

Biological background

In the following we give a basic description of the mammalian respiratory system, starting from a macroscopic anatomical view of human lungs down to the microscopic gas exchange units. By doing so we give an overview of the lung architecture, describe its basic mechanics and cover the most relevant stages in lung development. The relevance to neonatology is drawn and finally we make the link to current studies with small animals highlighting their importance in the study of functional biology. The underlying chapter mainly follows the synopsis of [1, 2], whereas detailed source references are given at the respective positions.

2.1 PULMONARY ANATOMY

Molecular oxygen represents one of the most fundamental components for our surviving by enabling us to burn our fuel that at the end runs all of our basic cellular processes. Hence, as an integrative part of the respiratory system and the mammalian organism, lungs are interactively connected with the central nervous system. Latter one provides the rhythmic drive for breathing, causing the diaphragm together with its muscular apparatus to move and interacts with the circulatory system establishing the gas transport between the tissue and the lungs.

Figuratively speaking, lungs are designed to provide an efficient pathway for the airflow starting from the mouth/nose down to the alveolar sacs. As shown schematically in Fig. 2.1, they can be divided into a branched system of airways, the *tracheo-bronchial tree*, and gas-exchanging parts, the *alveoli* [3]. The detailed branching scheme is sketched in Fig. 2.2, whereas the path of a breath can be described as follows. The gas first flows through the upper respiratory system, namely through the nasopharynx or the oropharynx (i. e. depending on whether the air is inhaled through the nouse or through the mouth), proceeds to the laryngopharynx and the larynx until reaching the trachea. The trachea then divides into the right and left mainstem bronchi, which further subdivide to form the five lobar bronchi. These form the origin of the five lung lobes, of which there are three on the right and two on the left side

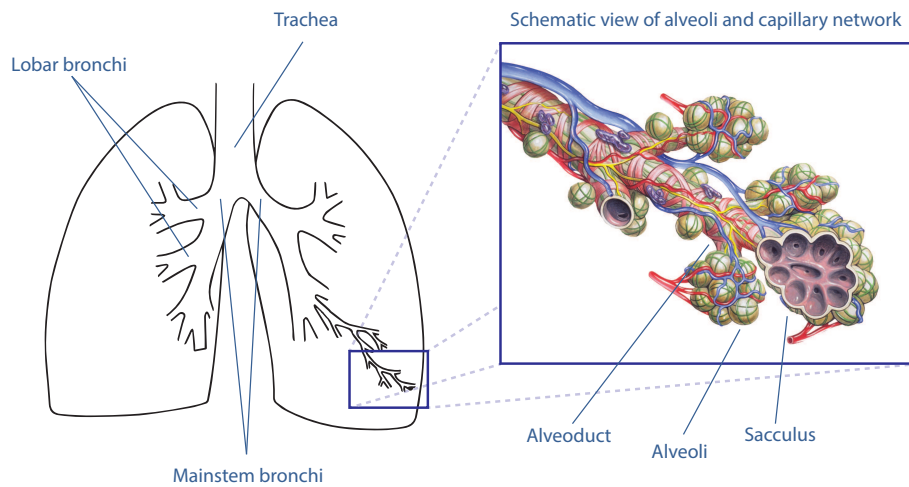


Figure 2.1. Schematic diagram of airway branching. The trachea branches into the two mainstem bronchi, which branch into the five lobar bronchi. The branching continues until reaching “dead ends”, the alveoli. The sketches are adapted from [1, 4].

(as indicated in Fig. 2.1). The branching continues through segmental bronchi, further subdividing into an extensive system of subsegmental and smaller bronchi until reaching terminal bronchioles, which represent the smallest conductive airspaces (i. e. where no gas exchange takes place). At this point the airways have been divided approximately 15-20 times, and it has been shown that the mean diameter of the airways is exponentially related to the order of branching, serving a fractal design principle in the branching scheme [5, 6]. Finally, terminal bronchioles further branch into alveolar ducts and eventually end up in “dead-ends”, the sacculi. The walls of the gas-exchanging airways are paved with alveoli. In the most ordinary definition, an alveolus is defined as the dead-end air space unambiguously identified by the alveolar opening and limited by a part of the alveolar wall [7]. Studies have shown that the bronchial tree in humans has 23 generations of branches [8] with a total of approximately 480 million alveoli [9]. The terminal respiratory unit, consisting of those generations of peripheral airways which are provided with alveoli and thus being involved in gas exchange, is called *acinus* (plural: *acini*) [10]. Although the number of alveoli represents a key structural determinant of lung architecture, it is the acinus that actually represents the *functional* unit of the lung in which all airspaces participate in gas exchange while being supplied by purely air-conducting airways [3]. Therefore, the total number of acini is defined as the *lung parenchyma*, and studies have shown that lung parenchyma occupies about 90% of the total lung volume [11], of which 86.5% are associated with air space and 13.5% with interalveolar septa [12]. More recently, studies have shown that the total number of acini might represent a robust quantitative measure in the lung being uncorrelated with neither the mean acinar volume nor the body weight [13].

As a consequence of the aforementioned complicated branching structure the human lung represents an organ with an enormous surface area, being pretty much the size of a tennis

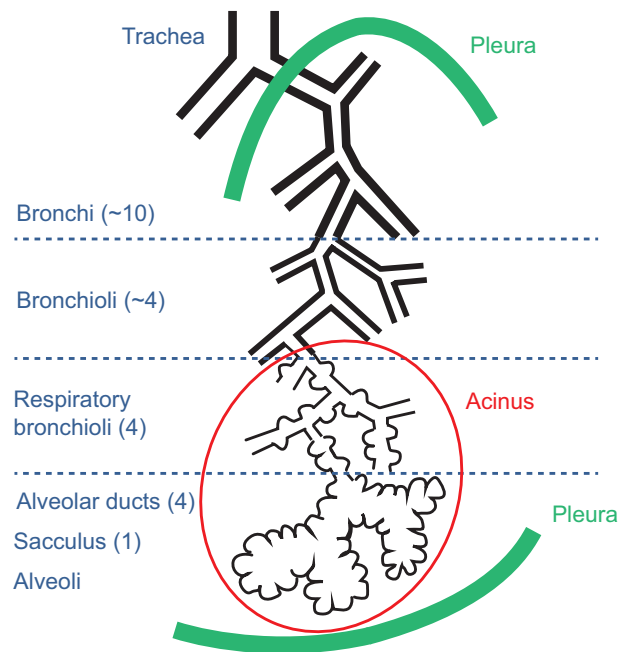


Figure 2.2. Sketch of the lungs branching tree. The average value of the generations formed by each category of airways is given in parentheses. The sketch is adapted with permission from [8].

court in an adult human [14]. Beside the huge total surface area, another crucial requirement for gas exchange is the transportation system for oxygen and carbon dioxide to and from other body tissues and organs. This part is handled by the pulmonary capillary network. It provides the human body with oxygenated blood after the oxygen has been absorbed through the respiratory epithelium. Similar to the airway branching, the pulmonary capillary network equally forms a branching system of smaller pulmonary arteries and arterioles, and capillaries lining the surface for gas exchange.

2.2 PULMONARY PHYSIOLOGY

For a proper description of pulmonary physiology it is necessary to review the lung as part of the whole *respiratory system*, which is formed as the unit of lungs and the chest wall. We first start by discussing the mechanical interplay of the lungs and the chest wall before giving a more detailed overview on the ventilation process itself.

2.2.1 The respiratory system

Under an idealized view, assuming a perfectly healthy organ, lungs occupy a particular resting volume if no additional/external force is applied. As we outlined before, lungs mostly consist of air (in relation to lung tissue), so its volume without applying an external force would be

much lower than its natural size. In particular, lungs tend to collapse if being removed from the chest wall, but within the chest wall this fact is prevented as they are embedded within the so-called thoracic cage surrounded by a serous membrane called the *pleura* and the chest wall. That said, we can now define the pressure that is required to increase the volume of the lung, called the *transpulmonary pressure* P_{trans} . It has a positive value and, when viewed inside the chest wall, it can be written as:

$$P_{\text{trans}} = P_{\text{alv}} - P_{\text{pl}}, \quad (2.1)$$

where P_{alv} is the *alveolar pressure* (internal lung pressure) and P_{pl} is the pleural pressure (external pressure within the pleural space). This relationship is depicted in a simplified manner in Fig. 2.3 showing that the pressure inside the lungs must be higher than the pressure outside to increase its volume. According to Eq. (2.1) and following the sketch in Fig. 2.3 it is obvious that either a positive pressure inside the airways must be applied or a negative pressure outside on the thorax. As a consequence of this relationship, two mechanical ventilation procedures are possible: while positive-pressure ventilation is nowadays the most common practice in clinics, negative pressure applied from outside to the chest wall historically played a particular role in the so-called *negative pressure ventilators*, acting basically as a vacuum chamber from a physical point of view. It follows from this relationship that breathing is accomplished by periodically changing the transpulmonary pressure, i. e. being positive during inspiration and negative during expiration. Thus, the transpulmonary pressure and lung volume exhibit a

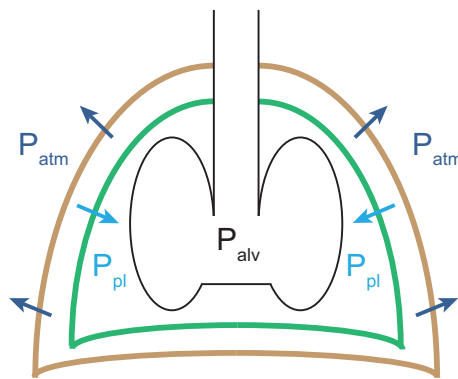


Figure 2.3. Simplified diagram for showing the pressures on both sides of the chest wall. The sketch is inspired from [1].

(curvilinear) relationship that is best described by the *compliance curve* of the lung. It reaches a saturation in lung distensibility when relatively high pressure is applied. Likewise, the *compliance curve* of the chest wall relates the volume enclosed by the chest wall to the pressure across the chest wall. Thereby, the chest wall can be imagined as a spring in the opposite direction pointing outside the thorax. This means that its volume would be relatively high if no external force was applied. The combination of the two curves finally leads to the definition of the *compliance curve of the respiratory system*, shown in Fig. 2.4. This relationship is

immediately obvious by introducing the following quantities: the **functional residual capacity** (FRC) is defined as the normal resting end-expiratory position in the respiratory system where the lung has the lowest volume, which however is still greater than the volume it would occupy as an isolated organ; the **total lung capacity** (TLC) is the volume of gas within the lung at the end of the maximum inhalation; and the **residual volume** (RV) gives the volume of maximal exhalation, where still a significant amount of gas is present within the lungs. At

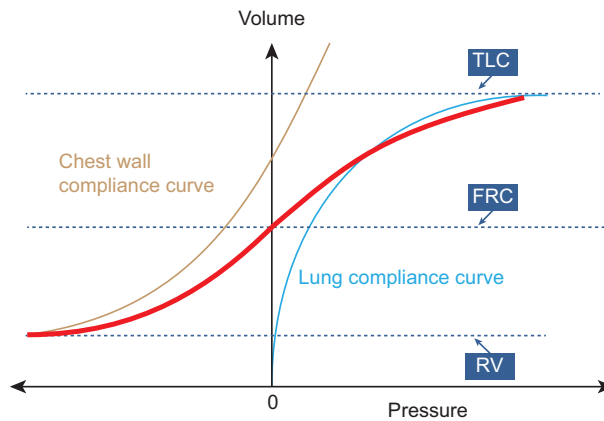


Figure 2.4. Sketch of the individual compliance curves of the chest and lung, that form the compliance curve of the respiratory system.

the *functional residual capacity* (FRC) lungs reach their end-expiratory position, forming a balance between the chest wall to expand outward and the lung to become smaller. At FRC the transpulmonary pressure is equal in magnitude to the pressure across the chest wall but in the opposite direction. Thus, pleural pressure is negative.

2.2.2 Ventilation

To describe the dynamics of the whole respiratory system, it is necessary to view both the lungs and the chest wall as elastic bodies. More precisely, lungs represent an imperfect elastic body that dissipates energy, and the compliance curve of the respiratory system exhibits a characteristic hysteresis that originates from both the bronchial and the parenchymal hystereses [15]. The so-called *tidal volume* V_T is the volume of each breath, however, it is not entirely used for gas exchange. Normal gas exchange within the organism is accomplished when an adequate volume of air is passed through the lungs for sufficient provision of oxygen and removal of carbon dioxide at the same time. We define two additional volumetric quantities: the *volume of dead space* (V_D) represents the portion of tidal volume that is not used for gas exchange (i. e. occupying the air volume in the conducting airways), while the volume that reaches the lung parenchyma is called the *alveolar volume* (V_A).

With this, we can now define the so-called *alveolar ventilation* (\dot{V}_A) as:

$$\dot{V}_A = f \cdot V_A, \quad (2.2)$$

where f is the breathing frequency. It describes the delivered air volume per time unit. When the oxygenated air reaches the gas exchange area, the transfer of oxygen and carbon dioxide is accomplished by diffusion. Thereby, the explicit processes between the alveolar space and blood take place in several compartments: alveolar gas, alveolar and capillary walls, plasma, membrane and the cytoplasm of the red blood cells.

With the definition of the alveolar ventilation, a fundamental relationship can be established:

$$P_{a\text{CO}_2} \sim \frac{\dot{V}_{\text{CO}_2}}{\dot{V}_A}, \quad (2.3)$$

where \dot{V}_{CO_2} is the body's rate of carbon dioxide production and $P_{a\text{CO}_2}$ is the partial pressure of carbon dioxide in arterial blood. This means that alveolar ventilation \dot{V}_A is directly proportional to the removal of carbon dioxide from the body (as an increase of \dot{V}_A decreases $P_{a\text{CO}_2}$). As a consequence, under normal exercise the carbon dioxide production rate \dot{V}_{CO_2} increases, but so does the alveolar ventilation \dot{V}_A so that $P_{a\text{CO}_2}$ stays mostly constant.

A quantification of the physiologic dead space, in particular the fraction of dead space V_D and tidal volume V_T , represents an important quantity in clinics and can be conducted through the *Bohr equation*:

$$\frac{V_D}{V_T} = \frac{P_{a\text{CO}_2} - P_{\text{ECO}_2}}{P_{a\text{CO}_2}}, \quad (2.4)$$

where $P_{a\text{CO}_2}$ is the partial pressure of carbon dioxide from arterial blood as stated above, P_{ECO_2} is the partial pressure of carbon dioxide in expired gas. For gas coming from the dead space, P_{CO_2} is close to 0 because the gas never came into contact with the CO_2 -enriched capillary blood. Hence, the Bohr equation is a useful measure for the determination of the ratio of the tidal volume in respect to the volume of dead space and thus for studying ventilation efficiency.

Finally, it is important to mention that the biggest challenge in understanding the detailed processes of lung ventilation is to make the connection between macroscopic measures/observations and processes happening on a microscopic level. For instance, the aforementioned lung hysteresis in the compliance curve is a macroscopic measurable quantity. However, it can only be explained by numerous models, as the link to the microscopic scale is still matter of intensive contemporary research [15, 16]. The fact that there is a particular relationship between tissue composition, microstructure and macrophysiology has been established beyond doubt. How it relates to physiological behavior, mechanical properties and the complex structural design of the lung, still remains to be answered [17].

2.3 LUNG DEVELOPMENT

The functional capacity of the human lung is determined by structural design and thus strongly dependent on the early stage of development. The primary goal of lung development is to

create a large gas exchange area with a very thin tissue barrier for supplying the organism with sufficient oxygen and to remove excess carbon dioxide [14, 18]. Two main processes are required for forming a functional lung: *branching morphogenesis* is required to build a tree-like tubular structure network and to form the conducting and respiratory airways, and *alveolar differentiation (septation)* describes the process of subdividing the formed airspaces into the final gas exchange units (by centripetal growing of new septa into the existing gas exchange units), the alveoli, and covers also the vascular refinement. The optimal organ design, achieved by fractal geometry [6], is characterized by the maximum number of its basic functional units as well as by its maximum possible efficiency for transporting gas and liquid to and from these functional units [19]. More precisely, the whole process of lung development can be subdivided into six separate but overlapping processes, of which each requires a set of certain developmental factors and possesses a certain milestone. These steps are summarized in Tab. 2.1, of which we give a short overview in the following.

Table 2.1. Stages of lung formation and major structural developments^a.

Developmental stage	Duration ^b	Characteristics
Embryonic	Human: E26-E49 Rat: E11-E13 Mouse: E9.5-E12	start of organogenesis; formation of major airways
Pseudoglandular	Human: E35-E119 Rat: E13-E18.5 Mouse: E12-E16.5	preacinar bronchial tree
Canalicular	Human: E112-E182 Rat: E18.5-E20 Mouse: E16.5-E17.5	Completion of conduction airways; epithelial differentiation; first airblood barrier; appearance of surfactant
Saccular	Human: E168-E266 Rat: E21-P4 Mouse: E17.5-P4	Expansion of airspaces
Alveolar	Human: E252 to 1-2 years ^c Rat: P4-P14 Mouse: P4-P14	Alveolarization by formation of secondary septa (septation)
Microvascular maturation	Human: 0-3 years Rat: P14-P21 Mouse: P14-P21	Remodeling and maturation of interalveolar septa of the capillary bed

^a The table is adapted from [2, 20].

^b E (embryonic day - days *post coitum*); P (postnatal day).

^c It continues until young adulthood.

Lung morphogenesis starts by forming two ventral buds from the primitive foregut. Subsequently, the two lung buds (primary bronchi) elongate and form the (major) conducting airways. The elongation stops, and they branch into the three right and two left (secondary) bronchi. Each of these five secondary bronchi will form the five future lung lobes. The whole process of repetitive elongation, stopping of elongation and subdivision is termed *branching morphogenesis* and falls within the *embryonic stage*. It leads to a multiplication of airways, forming the tree-like structure. Although it is known that 16 generations of the branching process are reproducible and the latter half exhibits more random distributions, it has been shown recently that the hierarchical and modular programme is genetically encoded and tractable [21].

Although the process of branching morphogenesis transitions into and mainly occurs during the *pseudoglandular stage*, the latter is initiated by the onset of cellular differentiation. This means that the formation of lung buds, trachea, primary bronchi and major airways are all lined with undifferentiated columnar epithelium. The subsequent pulmonary differentiation can be broken down to four different categories, where each category undergoes differentiation into a specific cell type. The differentiation ends at the transition to the next phase by setting up the functional characteristics of both the conducting airways (bronchial system) and the respiratory airways (pulmonary acinus) while the vascular system is developed in parallel.

The main characteristic of the *canalicular phase* is that at its end the lungs have developed a minimal gas-exchange capacity (including the completion of branching morphogenesis), which makes actual survival of the living organism possible. To accomplish this, again a number of steps takes place: the growth of the respiratory epithelium (by differentiation of the pulmonary epithelium), the formation of the respiratory bronchioles, the “birth” of the pulmonary acinus and finally a large increase in the capillary bed of the distal lung take place during this stage. Latter one includes the approaching of capillaries inside the mesenchym towards the future airways and the formation of the air-to-blood barrier directly under the parenchymal lung surface, i. e. the condition *sine qua non* for gas exchange.

The *saccular phase* is characterized by the widening of peripheral airways to form clusters of bigger air spaces, the so-called sacculi. In this stage the branching morphogenesis has stopped, and it is nowadays believed that the saccular stage represents somehow an intermediate stage between alveolarization and branching morphogenesis [8]. The previous assumption that branching morphogenesis and the subsequent alveolarization are two distinct processes has been refined recently, showing that both must be studied as a balanced choice and not individually [19]. In parallel it has also been shown that the branching pattern itself has a significant impact on air flow, also affecting the gas exchange [22].

During the late lung development, the *alveolar stage* encompasses both the initial part taking place *in utero* as well as the “classic” alveolarization that continues after parturition within the first two years of human life. It represents the second contribution to the increase of the internal gas exchange surface area, additionally to the process of branching morphogenesis. In doing so, alveoli are formed from already existing septa by creating new “secondary” septa. While it was long believed that the stage of alveolarization finishes within the first years of human development, in the recent years evidence has also been found for a so-called *late*

alveolarization that takes part until young adulthood [23, 24].

In the final step, the *microvascular maturation*, a capillary remodeling takes place leading to a thinning of the alveolar walls (i. e. septal thicknesses). The reason is that both the primary and secondary septa exhibit a double-layered capillary that performs gas exchange only on one side, namely the one pointing to the alveolar surface. By thinning the septa via fusion of the two capillaries to one capillary layer and reduction of the number of mesenchymal cells the gas exchange process becomes more efficient since every capillary is now in contact with two alveolar areas.

After this period, lung development is considered to be completed. The lungs further grow in volume as well as late lung alveolarization takes place.

2.4 RELEVANCE FOR NEONATOLOGY

As stated in the previous chapter, by the end of the canalicular period the human fetus is able to survive premature birth because by that time it has developed the necessary respiratory epithelium and the associated vascular bed for enabling basic gas exchange. Hence, lungs of small premature babies are still at a developmental stage, being surfactant deficient, partially liquid filled and prone to collapse at end-expiration [25]. This is why infants born very preterm need positive pressure ventilation to aerate their lungs and overcome the high surface tension and frictional forces caused by liquid-filled airways [26]. Ventilating preterm infants, despite being live-saving, has a huge negative side-effect as it can injure their lungs. Direct damage to the lung induced by mechanical ventilation can lead to inflammatory reactions (*baro-/volutrauma*), leading to the development of bronchopulmonary dysplasia (BPD) [27] or ventilator-induced lung injury (VILI) [28, 29]. These chronic lung diseases in the newborn may cause a potential lung function limitation in adulthood and in the worst case can be lethal.

As premature birth profoundly alters the timing of exposure to numerous experiences, its link to current lung diseases and disruptions is highly interesting and unexplored [30]. Although there has been remarkable progress in the care of neonates, all mostly related to the respiratory care of the preterm infant, there is still a tremendous need to improve current ventilation strategies. Recent studies suggest that a positive end-expiratory pressure (PEEP) plays an important role in protecting against lung injuries [31]. However, its influence on the development of a functional residual capacity (FRC) is still under debate [26, 32], and many efforts are currently put in the conception of causal relation.

2.5 ROLE OF SMALL ANIMAL IMAGING

Most of the nowadays available knowledge about human lungs (or more generally, the mammalian respiratory system) comes from animal studies. The fact that parts of the saccular developmental stage and the complete stages of alveolar and the microvascular development (see Tab. 2.1) in rodents like rats and mice occur postnatally, has made them commonly used

animal models where different stages of the lung development can be studied on a day-by-day basis in postnatal animals. Despite the similarities in the proportional shape of the gas exchange paths between rats and human lungs, making them physiologically very similar [33], there also exist certain differences, indicating that direct links between animals and humans cannot be derived in a straight-forward way [2].

Particularly in imaging, animal studies have played an exceptional role as they enable various functional, metabolic and molecular processes as well as morphological structures to be observed *in vivo*. Due to the steady progress in non-invasive imaging techniques, many technologies (such as CT or MRI) are nowadays available for dedicated small-animal studies [34]. In human lung imaging X-ray CT still represents the imaging modality of choice being the most sensitive way to image lungs *in vivo*, as stated in a recent review by van Rikxoort and van Ginneken [35]. However, the relatively low resolution and the fact that single alveoli are much too small to be seen in clinical CT, has brought small-animal lung imaging stronger into focus. Thus, techniques such as micro-CT, positron emission tomography (PET), fluorescence imaging and many more are commonly employed for studying ventilation, perfusion, pulmonary hypertension, lung inflammation and so forth. Herein, the availability of transgenic and knockout mice has contributed to an increased importance of these technologies, while the ability to manipulate the mouse genome to produce models of many human diseases has resulted in significant progress in understanding them. However, novel imaging methods are often required to exploit the full potential of these new mouse models, particularly for investigating disease progression and response to therapeutic agents [36].

As a last point, we want to note some general aspects of animal handling in animal experiments. As emphasized in [34], scientists dealing with animals have to bear in mind the so-called “3R principle”, i. e. the constant effort to *replace* animal studies when possible, *reduce* the number of used animals and *refine* the technique in order to reduce potential pain and stress in the animals, whenever possible. Thus, the planning and realization of animal experiments has to be taken with special care and often requires a huge amount of effort. This is why the development and application of longitudinal experimental techniques always plays a special role, where high statistical power can be achieved with a reduced number of animals, i. e. having animals as their own controls.

X-ray imaging

In the following chapter we introduce the basics of synchrotron-based X-ray imaging and mainly follow the descriptions from [37–40], whereas explicit references are given when necessary. Starting from the production of X-rays and their different interactions with matter, we introduce some basic coherence methods that are utilized at third-generation synchrotrons, until finally describing the theory of computed tomography (CT) with the accompanying post-processing steps being utilized in the underlying work.

3.1 X-RAY SOURCES

3.1.1 X-ray tube

The X-ray tube, introduced by Röntgen more than 100 years ago [41], is a vacuum tube in which electrons are accelerated with a high voltage onto a target (metal anode). When impinging on the target, they are abruptly decelerated and emit two kinds of electromagnetic (EM) radiation. One part corresponds to the so-called *bremstrahlung* which follows from the fact that any *accelerated* particle emits continuous EM radiation which is limited by the maximum kinetic energy of the accelerated electrons (and thus the applied tube voltage). Additionally to this component, a sharp line spectrum is superimposed, the so-called *characteristic X-ray* (fluorescent) radiation. This originates from the fact that the accelerated electrons can “remove” shell (atomic) electrons of the target’s material causing a vacancy in the target’s atomic structure. The subsequent relaxation of an electron from an outer shell into this vacancy leads to the emission of a characteristic (fluorescent) photon. The basic principle of X-ray creation is sketched in Fig. 3.1. As illustrated, two voltages are necessary, one for the emission of the electrons and the other for their acceleration towards the anode material. X-ray tubes are nowadays realized in different designs and widely used in various applications.

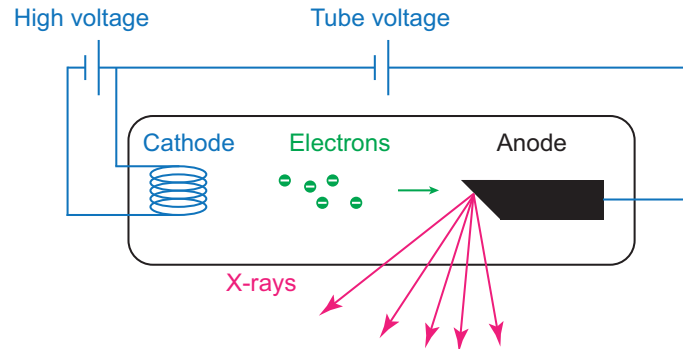


Figure 3.1. Principle of X-ray creation in an X-ray tube. Electrons are created by a heated cathode and subsequently accelerated by an applied tube voltage towards the anode. Due to the rapid electron deceleration when impinging on the anode material, X-rays are emitted in the perpendicular direction.

3.1.2 Synchrotron-based X-ray sources

As mentioned above, accelerated charged particles emit radiation with certain power characteristics. If the order of acceleration is significantly increased so that these particles approach the speed of light and thus by their nature become relativistic, it can be shown that radiation with particular characteristics is produced. This is achieved by forcing the charged particles to move on a circular trajectory where constantly a centripetal force (acceleration) must be applied to keep them on the circular track. By doing so, they will constantly emit electromagnetic radiation. This fact represents the basic principle of nowadays available synchrotron sources, and historically it was first observed as an (unwanted) energy loss in particle accelerators and storage rings. In course of time, dedicated (so-called *second generation*) synchrotron sources were constructed, while the newest *third-generation synchrotrons* are characterized by their heavy use of straight sections and so-called insertion devices.

Accordingly, three types of magnetic structures are commonly used for producing synchrotron radiation. We start with the discussion on the bending magnet, which is the X-ray source used at the TOMCAT beamline. Besides, bending magnets are present in every synchrotron as they are used to deflect the electrons to create in total a spherical trajectory (“ring”). Insertion devices, on the other hand, represent periodic magnetic structures that are placed into so-called straight sections of the synchrotron, as we discuss below.

Before going further, we first introduce some common units of interest that are used to characterize synchrotron sources [42]:

$$F = \frac{[\text{number of photons}]}{[\text{s}][0.1\% \text{ bandwidth}]} \quad \longrightarrow \quad (\text{“Flux”})$$

$$B = \frac{[\text{number of photons}]}{[\text{s}][\text{mrad}^2][\text{mm}^2][0.1\% \text{ bandwidth}]} \quad \longrightarrow \quad (\text{“Brightness”})$$

The flux F gives the total X-ray photon fluence, while the brightness B does so per unit beam size and unit solid angle.

The brilliance on the other hand is used to compare various X-ray sources to each other by including further source-specific parameters such as emittances, all summarized in the following under the term *optical source area*:

$$\text{Brilliance} := \frac{\text{Brightness}}{\text{Optical source area}}.$$

Bending magnet

Synchrotrons are storage rings that keep charged particles (electrons or positrons) at a constant speed (energy) and force them to move on a circular (more precisely: polygonal) trajectory. The energy of such a charged particle can then be written as:

$$E = \gamma mc^2 \quad \text{with} \quad \gamma = \sqrt{\frac{1}{1 - \beta^2}}, \quad (3.1)$$

with particle mass m , speed of light c and $\beta = v/c$ representing the fraction of the electron's velocity in respect to the speed of light. Obviously, for relativistic particles β will be close to 1 with $\gamma \gg 1$. To make the circular trajectory possible, magnetic fields perpendicular to the horizontal orbital plane are used. These can be e. g. coils fed with electric current, but commonly they are permanent magnets with a magnetic field B . The force acting on the charged particle is then given as

$$\mathbf{F} = e\mathbf{v} \times \mathbf{B}, \quad (3.2)$$

resulting in an acceleration perpendicular to the direction of the velocity \mathbf{v} (where e is the charge of the particle). It is called the *Lorentz force*. Large accelerations are obtained if particles with small rest masses such as electrons are used. The necessary magnetic field for causing a certain deflection can be calculated from the given radius of curvature ρ and the particle's energy:

$$\rho = \frac{m\gamma v^2}{F} \approx \frac{m\gamma c}{eB} \quad (3.3)$$

yielding values in the order of a few Teslas for the magnetic field B and particle energies of a few GeV.

The aforementioned relativistic treatment of the electrons yields a sharply-peaked cone in the direction of motion of the radiating charge with the opening angle θ given as:

$$\theta \approx \frac{1}{2\gamma}. \quad (3.4)$$

Thus, the factor $1/\gamma$ represents a typical opening angle of the radiation emitted from a bending magnet. The spectral characteristics are derived in a similar way and depend on the detailed motion over a time interval. From the fact that the radiation is emitted in a very sharp cone, it follows that there is a very short time interval under which the radiation can be observed from a particular tangential direction. Taking ρ as the radius of curvature, this interval can be written as:

$$2\tau = \frac{\rho}{c} \left| \frac{2}{\gamma\beta} - 2 \sin\left(\frac{1}{\gamma}\right) \right| \approx \frac{4\rho}{3c\gamma^3}. \quad (3.5)$$

By making use of Eq. (3.3) and the fact that $\omega = \tau^{-1}$, we arrive at the definition of the so-called *critical frequency*, given as follows:

$$\omega_{\text{crit}} = \frac{3\gamma^3 c}{2\rho} \quad \longrightarrow \quad E_{\text{crit}} [\text{keV}] = \frac{3ehB\gamma}{2m} \approx 0.6650E_e^2 [\text{GeV}] B [\text{T}]. \quad (3.6)$$

With this short derivation and by utilizing Heisenberg's uncertainty relation, it follows that a bending magnet emits a broadband energy spectrum, where the critical energy represents the median photon energy. This means that the number of photons above the critical energy corresponds to the number of photons that are emitted below.

With this, we can now formulate the formula for the aforementioned brightness:

$$B [\text{photons/s/mrad}^2/0.1\% \text{ bandwidth}] = 1.327 \times 10^{13} I [\text{A}] E^2 [\text{GeV}] H_2\left(\frac{E}{E_{\text{crit}}}\right), \quad (3.7)$$

with

$$H_2(y) = y^2 K_{2/3}^2\left(\frac{y}{2}\right). \quad (3.8)$$

where $K_{2/3}$ is the modified Bessel function of second kind. If we now integrate this formula over the vertical beam opening angle by considering the vertical angular divergence in dependence on the beam energy [42], we obtain the formula for the so-called *vertically integrated flux*:

$$F [\text{photons/s/mrad}/0.1\% \text{ bandwidth}] = 2.457 \times 10^{13} I [\text{A}] E [\text{GeV}] G_1\left(\frac{E}{E_{\text{crit}}}\right), \quad (3.9)$$

with

$$G_1(y) = y \int_y^\infty K_{5/3}(y') dy'. \quad (3.10)$$

More detailed expressions for characterizing bending magnet radiation (such as polarization, angular density etc.) is found in the literature [42–44]. We end the description on

bending magnets by showing the characteristic white beam radiation produced at the TOMCAT beamline in Fig. 3.2 and summarizing the beamline parameters in Tab. 3.1.

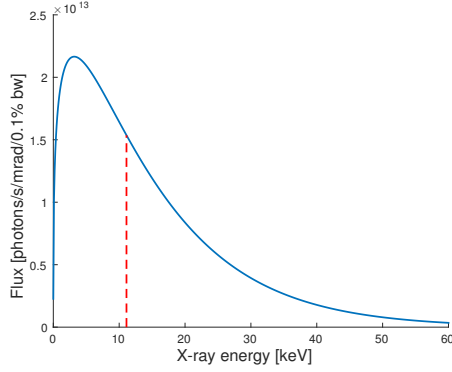


Figure 3.2. TOMCAT white beam spectrum. The red line indicates the critical energy.

Table 3.1. TOMCAT beamline parameters.

Parameter	Value
Magnetic field	2.9 T
E_{crit}	11.1 keV
Energy (ring)	2.4 GeV
γ	4697
Ring current I	400 mA
horizontal divergence	2.0 mrad
vertical divergence	0.6 mrad

Insertion devices

In analogy to the case of bending magnets where electrons are deflected to keep them on a circular trajectory, a transverse periodic structure according to the definition of the Lorentz force can induce harmonic oscillations to the electrons, thus forcing them to emit radiation each time they oscillate. This simple principle represents the basis for synchrotron radiation being created with so-called (multipole) *insertion devices*. These are installed in so-called straight-sections in synchrotrons, whereas each straight section is followed by a bending magnet.

Depending on the angular amplitude of these oscillations we can define two separate cases. If the radiation pattern of the emitted radiation can be described by a simple (incoherent) sum of the individual radiation fields coming from each oscillation (imposed by each individual magnet), the device is called a **wiggler**. Hence, a wiggler can be thought of as a composition of multiple (small) bending magnets, so that its radiated beam characteristics are the same as the one coming from a bending magnet with the same magnetic field. If, however, the angular deviation of the electron trajectory is very small and can be approximated by the previously introduced photon emission angle $1/\gamma$, we refer to the insertion device as an **undulator**. In this case the amplitudes of the radiation fields that are emitted from each single magnet interfere and result in a periodic radiation field. As a consequence, undulators exhibit narrow bandwidth radiation at well defined energies (harmonics).

In a more detailed mathematical treatment, the optical properties of the two insertion devices are distinguished by the definition of the dimensionless magnetic strength K for a periodic magnet parameter:

$$K = \frac{e\lambda_u B_0}{2\pi mc} \approx 0.934 \lambda_u [\text{cm}] B_0 [\text{T}], \quad (3.11)$$

where λ_u is the period of the oscillations, B_0 the amplitude of the magnetic field, e the electron charge, m the electron mass and c the speed of light. It can be shown that wigglers are described by large K -values ($K \gg 1$) while undulators represent low K -devices (with $K \approx 1$).

Finally it should be noted that the upcoming free-electron lasers (FEL-s) basically comply to the undulator regime with the difference that additionally the electron fields are well correlated (referred to as *micro-bunching*) so that the resulting radiation fields add up coherently (rather than their intensities, as in the undulator case).

3.2 X-RAY INTERACTION WITH MATTER

The way X-rays interact with matter represents the starting point of our further discussion. It serves as the basis for the theoretical understanding of nowadays established coherence methods in X-ray imaging and microscopy as well as all accompanying aspects such as optical elements and X-ray instrumentation.

X-rays, just like visible light, are electromagnetic waves with wavelengths in the order of an angstrom ($1 \text{ \AA} = 10^{-10} \text{ m}$). Thus, like all other quantum particles, they exhibit both particle and wave-like properties, and the relationship between wavelength λ and X-ray energy E can be written as follows:

$$\lambda = \frac{hc}{E} \quad \rightarrow \quad \lambda [\text{\AA}] \approx \frac{12.398}{E [\text{keV}]}, \quad (3.12)$$

with Planck constant h and speed of light c . Often X-rays are characterized by their energy given in eV and/or keV (with $1 \text{ eV} = 1.602176565 \times 10^{-19} \text{ J}$), rather than by their wavelength. The reason is two-fold: on the one hand we always deal with some kind of particle accelerators when describing X-ray sources, so e. g. it is straight-forward to draw the connection between a tube voltage of 10 kVp and from within the maximum available X-ray photon energy of 10 keV; on the other hand, when we describe interactions of X-rays with matter, the possible single processes that occur at an atomic level are highly dependent on the energy of individual X-ray photons.

Broadly speaking, (X-ray) photons can interact with atoms in two different ways. They can either be *scattered* (elastically or inelastically) or they can be *absorbed*, thus transferring their energy to the atoms. In the view of interfaces of different materials or their aggregation states, X-rays can also be *refracted* or *reflected*, which in this sense is equivalent to scattering. Likewise, *diffraction* refers to scattering from relatively well-defined (e. g. periodic) structures. In sum, after interacting with matter, the initial X-ray photon fluence will be decreased, due to the deflection or the absorption of incoming X-rays. This aspect is best described through the definitions of the mass attenuation coefficients and photon interaction cross-sections, respectively. Either of them is employed in the Beer-Lambert-Bouguer law (often referred to as “Beer’s law”) that describes the intensity I of a monochromatic X-ray beam after penetrating a layer of material:

$$I = I_0 e^{-\mu x} = I_0 e^{-\left(\frac{\mu}{\rho}\right) \rho x} \quad (3.13)$$

where I_0 is the intensity of a monochromatic X-ray beam before penetrating the layer of material with thickness x and density ρ , I is the intensity after penetration and μ is the energy- and material-dependent *linear attenuation coefficient*. The factor μ/ρ is called the *mass attenuation coefficient* and can be written in relation to the *total cross section per atom* σ_{tot} as follows:

$$\mu_m = \frac{\mu}{\rho} = \frac{\sigma_{\text{tot}}}{uA} \quad (3.14)$$

where u is the atomic mass unit, defined as one twelfth of the mass of an unbound neutral atom of ^{12}C in its nuclear and electronic ground state [$1 u = 1.660538921(73) \times 10^{-27} \text{ kg}$] and A is the relative atomic mass of the target element, i. e. the number of atomic mass units. Its use is more purposeful as it is typical of the absorbing material but independent on its aggregate state, e. g. the mass attenuation coefficient μ_m for water and steam will be the same while the linear absorption coefficient μ will differ.

All principal photon interactions can then be written as a sum contributing to the total cross section σ_{tot} :

$$\sigma_{\text{tot}} = \sigma_{\text{pe}} + \sigma_{\text{coh}} + \sigma_{\text{incoh}} + \sigma_{\text{pair}} + \sigma_{\text{trip}}, \quad (3.15)$$

where σ_{pe} is the cross section of the atomic *photoelectric absorption*, σ_{coh} and σ_{incoh} are the *coherent* (elastic) and *incoherent* (inelastic) scattering cross sections, σ_{pair} is the cross section for the electron-positron *pair production* of the nucleus and σ_{trip} is the one of *triple production* (two electrons, one positron) of the atomic electrons [45]. In the following we limit ourselves to the former three contributions which are the only dominant at photon energies between 1–100 keV, while the pair and triple productions cross sections are relevant at photon energies higher than 1 MeV. These principal cross sections as well as the total one are depicted in Fig. 3.3 for the X-ray energy range of 1–120 keV. In the following for each of these interactions we give a short description and indicate their significance for the different imaging methods.

3.2.1 Photoelectric absorption

We start with the simplest of all interaction processes, being best illustrated by the atomic *aufbau principle*. Therein each electron within an atom occupies a certain orbital (shell), characterized by a certain energy level E_n . An X-ray photon with a sufficient energy $E_{\text{ph}} = h\nu$ gets absorbed by the atom by transferring its energy to one of the shell electrons. Subsequently, the electron leaves the atom with a kinetic energy that is equal to the photon energy E_{ph} minus its binding energy E_n , leaving the atom ionized. The emitted electron is termed *photoelectron*, while the entire process is called *photoelectric absorption*.

After having produced an atom with a core vacancy, the vacancy is filled with an electron from a higher shell. There are now two types of subsequent processes that may occur. Firstly, the excess energy that was created after the electron recombination from the upper shell can result in the emission of a so-called *characteristic X-ray photon* exhibiting a characteristic energy corresponding to the energy difference of the two shells; alternatively, the excess energy

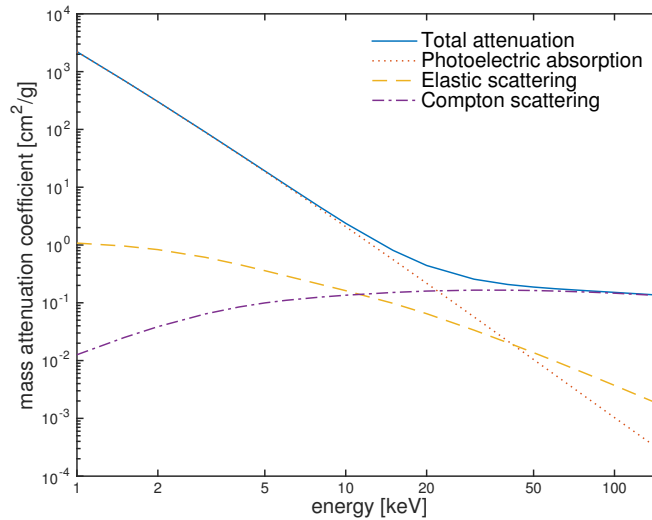


Figure 3.3. Total mass attenuation coefficient for carbon with individual contributions from other principal cross sections. The data is extracted from the XCOM database [45].

can be transferred to an electron from an even higher shell that is emitted in return with a characteristic energy, as well. The former process is termed *fluorescent emission*, while the latter one is known as the *Auger effect*. Naturally, these processes are competing, however, fluorescent emission has a much higher probability in materials with increasing atomic numbers Z . Nevertheless, both effects can be employed in various techniques for studying material compositions and properties.

In a macroscopic view, the intensity through the sample fulfills the aforementioned Beer-Lambert-Bouguer law and is quantitatively given by the *linear absorption coefficient*. A first empirical evaluation for showing the monochromatic nature of fluorescent X-rays has been derived by Moseley (*Moseley's law*), showing that each atom leaves a unique fingerprint by its fluorescence radiation. A unified treatment is derived from Schrödinger's wave equation.

3.2.2 Scattering

As we learned above, photoelectric absorption occurs when a(n) (X-ray) photon transfers its energy to a bound electron which in return overcomes its potential energy to leave the atom. If considering now for a moment a free (unbound) electron, we can identify an alternative occurring process, namely in the sense that the electron is caused to oscillate at the frequency imposed by the electromagnetic (EM) field of the passing electromagnetic wave. In view of electrodynamics theory, the electron (more generally: any charged particle) itself radiates a photon of the same energy (frequency). A similar effect also applies to the case of bound electrons, and from this brief description it follows that the actual origin of a *scattered* X-ray photon can be described as the resonant oscillatory response of an electron, impressed

by a primary EM-field. This is equivalent to a corpuscular view of photons and electrons where both the conservation of momentum and the conservation of energy apply. Thus it is self-explanatory that we can immediately define two kinds of scatterings, namely the *elastic scattering* where the scattered X-rays have the same energy (wavelength) and the so-called *inelastic scattering* where the energy (wavelength) of the primary X-ray is altered after being scattered.

With the above explanation, we have noted the most simplified but fundamental principle of X-ray scattering. The complete scattering theory, including the process of photoelectric absorption, is fully covered within quantum theory and explains the connected nature of X-ray refraction, reflection and absorption. However, for understanding and quantifying the basic phenomena, generally a semi-classical approach is sufficient, e. g. it has been shown that elastic scattering can be described solely in view of a semi-classical approach yielding the same result as a quantum mechanical treatment [46, p. 140].

Elastic scattering

We pick up on the statement from above to derive two fundamental quantities by a simplified approach. In doing so, we consider a single electron that is bound to an atom by a restoring central force coming from the positively charged nucleus. In classical mechanics this problem is known as the *harmonic oscillator* and the equation of motion reads as:

$$m_e \frac{d^2 \mathbf{x}}{dt^2} + m_e \gamma \frac{d\mathbf{x}}{dt} + m_e \omega_s \mathbf{x} = -e(\mathbf{E} + \mathbf{v} \times \mathbf{B}_i), \quad (3.16)$$

where the first term represents the acceleration of the electron with mass m_e , the second one is a dissipative force that takes into account energy losses (while we assume that $\gamma/\omega_s \ll 1$), the third term represents the restoring force of the oscillator with resonant frequency ω_s and the right-hand side term is the Lorentz force impressed by the EM-field of the impinging photon (i. e. X-ray wave).

It can be shown that a solution to the above equation can be obtained by assuming

$$\mathbf{E} = \mathbf{E}_i e^{-i\omega t} \quad \text{and} \quad \mathbf{x} = \mathbf{x}_0 e^{-i\omega t}, \quad (3.17)$$

where the first term represents a valid solution to Maxwell's equations. After inserting these expressions in Eq. (3.16) and taking into account that the second term of the right-hand side can be neglected because

$$\mathbf{v} \times \mathbf{B}_i = \frac{1}{c} [\mathbf{v} \times \mathbf{k}_0 \times \mathbf{E}(\mathbf{r}, t)] \sim \mathcal{O}(v/c), \quad (3.18)$$

which is negligible for non-relativistic oscillation velocities, we obtain:

$$m_e (-i\omega)^2 \mathbf{x}_0 + m_e \gamma (-i\omega) \mathbf{x}_0 + m_e \omega_s^2 \mathbf{x}_0 = -e\mathbf{E}. \quad (3.19)$$

Subsequently the final solution reads as:

$$\mathbf{x}_0 = \frac{1}{\omega^2 - \omega_s^2 + i\gamma\omega} \cdot \frac{e\mathbf{E}}{m_e}. \quad (3.20)$$

This result is used to derive the expression for the semi-classical *scattering cross-section* for a bound electron with resonant frequency ω_s :

$$\sigma_{\text{scat.}} = \frac{8\pi}{3} r_e^2 \frac{\omega^4}{(\omega^2 - \omega_s^2)^2 + (\gamma\omega)^2}, \quad (3.21)$$

with classical electron radius

$$r_e = \frac{e^2}{4\pi\epsilon_0 mc^2}. \quad (3.22)$$

We now distinguish between two simplifying conditions. First we revisit the previously mentioned case of a “free” electron, where both the dissipative energy loss and the restoring force are zero, so that $\omega_s = 0$ and $\gamma = 0$. For the scattering cross-section we then obtain

$$\sigma_{\text{scat.}} = \frac{8\pi}{3} r_e^2, \quad (3.23)$$

which represents the so-called *Thomson cross-section*.

Alternatively, if we consider frequencies much smaller than the resonant one so that $\omega \ll \omega_s$, we obtain:

$$\sigma = \frac{8\pi}{3} r_e^2 \left(\frac{\omega}{\omega_s} \right)^4 \sim \frac{1}{\lambda^4}, \quad (3.24)$$

known as the so-called *Rayleigh cross-section*.

While Thomson scattering occurs at free electrons and is independent on the wavelength, Rayleigh scattering exhibits a strong wavelength-dependence and becomes imprecise near resonances. Both contributions, however, are elastic and add up coherently in definite phase relations to each other. That said, they represent the main effects exploited in the investigation of structure as we will show below.

Inelastic scattering

While coherent scattering follows completely from the predictions of electrodynamics theory, the very same becomes invalid within a quantum mechanical description where the dualistic nature of the photon is considered. Therein, an atom is more accurately described as being excited first from state k to an intermediate state s , associated with an absorption of energy, then followed immediately by a transfer from state s to state l , where a quantum with

a different energy is radiated again. In this view, scattering becomes a process of absorption and emission similar to fluorescence, and the emitted radiation is *incoherent* because it represents transitions from one magnetic state of the electron to another. Historically this kind of scattering, so-called *Compton scattering*, was first observed at free electrons as an additional component to the aforementioned Thomson scattering, where a frequency (wavelength) shift of the scattered radiation was found. At that time, this insight gave a fundamental support for the emerging quantum theory [37]. Later, the concept has been theoretically described by the Klein-Nishina cross-sections, where relativistic quantum mechanics were taken into account and are used today for calculating the intensity of scattered rays [47]. As a final remark, Compton scattering occurs at a very broad energy range for both bound and free electrons. At higher energies it contributes significantly to the total cross-section (as shown in Fig. 3.3).

3.3 PHASE-CONTRAST IMAGING

We now put the X-ray image formation on a theoretical basis by introducing the complex refractive index for X-rays. We continue by presenting some common approximations made in X-ray phase imaging to find an appropriate formulation of the phase problem, which represents the starting point for all phase retrieval methods in X-ray phase contrast imaging. Finally we give an overview of the currently applied phase retrieval methods until reaching the point to introduce the methods utilized in the present work.

Complex index of refraction

Although we have only treated a single-electron atom so far, the step towards multi-electron atoms and interactions with electrons from multiple atoms (i. e. molecules) is conducted by considering that each electron responds differently to the impressed EM-field of the X-rays. A detailed (semi-classical) treatment of a multi-electron atom leads e. g. to the definition of the *complex atomic scattering factor*:

$$f(\Delta\mathbf{k}, \omega) = \sum_{s=1}^Z \frac{\omega^2 e^{-i\Delta\mathbf{k} \cdot \Delta\mathbf{r}_s}}{\omega^2 - \omega_s^2 + i\gamma\omega} \quad (3.25)$$

where ω_s are the resonance frequencies of the single electrons located at r_s positions, $\Delta\mathbf{k}$ is the difference between the incident wave vector and the one of the scattered field, and the exponential term describes the phasor of the scattered fields due to differing electron positions. In general, the atomic scattering factor describes the amplitude of the wave scattered from an atom in a certain direction, relative to the one which would be scattered in that direction by a free electron [37, p. 300]. That said, the *total scattering cross-section* is then defined in analogy to Eq. (3.21):

$$\sigma = \frac{8\pi}{3} |f|^2 r_e^2. \quad (3.26)$$

If we now consider only the contribution at angle zero (according to the so-called *optical theorem*), for which $\Delta\mathbf{k} \cdot \Delta\mathbf{r}_s \rightarrow 0$, we arrive at the *forward scattering factor*, consisting of a real and a complex part:

$$f^0(\omega) = \sum_{s=1}^Z \frac{g_s \omega^2}{\omega^2 - \omega_s^2 + i\gamma\omega} = f_1^0(\omega) - if_2^0(\omega), \quad (3.27)$$

where g_s has now been included to account for transition probabilities (oscillator strengths) for the single electrons.

A further detailed treatment of EM-wave propagation in a medium where according to dispersion theory the dielectric constant is expressed as a complex quantity leads to the definition of the complex index of refraction, which is directly related to the above forward scattering factor:

$$n(\omega) = 1 - \delta + i\beta = 1 - \frac{n_a r_e \lambda^2}{2\pi} (f_1^0 - if_2^0). \quad (3.28)$$

Finally, the two values directly relate to the absorption coefficient and the phase shift of a material by (each with different proportionality to the X-ray energy E):

$$\mu = \frac{4\pi\beta}{\lambda} \approx \mathcal{O}\left(\frac{1}{E^3}\right) \quad \longrightarrow \quad (\text{“absorption coefficient”}) \quad (3.29)$$

$$\phi = \frac{2\pi\delta}{\lambda} \approx \mathcal{O}\left(\frac{1}{E}\right) \quad \longrightarrow \quad (\text{“change of phase”}). \quad (3.30)$$

$$(3.31)$$

Image formation

With the advent of first industrial X-ray sources the basics of X-ray science have been developed in the first half of the 20th century. The main interaction processes between X-rays and matter have been studied ever since and found different ways of application. In parallel, with the development of first lasers in the 1960s, optical coherence theory came more and more into focus [48]. Soon after, first studies were performed that investigated the question how phase changes from coherent and incoherent X-ray sources could be measured and eventually inverted (“phase retrieved”) for a better characterization of materials structures. It was only with the design and construction of first high-brilliant X-ray sources and the advent of third-generation synchrotrons in the mid 1990s that X-ray phase contrast has gathered a lot of interest. Consequently, tremendous efforts in developing new techniques could be observed within the last two or three decades.

We refresh our discussion from before by stating that X-ray interaction with matter is best described through the introduction of the complex index of refraction. An electromagnetic (plane) X-ray wave, after having passed through an object, can then be written as:

$$\mathbf{E}(\mathbf{r}, t) = \mathbf{E}_0 e^{-i(\omega t - \mathbf{k} \cdot \mathbf{r})}, \quad (3.32)$$

and by including the following substitution

$$\frac{\omega}{k} = \frac{c}{n} = \frac{c}{1 - \delta + i\beta} \quad (3.33)$$

we obtain:

$$\mathbf{E}(\mathbf{r}, t) = \underbrace{\mathbf{E}_0 e^{-i\omega(t-r/c)}}_{\text{vacuum propagation}} \cdot \underbrace{e^{-i(2\pi\delta/\lambda)r}}_{\phi\text{-shift}} \cdot \underbrace{e^{-(2\pi\beta/\lambda)r}}_{\text{decay}}. \quad (3.34)$$

Thus, the wave-object interaction is described as a transmittance function by which an electromagnetic wave that propagates through vacuum (first term) undergoes a phase shift (second term), induced by the medium after traveling a distance r , and finally decays in its amplitude (third term) which again is dependent on r due to the aforementioned Beer–Lambert–Bouguer law. In the following we adopt a somewhat different notation usually employed in related literature and for simplicity reasons disregard the time-dependency, as we are only interested in stationary fields [49–52]. The above equation then reads as

$$T(\mathbf{r}) = |T(\mathbf{r})| e^{-i\phi(\mathbf{r})} = e^{-\mu(\mathbf{r}) - i\phi(\mathbf{r})} \quad (3.35)$$

and is called the *transmission function*, where T is the complex wave-field at the exit plane of the object. In this formulation both the Born and the projection approximations were adopted, which are very well obeyed in all applications to date [52]. While the Born approximation represents a rather general formulation in quantum theory by which the incident and scattered fields can be separated, the projection approximation assumes a *thin* object so that both the absorption and phase shift induced by the object can be considered as projections through it (along the z -direction) and written in the form of line integrals:

$$\mu(\mathbf{r}) = \frac{2\pi}{\lambda} \int \beta(x, y, z) dz \quad \text{and} \quad \phi(\mathbf{r}) = -\frac{2\pi}{\lambda} \int \delta(x, y, z) dz. \quad (3.36)$$

where β and δ are the imaginary and real part of the refractive index, respectively.

After passing through, the intensity pattern at further distances from the object can be obtained by the use of the Fresnel propagator, while being called the *Fresnel diffraction pattern*. Later, in Sec. 4.2, we give a detailed overview of the conditions and approximations that need to be conducted to derive the formalism. Therefore in the following it is enough to state that the recorded intensity field I (i. e. the image at the detector) at a distance D from the object's exit plane is given as follows:

$$I_D(\mathbf{r}) = |T(\mathbf{r}) \otimes P_D(\mathbf{r})|^2, \quad (3.37)$$

with the Fresnel propagator

$$P_D(\mathbf{r}) = \frac{1}{i\lambda D} \exp\left(i \frac{\pi}{\lambda D} |\mathbf{r}|^2\right). \quad (3.38)$$

Thus, the intensity at a random propagation distance D is given by the convolution of the exit wave field with the Fresnel propagator. Following the theory of Fourier transformations, this expression significantly simplifies after a transformation to the Fourier space. We denote $\hat{I}_D(\mathbf{f})$ the Fourier transform of $I_D(\mathbf{r})$, which then reads as [49]:

$$\hat{I}_D(\mathbf{f}) = \int T\left(\mathbf{x} - \frac{\lambda D \mathbf{f}}{2}\right) T^*\left(\mathbf{x} + \frac{\lambda D \mathbf{f}}{2}\right) \exp(-2\pi \mathbf{x} \cdot \mathbf{f}) d\mathbf{x}. \quad (3.39)$$

If $\hat{T}(\mathbf{f})$ is the Fourier transform of the transmission function from Eq. (3.35), the convolution from above transforms to multiplicative terms [50]:

$$\hat{I}_D(\mathbf{f}) = e^{ikz} \hat{T}(\mathbf{f}) \hat{P}_D(\mathbf{f}), \quad (3.40)$$

where $\hat{P}_D(\mathbf{f})$ is the Fresnel propagator given in Fourier space:

$$\hat{P}_D(\mathbf{f}) = e^{-i\pi\lambda D|\mathbf{f}|^2}, \quad (3.41)$$

which is often referred to as the *optical transfer function* of free-space propagation.

So far we have strictly considered a coherent plane wave. However, as we explain in Sec. 4.2, synchrotron-emitted X-rays are only partially coherent, which mathematically can be described by the so-called mutual intensity function [53]. It describes the statistical similarity (thus spatial coherence) of the X-ray wavefields at two positions and thus gives the distance over which correlations are reduced to some predetermined level. In the case of the above equations we can define the *transverse coherence length* l_c as:

$$l_c = \frac{2}{\pi} \frac{\lambda R}{\sigma} \quad (3.42)$$

where R is the distance to the X-ray source, σ is the source size and λ the wavelength. With the definition of the coherence function

$$g(\mathbf{r}) = \exp\left[-\frac{|\mathbf{r}|^2}{l_c^2}\right] \quad (3.43)$$

the previously obtained intensity pattern in Eq. (3.40) transforms to

$$\hat{I}_D(\mathbf{f}) = e^{ikz} \hat{g}(\mathbf{f}) \hat{T}(\mathbf{f}) \hat{P}_D(\mathbf{f}). \quad (3.44)$$

where \hat{g} is now the Fourier transform of the function g .

With this we now can conclude the section as follows. Coherent X-rays, after interacting with matter, will have a well-defined amplitude and phase distribution described by the transmission function. By wave propagation, a quantitative relationship between the phase shift induced by the object and the recorded intensity pattern can be established, which is generally

referred to as a *phase-contrast image*. Due to partial coherence, however, the visibility of phase-contrast images will be reduced, in particular the high spatial frequencies of the images, which is why coherence *per se* represents the most fundamental quantity in phase-contrast imaging [54, 55]. In relation to the detector's pixel size it has to be several times higher in order to observe phase effects as described above. Estimating the (vertical) coherence length at the TOMCAT beamline (with results obtained in Sec. 4.2) yields approximately $l_c \approx 20 \mu\text{m}$ and ultimately justifies the usage of a synchrotron X-ray source in order to achieve the envisaged resolutions in our phase-contrast images.

Phase retrieval methods

With the above formalism we have now derived the so-called *forward model* in (propagation-based) phase-contrast imaging. As shown therein, the formation of a phase-contrast image is the result of coherent X-ray beams impinging on a sample. The task of *phase retrieval* is now to retrieve the phase shift in the transmission function Eq. (3.35), i. e. to obtain a term which is proportional to (or in the best case represents) the electron density of the sample. For doing so, the goal is to invert Eq. (3.39). In the following we limit ourselves to two approaches that are commonly used in order to discuss some basic properties.

In the so-called **CTF-formulation**, the forward model is simplified by assuming a weak absorption and slowly varying phase shift, meaning that both δ and β are relatively small, which can be used for a Taylor expansion by omitting higher order terms. Thus we can first approximate the transmission function from Eq. (3.39) as follows:

$$T(\mathbf{r}) \approx 1 - \mu(\mathbf{x}) + i\phi(\mathbf{x}), \quad (3.45)$$

and after substituting into Eq. (3.39) we obtain:

$$\hat{I}_D = \delta(\mathbf{f}) - \underbrace{2 \cos(\pi\lambda D|\mathbf{f}|^2) \hat{\mu}(\mathbf{f})}_{\text{amplitude contribution}} + \underbrace{2 \sin(\pi\lambda D|\mathbf{f}|^2) \hat{\phi}(\mathbf{f})}_{\text{phase contribution}} \quad (3.46)$$

where $\delta(\mathbf{f})$ is the unit impulse function, $\hat{\mu}(\mathbf{f})$ is the Fourier transform of the absorption and $\hat{\phi}(\mathbf{f})$ is the Fourier transform of the phase. As shown, the image formation process under the above assumption is described by taking the Fourier transform of the transmission function and by multiplying it with another complex function. This function is called the *contrast transfer function* and has a real and imaginary part. It can be shown that the main condition of the above derivation, namely the assumption of a weak object interaction, can also be reformulated by putting a less restrictive condition of a “weak absorption” and ”slowly varying phase” [49]:

$$\mu(\mathbf{r}) \ll 1 \quad \text{and} \quad |\phi(\mathbf{r}) - \phi(\mathbf{r} + \lambda D\mathbf{f})| \ll 1. \quad (3.47)$$

The above expression represents the starting point of all CTF-based phase-retrieval methods, which are well-described in many works [51, 56–58]. For us, the result inhibits two important

aspects. On the one hand, due to the sinusoidal term in Eq. (3.46) the phase contribution has a zero-crossing at propagation distance zero, meaning that at low propagation distances D there will be no phase information, but it also underlines the fact that phase-retrieval methods are prone to artifacts at low frequencies \mathbf{f} (which we discuss later). The other aspect can be described by assuming a small propagation distance D . In such a case the CTF in Eq. (3.46) can be linearized. After doing so and inverting it we obtain [52]:

$$I_D(\mathbf{r}) = 1 - 2\mu(\mathbf{r}) - \frac{D}{k} \nabla^2 \phi(\mathbf{r}), \quad (3.48)$$

which describes the recorded Fresnel diffraction image in the so-called “near-field” having an additional Laplacian (second derivative) of the phase. Thus, after a small propagation distance, one can observe additional details in the recorded images, mainly visible at the edges, which later on we refer to as the *edge-enhancement regime*. Apart from this regime, there also exists the *holographic regime*, explained in detail in [53], which for our case plays no significant role.

In the alternative **transport-of-intensity** (TIE) approach, the transmission function in Eq. (3.39) is linearized in respect to the propagation distance D , again by a Taylor expansion and by leaving out higher-order terms:

$$T\left(\mathbf{r} \pm \frac{\lambda D \mathbf{f}}{2}\right) \approx T(\mathbf{r}) \pm \frac{\lambda D \mathbf{f}}{2} \cdot \nabla T(\mathbf{r}). \quad (3.49)$$

After substituting back into Eq. (3.39):

$$I_D(\mathbf{r}) = I_0(\mathbf{r}) - \frac{\lambda D}{2\pi} \nabla [I_0(\mathbf{r}) \nabla \phi(\mathbf{r})] \quad (3.50)$$

where I_0 is the intensity at $D = 0$. By considering again very small distances D only, the difference $[I_D(\mathbf{x}) - I_0(\mathbf{x})]/D$ can be approximated by a partial derivative, and the above equation transforms to:

$$\nabla [I_0 \nabla \phi(\mathbf{r})] = -\frac{2\pi}{\lambda} \frac{\partial}{\partial z} I_0(\mathbf{r}), \quad (3.51)$$

which is known as the so-called “transport-of-intensity equation”, originally introduced by Reed Teague [59]. It relates the propagation of the intensity distribution to the phase distribution in a wave in the paraxial approximation [60].

Although up to now we have only looked at the propagation-based (inline) formulation of phase-contrast imaging, its general idea should be clear. Coherent X-rays passing through a sample are changed in amplitude and phase, and “phase imaging” actually represents a technique of turning the phase-shifts introduced by the sample into intensity patterns that can be recorded with the detector.

In a recent review, Bravin et al. [61] give a detailed summary of the nowadays available phase-contrast techniques and identify five main categories. Basically, they state that it is not

possible to extrapolate data for an *a posteriori* evaluation and comparison of the techniques due to the huge variety of experimental conditions. All methods, however, can be viewed as being unified when aiming for “quantitative phase retrieval”, i. e. the reconstruction of the electron densities within an object [52, 55].

Single-shot intensity and phase extraction

So far we have introduced two different formulations of phase-contrast imaging, the CTF-approach and the TIE-approach. We have also seen that CTF-based methods are limited in the sense that they rely on weak-absorbing objects, which is a crucial limitation in our case when imaging whole animals, since a considerable amount of X-rays is also being absorbed. The TIE-approach, on the other hand, has been widely used in the field being well-suited for a wide range of objects and applications, however it was always limited to images at two different distances away from the object [62–64] in order to reconstruct the phase. However, Paganin et al. [65] in a later work showed how to solve the TIE-equation by using only a single defocused image and by assuming a homogeneous object, i. e. consisting of a single material. The advantages were obvious, namely that on the one hand it could be used for mixed objects (phase and absorption), even with a certain polychromaticity of the X-ray beams, and on the other hand it represented a so-called single-shot method being well suited for fast X-ray imaging. In the following we shortly discuss Paganin’s result with its features, as it has been the method of choice for all our experiments.

The assumption of a homogeneous object can be written as follows:

$$I_0 = I_{\text{in}} e^{-\mu T(\mathbf{r})} \quad \text{and} \quad \phi = -\frac{2\pi}{\lambda} \delta T(\mathbf{r}) \quad (3.52)$$

where I_{in} is the uniform intensity of the incident radiation and where $T(\mathbf{r})$ is the projected thickness, which in the case of a homogeneous object can be assumed to be proportional to the phase ϕ . Paganin et al. [65] showed that by inputting these into the TIE-equation in Eq. (3.51) one obtains the expression for the projected thickness as follows:

$$T(\mathbf{r}) = -\frac{1}{\mu} \log \left\{ \mathfrak{F}^{-1} \left[\mu \frac{\mathfrak{F}(I_{R_2}/I_{\text{in}})}{R_2 \delta |\mathbf{k}|^2 + \mu} \right] \right\}, \quad (3.53)$$

where \mathfrak{F} and \mathfrak{F}^{-1} denote the Fourier transform and its inverse, I_{R_2} the intensity at a distance R_2 and \mathbf{k} the coordinates in the Fourier space. The equation reads as follows: one records the intensity image at a distance R_2 from the object, forms its Fourier transform and divides it with the uniform intensity of the incident radiation I_{in} . Subsequently the result is divided with a function (still in the Fourier space), and the result is inverse Fourier transformed to yield the projected thickness. The computation of this expression is very efficient due to the possibility of formulating it by the use of the Fast Fourier transform (FFT). However, the main problem is also obvious in the sense that the resulting images are blurred, as the above equation basically corresponds to a low-pass filter. Nevertheless, Paganin phase-retrieved images significantly improve contrast as we discuss later in Sec. 5.

3.4 PRINCIPLES OF X-RAY TOMOGRAPHY

The main property of X-rays, namely the fact that they penetrate matter with the effect that they change their phase and/or amplitude depending on the inner structural composition, can be exploited to obtain three-dimensional information on the investigated material. In the following we derive the mathematical basics for establishing the link between projections and full (3D) tomographic reconstructions and give an overview on the methods that were used in the present work.

To derive the necessary formulas we assume a simplified case, where the object is irradiated by *parallel* X-ray beams (in contrast to *fan* and *cone* beam geometries) and represented by a two-dimensional function:

$$f(x, y) \in \mathbb{R}^2. \quad (3.54)$$

Additionally, we define a line $r_{\theta,t}$ through this object characterized by its angle θ to the abscissa and distance t from the center. With these two parameters the line equation reads as:

$$r_{\theta,t}: \quad x \cos \theta + y \sin \theta = t, \quad (3.55)$$

and we define the line integral $P_{\theta}(t)$ with:

$$P_{\theta}(t) = \int_{r_{\theta,t}} f(x, y) ds = \int_{-\infty}^{+\infty} \int_{-\infty}^{+\infty} f(x, y) \delta(x \cos \theta + y \sin \theta - t) dx dy, \quad (3.56)$$

where δ is the Dirac delta function. This equation corresponds to the two-dimensional *Radon transform* or, more generally, is referred to as the *tomographic forward projection* [66]. Moreover, it corresponds directly to the Beer-Lambert-Bouguer law in Eq. (3.13), meaning that every X-ray image represents a line integral through the imaged object. For simple geometries that are described by specific families of functions it can be calculated analytically. With this we can state that the main task of *tomographic reconstruction* is to reconstruct the object function $f(x, y)$ from its measured projections $P_{\theta}(t)$ at different values of θ and t .

Further on, by introducing the Fourier transform of the Radon transform $P_{\theta}(t)$ with

$$\hat{P}_{\theta}(\omega) = \int_{-\infty}^{+\infty} P_{\theta}(t) e^{-2\pi i \omega t} dt \quad (3.57)$$

and the Fourier transform of the object function $f(x, y)$ with

$$\hat{f}(u, v) = \int_{-\infty}^{+\infty} \int_{-\infty}^{+\infty} f(x, y) e^{-2\pi i (ux+vy)} dx dy, \quad (3.58)$$

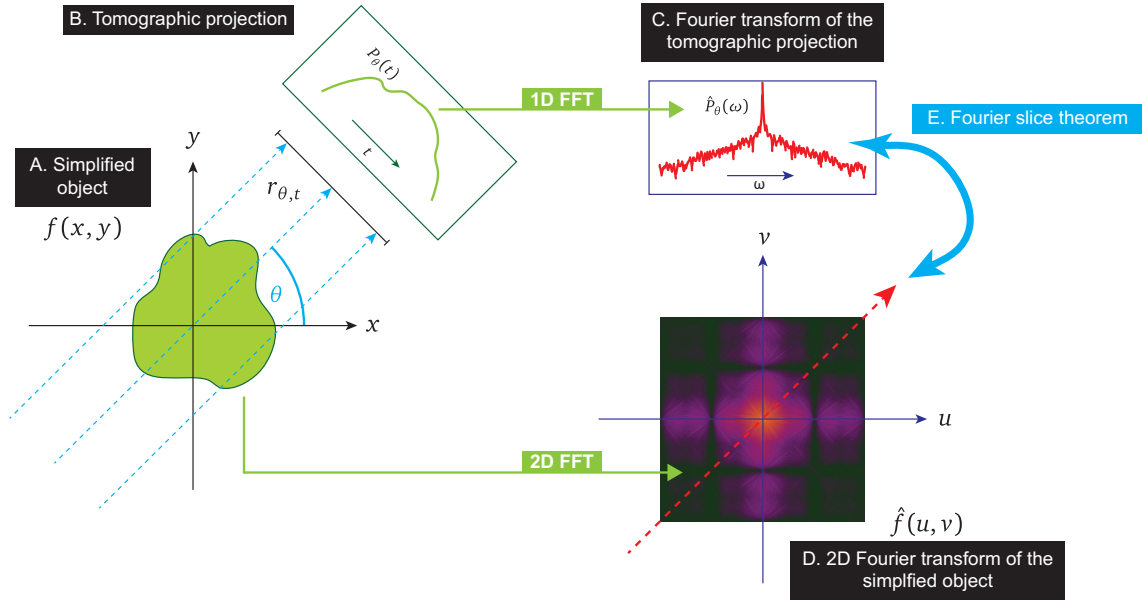


Figure 3.4. Demonstration of the Fourier slice theorem: from a two-dimensional object (A) tomographic projections are obtained with the two-dimensional Radon transform (B). The Fourier transform of a tomographic projection (C) taken a certain angle θ corresponds to the line profile at the same angle of the two-dimensional Fourier transform of the object function (D). This identity is described by the *Fourier slice theorem* (E).

we can formulate the *Fourier slice theorem* as follows:

$$\hat{P}_\theta(\omega) = \hat{f}(u, v) \Big|_{\substack{u=\omega \cos \theta \\ v=\omega \sin \theta}} = \hat{f}(\omega \cos \theta, \omega \sin \theta). \quad (3.59)$$

The whole relation is also illustrated in Fig. 3.4 and underlines the fact that the Fourier slice theorem represents the most fundamental theorem in computed tomography. It states that the Fourier transform of a tomographic projection taken at a particular angle θ is the same as taking a line along the same angle in the 2D Fourier space of the object. It also highlights the intrinsic relationship between CT and Fourier theory and indicates that, provided that a sufficient number of projections at different angles is obtained, the Fourier image of the object can be assembled, and subsequently the object's function itself can be retrieved.

The common (and standardized) approach of retrieving the object function $f(x, y)$, i. e. to invert Eq. (3.56), is the so-called *filtered back projection* (FBP). It is derived by forming the inverse Fourier transform of Eq. (3.58)

$$f(x, y) = \int_{-\infty}^{+\infty} \int_{-\infty}^{+\infty} \hat{f}(u, v) e^{2\pi i(ux+vy)} du dv, \quad (3.60)$$

and by utilizing the following substitutions:

$$u = \omega \cos \theta \quad v = \omega \sin \theta \quad \longrightarrow \quad du dv = \omega d\omega d\theta.$$

After a few simplification steps the detailed expression for the *filtered back projection* (FBP) reads as [66]:

$$f(x, y) = \int_0^\pi \left[\int_{-\infty}^{+\infty} \hat{P}_\theta(\omega) |\omega| e^{2\pi i \omega t} d\omega \right] d\theta. \quad (3.61)$$

In a more general form Eq. (3.61) can be expressed as:

$$f(x, y) = \int_0^\pi q_\theta(x \cos \theta + y \sin \theta) d\theta \quad (3.62)$$

with

$$q_\theta(t) = \int_{-\infty}^{\infty} \hat{h}(\omega) \hat{P}_\theta(\omega) e^{2\pi i \omega t} d\omega, \quad (3.63)$$

where the single projections $P_\theta(t)$ are first convolved with a filter $h(t)$ [being equivalent to a multiplication in Fourier space, as shown in Eq. (3.63)] and then *backprojected* onto the object plane [see Eq. (3.62)]. In the above case the filter with $\hat{h}(\omega) = |\omega|$ results from the transform from Cartesian to Polar coordinates and is commonly called *Ramp filter* (or *Ram-Lak filter*). In practice, however, when dealing with discretized and noisy datasets an alternative and more empirical choice of the filter usually leads to improved signal-to-noise ratios in the reconstructed images [67]. In summary, the filtered backprojection (FBP) represents a two-step approach by simply describing a way of adding the respective pixels in the image plane [66].

An alternative approach, and in fact more intuitive, is to make direct use of the Fourier slice theorem in Eq. (3.59) and retrieve the object from its two-dimensional Fourier transform $\hat{f}(u, v)$ in Eq. (3.60) that priorly has been constructed by sufficient sampling of $\hat{P}_\theta(\omega)$. This approach represents the starting point of all Fourier methods in CT-reconstruction algorithms and the main challenge consists in interpolating the radial Fourier samples, coming from the tomographic projections, onto a Cartesian grid with coordinates u and v , from which the two-dimensional inverse Fourier transform is subsequently computed. Since standard interpolation schemes in the Fourier domain fail to provide accurate reconstructions, a so-called *regridding* technique has been proposed that performs the interpolation as a sophisticated convolution with a smooth window function. As such it has been established as a robust method of reconstruction in computed tomography and magnetic resonance imaging (MRI) [68–71]. The main advantage of the so-called *gridrec* algorithm, which is the method of choice in the underlying

thesis, lies in the fact that it can be implemented very efficiently on any PC without the need of GPU-s (graphical processing units). Moreover, the whole CT-reconstruction pipeline, present at the TOMCAT beamline [72], has been designed around this algorithm and is available for standard usage.

Independent of the method of choice for the CT reconstructions, the challenge in our case is the fact that we deal with *under-sampled* datasets in at least two different ways. The first under-sampling becomes effective when imaging lungs within the thorax, where we usually reconstruct at high resolution only a small volume from a larger sample. This case of so-called *region-of-interest* (or *interior*) tomography represents an ill-posed problem and leads e. g. to low-frequency artifacts or DC-shifts in the reconstructed images, due to the fact that the projection data is truncated [73, 74]. In the most simple solution to this problem it is, however, enough to simply enlarge the single projections horizontally by padding the enlarged images with additional pixel values that correspond to the respective edge pixels [73]. This technique is routinely performed throughout all our CT reconstructions and a so-called *edge-padding* factor of about 0.5 – 0.75 in respect to the original tomographic projection size is applied. The second type of under-sampling follows the fact that we deal with *in vivo* samples. Therein the main goal is to reduce the number of tomographic projections as well as the projection’s exposure time with the overall goal of reducing the animal’s exposure to X-ray radiation. Commonly, this procedures lead to a decrease of the signal-to-noise ratios in the reconstructed images as well as the appearance of typical *streak artifacts*, which in the case of lungs (where a high number of small hierarchical features is present) resemble so-called *speckles* that further reduce the image quality.

In Figs. 3.5 and 3.6 the effects of reducing the number of tomographic projections are shown for the two optics that were used in our experiments. As it is clearly visible, the reduction cannot be done arbitrarily as important biological features get removed. The effect is also stronger for the high-resolution optics, as shown in Fig. 3.6. We end the section by summarizing the necessary steps for obtaining CT-reconstructed volumes in the order of how they are conducted at the experimental site:

- (1) Acquisition of dark images and so-called flat-field images. While dark images correspond to the detector’s noise, flat-field images are the images of the flat beam-profile, i. e. without having the sample in the beam. We usually acquire both before starting the tomographic scan of the sample.
- (2) Acquisition of the tomographic projections.
- (3) Flat-field and dark-image correction: the acquired projections are corrected with the above images. This can be described by the following formula:

$$I_{\text{corr}} = \frac{I_{\text{proj}} - I_{\text{dark}}}{I_{\text{flat}} - I_{\text{dark}}},$$

with the tomographic projection I_{proj} , the dark-image I_{dark} , the flat-field image I_{flat} and the corrected image I_{corr} . The dark and flat-field images represent median and mean images over multiple samples, respectively.

- (4) Phase-retrieval (as explained in Sec. 3.3).
- (5) Creation of so-called *sinograms*, which is a typical image representation of tomographic projections where each line of the sinogram represents a tomographic projection at a different angle.
- (6) Ring-removal: several so-called ring-artifacts can be present in the tomographic reconstructions [as shown in Fig. 3.7(a)]. Therefore a wavelet-filtering method [75] is applied on the sinograms which leads to corrected reconstructions. The result is visible in Fig. 3.7(b).
- (7) CT reconstruction.

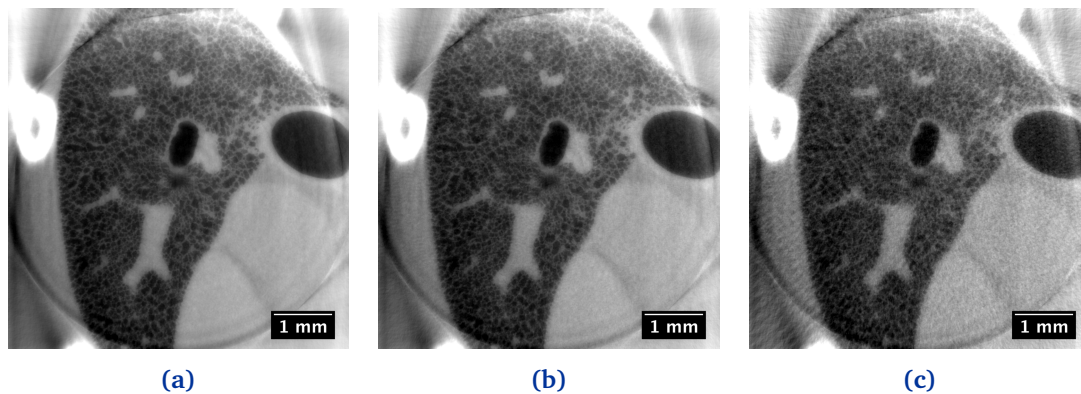


Figure 3.5. Demonstration of the reduction of number of projections for the $2.9\ \mu\text{m}$ -pixel-size optics: (a) 900 projections; (b) 500 projections; (c) 200 projections.

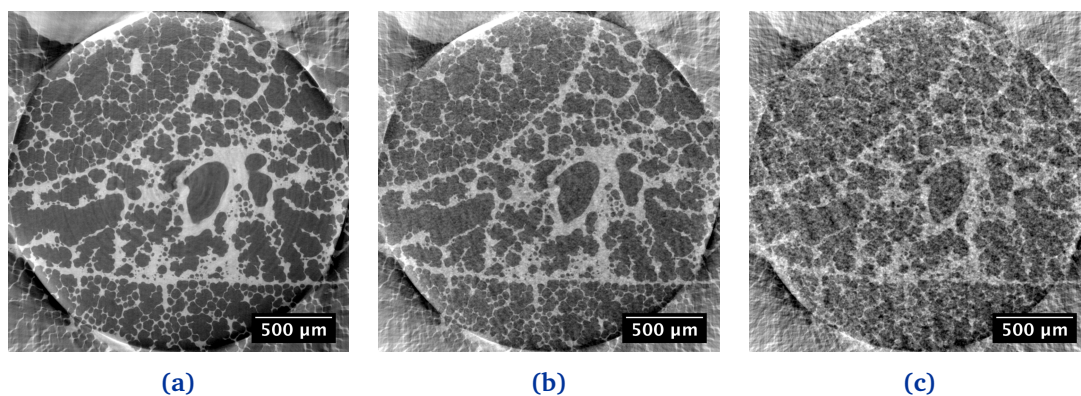


Figure 3.6. Demonstration of the reduction of number of projections for the $1.1\ \mu\text{m}$ -pixel-size optics: (a) 900 projections; (b) 500 projections; (c) 200 projections.

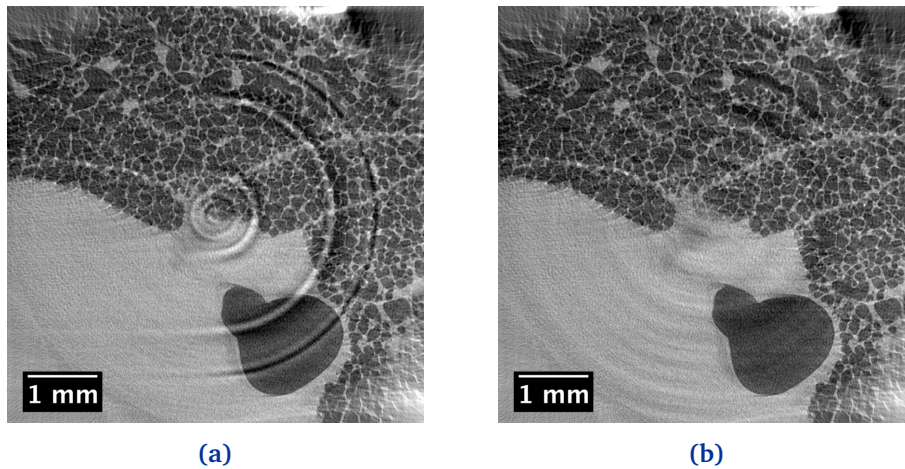


Figure 3.7. Comparison of a tomographic slice with strong “ring artifacts” before and after wavelet-filtering [75]: **(a)** Without wavelet filter; **(b)** with wavelet filtering. The artifact is caused by a very dirty “scintillator” that is not correctly flatfield-corrected and enhanced by the phase retrieval.

3.5 POST-PROCESSING

So far we have extensively described the image formation process, which in our case is finalized once the tomographic reconstructions have been conducted and three-dimensional volumes of our samples are available. This stage, however, only represents the first module in *image processing* being complemented by further stages such as *image enhancement*, *visualization* and *(quantitative) image analysis*, which in turn are all subdivided into further smaller steps. Commonly, the basic problem arises from the *semantic gap*, describing the discrepancy between what we *see* and how this cognitive interpretation is represented in the simple structure of discrete pixel values. Thus, a common challenge is to define an automated processing flow which ideally renders the human cognitive understanding and can be expanded to analogous problems. In our case, we consolidate all core steps of image analysis taking place after CT-reconstruction under the term *post-processing*. It is the purpose of the following chapter to give an overview of these steps, whereas we mainly follow the synopsis of [76].

Image Registration

The goal of *image registration* is to find anatomical correspondences between two or more images. Mathematically, this is equivalent to finding a function which maps any point of an input (image) volume I_{in} into the corresponding point in the reference image volume I_{ref} . Let us define the input image as

$$I_{\text{in}} = g(x, y, z), \quad (3.64)$$

where g gives the matrix element (gray value) of the 3D image matrix depending on its location:

$$\begin{aligned} x \in [1, \dots, N_x] &\longrightarrow (\text{number of lines}) \\ y \in [1, \dots, N_y] &\longrightarrow (\text{number of columns}) \\ z \in [1, \dots, N_z] &\longrightarrow (\text{number of tomographic slices}) \end{aligned}$$

We can now formulate the image registration \mathbf{T} by defining a transformation of the form:

$$\mathbf{T} : g(x, y, z) \mapsto g(x', y', z'). \quad (3.65)$$

In the case of the so-called *rigid transform*, the volumes are assumed to be identical and only *rotated* and *shifted* in the three euclidean dimensions in respect to each other. This condition is well matched in our experiments, when acquiring lung tomograms at different pressures and at high spatial resolutions. Namely, the regions of interest are shifted and/or rotated in respect to each other, caused by the volumetric changes in the animal's thorax. The rigid transform can then be written in matrix form and defined as follows:

$$[\mathbf{T}] \begin{pmatrix} x \\ y \\ z \end{pmatrix} = \begin{pmatrix} r_{11} & r_{12} & r_{13} & t_x \\ r_{21} & r_{22} & r_{23} & t_y \\ r_{31} & r_{32} & r_{33} & t_z \\ 0 & 0 & 0 & 1 \end{pmatrix} \begin{pmatrix} x \\ y \\ z \\ 1 \end{pmatrix} = \begin{pmatrix} x' \\ y' \\ z' \\ 1 \end{pmatrix} \quad (3.66)$$

Since we usually deal with large 3D image datasets, each being in the order of 8 GB, an automatic process in finding the matrix \mathbf{T} can be computationally expensive. Thus we adopted a semi-automatic approach, which we applied when comparing different volumes to one another. It consists of three steps:

- (1) The 3D image data is first down-scaled by a factor of four in all dimensions to enable fast data handling or turned into a so-called octree file format, which enables automatic down-scaling when loading the image. This is repeated for all datasets.
- (2) The datasets are then manually registered, and the region of interest is set so that all datasets overlap. This step is visualized in Fig. 3.8. The process is conducted in MeVis-Lab (MeVis Medical Solutions AG) and yields the transformation matrix \mathbf{T} .
- (3) In the last step, the transformation matrix is rescaled in order to comply to the original (unscaled) dataset. As a result, the datasets together with the transformation matrix \mathbf{T} are input into an automatic algorithm (MATLAB) to yield registered and cropped datasets [77].

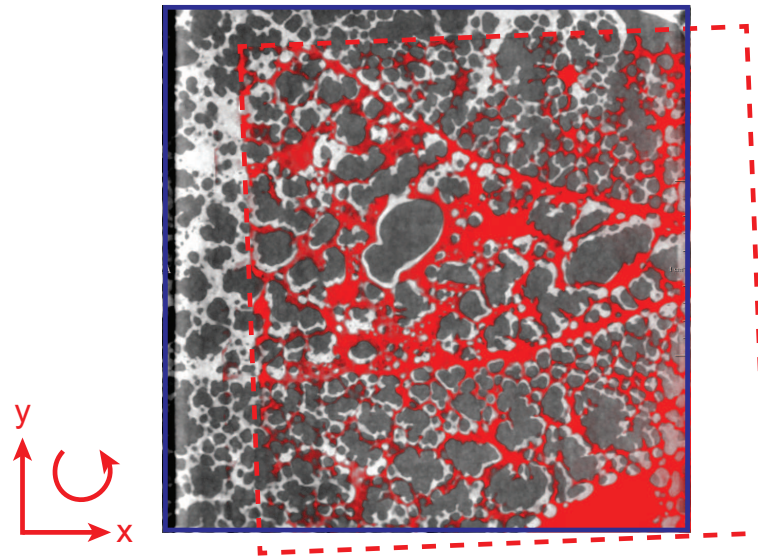


Figure 3.8. Visualization of the manual registration process of two lung volumes at different peak-inspiratory pressures: 10 cmH₂O and 20 cmH₂O. The second volume is rotated and shifted in respect to the first one in order to compute the transformation matrix.

Segmentation

The goal of image segmentation is to divide the image into meaningful parts (connected regions), representing a starting point for further image classification (and further analysis). The general idea of segmentation is two-fold: (i) to find a set of image “segmenting objects” (e. g. image pixel values) fulfilling the same homogeneous criterion (e. g. identical gray values or texture); and (ii) to identify the boundaries of these areas. Despite the simple principle, image segmentation represents a long-standing problem in computer vision, and a huge variety of methods are available nowadays whereas in most cases the result can only be validated visually [78]. Generally, all segmentation methods can be categorized as follows:

- (1) **Pixel-based:** imposing segmentation criteria on each pixel throughout the whole image (disregarding the surroundings).
- (2) **Edge-based:** usually based on edge-extraction and edge-completion algorithms.
- (3) **Region-based:** based on a certain distance or similarity measure to guide the assignment of neighbored pixels or regions.
- (4) **Model-based methods:** state of the art methods applying prior knowledge and various model-driven algorithms for shape-recognition.

Concerning our samples, the main goal of segmentation is to separate the air volumes from lung tissue (septa and blood vessels), creating so-called *binary*(-segmented) images. In most cases we simply use a global thresholding technique, assuming that the image segment

of interest is specified just by its gray value. In Chapter 6 we describe in detail a method that we have specifically developed for our lung samples.

Visualization

Visualizing data becomes particularly important when dealing with 3D datasets. On the one hand, it gives first ideas on particular trends or hypotheses; on the other hand, it also steers the direction for further analysis. However, it has to be treated with care since any visualization process also means data reduction and thus can only be an accompanying part to quantitative analysis [78]. Generally we distinguish two different approaches. So-called *indirect methods* require segmented datasets as input and extract intermediate polygonal representations of the volume before being rendered using the graphics hardware. A common representative is the so-called *marching cubes algorithm*, which is employed for transforming a volume into a triangulated surface (as used for instance in Chapter 6). *Direct methods*, on the other hand, directly project pixels on the image plane (e. g. computer screen) to create an image of the 3D dataset. *Ray casting* represents such an example, where one ray is casted from each pixel in the 3D volume to the viewer. If on its way only the maximum intensity is kept, it is referred to as *maximum intensity projection*. We can conclude that there exist a vast variety of further methods, whereas often the choice for the best method depends either purely on the regarded dataset or is a result of various trial-and-errors.

Quantitative analysis

The general motives of quantitative analyses are to quantify as many parameters as possible, such as intrinsic volumes, shapes, characterize anisotropy and so forth, with the goal of giving unique and global characterizations of the regarded volumes. It would exceed the scope of the present work to give a sufficient overview on all the available methods. Instead we note the following: the general idea arises from the fact that inspecting 3D data can be an extremely tedious task; particular trends are often very hard to see and/or can be highly misleading due to the missing third dimension; moreover, certain features become prominent only when extracted by quantitative means. Thus, the only way to use the full spatial information that is contained in 3D images requires the introduction of various measures that can ideally be computed automatically. This step ultimately provides the basis towards the development of a “visual sense for machines” [76].

X-ray instrumentation

We now discuss in detail several “practical” aspects of the project, without which basically none of the following work would have been possible. By doing so, we hope to convey to the interested reader some of the general ideas and solutions that were found within this project. Many of the aspects proposed hereinafter should be potentially useful in many similar situations.

4.1 BEAM STABILITY MEASUREMENTS

Introduction

Beam profile fluctuations represent a major problem in various beamline experiments. In particular, in ultra-fast experiments where exposure times of single projections are of the order of milliseconds or even in the sub-millisecond range, a fluctuating beam profile leads to a distorted flat-field correction. The effect is further enhanced when imaging is conducted with monochromatic X-rays coming from a double multilayer monochromator (DMM), as they usually induce significant modifications to the beam profile [79]. Moreover, in single-shot phase retrieval methods such as the method by Paganin et al. [65] these distortions are also interpreted as false phase shifts and even further amplified. Taken together, all contributions lead to a reduced contrast-to-noise ratio in the final CT reconstructed data, hence exacerbating any further data analysis.

An example of this effect is shown in Fig. 4.1. Due to the fluctuating beam profile (image background), at first the projection image in Fig. 4.1(a) is not successfully flat-field corrected [visible in the slight stripe artifacts, see Fig. 4.1(b)], but a few milliseconds later it is [see Fig. 4.1(c)]. A more detailed study was reported by Homann et al. [80], where the authors conclude that such a distorted flat-field correction ultimately leads to a decrease in spatial resolution.

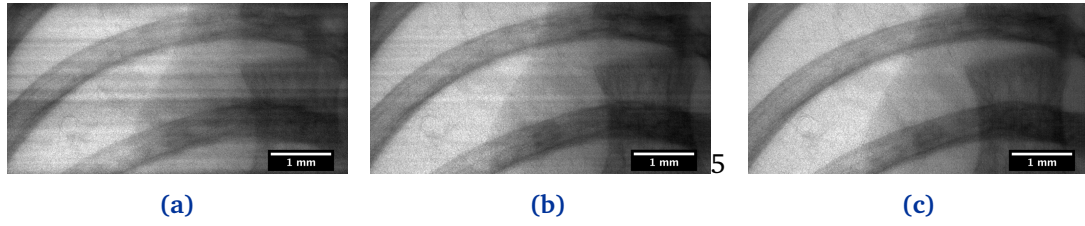


Figure 4.1. Demonstration of a distorted flat-field correction arising from a fluctuating beam profile: **(a)** Original X-ray radiograph (projection image) of a mouse thorax; **(b)** “bad” flat-field-corrected projection image; **(c)** “good” flat-field-corrected projection image. The “good” projection image was taken just a few milliseconds after the “bad” one, where the stripes from the beam profile that changed during this very short time interval are clearly visible.

Methods

In our approach the goal was to characterize the vibration pattern of the image background and compare it to previous seismic measurements that were conducted at the TOMCAT beamline. For doing so, we acquired pure flat-field images with very short exposure times and under various conditions in order to track down or identify possible vibration sources. All measurements were conducted with the fast CMOS detector (pco.Dimax) and an effective pixel size of $3.1 \times 3.1 \mu\text{m}^2$. In Tab. 4.1 the various settings for the data acquisition are summarized, and in the following we describe the methodology for conducting such measurements. Similar measurements had been reported before by Bunk et al. [81], where oscillating beam profiles were fitted with one-dimensional and/or two-dimensional Gaussian functions in order to follow their fluctuations. As we will show in the following, we extended this approach to arbitrary patterns with further information on time-dependency in the spectrum.

Assuming that the profile (pattern) of the image background vibrates according to certain frequencies, the complete approach can be regarded as a so-called “template matching” problem. Therein, a small patch of an image (*template*) is compared with the complete *image* in order to find the position where it fits best and thus from which position the patch was extracted. If the template is changing its position within the image over time, the “template matching” result will be time-dependent as well. Naturally, there exist numerous methods for treating such problems that all are advantageous and/or disadvantageous in certain points. If defining $I(i, j)$ as the *image* and $R(i, j)$ as the *template*, then one of the most common metrics is the so-called *sum of squared differences* $I_{\text{SSD}}(r, s)$ defined as follows:

$$I_{\text{SSD}}(r, s) = \sum_{(i, j) \in R} [I(r + i, s + j) - R(i, j)]^2, \quad (4.1)$$

where $I_{\text{SSD}}(r, s)$ itself is an image where each pixel represents the squared sum of differences between the image $I(i, j)$ and the template $R(i, j)$ [82]. Further on, it can be shown that the

Table 4.1. Different setups for acquiring ultra-fast flat-field images. Setups 1-5 represent measurements with monochromatic beams and the two different monochromators, while setups 6-9 were conducted with various filter settings for the white beam. The front-end filters are associated with the amount of X-ray power density that is let through (e. g. a 5% filter setting reduces the white beam power density by 95%).

Setup	Energy [keV]	Filter configuration	Front-end filter	exposure time [ms]
1 ^(a)	20	250 μm Al	100%	0.98
2 ^(a)	20	no filter	100%	0.98
3 ^(b)	22	100 μm Al + 10 μm Fe	50%	0.98
4 ^(b)	22	no filter	50%	0.98
5 ^(b)	22	no filter	100%	0.98
6 ^(c)	polychromatic	no filter	50%	0.25
7 ^(c)	polychromatic	no filter	5%	0.98
8 ^(d)	polychromatic	no filter	100%	0.98

^a [Ru/C]₁₀₀ monochromator and Lu:Ag scintillator (100 μm thickness).

^b [W/Si]₁₀₀ monochromator and Lu:Ag scintillator (100 μm thickness).

^c White beam and Lu:Ag scintillator (100 μm thickness).

^d White beam with Yag:Ce scintillator (18 μm thickness).

above equation can be transformed to:

$$I_{\text{SSD}}(r, s) = \underbrace{\sum_{(i,j) \in R} [I(r+i, s+j)]^2}_{A(r,s)} + \underbrace{\sum_{(i,j) \in R} [R(i, j)]^2}_B - 2 \cdot C(r, s), \quad (4.2)$$

where $A(r, s)$ is the quadratic sum of the respective image patch of I at the offset (r, s) , B is the quadratic sum of all values in the template R , and $C(r, s)$ can be written as:

$$C(r, s) = \sum_{(i,j) \in R} I(r+i, s+j) \cdot R(i, j) = [I \otimes R](r, s). \quad (4.3)$$

Latter expression of $C(r, s)$ represents the so-called *linear cross-correlation* between I and R and is particularly useful as it can be calculated very efficiently in the Fourier space. The resulting image $I_{\text{SSD}}(r, s)$ will have a minimum value at (r, s) , where the template R matches the image the best. However, the situation gets more complicated if the comparing images have varying illuminations, are distorted (stretched between one another) or additionally rotated, which is why various (more complicated) approaches have been proposed [83].

In our study we did not assume further distortions, but applied a slightly improved method, namely the *normalized cross-correlation* which corrects for varying background illumination,

but without the loss in computation speed [84]. It is defined like the correlation coefficient:

$$C_{\text{norm}}(r, s) = \frac{\sum_{(i,j) \in R} [I(i, j) - \tilde{I}(r, s)] \cdot [R(i, j) - \tilde{R}]}{\sqrt{\sum_{(i,j) \in R} [I(r + i, s + j) - \tilde{I}(r, s)]^2} \cdot \sqrt{\sum_{(i,j) \in R} [R(i - r, j - s) - \tilde{R}]^2}} \quad (4.4)$$

with \tilde{R} being the mean of the template, and $\tilde{I}(r, s)$ being the mean of $I(i, j)$ in the region under the template. However, as opposed to the case of the correlation coefficient, it is calculated in the Fourier domain and then normalized with precomputed integrals. Thus, it is very efficiently implemented in MATLAB (Mathworks, Inc.) within the function “normxcorr2”. The result is visible in Fig. 4.2.

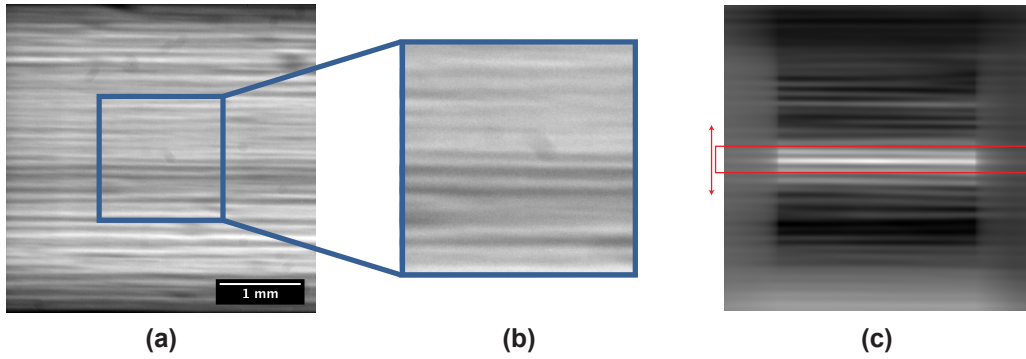


Figure 4.2. Demonstrating the calculation of the normalized cross-correlation C_{norm} from Eq. (4.4): **(a)** original image I ; **(b)** extracted image template R ; and **(c)** is the normalized cross-correlation C_{norm} . If the pattern in image I fluctuates over time, the brightest line in **(c)** will oscillate as well (indicated by the arrows).

The normalized cross-correlation is calculated by taking an original flat-field image I [see Fig. 4.2(a)], defining a region therein as the template R [see Fig. 4.2(b)] and then calculating C_{norm} according to Eq. (4.4) [see Fig. 4.2(c)]. If the flat-field image in Fig. 4.2(a) now oscillates over time, the brightest line in Fig. 4.2(c) will oscillate as well (indicated by the red rectangle and the arrows). Recording this displacement as a function of time yields the so-called displacement function $D(t)$, which can then be used for spectral analyses in order to find frequencies of the flat-field vibration.

Before discussing the results, it is noteworthy to point out that this analysis scheme was also verified with a simple model for simulating various vibration patterns of the flat-fields. The pseudocode is summarized in Algorithm 4.1: an arbitrary template is input and placed at different positions of the flat-field image I_{flat} according to sinusoidal time-dependent offsets Δ_{off} with discrete frequencies $\nu = (\nu_1, \nu_2, \dots, \nu_N)$; after calculating the normalized cross-correlation the displacement function $D(t)$ is obtained and - assuming the model and evaluation is correct - corresponds to the aforementioned time-dependent offset Δ_{off} .

Algorithm 4.1: Vibration pattern simulation

```

input : A simulated sinusoidal template  $R_{\sin}(i, j)$ 
output: Displacement function  $D(t)$ 

for  $k \leftarrow 0$  to  $T$  do                                     //  $k$ ...discrete time points
     $\Delta_{\text{off}}(k) = C \cdot \sum_i^N \sin(2\pi \cdot \nu_i \cdot \Delta t \cdot k)$ ;
    for  $i \leftarrow 1$  to  $h$  do                                     //  $h$ ...height of image
        for  $j \leftarrow 1$  to  $w$  do                                     //  $w$ ...width of image
             $I_{\text{flat}}(i + \Delta_{\text{off}}(k), j) \leftarrow R_{\sin}(i, j)$ ;
         $C(r, s) \leftarrow \text{normxcorr}(I_{\text{flat}}, R_{\sin})$ ;
     $D(k) \leftarrow \text{FindPositionOfMaximum}(C(r, s))$ ;

```

Results and Conclusion

We first applied a short-time Fourier transform (STFT) in order to investigate the time dependency of the spectral information. The overlap, window size and number of windows of the STFT were chosen so to achieve a spectral precision of ± 1 Hz. Both, the background displacement signal $D(t)$ and its spectrogram are plotted in Fig. 4.3(a) and Fig. 4.3(b), respectively. Both plots correspond to the measurement with “Setup 1” (see Tab. 4.1). As it can be seen, the spectrum was quite constant over the measured time interval. For this reason, in all further analyses we regarded the mean power spectral density (PSD).

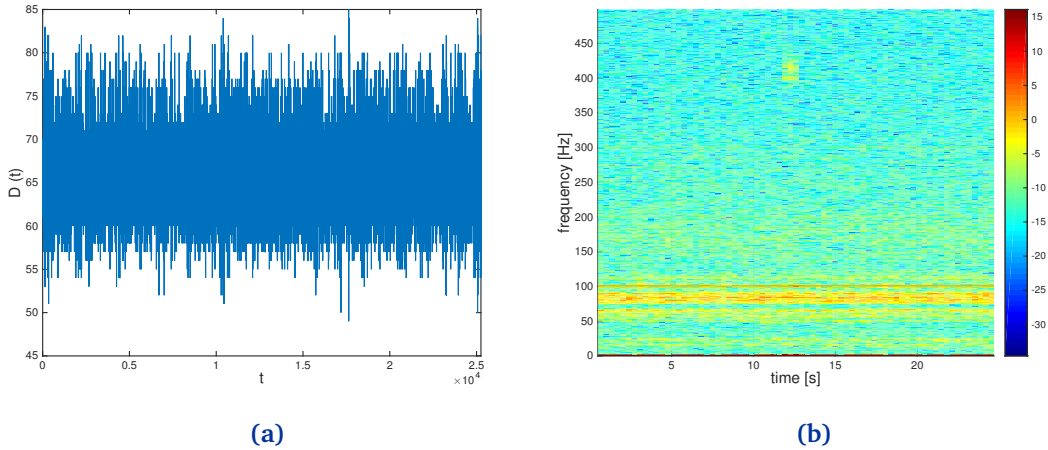


Figure 4.3. Result of the normalized cross-correlation that is used for further processing: **(a)** Displacement vector of the flat-field images after calculating the normalized cross-correlation and extracting the time-dependent positions of best matches; **(b)** the associated spectrogram of the time-depended power spectral density (PSD) signal. The color-code is plotted logarithmic for better clarity.

In Fig. 4.4 the mean PSD-s from both monochromators (the $[\text{Ru}/\text{C}]_{100}$ and the $[\text{W}/\text{Si}]_{100}$ monochromator) are plotted with and without additional filters, thus covering setups 1-5 from Tab. 4.1. As it can be seen, the spectral information is almost completely independent on the composition of filters that are used. Moreover, the spectral footprints of the two monochromators are almost identical with very small deviations that can be attributed to noise or the fact that the beam profiles produced by each of them are very different (being more pronounced for the $[\text{Ru}/\text{C}]_{100}$ monochromator). We supposed that the latter effect was mostly responsible for the small deviations, as it can alter the results of the template matching problem, i. e. if the template being matched with the complete image has a very small signal-to-noise ratio. Furthermore, in the present (logarithmic) representation the noise baseline was found to be around: $\log \text{PSD}_{\text{noise}} \approx -6$.

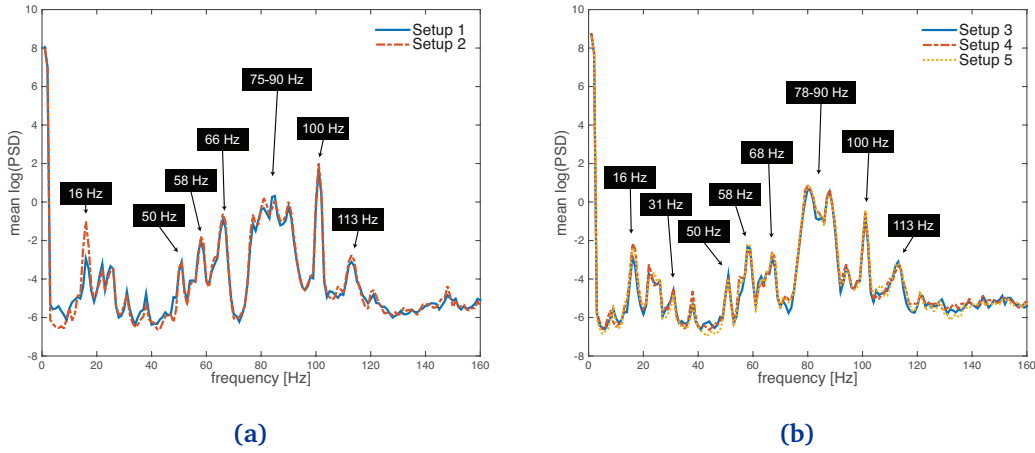


Figure 4.4. Mean power spectral densities (PSD) of the fluctuations associated with the two different monochromators: **(a)** shows the mean PSD for the $[\text{Ru}/\text{C}]_{100}$ monochromator with and without filters; **(b)** shows the mean PSD for the $[\text{W}/\text{Si}]_{100}$ monochromator with various filter settings.

Calculations following the same approach were also conducted for the white beam case with various filter settings, however, with a somewhat different “template-matching” analysis. We earlier mentioned that monochromatic beams produced by double multilayer monochromators (DMM) usually produce flat-field images with typical stripe artefacts [79]. These are easy to track and analyse with the template-matching approach, but for the filtered white beam where the beam profile is mostly flat (except at the borders), this is not the case. We overcame this problem by looking at the border region and extracting the beam profile from therein. Subsequently, the differential signal was calculated and the displacement vector $D(t)$ was obtained by tracking the maximum peak. Both, the mean PSD-s and the method for tracking the slope of the beam profile are plotted in Fig. 4.5(a) and Fig. 4.5(b), respectively. It is visible that none of the white beam settings exhibited a regular vibration pattern.

We can conclude that most vibrations were found under the monochromatic beam setting, with very pronounced frequencies around 16 Hz, 55 Hz, 66 Hz, the whole range of 75-90 Hz

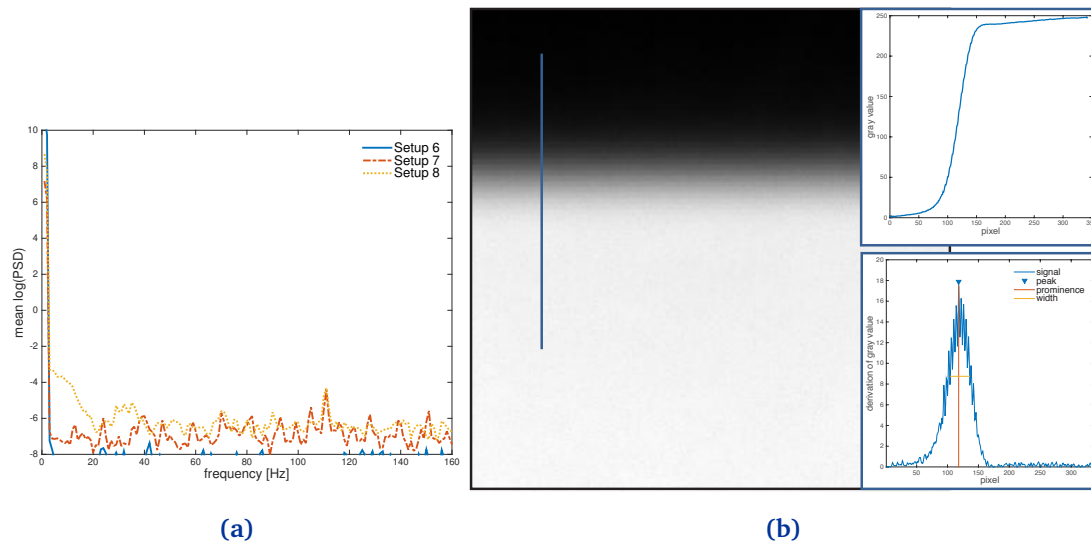


Figure 4.5. Mean power spectral densities (PSD) of the white beam fluctuations associated with different filter settings: **(a)** shows the results from different filter settings; **(b)** shows the method for tracking the beam fluctuations at the border. First the beam profile is extracted and subsequently its derivative is calculated, which is then tracked as the beam fluctuates.

and 100 Hz. The polychromatic beam settings from Fig. 4.5(a) did not exhibit any pronounced vibration frequencies, as most values were below the noise baseline (identified above) except a slightly visible peak at about 113 Hz. Comparing these results to previously performed seismic vibration measurements in Fig. 4.6, which were measured during a synchrotron shutdown period in April 2010, no significant correlations were found. We can attribute this fact back to two possible reasons: on the one hand, the vibration source might not have been captured correctly with the seismic devices indicating a non-optimal placement of the sensors; on the other hand, provided that the sensors had been placed correctly to measure all possible vibration sources, the vibration conditions might have changed drastically under synchrotron operation. Latter hypothesis indicates that a true comparison could only be achieved if the measurements were both repeated under regular machine operation.

Finally, although our findings were inconclusive in the sense of identifying a unique vibration source, we observed the vibrations to be present only in the monochromatic beam settings, and we propose a methodology for repeating the same measurements in combination with further seismic measurements. The chosen representation, i. e. the logarithmic mean PSD-plot, is not very intuitive if one is interested to find the real displacement per frequency. It is, however, straight-forward to transform the power spectral density to a so-called *power amplitude density* by taking the square root, which then corresponds to the actual displacement. When conducting this calculation we found a mean displacement of about 3 – 6 pixels for all frequencies (corresponding to a maximum of 9 – 18 μm of the beam profile at the position of the detector). From the original displacement function in Fig. 4.3(a), one would rather expect a displacement of about 13 pixels which however occurs when the single small vibration fre-

quencies superimpose to form a big peak. Hence, ideally all frequencies should be removed in order to obtain a stable background image.

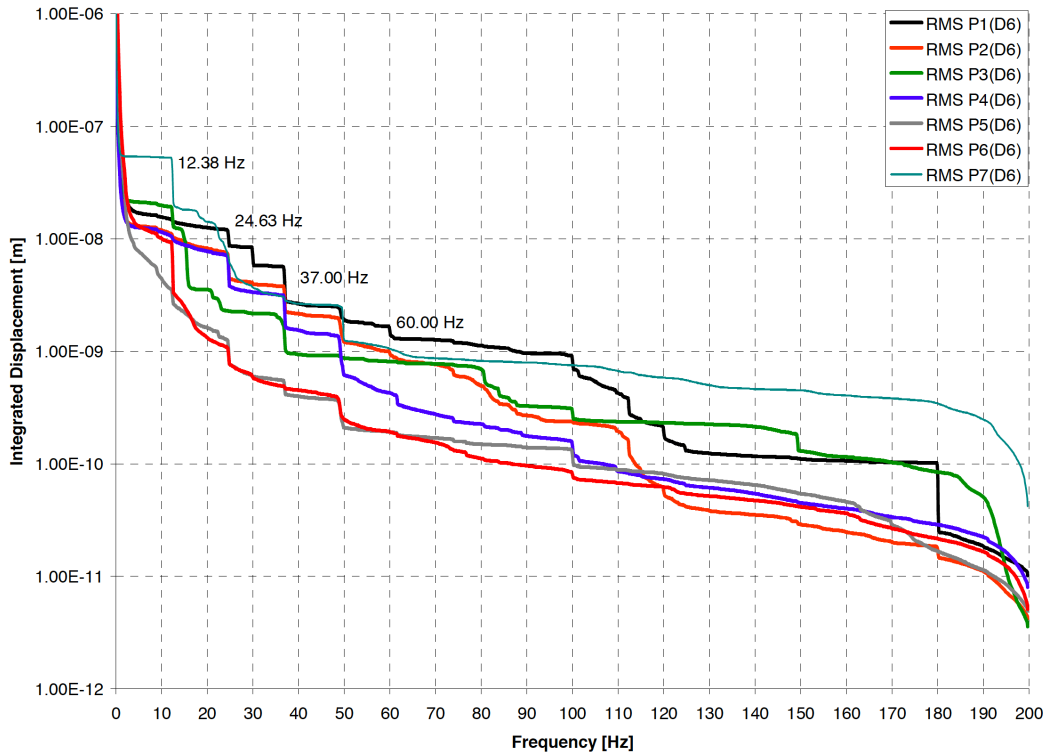


Figure 4.6. Seismic vibration measurements during shutdown in April 2010. The plot has been adopted with permission from X. Wang (AMI, PSI).

4.2 COHERENCE CHARACTERIZATION

The following chapter represents a reprinted manuscript published as: G. Lovric, P. Oberta, I. Mohacsi, M. Stampanoni, and R. Mokso, *Optics Express*, **22**(3), 2745, 2014 [85].

4.2.1 Abstract

A reliable measurement of beam coherence is important for optimal performance of a number of coherence methods being utilized at third-generation synchrotrons and free-electron lasers. Various approaches have been proposed in the past for determining the source size and hence the degree of coherence; however, they often require complex setups with perfect optics and suffer from undefined uncertainties. We present a robust tool for X-ray source characterization with a full quantitative uncertainty analysis for fast on-the-fly coherence measurements. The influence of three multilayer monochromator crystals on the apparent source size is evaluated using the proposed method.

4.2.2 Introduction

Coherence represents one of the most fundamental features of third-generation synchrotrons and upcoming hard X-ray free-electron lasers being exploited in a vast amount of experimental approaches [86]. Well-established techniques such as X-ray photon correlation spectroscopy [87], coherent X-ray diffraction imaging [88], lensless imaging [89], phase contrast imaging [56, 60, 90, 91] as well as the recently developed ptychography [92], polyCDI [93] and GI-USAXS [94] are only a few to be named. Accordingly, the precise knowledge of source size and its modification by X-ray optical elements remains a crucial part in beamline construction, in methods development as well as in different kinds of simulations and evaluations dealing with image formation therein.

By identifying coherence as the ability to observe interference phenomena, we have to differentiate temporal coherence, determined by the spectral bandwidth (monochromaticity), from spatial (transverse) coherence, being directly related to the intensity distribution across the source, i.e. the effective source size of the radiation [95, 96]. Thus, deploying a strategy to measure the source size is tantamount to determining the degree of spatial coherence in a selected cross section of an X-ray beam.

In the past, various methods have been reported for coherence measurements of synchrotron X-ray sources and more recently for free-electron lasers in the hard X-ray regime. Paterson *et al.* [97] successfully utilized Young's double-slit experiment [95] with X-rays, providing an efficient method for measuring coherence of undulator radiation that had previously only been applied in the visible and EUV light regime [98, 99]. Leitenberger *et al.* [100] extended the technique to hard X-rays and deployed (double and single) pin-hole diffraction using an energy-dispersive detector for simultaneously studying coherence properties of a large spectral range [101, 102]. Various analog interferometric methods, such as the characterization of Fresnel interference fringes produced by a round fiber or slit [96], the use of

an intensity [103], a shearing [104] or a prism [105] interferometer and the evaluation of diffraction patterns created from a phase-shifting mask [106], have each been reported. More recently, Young's experiment has been used to study the spatial and temporal coherence of single, femtosecond X-ray pulses generated by a hard X-ray free-electron laser [107]. A complementary approach to transverse coherence measurements has been introduced by Cloetens *et al.* [108] by comparing the first Fourier coefficients in the so-called Talbot images, where self-imaging of a periodic object occurs. Subsequently, this was refined by recognizing that in a fully-coherent beam the higher-order Fourier coefficients are also preserved in partial Talbot distances [109], reducing the necessary number of distances to be taken in an experiment.

The above methods also have certain drawbacks, e.g. in terms of a challenging setup and/or alignment [104, 107], by requiring energy-resolved detectors [101, 102] or by being very sensitive to imperfections in the used optical elements [106, 109]. In addition, all methods have in common that they provide only a very limited uncertainty analysis for the measured source size values.

In this paper we address these weaknesses by proposing a method with a simple setup, previously introduced in [109], omitting the assumption of perfect optical elements (gratings) and precise knowledge of the X-ray energy spectrum. We show that with a combined approach of modeling and evaluating experimental data it becomes possible to make the calculation fully automatic and quantitative. In addition to earlier methods, the quantitative nature of our approach is supported by a detailed uncertainty analysis, incorporating all relevant error sources in a simplified error model.

In general, the methodology for measuring source size can be applied when evaluating coherence preservation of reflective and diffractive X-ray optical elements [110–112]. We apply our method to determine the effective X-ray source size influenced by a Si(111) and three multilayer monochromators and we show that the straightforward setup and data evaluation of our approach favors its routine use for this purpose. The fitting procedure can also be used for improving the characterization of recently proposed grating geometries for interferometric imaging [113].

4.2.3 Methods

Experimental setup

The experiments were carried out at the X02DA TOMCAT beamline of the Swiss Light Source (SLS) at the Paul Scherrer Institute (Villigen, Switzerland), and the setup is depicted in Fig. 4.7. The X-ray beam, produced by a 2.9 T super-bending magnet on a 2.4 GeV storage ring (with ring current $I = 400$ mA, top-up mode), was monochromatized with a Si(111) double-crystal (DCM) and two different double-multilayer monochromators (DMM), respectively. The latter two consist of different compositions, coated on a Si(111) substrate, for use at different energy ranges: $[\text{Ru/C}]_{100}$ (100 layers, 4 nm periodicity) for energies below 22 keV and $[\text{W/Si}]_{100}$ (100 layers, 3 nm periodicity) for energies above [114]. The source size was measured at the following energies using always one of the standard monochromators: 14 keV,

15 keV, 16 keV, 17 keV, and 21.8 keV. We explain later on why this choice of energies was particularly suitable. For the characterization of a V/B₄C multilayer crystal (3.02 nm periodicity) the X-ray energy was set to 18 keV using the Si(111) monochromator, and the crystal was placed on a goniometer 1480 mm upstream from the grating. The detailed setup for the measurement of the V/B₄C multilayer crystal has been reported elsewhere [112].

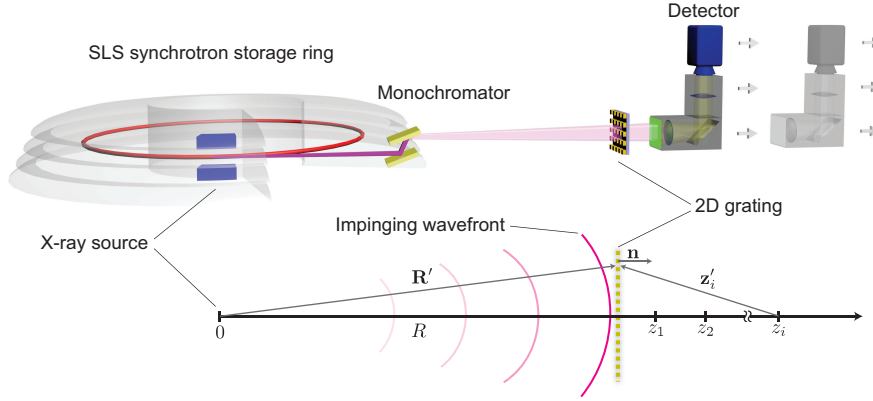


Figure 4.7. Experimental setup at the X02DA TOMCAT beamline to measure the coherence properties of the superbending magnet source.

A 2D mixed phase and absorption grating (see Fig. 4.8) was placed at $R = 26.3$ m and $R = 26.5$ m distances from the source, respectively. A CCD detector coupled with visible light optics ($20\times$ magnification) and a $20\mu\text{m}$ thick scintillator were used for acquiring images, yielding an effective pixel size of $0.38 \times 0.38 \mu\text{m}^2$. The grating was aligned with a goniometer (about the z -axis), whereby small z -tilts can also be corrected by rotating the detector which introduces a negligible effect of projecting the respective source sizes onto one another. Tilts about the x - and y -axes were treated computationally and are discussed later on. Thus, it is noteworthy that in the most simplified setup the grating can be aligned purely by eye, making obsolete the use of high precision motors. For the characterization of the V/B₄C multilayer, the pixels of the acquired images were binned by a factor of 2, yielding an effective pixel size of $0.76 \times 0.76 \mu\text{m}^2$. The detector was moved to various propagation distances z ranging from $0.002 - 2.102$ m. At each distance an image was taken and corrected with the respective dark and flat-field images, prior to further analysis. Due to different X-ray fluxes under each experimental condition, the exposure times t_{exp} were adjusted as follows: $t_{\text{exp}} = 0.2$ s for the [Ru/C]₁₀₀, $t_{\text{exp}} = 1.5$ s for the [W/Si]₁₀₀ and $t_{\text{exp}} = 36.0$ s for the combined Si(111) and V/B₄C multilayer measurement. The time required for acquiring a full set of 106 Talbot images was between 30 and 120 min.

Theoretical background

For interpreting the Fresnel diffraction images after the interaction of the X-ray beam with the periodic grating, we summarize the model for the above described experimental imaging setup by starting from an idealized point source emitting a spherical wave. The wave field ψ

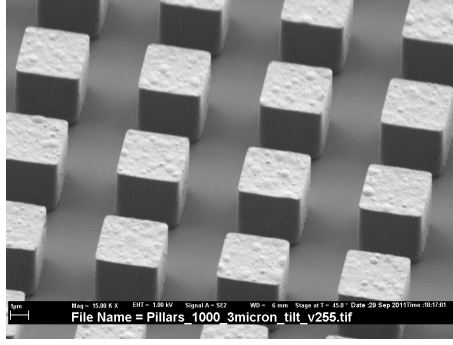


Figure 4.8. SEM image of the 2D grating. The grating was fabricated to have a regular gold pattern on a silicon substrate with following parameters: $w = 3.65 \mu\text{m}$ (width of gold pillars) with $h = 3.39 \mu\text{m}$ (height), $d_c = 0.53$ (duty cycle), $\alpha = 4.2^\circ$ (angle) and $2 \times 2 \text{mm}^2$ grating size.

at a distant point \mathbf{r} can be described as

$$\psi(\mathbf{r}) = A \cdot \frac{\exp(i\mathbf{k} \cdot \mathbf{r})}{|\mathbf{r}|}, \quad (4.5)$$

with wave vector \mathbf{k} and amplitude A . For simplicity, we disregard the time dependency by observing the wave only at $t = 0$. The wave field disturbance after passing a diffraction object such as a 2D grating is described by Huygens-Fresnel principle, stating that the result is a superposition of secondary wavelets emerging from every point of the initial wavefront [95]. Detailed mathematical treatment yields two possible solutions, namely the two Rayleigh-Sommerfeld solutions and the Fresnel-Kirchhoff diffraction formula, which are equivalent for the present setup [115]. Using the latter of the two, we arrive at:

$$\psi(\mathbf{r}) = \frac{A}{2i\lambda} \iint_G \frac{e^{i\mathbf{k}(\mathbf{R}' + \mathbf{z}')}}{|\mathbf{R}'| \cdot |\mathbf{z}'|} [\cos(\mathbf{n}, \mathbf{z}') - \cos(\mathbf{n}, \mathbf{R}')] dG, \quad (4.6)$$

where G is the area along the diffraction object (grating), \mathbf{n} the normal vector to it, and \mathbf{z}' and \mathbf{R}' represent position vectors indicated in Fig. 4.7. It is then possible to simplify the above expression by regarding a big source-to-grating distance (i. e. Fresnel approximation) to give:

$$\psi(\mathbf{r}) = \frac{A}{2i\lambda} \iint_G \frac{e^{i\mathbf{k}\mathbf{R}'}}{|\mathbf{R}'|} \cdot \frac{e^{i\mathbf{k}\mathbf{z}'}}{|\mathbf{z}'|} [1 + \cos(\mathbf{n}, \mathbf{z}')] dG. \quad (4.7)$$

In the following formulation we restrict ourselves to the case of a 2D grating with grating coordinates x_0 and y_0 that are normal to the axis z . Since the grating can be seen as an operator changing the amplitude and/or phase of the impinging wavefront at defined values x_0 and y_0 , it can be expressed as a function multiplied with the wavefront at the grating position. Further on, we consider only small angles and utilize the fact that the aperture diameters

(i. e. grating pitch) of the object are orders of magnitudes greater than the wavelength, which makes the Rayleigh-Sommerfeld and Fresnel-Kirchhoff formulas identical and omits the above cosine term [115]. Equation (4.7) then transforms to:

$$\psi(\mathbf{r}) = \frac{A}{i\lambda} \int_{-\infty}^{+\infty} \int_{-\infty}^{+\infty} \frac{e^{ikR'}}{R'} \cdot G(x_0, y_0) \cdot \frac{e^{ikz'}}{z'} dx_0 dy_0, \quad (4.8)$$

with

$$R' = (R^2 + x_0^2 + y_0^2)^{\frac{1}{2}}, \quad (4.9)$$

source-to-grating distance R and $k = |\mathbf{k}|$. After applying the so-called paraxial approximation and combining the grating function G and the phasor of the impinging wavefront in function $f(x_0, y_0)$ we finally get:

$$\psi(\mathbf{r}) = \frac{Ae^{ikz}}{i\lambda R} \int_{-\infty}^{+\infty} \int_{-\infty}^{+\infty} f(x_0, y_0) \cdot \exp \left\{ \frac{ik}{2z} [(x - x_0)^2 + (y - y_0)^2] \right\} dx_0 dy_0, \quad (4.10)$$

where x and y are now the coordinates of the imaging plane. This equation can now be evaluated by two different approaches: either by applying the paraxial approximation to the phasor of the impinging wavefront [116] which leads to the definition of the defocussing distance D and magnification M :

$$D := \frac{Rz}{R+z} = \frac{z}{M}, \quad (4.11)$$

or by identifying above equation as a convolution of $f(x, y)$ with the Fresnel kernel. We choose the latter for simplicity reasons and get:

$$\psi(\mathbf{r}) = C \cdot f(x, y) \otimes \exp \left[\frac{ik}{2z} (x^2 + y^2) \right], \quad (4.12)$$

where C is a constant, proportional to the amplitude of the impinging wave.

To account for the finite source, the Van-Cittert-Zernike theorem is then applied assuming an extended quasi-monochromatic incoherent (i. e. partially coherent) source. Assuming further a Gaussian-shaped source [86], we use the so-called projected source sizes $\sigma_{\text{proj,H}}$ and $\sigma_{\text{proj,V}}$ with

$$\sigma_{\text{proj},i} = \frac{\sigma_i \cdot z}{R\sqrt{8\ln 2}}, \quad (4.13)$$

where σ_i is the FWHM of the horizontal and vertical source size, respectively [117]. The final expression for the intensity of the Fresnel diffraction pattern I at $\mathbf{r} = (x, y, z)$ is thus given by:

$$I(\mathbf{r}) = \left| C \cdot f(x, y) \otimes \exp \left[\frac{ik}{2z} (x^2 + y^2) \right] \right|^2 \otimes \exp \left[- \left(\frac{x^2}{2\sigma_{\text{proj,H}}^2} + \frac{y^2}{2\sigma_{\text{proj,V}}^2} \right) \right]. \quad (4.14)$$

The function $f(x, y)$ describes the wavefront just after passing the grating and reads as:

$$f(x, y) = \exp[-ik\delta h(x, y)] \times \exp[-k\beta h(x, y)] \times \exp\left[ik(R^2 + x^2 + y^2)^{\frac{1}{2}}\right], \quad (4.15)$$

where $h(x, y)$ is the grating function with coordinates x and y , δ and β are the refractive and absorption indices, respectively. The function $h(x, y)$ can be expressed e. g. as a binary function

$$h(x, y) = \begin{cases} h, & \text{for } na \leq x, y < na + w \\ 0, & \text{else.} \end{cases} \quad (4.16)$$

with the grating's gold pillar height h , integer n , grating period a and grating's gold pillar width w . According to the fabrication process of the grating, function $h(x, y)$ was slightly modified in the numerical implementation to include a slight trapezoidal shape of the grating with angle α .

Source size calculation

In theory, for calculating the spatial degree of coherence of the beam in the plane of the grating (and with that the source size), the recorded diffraction patterns are further expanded into a 2D Fourier series with coefficients $\tilde{I}(k_x, k_y, z) = \mathfrak{F}[I(x, y, z)]$. By calculating these coefficients at different propagation distances z_i , it is possible to obtain the degree of coherence [109]. The results will be distorted, however, if outliers exist at the respective points of interest, caused for instance by imperfect grating parameters and/or alignment as well as statistical errors originating from (imprecise) dark-/flat-field corrections and eventual beam fluctuations. We therefore propose a formalism that requires only approximate knowledge about all parameters affecting the results.

First, we define horizontal and vertical Talbot image line profiles by averaging column- and line-wise:

$$f_H(x, z) = \frac{1}{n_y} \sum_y I(x, y, z) \quad \text{and} \quad f_V(y, z) = \frac{1}{n_x} \sum_x I(x, y, z), \quad (4.17)$$

where n_y and n_x are the number of pixels in the vertical and horizontal directions, respectively. We then extract principle Fourier components of the line profiles, analog to [109], by:

$$F_H(z) := \mathfrak{F}[f_H(x, z)](k_x) \quad \text{and} \quad F_V(z) := \mathfrak{F}[f_V(y, z)](k_y), \quad (4.18)$$

with $k_x = p_{\text{size}} \cdot n_x / (Ma)$, $k_y = p_{\text{size}} \cdot n_y / (Ma)$ depending on the pixel size p_{size} , the grating period a , magnification M and the total number of pixels. From now on, we omit the explicit notation for horizontal and vertical Fourier coefficients, as they are treated equally further on, but distinguish those obtained from simulated and experimental Talbot images, denoted as $F_{\text{sim}}(z)$ and $F_{\text{exp}}(z)$. The further approach is as follows: based on the fact that Talbot images can be correctly modeled given that all experimental parameters are known [see Eq. (4.14)],

the source size can be determined implicitly by using an appropriate set of simulation variables. More precisely, Fourier coefficients $F_{\text{sim}}(z)$ can be varied depending on the source size (and other parameters) and fitted by means of weighted least-squares to $F_{\text{exp}}(z)$.

In doing so, we define a modified least-squares error (LSE) p as a measure for the quality of the fit between $F_{\text{sim}}(z)$ and $F_{\text{exp}}(z)$:

$$p(\mathbf{z}, E, \sigma, d_c, \alpha) = \sum_{i=1}^{n_z} \left\{ \left[F'_{\text{exp}}(z_i) - F'_{\text{sim}}(z_i, E, \sigma, d_c, \alpha) \right]^2 \cdot F'_{\text{exp}}(z_i) \right\}, \quad (4.19)$$

with propagation distances $\mathbf{z} = (z_1, \dots, z_i, \dots)$, energy E , source size σ , grating's duty cycle d_c , trapezoidal angle α , total number of propagation distances n_z and

$$F'_{\text{exp}}(z_i) = \frac{F_{\text{exp}}(z_i)}{(1/n_z) \sum_{i=1}^{n_z} F_{\text{exp}}(z_i)} \quad \text{and} \quad F'_{\text{sim}}(z_i) = \frac{F_{\text{sim}}(z_i)}{(1/n_z) \sum_{i=1}^{n_z} F_{\text{sim}}(z_i)}, \quad (4.20)$$

being the normalized experimental and simulated principal Fourier coefficients. In the following, we denote p as the “weighted LSE”. Obviously, if a particular set of parameters minimizes p so that it approaches 0, the solution is found. Considering that, we only need to define minimum and maximum margins for each parameter that are consistent with the experimental setup and conduct an efficient search in the parameter space for minimizing p .

The detailed flowchart of the complete algorithm is depicted in Fig. 4.9: for each parameter E , σ , d_c and α , n_{max} intervals are “nested” between given minimum and maximum margins. Fourier coefficients for the simulated and experimental Talbot images are then calculated for each direction (horizontal and vertical) independently. Within this step, the averaged line profiles from Eq. (4.17) are additionally multiplied with a Hanning window function to reduce leakage and aliasing effects [118]. After normalization, the weighted LSE p is calculated and compared to the value of p_{start} , which upon initialization can be any big number (e. g. $p_{\text{start}} = \infty$) and for any further iteration contains the lowest occurrence of p heretofore. If p is lower than p_{start} at this point then the whole set of parameters is written to temporary memory and p_{start} is overwritten by the current value of p . These steps are repeated until all intervals for all parameters have been run through. Thereafter, the parameters corresponding to the lowest value of p are loaded and used to nest intervals for the next iteration. The nesting is implemented similarly to a bisection method (also known as binary search algorithm), where n_{max} sections are used rather than two only. Finally, after repeating the nesting k_{max} times, the calculated source size along with other parameters can be loaded from temporary memory.

The fitting procedure is demonstrated in Fig. 4.10 for an X-ray beam of 21.6 keV monochromatized by the Si(111) double-crystal monochromator. Fourier coefficients were obtained from 106 different propagation distances and starting parameters were set to: $E_{\text{min}} = 21.5$ keV, $E_{\text{max}} = 22.5$ keV, $\sigma_{\text{min}} = 0$ μm , $\sigma_{\text{max}} = 200$ μm , $d_{c,\text{min}} = 0.50$, $d_{c,\text{max}} = 0.54$, $\alpha_{\text{min}} = 0^\circ$ and $\alpha_{\text{max}} = 4.2^\circ$.

We analyze this approach in more detail. The normalization of the Fourier coefficients [in Eq.(4.20)] with their respective mean values (rather than e. g. the maximum ones) is

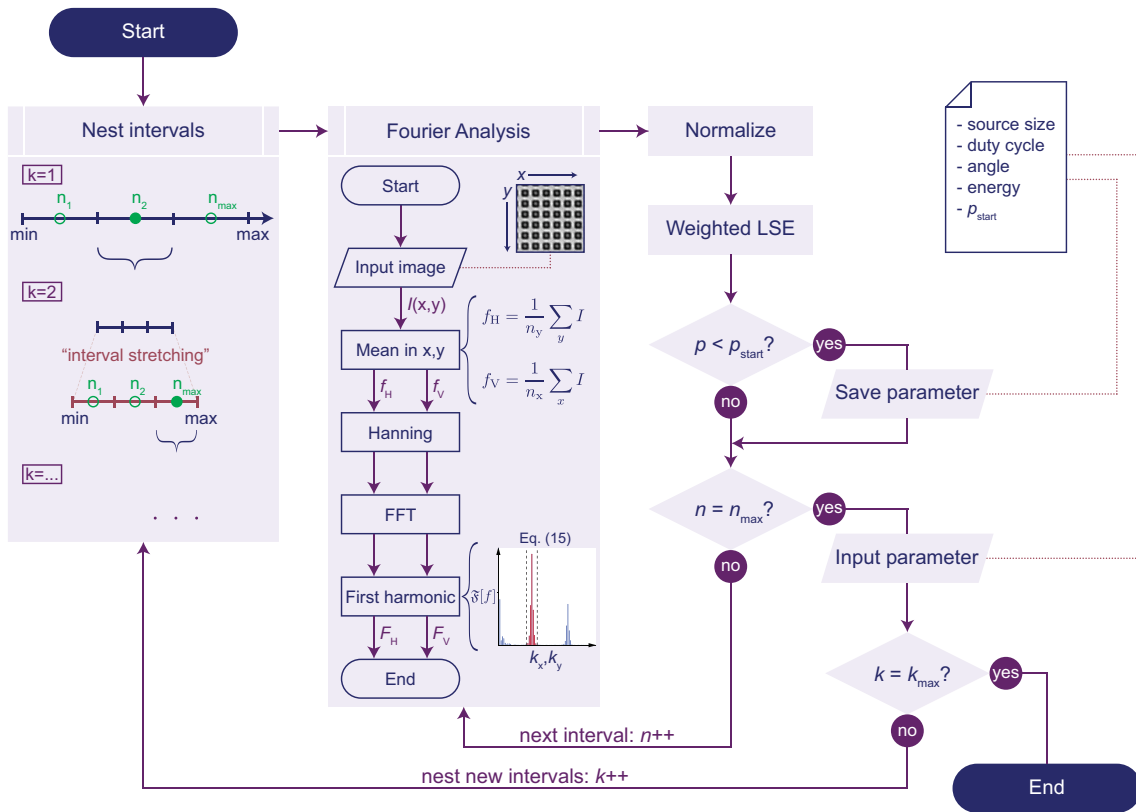


Figure 4.9. Flowchart for calculating the source size. First, intervals for each parameter E , σ , d_c and α are nested. In the second subroutine (“Fourier Analysis”) both simulated and experimental Talbot images are loaded, which are in return used for calculating the weighted LSE. The program is exited when the weighted LSE has been calculated for all intervals n_{max} and all iterations k_{max} .

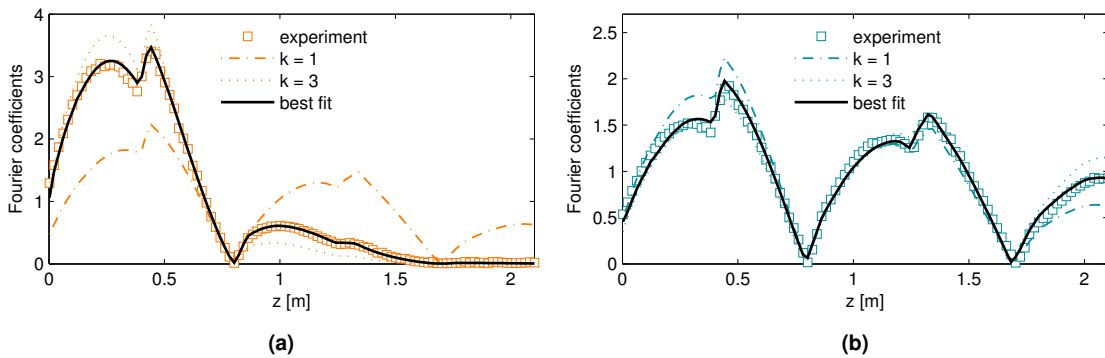


Figure 4.10. Demonstration of the fitting algorithm from Fig. 4.9 for the Si(111) DCM. The experimental Fourier coefficients as well as two iterations from the fitting algorithm are plotted in dependency on the propagation distance z . The “best fit” (solid line) was calculated by loading all parameters obtained from the fitting algorithm and using them as an input for Eqs. (4.14) and (4.18).

done in order to equally account for Fourier coefficients over the whole range of z_i when fitting to the experimental data. The weighting in Eq. (4.19) follows another simple principle: small values of Fourier coefficients contain less information (more noise), and thus, deviations arising from these coefficients are penalized by the additional weighting when minimizing p . The only remaining ambiguity in this respect arises from the fitting procedure itself, namely the treatment of local minima which represents a common challenge for most iterative processes. In the present work we address this issue by multiplying each interval that is parted upon interval nesting with an additional factor s . To be exact, each parted interval is additionally “stretched” by an arbitrary factor s (as indicated in Fig. 4.9), thus enabling each parameter to “climb out” of a local minimum in a subsequent iteration step. Naturally, there exist more sophisticated methods for treating local extrema, which are not discussed further, as they were not required in the present study. Finally, all parameter margins are set in consistence with the experimental setup: the X-ray energy margin originates from the fact that the aligned energy might not be correct due to impreciseness in the monochromator calibration; the source size margin can be set arbitrarily in a region where the source size is approximately expected; and the margins for the grating’s duty cycle and angle on the one hand account for grating’s fabrication impreciseness, and on the other hand for imprecise grating alignment in the beam. In particular, the latter two account for tilts about x - and y -axes causing more pronounced trapezoidal pillar shapes [113].

We can conclude that with the above approach it is possible to conduct the complete source size calculation implicitly in an automated way and, more importantly, without any user interaction, by recursively finding an optimized set of fit parameters. The great advantage is that the information from all Fourier coefficients is used, making the method robust to statistical errors and precise at the same time. The total number of iterations for the two (horizontal and vertical) source sizes is calculated by

$$N_{\max} = 2 \cdot n_{\max}^4 \cdot k_{\max} \cdot n_z, \quad (4.21)$$

giving $N_{\max} = 120,204$ for the present example of $n_{\max} = 3$ intervals, $k_{\max} = 7$ iterations with $s = 1.5$ and $n_z = 106$ propagation distances. The complete calculation took about 10 min on a single PC (Pentium i5, Mathworks Matlab), whereas a single iteration step lasted around 6 ms. In order to boost the calculation time, the simulation from Eq. (4.14) was conducted in 1D independently for the horizontal and vertical directions.

Uncertainty analysis

We complete the above formalism by treating the influence of measurement uncertainties to the overall source size calculation.

The approximation made within Fresnel-Kirchhoff diffraction formula correctly describes the physical problem if all distances R, R', z, z' as well as all object’s structures (such as grating pitch etc.) are orders of magnitudes greater than the wavelength λ [115]. This condition is in full agreement with the investigated energy range of 10–40 keV. The paraxial approximation

from Eq. (4.10) is justified by the fact that we are concerned with regions very close to the optical axis. On the other hand it has also been shown that combined paraxial-Fresnel approximation is more accurate than either one imposed separately [119]. As a result, we only need to treat measurement uncertainties affecting Eq. (4.14) in order to account for the overall source size measurement accuracy. In the following we consider maximal error margins for each error source.

Starting from the assumption that the grating has a perfect shape ($\alpha = 0^\circ$, $d_c = 0.5$), that all of its parameters are known (h , w) and that it is perfectly aligned in the beam, the experimental results will still differ from the theoretical prediction due to the uncertainty in the adjusted propagation distance of the detector, which will affect the Fresnel kernel and for our experiment we estimate to be less than $\Delta z = 2$ mm. The maximal error margin for the source size can be evaluated numerically from this value by including it in the weighted LSE from Eq. (4.19) and postulating that the precision of z is directly determining the precision of the source size σ :

$$p(\mathbf{z} \pm \Delta z, E, \sigma, d_c, \alpha) \stackrel{!}{=} p(\mathbf{z}, E, \sigma \pm \Delta \sigma, d_c, \alpha). \quad (4.22)$$

Thus, the source size uncertainty $\Delta \sigma$ is calculated by two subsequent simulations for finding an appropriate value of $\Delta \sigma$ that equally alters the weighted LSE p as Δz . This relation is derived from the fact that it is impossible to define the origin of $p \neq 0$ from the acquired experimental data and the subsequent calculation of p . Likewise, z is also directly connected with the energy uncertainty which arises from the fact that the energy cannot be selected very precisely by the monochromator (see above). For this reason, the energy uncertainty is treated the same way by requiring that

$$p(\mathbf{z} \pm \Delta z, E, \sigma, d_c, \alpha) \stackrel{!}{=} p(\mathbf{z}, E \pm \Delta E, \sigma, d_c, \alpha), \quad (4.23)$$

meaning that it is impossible to determine whether $p \neq 0$ arises from Δz or ΔE , which is why they have to be treated equally in order to cover maximal error margins.

In a more realistic case, however, we also have to account for fabrication imperfections in the grating which influence the two grating terms (absorption, phase shift) and the impinging wavefront from Eq. (4.15), or more generally, the wavefront right after the grating that is then propagated. For doing so, we define an effective wave vector uncertainty Δk_{eff} and require that it incorporates all uncertainties originating from the grating's fabrication process:

$$i(k \pm \Delta k_{\text{eff}})h(\delta + i\beta) \stackrel{!}{=} i(k \pm \Delta k)(h \pm \Delta h)[\delta + i\beta \pm (\Delta \delta + i\Delta \beta)], \quad (4.24)$$

where Δh is the uncertainty of the fabricated grating's pillar height and $\Delta \delta$ and $\Delta \beta$ are the dispersion and absorption uncertainties, respectively. The latter two originate from imperfections in the grating's gold structures that have a slightly altered gold density and thus induce slightly different phase shifts and absorption levels for X-rays. By evaluating Eq. (4.24) we obtain:

$$k \pm \Delta k_{\text{eff}} = \left[k \pm \Delta k \pm k \frac{\Delta h}{h} + \frac{\Delta k \Delta h}{h} \right] \cdot \left[1 \pm \frac{\Delta \delta + i\Delta \beta}{\delta + i\beta} \right], \quad (4.25)$$

which can further be approximated by making use of $\Delta k \approx k \frac{\Delta h}{h}$ and $\frac{\Delta k \Delta h}{h} \ll \Delta k$. The last term is evaluated separately:

$$\frac{\Delta \delta + i \Delta \beta}{\delta + i \beta} = \frac{\Delta \delta / \delta}{1 + \beta^2 / \delta^2} + \frac{\Delta \beta / \beta}{1 + \delta^2 / \beta^2} + i \frac{\Delta \beta / \delta}{1 + \beta^2 / \delta^2} - i \frac{\Delta \delta / \beta}{1 + \delta^2 / \beta^2}. \quad (4.26)$$

Estimating the maximal order of magnitude for each term and the given X-ray energy range yields:

$$\vartheta_{\max} = \frac{\mathcal{O}(10^{-2})}{1 + \mathcal{O}(10^{-3})} + \frac{\mathcal{O}(10^{-2})}{1 + \mathcal{O}(10^2)} + i \frac{\mathcal{O}(10^{-3})}{1 + \mathcal{O}(10^{-3})} - i \frac{\mathcal{O}(10^{-1})}{1 + \mathcal{O}(10^2)} \approx \mathcal{O}(10^{-2}). \quad (4.27)$$

Now Eq. (4.25) can be simplified to

$$k \pm \Delta k_{\text{eff}} \approx k \pm 2\Delta k \pm (k \pm 2\Delta k) \mathcal{O}(10^{-2}), \quad (4.28)$$

finally leading to the effective wave vector and energy uncertainty:

$$|\Delta k_{\text{eff}}| \approx 3\Delta k \quad \longrightarrow \quad \Delta E_{\text{eff}} = c \cdot \hbar \cdot \Delta k_{\text{eff}}, \quad (4.29)$$

with the speed of light c and Planck's constant \hbar . In the latter approximation we used the fact that $k \cdot \mathcal{O}(10^{-2}) \approx \Delta k$ and $2\Delta k \cdot \mathcal{O}(10^{-2}) \ll \Delta k$. We can thus state that the most pronounced error from the grating's fabrication process will result in a slightly modified phase shift and absorption, which can be consolidated into an effective energy uncertainty. The only remaining error sources in this respect are the grating's duty cycle and angle that are determined very precisely in the fitting process, as they significantly influence the shapes of the curves in Fig. 4.10. This means that, once the best fit has been found, the source size uncertainty no longer depends on the uncertainties of these parameters. As mentioned above, their values depend mainly on the grating's fabrication process as well as the alignment of the grating in the beam.

Finally, we shortly discuss the uncertainties of the wave vector Δk and the propagation distance Δz affecting the Fresnel kernel in Eq. (4.14). Following the same strategy as before to consolidate both values into an effective wave vector uncertainty, we write

$$\frac{i(k \pm \Delta k_{\text{eff}})}{2z} \stackrel{!}{=} \frac{i(k \pm \Delta k)}{2(z \pm \Delta z)} \quad (4.30)$$

and obtain:

$$|\Delta k_{\text{eff}}| = \frac{|z\Delta k - k\Delta z|}{z + \Delta z}. \quad (4.31)$$

To evaluate this equation we regard two marginal conditions. For $\Delta z \ll z$, it is trivial to show that $\Delta k_{\text{eff}} \approx \Delta k$, meaning that for longer propagation distances the precision of the detector's travel range will be negligible. For $\Delta z \approx z$ we get the relatively big value of $\Delta k_{\text{eff}} \approx k/2$, but it can be shown that the magnitude of Δk is proportional to the magnitude of Δz . This

means, if we require Eq. (4.31) to have the same order of magnitude as Δk_{eff} from before, it is in fact enough to measure the first Fourier coefficients several centimeters away from the grating. For our case, this constraint is obsolete since the fitting algorithm equally takes all Fourier coefficients into account, and if a few coefficients are incorrect, the final results will not be altered. Moreover, uncertainties affecting the Fresnel kernel have already been taken into account in Eqs. (4.22) and (4.23).

4.2.4 Results and discussion

Two separate experiments were conducted to characterize all three standardly used monochromators at the X02DA TOMCAT beamline. Fourier coefficients for the Si(111) DCM are depicted in Fig. 4.10., whereas Fig. 4.11 and Fig. 4.12 correspond to measurements with the multilayer monochromators. The influence on the beam coherence from the V/B₄C multilayer crystal is shown in Fig. 4.13. The source size values obtained with the fitting algorithm as well as all calculated uncertainties are listed in Tab. 4.2 and graphically represented in Fig. 4.14.

The vertical source size of the beam was found to be about 30% smaller using the Si(111) monochromator crystals when compared to the multilayer monochromator stripes. Likewise, a smaller vertical source size was measured at higher X-ray energies which can be explained by a smaller vertical beam divergence at higher energies as a characteristic of bending magnet radiation. The two multilayer monochromator stripes, which were both measured at the same energy, showed no significant differences (as shown in Fig. 4.11).

In the second experiment the horizontal source size was found to be about 17% bigger than in the first one. This variation in time is attributed to the storage ring operation conditions, in particular the undulator gap opening at the nearby X05LA FEMTO beamline. The broadening of the electron beam at the TOMCAT beamline was caused by closing the gap at the FEMTO beamline when the second set of coherence measurements were performed. The vertical source size, on the other hand, depends on the status of the orbit and coupling correction and may change more frequently depending on the machine operation mode. This is why the vertical source size for the [Ru/C]₁₀₀ monochromator at lower energies was smaller during the second experiment. Table 4.2 also highlights the actual value of the X-ray energy that resulted from the fitting procedure. The values were found to be systematically lower than the aligned energy based on the pre-calibrated monochromators, being indicative of how precise the X-ray energies can actually be set during beamline operation. The respective energy uncertainties ΔE_{eff} correspond to effective uncertainties in the aligned mean energy. Thus they must not be confused with the energy bandwidth of the monochromated beam which is in the range of a few percent [114].

For measuring the influence of a V/B₄C multilayer crystal on the X-ray beam, the previously introduced fitting algorithm had to be slightly modified. First, since the energy E is determined precisely during an initial reference measurement with the Si(111) monochromator and the grating, E can be regarded as a constant parameter (from that point on). Secondly, the source-to-sample distance R in Eq. (4.15) was added as a fitting variable, while in Eq. (4.13) it was left unchanged with $R = 26.5$ m. By doing so, the wavefront curvature of the X-ray beam after

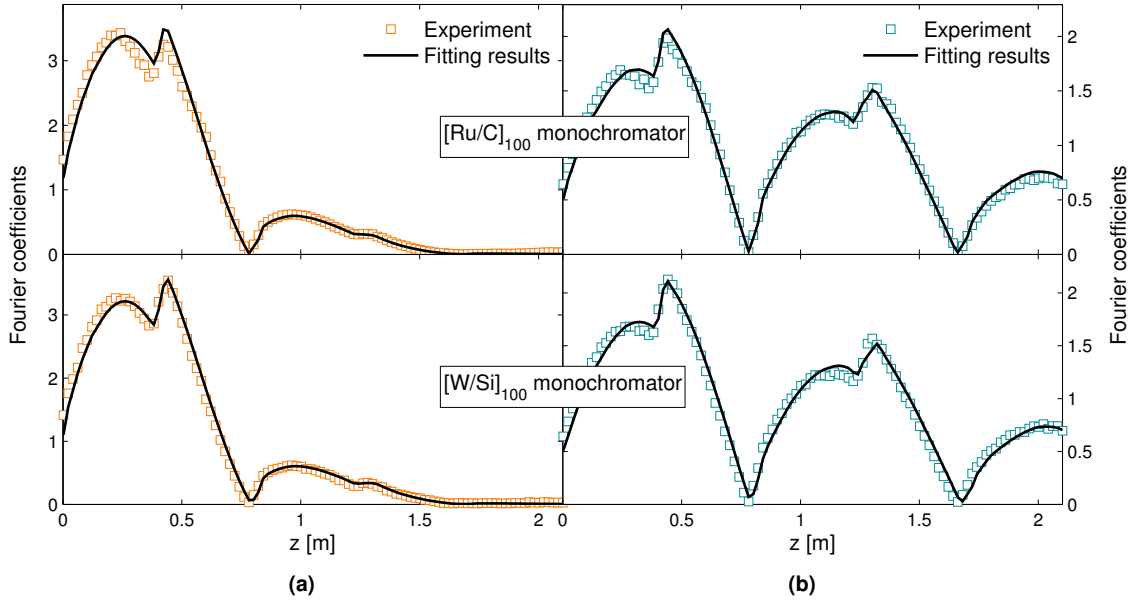


Figure 4.11. Principal Fourier coefficients in horizontal (a) and vertical (b) direction as functions of the propagation distance z for two multilayer monochromators at approx. 21.4 keV X-ray energy. Simulated Fourier coefficients (solid line) were calculated with parameters obtained from the fitting algorithm.

being reflected from the V/B₄C multilayer was studied independently from the source size. Thus, we found that the horizontal beam characteristics were not altered significantly by the multilayer, yielding a horizontal source size of 154 μm and a curvature radius of 25.0 m. In the vertical direction, the curvature radius of the beam was decreased to 4.5 m, while the source size was found to be 43 μm . This effect is obvious from the shifted value of the Talbot plane to $z = 0.7$ m [in Fig. 4.13(b)] in the vertical direction as compared to $z = 0.6$ m in the horizontal direction. From Fig. 4.13 it is also clearly visible that in the range of $z = 0 - 0.4$ m, the fitting results for the vertical coefficients are not as good as for the horizontal ones. As discussed above, this effect can be affiliated to a local minimum in the fitting procedure regarding the grating’s duty cycle and/or trapezoidal angle.

In earlier studies [109, 112], the first Fourier coefficients exhibit smooth behavior as a function of the defocusing distance, while our data (see e. g. Fig. 4.12) shows “dips” in the plots of the Fourier coefficients. This makes our plots less similar to the usual visibility curves in the literature. For a mixed phase-absorption grating, which we used for our measurement, this is predominantly a consequence of the deviation in the duty cycle from the ideal 0.5 and the trapezoidal shape of the grating.

Finally, we briefly discuss some other aspects of our method. In the beginning, two assumptions were made from which the formalism was derived, namely that experimental data is captured only with a limited precision and that all data can be modeled correctly if experimental parameters are known. Since the source size calculation takes place in the Fourier space, the

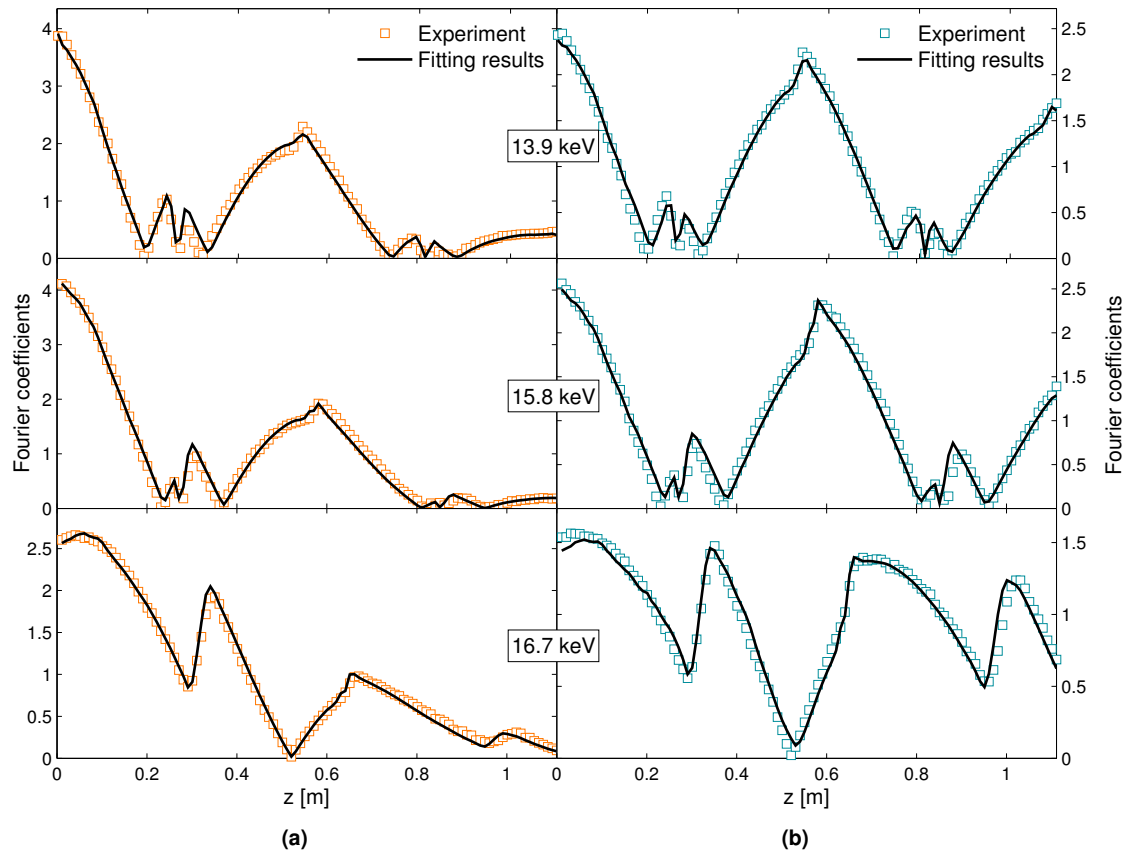


Figure 4.12. Principal Fourier coefficients in horizontal (a) and vertical (b) direction for the $[\text{Ru/C}]_{100}$ monochromator crystal set to three different X-ray energies. Simulated Fourier coefficients (solid line) were calculated with parameters obtained from the fitting algorithm.

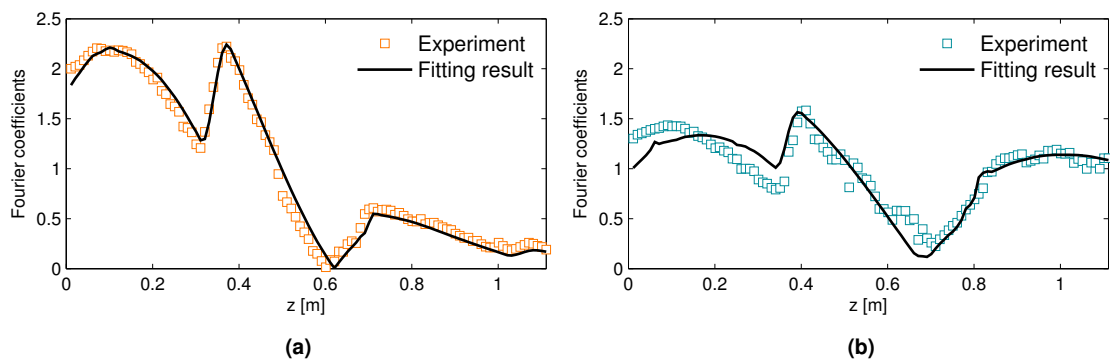


Figure 4.13. Principal Fourier coefficients in horizontal (a) and vertical (b) direction for the $\text{V/B}_4\text{C}$ multilayer crystal at 18.0 keV X-ray energy. Simulated Fourier coefficients (solid line) were calculated with parameters obtained from the fitting algorithm.

Table 4.2. Horizontal and vertical full-width-at-half-maximum (FWHM) source sizes and fitted energies E for the two experiments (setups) conducted at the X02DA TOMCAT beamline. Additionally, the source-to-grating distance R and the maximum detector’s travel range z are listed. For the characterization of the V/B₄C multilayer the source-to-grating distance was included as a variable in the fitting algorithm, independently for both the horizontal and the vertical direction. All uncertainties represent maximal error margins

Setup	Multilayer	E [keV]	σ_H [μm]	σ_V [μm]	R [m]	z [m]
I	[Ru/C] ₁₀₀	13.90 ± 0.15	133 ± 4	52 ± 4	26.3	1.1
I	[Ru/C] ₁₀₀	21.30 ± 0.10	128 ± 1	45 ± 1	26.3	2.1
I	[W/Si] ₁₀₀	21.50 ± 0.20	125 ± 2	46 ± 1	26.3	2.1
I	Si(111)	21.60 ± 0.15	124 ± 1	35 ± 1	26.3	2.1
II	[Ru/C] ₁₀₀	14.70 ± 0.15	149 ± 4	42 ± 3	26.5	1.1
II	[Ru/C] ₁₀₀	15.75 ± 0.15	150 ± 4	44 ± 2	26.5	1.1
II	[Ru/C] ₁₀₀	16.65 ± 0.15	147 ± 4	38 ± 4	26.5	1.1
II	Si(111)+V/B ₄ C	18.00 ± 0.10	154 ± 2	43 ± 2	25.0 (H) 4.6 (V)	1.1

variation of simulated Fourier coefficients has been investigated therein. The energy range was chosen so that the grating equally represents a phase and absorption grating in order to cover preferably the most complicated case. It is clear, however, that lowering and/or increasing the X-ray energies would facilitate further simplifications to the model [i. e. in Eq. (4.15)]. We found that the necessary number of Talbot images, and with that Fourier coefficients, depends not only on the chosen range of z , but also on the quality of the data. For instance, in the presence of noisy data, many Talbot images are required for obtaining a correct fit and for reducing statistical errors (e. g. from beam fluctuations). Decreasing the travel range of the detector, on the other hand, simplifies the experimental setup, but may increase the calculated uncertainty which we showed to be directly connected to the uncertainty of the adjusted detector’s propagation distance (Δz). Applied to the [Ru/C]₁₀₀ multilayer at 21.3 keV, a reduction to 56 Talbot images and $z = 1.1$ m yields $\sigma_H = (131 \pm 3) \mu\text{m}$ and $\sigma_V = (44 \pm 2) \mu\text{m}$, which represents only a marginally greater uncertainty. For other experimental conditions, however, these results may vary as the values depend both on the curve shapes and the measured range of z . Concerning the data from Tab. 4.2, the same parameters were used in the fitting procedure, while the source size and energy uncertainties were calculated for each dataset separately.

4.2.5 Conclusion

We have developed an evaluation method for coherence measurements based on the fractional Talbot effect that can be performed without the need of optically perfect X-ray diffractive elements and does not require precise alignment in the experimental setup. The method is applicable to arbitrary X-ray energies and supports a full quantitative uncertainty analysis of the complete source size measurement. We showed that the characterization of the influence on source size by diffractive optics, such as multilayer crystals, can easily be performed with

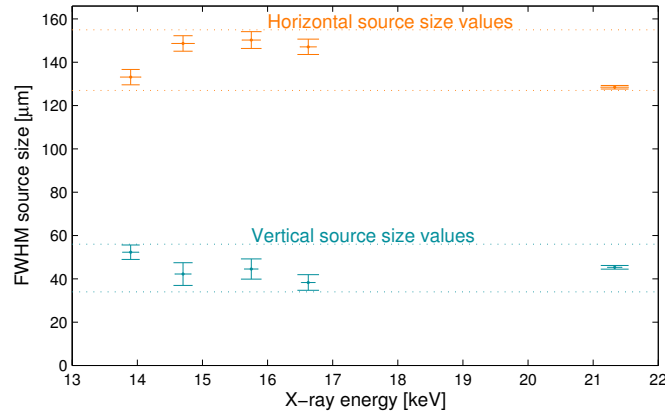


Figure 4.14. Calculated source sizes for the $[\text{Ru}/\text{C}]_{100}$ multilayer, where the horizontal and vertical lines denote the source size and energy measurement uncertainties, respectively.

X-ray beams of relatively low transversal coherence length. Finally, for the first time we evaluated the reliability of such measurements. All calculation tools are published under GNU General Public License and available for download at the TOMCAT homepage [120].

4.2.6 Appendix

For fabricating the grating, we used the method established by Gorelick *et al.* [121] to produce high aspect-ratio gold nanostructures by electroplating a direct written PMMA mold. We evaporated a Cr/Au/Cr (5/20/5 nm) plating base on a silicon substrate and subsequently spin-coated with a 4 micron thick PMMA resist. The grating patterns were directly written to the resist using a 100 keV Vistec EBPG 5000plus electron beam writer. The exposed chips were developed for 60 s in a mixture of isopropanol and water (7:3 by volume) [122]. The plating base's topmost chromium layer was removed by 30 s RIE plasma etching in a mixture of chlorine and carbon monoxide. The mold was filled with electroplated gold using a cyanide-based bath with a nominal density of $17 \text{ g}/\text{cm}^3$ and a nominal cobalt content of 1-2%, corresponding to three components contributing to the optical properties in the X-ray range.

4.2.7 Acknowledgments

We acknowledge Gordan Mikuljan for his great support in setting up the experiment at the beamline, Silvia Peter, Christian David and Ismo Vartiainen for fruitful discussions during data analysis, Alexander Rack, Timm Weitkamp for contributing to the general understanding of concepts for coherence measurements and Andreas Streun for providing us details about synchrotron machine operation. This study was supported by the National Competence Center in Biomedical Imaging (NCCBI), grant No. 1126.0076, and the Swiss National Science Foundation (SNF), grant No. CR2312-135550.

4.3 DOSIMETRY

The assessment of radiation dose nowadays represents a standardized procedure being particularly important in clinical X-ray imaging [123]. In small animal research, micro-CT systems are now increasingly used in various preclinical studies, mainly due to the availability of small animal models covering a wide range of biological fields [124]. Hence, lots of efforts have been put into the study of small animal radiation doses, e. g. with high-precision voxel-based Monte Carlo models for internal dose calculations [125], but mostly those have been limited to magnifications with pixel sizes down to $50 \times 50 \mu\text{m}^2$ [126]. Following the fact that in our project we require pixel sizes to be smaller than an order of magnitude as well as the aspect of utilizing a synchrotron X-ray source, our approach towards dosimetry had to be treated from the ground up.

In the following, we start with a short discussion about two basic principles related to dose in imaging. We then introduce our simplified model for calculating radiation dose and compare the obtained values with biological responses to radiation, particularly lungs. Finally we present our methodology for radiation dose assessment at the beamline.

4.3.1 Essentials

In the quest to improve spatial resolution in any imaging technique such as X-ray tomography, inevitably we have to call to our mind two simple but fundamental principles. Starting with the famous *Rose criterion*, stating that the performance of an ideal device is completely specified by the quantum efficiency of its photo process, it is clear that the *reduction* of radiation dose (exposure) and the *increase* of spatial resolution (which actually represents a fractionation of the quantum efficiency) represent two competing processes [127]. Moreover, it was recognized that the number of (photon) quanta, necessary to achieve a certain signal-to-noise ratio, scales with the inverse fourth power of the pixel size. An equally important aspect in tomographic imaging has been given by the so-called *dose-fractionation theorem* (often referred to as *Hegerl-Hoppe theorem*), stating that a 3D reconstruction requires the same integral dose as a conventional 2D micrograph, taken that the levels of significance and resolution are identical. Originally introduced by Hegerl and Hoppe [128] with a very simplified model, it has later been experimentally verified by McEwen et al. [129], stating that a significant 3D reconstruction can be computed from “insignificant” projections. In the sense of X-ray tomographic imaging, both theorems can be interpreted in the way that radiation dose is directly connected with image information, but they lack direct comparison or estimation possibilities. The Rose criterion was established on the theory of photon quanta adding up to create a signal, but the image formation process to create these quanta is left untreated. Likewise, the Hegerl-Hoppe theorem suggests that the total dose is “fractioned” over a particular number of projections, but gives no direct quantitative relationship between the number of projections and exposure times. In sum, the increase of resolution in tomographic imaging is linked with an increase of radiation dose which can be addressed only by an optimization process of all experimental parameters (as discussed later in Chapter 5) in order to assess its limit.

4.3.2 Dose calculations

For simplicity reasons, in the following we first assume a homogeneous object and monochromatic X-rays. The *total absorbed dose* is then defined as the mean energy transferred to the matter (object) per unit mass, or more specifically in the case of X-rays, the mean energy transferred to the electrons contributing to ionization. Thus it is written as:

$$D = \frac{E_{\text{abs}}}{m} = \frac{E_{\text{abs}}}{V\rho} \quad (4.32)$$

where D is the radiation dose in Gray [Gy] (SI system of units), E_{abs} is the absorbed energy in Joule [J] and m is the mass in kilogram [kg]. Often, the mass is rather expressed by its volume V and density ρ . As we have learned before in Sec. 3.2.2, X-ray interactions with matter are described according to the Beer-Lambert-Bouguer law and by defining appropriate cross-sections for each interaction process. In a similar way, by the use of the so-called *mass energy absorption coefficient* μ_{en}/ρ , the absorbed energy can be expressed by the number of photons and their energy $h\nu$. From Eq. (3.13) in Sec. 3.2.2, the X-ray absorption complies to an exponential attenuation law and reads as:

$$E_{\text{abs}} = (I_0 - I_{\text{exit}})h\nu = \left[I_0 - I_0 e^{-\left(\frac{\mu_{\text{en}}}{\rho}\right)\rho\Delta l} \right] h\nu = I_0 \left[1 - e^{-\left(\frac{\mu_{\text{en}}}{\rho}\right)\rho\Delta l} \right] h\nu, \quad (4.33)$$

where I_0 is the number of incident photons, I_{exit} is the number of photons at the exit plane of the object and Δl is the length of the object. In contrast to the previously defined mass attenuation coefficient, the mass energy-absorption coefficient involves the further emission of radiation produced by charged particles when travelling through the medium [130]. Thus, it is of particular interest for dosimetric considerations of X-ray absorption. The above relations are sketched in Fig. 4.15 whereas the object length (in this example) is given as $\Delta l = 5\Delta x$.

After this brief derivation it should be clear that the formula in Eq. (4.32) can be extended arbitrarily to calculate radiation doses in all kinds of objects geometries and compositions, given that these are known *a priori*. In particular, when considering the tomographic case and in order to calculate exact mean organ doses, paths of single photons are followed through the object by means of Monte Carlo simulations to calculate where they deposit energy [131]. For our further discussion it is, however, enough to maintain the simplified view.

In the following we introduce an often used and more generic representation of radiation dose, the so-called *entrance skin dose* (often also called *skin dose* or *entrance dose*). For doing so, we consider the previously introduced bulk object and imagine it as being sectioned in slices of thicknesses Δx perpendicular to the X-ray direction, as shown in Fig. 4.15.

With the knowledge from before we can immediately derive the absorbed dose in the first slice by:

$$D = \frac{E_{\text{abs}}}{m} = \frac{\Delta I h\nu}{V\rho} = \frac{(I_0 - I_1)h\nu}{\rho A \Delta x} \quad \text{with} \quad (I_0 - I_1) = I_0 \cdot \left[1 - e^{-\left(\frac{\mu_{\text{en}}}{\rho}\right)\rho\Delta x} \right], \quad (4.34)$$

where E_{abs} is the absorbed energy, ΔI the number of absorbed photons with energy $h\nu$, I_0 is the number of photons impinging on the object and I_1 is the reduced number of photons after being partly absorbed by the object, V is the volume of the object with density ρ , A is the area of the object's cross section with object thickness Δx and μ_{en}/ρ is the mass energy-absorption coefficient. We now introduce the following substitution:

$$y := -\Delta x \mu_{\text{en}} \quad (4.35)$$

by which we can rewrite Eq. (4.34) to:

$$D = \frac{I_0}{A} \cdot \frac{e^y - 1}{y} \cdot \left(\frac{\mu_{\text{en}}}{\rho} \right) h\nu. \quad (4.36)$$

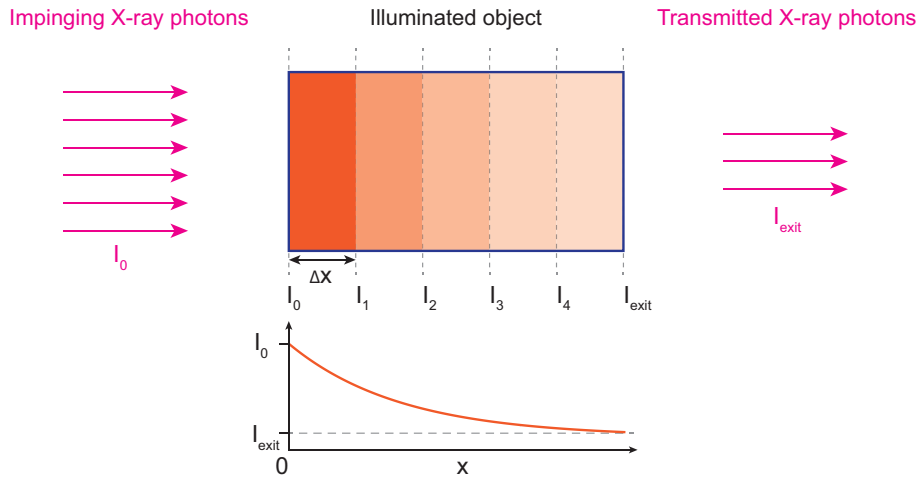


Figure 4.15. Illustration of the exponential absorption law through a bulk object and the derivation of the *entrance skin dose*.

Provided that the object is homogeneous, we can now derive the maximal dose in the object from the above expression which due to the exponential attenuation law is only present in the first plane affected by the impinging X-ray photon intensity I_0 ; obviously, all other photon intensities within the object (I_1 , I_2 etc.) will be smaller. Thus we form the *limes* towards an object with thickness $\Delta x \rightarrow 0$ and obtain

$$\lim_{\Delta x \rightarrow 0} D \equiv \lim_{y \rightarrow 0} D = \frac{I_0}{A} \cdot \underbrace{\frac{e^y - 1}{y}}_{=1} \cdot \left(\frac{\mu_{\text{en}}}{\rho} \right) h\nu, \quad (4.37)$$

which gives the definition of the *entrance skin dose*:

$$D = N \cdot \left(\frac{\mu_{\text{en}}}{\rho} \right) h\nu, \quad (4.38)$$

where N is now the total number of impinging photons per surface area, given in the same unit as $1/\mu_{\text{en}}^2$. This definition can also be rewritten in more practical units [132]:

$$D [\text{Gy}] = \frac{I_0 h \nu}{\mu^{-1} \rho} \approx 1.602 \times 10^{-4} \cdot \frac{I_0 [\text{photons}/\mu\text{m}^2] \cdot h \nu [\text{eV}]}{\mu^{-1} [\mu\text{m}] \cdot \rho [\text{g}/\text{cm}^3]}. \quad (4.39)$$

It follows from these definitions that the skin entrance dose from Eq. (4.38) gives an upper dose estimation limit, taken that the material compositions (namely μ_{en} and ρ) are known, which obviously is not always the case. This can, however, be misleading to some extent when considering a tomographic acquisition, in particular in our case, when dealing with local tomography (where the ratio of FOV to volume size is very small). Namely, in such a case the skin entrance dose will not exceed a certain limit (depending on the scan parameters such as the scanning time etc.), but the highest radiation dose will occur in the imaged FOV of the object. To estimate its upper limit, from the skin entrance dose we can define a so-called “maximum dose” with

$$D_{\text{max}} := D_{\text{skin}} \times n_{\text{proj}}, \quad (4.40)$$

with D_{skin} being the skin entrance dose of a single exposure and n_{proj} giving the number of tomographic projections. We illustrate this by assuming a simple object such as a water cube depicted in Fig. 4.16. In doing so, we adapt realistic experimental parameters summarized in Tab. 4.3 and calculate with the formulas from above [Eqs. (4.32) and (4.38)] total absorbed doses and entrance doses for three simplified cases: (i) for one radiograph, (ii) a two-projection tomogram (at projection angles $\theta = 0^\circ$ and $\theta = 90^\circ$) and (iii) a 400-projections tomogram over the full 180° -range.

Table 4.3. List of scan parameters for illustrating the difference between total absorbed dose and entrance dose.

Parameter	Value
Energy	21 keV
Exposure time	3 ms
Flux [photons/s/mm ²]	7×10^{11}
n_{proj}	400
μ_{en} (water)	0.4727
FOV	$1 \times 1 \text{ cm}^2$
d	2.5 cm

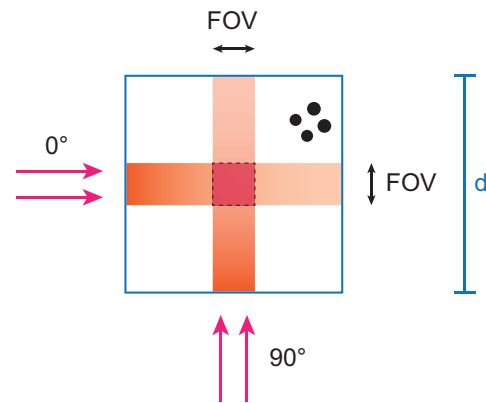


Figure 4.16. Sketch for comparing total absorbed dose to skin entrance dose.

The results are summarized in Tab. 4.4 and are explained as follows. If we only acquire one single tomographic projection ($n_{\text{proj}} = 1$, imaged at $\alpha = 0^\circ$), the entrance dose gives

the dose absorbed in the first plane of the object while the total absorbed dose represents a mean value along the indicated path in direction $\alpha = 0^\circ$. When taking two projections the entrance dose remains constant, while the total absorbed dose increases only slightly because twice the amount of photons is now distributed in a bigger volume. The maximum dose from Eq. (4.40) can now be interpreted as the upper limit of the radiation dose that would be deposited in (parts of) the imaged FOV if the surrounding tissue/material was 100% penetrable (meaning no X-ray photons had been absorbed before reaching the sample's FOV). Likewise, in the case of a full tomographic scan, the total absorbed dose remains significantly smaller as it is distributed in a bigger volume, i. e. the full object. The different meanings of the two

Table 4.4. Comparison between total absorbed dose and maximum dose. The indicated volume is used for calculating the total absorbed dose.

n_{proj}	Volume	Total absorbed dose	Maximum dose
1	2.50 cm ³	0.20 [Gy]	0.33 [Gy]
2	4.00 cm ³	0.24 [Gy]	0.67 [Gy]
400	6.25 cm ³	31.3 [Gy]	133.6 [Gy]

quantities should be immediately clear from this small example. For the radiographic case the values give comparable results with the entrance dose giving the upper dose limit that is delivered to (a part of) the sample. For two and more projections the difference between the two quantities becomes more prominent. The maximum dose from Eq. (4.40), in the best case, can only give an upper limit of the radiation dose present in the imaged field of view (indicated by the central cube in Fig. 4.16), which in the case of local tomography will receive the highest radiation dose. However, there is in fact no region within the sample that will receive such a high dose. The total absorbed dose, on the other hand gives a dose value distributed over the considered volume, but gives an underestimation of the dose present in the field of view which depends on the imaged size of the volume and the field of view, respectively. The problem further complicates if supposing an object with strong-absorbing inhomogeneities, such as in our case (low-absorbing) lungs with stronger-absorbing parts such as bones and heart. In Fig. 4.16 this is pictured in a simplified manner (not considered in the above calculations) by black circles indicating the strong-absorbing regions. When conducting tomography, in such a case a significant amount of dose would be concentrated in this part of the object, further contributing to the overestimation of maximum dose.

Based on these considerations, we established a simple mouse model that was subsequently experimentally tested during a student's semester thesis project [133] and later on (see Chapter 5) used to develop a dose optimization framework for X-ray tomographic imaging. In this model we first estimated the thorax diameter of an adult mouse to be about 2.5 cm in size; subsequently, we simplified the tissue composition, to consist simply of water and air (while in reality one would expect a mix of bone, tissue and air). With this approach, all undetermined values were reduced to one unknown value, i. e. the ratio C of water in respect to air. This ratio was then determined by employing calibrated silicon PIN diodes [134] for determining the X-ray absorption in water and by comparing it to a frozen mouse sample. We measured

the ratio to be

$$C = 0.42 \pm 0.05, \quad (4.41)$$

with the uncertainty being dependent on the imaged FOV (namely depending on how many bones are present in the FOV). Subsequently, the values were inserted into Eq. (4.32) in the form of a modified water density

$$\rho_{\text{mod}} = C \rho, \quad (4.42)$$

corresponding to about 30 – 40% absorbed X-ray flux in a mouse sample at $E = 21$ X-ray energy.

With this approach we modeled the dose values obtained in Chapter 5. Furthermore, by making use of the polychromatic energy spectrum (see Sec. 3.1.2) present at the TOMCAT beamline, we estimated the dose for the polychromatic case. In this setting, however, we found that we would require about four times higher dose values than for mono-energetic beams, in order to obtain scans with the same exposure times and image quality. For this reason, the polychromatic case did not play any major role for future considerations.

In conclusion we can state the following: with total absorbed doses of about 10 Gy per tomographic scan under the monochromatic setting of 21 keV X-ray energy, we could expect localized organ doses in the lung that would be multiple times (or even an order of magnitude) higher, given by the upper limit of the maximum dose. Consequently, our dose calculation protocol included the detailed determination of X-ray flux followed by a calculation of both the total absorbed dose and the entrance skin dose.

4.3.3 Discussion

In interpreting our results, it should be clear that using any ionizing probe such as X-rays, radiation damage sets the ultimate limit on information that can be obtained in microscopy [132]. Compared to other synchrotron-based imaging techniques, where high X-ray fluxes are routinely available, a wide range of different radiation doses and their effects on the investigated samples have been reported. While in soft X-ray microscopy and macromolecular crystallography (MX) the doses usually amount in the order of tens to hundreds of MGy [135, 136], biological samples are significantly more sensitive. Studies conducted with fixed bone show that high doses of the order of 35-70 kGy lead to degradation in strength, ductability and toughness [137]. Soft biological tissue, such as dissected inner ears in frog samples, showed strong sample degradation already after 1.5 kGy dose or 6 s of exposure [138], while in other studies high spatially-localized doses (of up to 20 Gy) are routinely applied *in vivo* [36]. Complementary research, conducted in the field of X-ray diffraction microscopy, indicate that rather high doses are expected when aiming to resolve sub-micrometer features [139].

To analyze the response of lungs to high X-ray radiation flux, radiation therapy studies are of particular interest. Jassem and Jassem [140] stated that the lung is a dose-limited organ

and three phases of lung response to dose have been identified in humans: the *early phase* occurring about one month after irradiation and representing the “latent period of pneumonitis”; the *intermediate period* of “acute pneumonitis” taking place between 1-6 months after irradiation; and the late phase of “fibrosis” is usually observed after six months. While lung tumor treatment sometimes necessitates doses in the order of up to 90 Gy to affect tumor growth, the aforementioned post-radiation lung injuries are usually heavily dependent on the amount of the irradiated volume [141]. Later aspect plays an increasing role when whole lungs are irradiated compared to small regions in the lung [142]. In all cases lung structural effects were not visible until approximately 6 weeks after irradiation, which has been shown by various histological studies [143]. Even after an X-ray irradiation of 90 Gy through a 3 mm collimator, which directly compares to the field of view present in our experiments, no morphological abnormalities were observed after one week, however mild interstitial inflammatory cell infiltration could be observed in histopathological examinations [144]. In many of those studies, in particular the interest into physical and molecular factors contributing to radiation-induced pulmonary injury, murine and rat animal models have been established [145]. Like before, inflammation processes and the increase of breathing rates were observed only after four weeks of 16-22 Gy irradiation of 50% of the lung volume, further showing strong regional dependencies [146] as well as dependences on the irradiated volumes [147]. Other studies, investigating the long-term effects of equally high single-exposure doses concluded that severe localized scarring and thickening of vessel walls is observed following many weeks after irradiation [148, 149].

Comparing these findings and our results from before, we can conclude that our envisaged technique permits acute (terminal) *in vivo* experiments where no immediate effects from the radiation on the investigated biological samples are present, neither affecting the condition of the animal nor the physiological tissue composition of lungs. Obviously, the situation would aggravate significantly if aiming at the development of an animal model and imaging technique to be applied in longitudinal studies. We address this issue shortly in the closing remarks of the underlying thesis (in Chapter 8).

4.3.4 Conclusion

Finally, the aim was to establish an X-ray flux (dose) measurement technique with highest flexibility to cover a wide range of X-ray energies available at the TOMCAT beamline. Although various such techniques are routinely employed at synchrotrons, such as the use of TLD-s, MOSFET-s, PIN diodes and parallel-plate ionization chambers [150–152], usually a detailed calibration is necessary for being able to conduct absolute measurements. The aforementioned PIN diodes that were used during the first experiments permitted precise measurements, but the measured uncertainty was unknown as it would require a precise determination of the thicknesses of the diode and its layers [134]. At the TOMCAT beamline an ionization chamber is available for flux monitoring, but was not calibrated for absolute flux measurements.

As a consequence, we decided to construct a system consisting of high-precision passivated implanted planar silicon (PIPS) diodes coupled to a multi-gain low-current amplifier that was

subsequently calibrated by cryogenic radiometry, achieving precisions less than a few percent [153, 154]. The complete system is shown in Fig. 4.17 and consists of a 500 μm PIPS-diode (CANBERRA Industries Inc.) with a custom-made casing (designed by B. Meyer and C. Frieh, LSK/SYN-group of PSI), a multi-gain low-current amplifier (FEMTO Messtechnik GmbH) and remote gain controls implemented in EPICS. The inner workings are shown in Fig. 4.18. To reduce the dark noise, the PIPS-chip is covered with a 25 μm Kapton CB foil which is an opaque, black substrate film offering low light transmission, reflectivity and superior durability. The diodes can also be used in white-beam configuration as they permit heavy temperature loads up to 100 $^{\circ}\text{C}$.

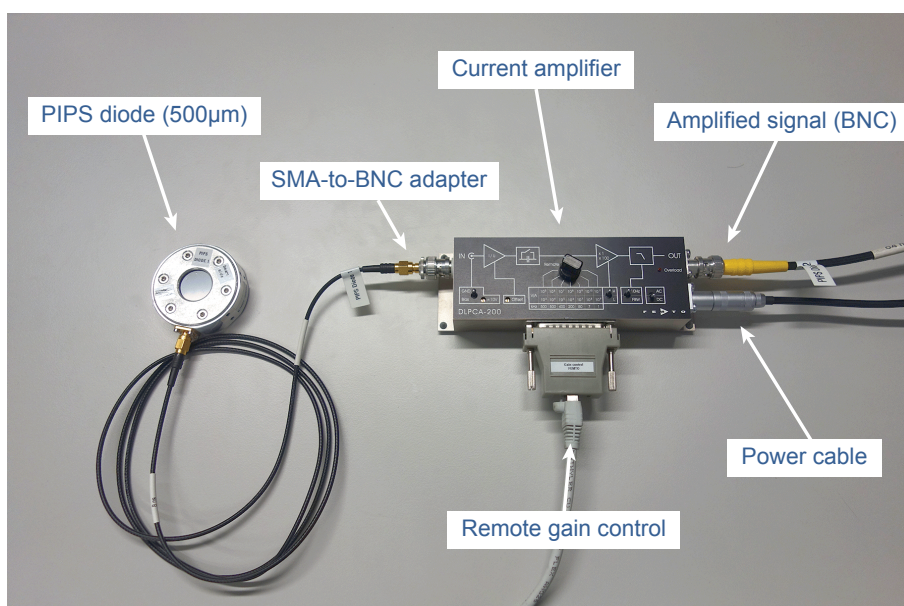


Figure 4.17. Absolute flux measurement system consisting of a PIPS diode and a multi-gain current amplifier.

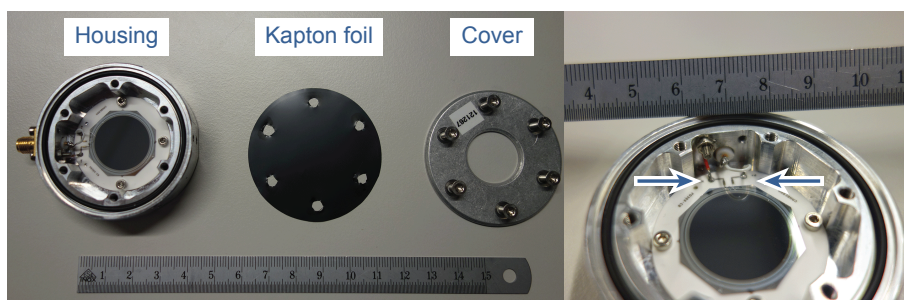


Figure 4.18. Inner workings of the PIPS diode. The PIPS chip is covered with a 25 μm dark kapton foil that is sealed with a (dark) rubber band to prevent visible light increasing the dark current of the detector. The arrows in the right part of the image indicate the connectors from the PIPS chip.

4.4 *In vivo* ENDSTATION

The construction and commissioning of the final *in vivo* endstation used for the first tomographic *in vivo* experiments at the micrometer scale undertook various steps and stages which to some extent can be essential for similar experiments in other laboratories. For this reason, we try to give a descriptive summary of all components and instruments that were installed and commissioned in the course of the underlying project, both outside and at the beamline, and are now standard at the X02DA TOMCAT beamline/laboratory, further extending the initial beamline design [114].

The device list with the main components is summarized in Tab. 4.5, while the *in vivo* endstation is depicted in Fig. 4.19. The X-ray beam direction is indicated from left to right by the pink arrow. Each component requires a separate mounting which can take up to several hours assuming that no preparatory work has been done before. In imaging experiments, the animal is placed at the position of the alignment pin, as shown in Fig. 4.19 (G).

In the following we describe in more details the integration of the new rotation stage, the custom-designed/made sample holders with the accompanying alignment system, the small animal ventilator, the ECG device and finally the full animal handling protocol.

Table 4.5. Complete device list of components necessary to operate the *in vivo* endstation.

Name	Device description and specification
Sample holders	with complete alignment system and adapted to different animal sizes (see Sec. 4.4.2)
PIPS diodes	for measuring absolute X-ray photon fluxes (see Figs. 4.17 and 4.18)
Small animal's ventilator	FlexiVent (SCIREQ Inc.) small animal's ventilator with a dedicated PC (running FlexiWare software) for controls and all necessary equipment (see Sec. 4.4.3)
ECG device	SA Instruments, Inc. (see Sec. 4.4.4)
Signal box	custom-made FPGA-based signal routing box with EPICS implementation (see Sec. 4.4.1)
Isoflurane setup	isoflurane blender, absorber and flow system (described in more detail in Sec. 4.4.5)
Heating lamps	150 W for maintaining animals' normal body temperature
Calibrated manometer	for calibrating FlexiVent against atmospheric pressure
Oscilloscope	MSO3000/DPO3000 series (in fact any common laboratory oscilloscope compatible)



Figure 4.19. *In vivo* endstation with its main components. The beam direction is indicated from left to right by the pink arrow. Upon the beginning of the imaging experiment, the animal is placed at the position of the alignment pin (visible in A and G). In A, the laser pin light that is used for aligning the region of interest (ROI) is visible, as well.

4.4.1 Rotation stage

From the outset of the project we sought for a rotation stage solution that would preferably be as flexible as possible to be compatible with various kinds of acquisition modes in ultra-fast tomography, being precise in the positioning and fast in rotation and triggering. In this very early stage we identified several requirements, both from the hardware and software side that would be necessary for performing various kinds of ultra-fast tomography experiments, including those particular to the underlying project:

- (1) Possibility to receive triggers from the rotation axis upon the following events: (i) starting/ending of rotation, (ii) reaching a defined rotation speed, (iii) crossing a defined angular position with an arbitrary inter-sampling and (iv) after rotating for a particular angle.
- (2) Sending trigger signals to the rotation axis to (i) start the rotation and (ii) rotate by a certain angular increment (so-called “step and snap” mode).
- (3) High-precision positioning in stepper mode with the aim to allow usage for nanoscopic imaging that had previously been performed at the TOMCAT beamline [155].
- (4) Ultra-small mechanical errors (tilt, wobble, radial error), below 100 nm at the sample position (about 150 mm above the table level).
- (5) High-speed rotation (up to 10 Hz) with precise rotation speed and ideally with feedback of the angular position.
- (6) Long life-expectancy slip ring for 60 cable lead-throughs for motors and their encoders located on top of the rotation axis.
- (7) Adjustment of rotation acceleration and deceleration, e. g. for starting the tomographic acquisition only after reaching an equilibrium in centrifugal and centripetal forces when dealing with sensitive samples and high rotation speeds.

After an in-depth analysis and various comparisons we settled for a semi-custom design solution, proposed by Aerotech Inc. and final adaptation conducted by the mechanical engineering department of PSI (Abteilung Maschinen-Ingenieurwissenschaften, AMI). Concerning the slip ring we investigated the possibility of fiber brushes and non-contact energy and data transmission, however, we concluded that these will not meet our requirements, particularly the need of providing a high number of cable lead-throughs. Namely, on top of the rotation axis two linear translation stages (stepper motors) are mounted, which are used for aligning the desired region-of-interest (ROI) when conducting tomography. Each of these two bipolar stepper motors requires 4 phase connectors, 4 end-limit switches and finally 9 connectors for the high-precision encoders. In sum, this amounts to 34 connectors, and taking into account that we also wanted to provide additional cable lead-throughs for custom equipment, we defined the slip ring to have 60 channels.

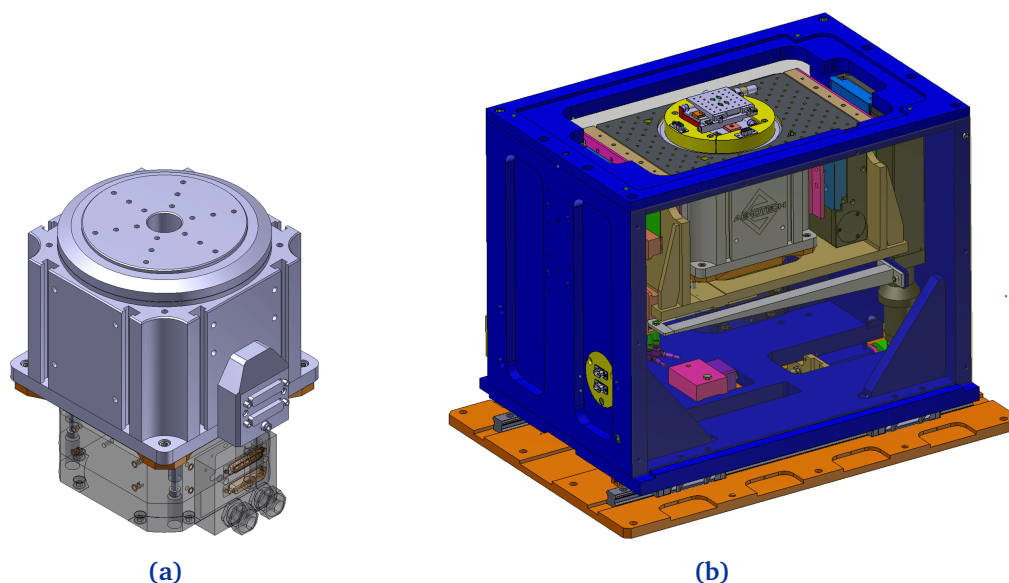


Figure 4.20. CAD drawings of the air bearing rotation axis system and its integration at the endstation. The system (a) consists of a high-precision air bearing rotation stage that is synchronized with a mechanical rotation stage underneath, which drives the slip ring with its 60 cable connections. The grommets of these connections are clearly visible in the bottom part. The whole system is integrated in a custom-made sample manipulator stage (b), and two additional stages are mounted on top for region-of-interest selection when performing CT-scans.

The result of this short-term collaboration with PSI-AMI is visible in Fig. 4.20, where both the rotation axis system and its implementation on the optical table of the TOMCAT beamline are visible. The complete system represents a combined air bearing rotation axis synchronized with a mechanical rotation stage for driving the slip ring. In this way, the high-precision air bearing stage is fully decoupled from all mechanical parts, so the high-precision positioning accuracy is not affected during rotation. The synchronization is achieved through the rotation axis software by so-called “calibration” (.cal) and “parameter” (.prm) files which are provided by the manufacturer and loaded into the Aerotech software. Additionally, mechanical blockades were installed between the two rotation stages, preventing potential cables twisting, in case the two stages would lose their synchronization (e. g. if one fails). The 60-channel slip ring has been designed for a maximum speed of 10 Hz with a minimum service life allowing for millions of revolutions. As a consequence, two DB-9 connectors are available on top of the rotation axis for arbitrary user-specific connections.

A rough sketch of the further controls implementation which has been developed during another parallel collaboration by the controls section of PSI is depicted in Fig. 4.21. The two rotation axis controllers (one for the air bearing and one for the mechanical axis), operated in a master-slave mode (through a Firewire interface), interact with the Aerotech software running on a dedicated PC with a real-time extension. The EPICS channels (i. e. EPICS database in

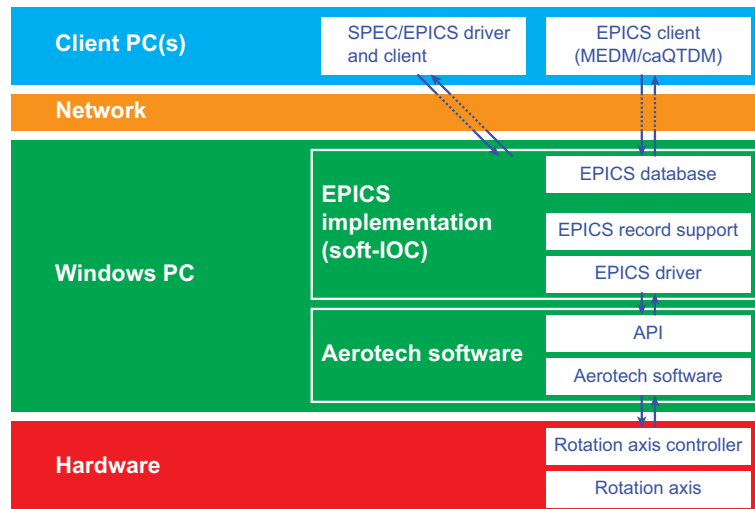


Figure 4.21. Sketch of the Aerotech EPICS driver (software) implementation for using the rotation axis in the beamline environment. On the client PC-s the axis can be steered either by EPICS panels or by scripts (Spec, Python), for optimal experimental integration.

Fig. 4.21) in the so-called IOCs (input/output controller) interface to the hardware via the EPICS driver [156]. The clients connect to these EPICS channels using the EPICS channel access (CA) protocol and can be run on nearly any computer accessible through the network. The control panel (EPICS client GUI) is visible in Fig. 4.22. In the following we give a short survey of the possibilities in accordance with this panel. However, as mentioned above, all settings/modes that are described therein are easily scripted and expanded into full image acquisition protocols through the use of appropriate scripts that are run on the EPICS client level.

From this driver implementation the rotation stage now distinguishes between two types of rotations: *incremental* and a so-called *freerun mode*. Former one is done with the use of absolute high-precision angular positioning (see “Section 1” of Fig. 4.22) while the latter one will rotate the axis until it is manually stopped. The velocities for both modes can be arbitrarily set, while a negative velocity means rotation in the opposite direction (see “Section 2” of Fig. 4.22). In freerun mode the velocity and acceleration can be arbitrarily set/changed, however the new values will only be accepted if “Start freerun” is chosen from the Panel (Section 2 of Fig. 4.22). During incremental movement these values cannot be changed. The maximum speed, also in terms of slip ring specifications, is $3600^\circ/\text{s}$.

For moving the axis to its zero-position, there are three possibilities: (i) so-called *homing* (also visible in “Section 2) implements the standard Aerotech procedure for moving the axis to the built-in limit switch with a subsequent manual offset, defined in the EPICS driver, for reaching a defined alignment in respect to the beam and sample mounting; (ii) setting the absolute position to zero; and (iii) moving the axis to zero with modulo 360° . In our experiments we usually made use of both types. The modulo- 360° positioning is useful when



Figure 4.22. Control panel of the Aerotech EPICS driver implementation.

acquiring several tomograms one after another, and at the end of the scan the sample needs to be brought back into the neutral position without conducting the full rotations back. In our *in vivo* experiments however, the modulo function is undesired as it would twist the cables from the ECG and ventilator tubes (visible below in Fig. 4.31), and there would be a high risk of damaging them.

The measurement configuration (Section 3 in Fig. 4.22) provides several trigger modes that are implemented through so-called “tasks” in the Aerobasic programming language (representing an integrative part of the Aerotech A3200 software controller) and that are mainly based upon Aerotech’s PSO system (position synchronized output):

- (1) **Fix distance toggle:** is used to set an angular distance, and when the rotation stage starts rotating it fires trigger signals, toggling between “HIGH” and “LOW”, every time the rotation axis rotated for this angular distance. An offset can be set as well as the

number of total trigger signals. The theoretical limit to this setting corresponds to the internal setting of the PSO.

- (2) **Snap and step:** triggers a TTL signal every time when the rotation axis moved. The detailed function is as follows: The user sets an angular increment and starts the scan; subsequently, the rotation axis rotates according to this increment and fires a “HIGH” signal to the camera; at the same time the rotation axis controller awaits a “LOW” signal from the camera; finally, after the camera has finished the single-image acquisition, it sends a “LOW” signal to the rotation axis controller after which the rotation axis begins to move again. This mode is used for high-precision “slow” tomography.
- (3) **Sequence mode:** is the most flexible mode where several sequences can be defined, then again each sequence defining an angular distance for which the trigger signal is set to “LOW” and another one to “HIGH”. This is best explained through an example, namely if one sets both “LOW” and ”HIGH” in “Sec_1” to 180° then the rotation axis will fire a continuous “LOW” TTL-signal for the first 180°-rotation and a “HIGH” signal for the next 180°-rotation while continuously rotating. This is particularly useful in various time-resolved studies and can be modified as necessary.

When dealing with TTL-triggers that can be obtained from the rotation axis, we distinguish between the PSO and the *velocity trigger*: while the PSO can be set to fire trigger signals according to a particular position, the velocity trigger fires triggers according to measured rotation speeds of the rotation axis. Usually, the velocity trigger requires some precision margin because the rotation is prone to small variations in rotation speed.

Finally, since the rotation axis only offers two outputs (PSO and velocity trigger) in order to enable all possible combinations of triggering, a so-called “Signal box” has been developed by the controls section of PSI. It represents a small FPGA-based device for various combinations of signal routing to enable triggering in all possible directions [see e. g. Fig. 4.29(b)] for the explicit routing in our *in vivo* experiments). It is configured via a serial connection and hence serves as an extension to the Aerotech rotation axis. As a sideline, it should be noted that signals from the Signal box (due to the FPGA) are not pure TTL signals, but use a 0V/3.3V low/high configuration.

4.4.2 Sample holders and alignment system

Performing X-ray imaging at synchrotrons with alive animals represents an extremely complex and challenging task. The fact that it requires a number of custom-made solutions that are adapted to the respective experiment and application has already been reported by other groups dealing with similar problems [157]. In the following we describe in great detail the sample-holder and alignment-system design that has been developed as part of the underlying project.

At the beginning, as before in the case of the rotation stage, we identified several requirements put towards *in vivo* sample holders:

- (1) A firm attachment of the sample holder to the rotation stage, enabling precise positioning and easy (fast) mounting/unmounting.
- (2) The animal should be fixed as much as possible, however allowing for the animal's thorax to move freely upon breathing. This requirement brought to mind that expediently we would need different sizes adapted to different animals (mice and rats of different ages).
- (3) The holders should be transparent for visual sample alignment, thin-walled in order to keep effects on the X-ray beam (phase shift and absorption) at a minimum, and finally they should be as firm as possible for mounting the ECG-electrode cables and ventilator tubes.

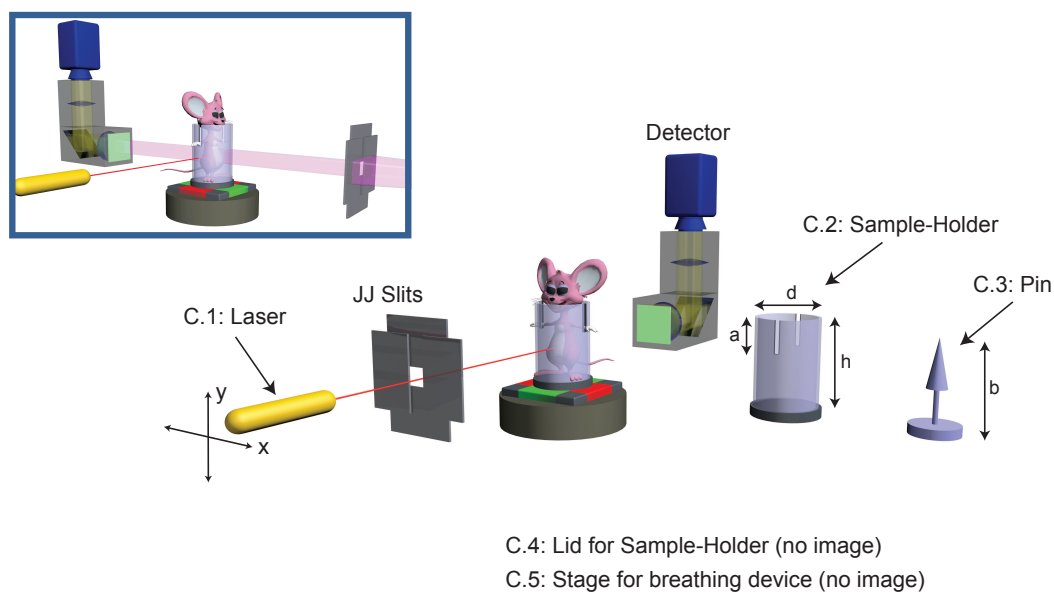


Figure 4.23. Sketch of the original sample-holder alignment system, as described in the functional specification document (“Pflichtenheft”) from January 15, 2013. The inset on the top left side depicts the final alignment system design. The 3D mouse model is adapted from [158].

The initial design of the sample holder and of the sample alignment system is shown in Fig. 4.23 and foresaw a laser parallel to the X-ray beam for enabling “cold” sample alignment, i. e. without the need of exposing the animal to X-rays. However, as it turned out, this solution would have required lots of efforts, also affecting the vacuum flight tube (indicated by the pink arrow in Fig. 4.19). Instead, we chose to place the alignment laser perpendicular to the X-ray beam, which in terms of functionality makes no difference to the initial design (as shown in the inset in Fig. 4.23).

The fabricated sample holders are depicted in Fig. 4.24. As it can be seen, they all share the same footing which makes them easily exchangeable.

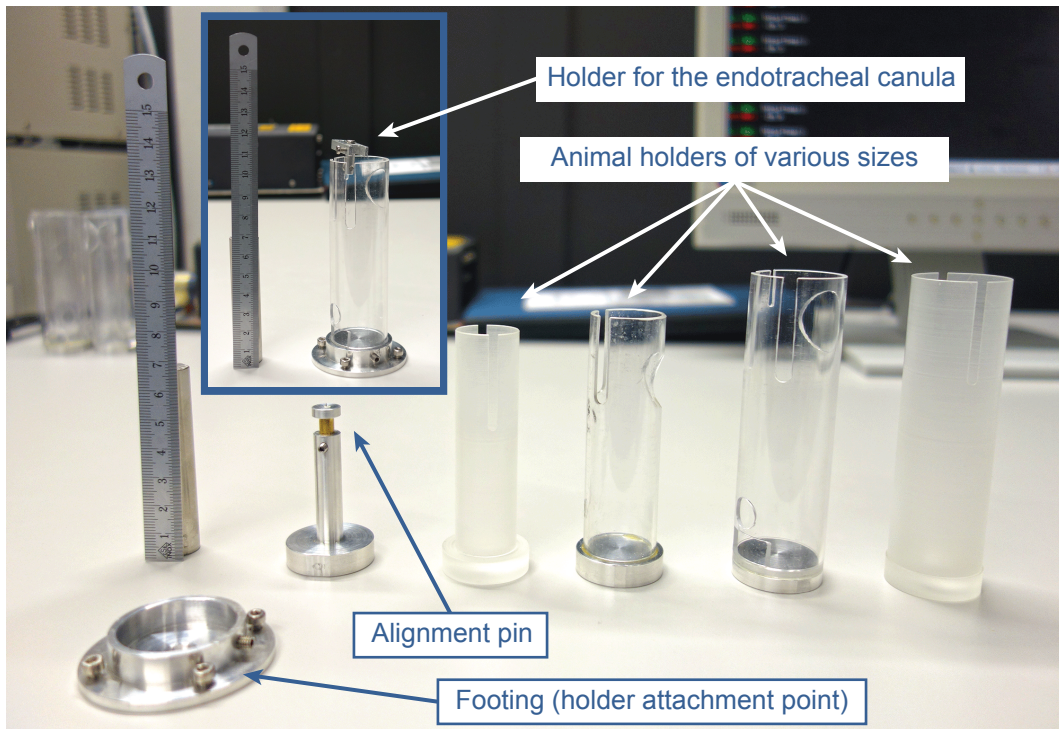


Figure 4.24. Animal sample holders of various sizes (in diameter and height) adapted to rats that are 7-14 days old and mice from 14 days to adulthood. The holder for the endotracheal cannula is mounted during the animal's preparation process. The upper holes serve the purpose of fitting the animal better, while the lower holes are used for monitoring rectal temperature and attaching the electrodes for recording the ECG signal.

The first version represented in-house fabricated (with a lathe) semi-transparent tubes made of PS (polystyrene). The advantage of these holders is that they can be fabricated to be very thin (with wall thicknesses about 0.5 mm), however with the disadvantage of being only semi-transparent. For this reason we preferred the use of transparent holders made of PC (polycarbonate) with wall thicknesses of 1.5 mm. These turned out to be very robust, while being very well suited for X-rays. At X-ray energies of 21 keV we did not observe any degradation effects, and the absorption of a 1.5 mm PC-material was measured to amount less than 3%. Various sizes of sample holders with inner diameters between 20 mm and 30 mm were fabricated in order to be compatible with various sizes (ages) of the animal models in use.

The complete alignment procedure is described as follows: at the beginning of the experiment the alignment pin (C.3 from Fig. 4.23 and also visible in Fig. 4.24) is placed on top of the rotation stage and centered so that its tip is located in the center of the field of view (FOV) in the X-ray image. Subsequently, the visible-light laser is placed perpendicular to the X-ray beam direction and aligned so that it points at the pin. At this point, the laser is pointing at the exact same position as the center of the X-ray beam, in respect to the rotation axis center.

The animal is then placed on top of the rotation stage, and the region of interest (ROI) for lung imaging is selected by adjusting the animal's height and lateral position to the point of the laser pointer (see e. g. Fig. 4.19 A). We tested the whole setup by aligning a particular ROI after which we removed the animal and then tried to find the same ROI by the described technique. The resulting precision was about $400\ \mu\text{m}$, meaning that the ROI in the reconstructed tomographic slice was not more than $400\ \mu\text{m}$ off.

4.4.3 Small animal ventilator

Small animal ventilators are nowadays routinely used in pulmonary research, both for lung imaging as well as for various *in vivo* lung function measurements. For our purposes we defined the following necessary features:

- (1) Set of standard ventilation features: definition of peak-inspiratory pressure (PIP), positive end-expiratory pressure (PEEP), ventilation parameters and so forth.
- (2) Possibility to conduct stable breath-holds and various pressure/volume waveforms such as deep inflation.
- (3) Definition of custom-made (perturbation) curves that can be adapted to the respective imaging scheme.
- (4) Remote control via a PC for being able to install the ventilator at the beamline and to control the experimental hutch from outside.
- (5) Availability of TTL-trigger signalling for the synchronization with image acquisition.

Particularly when dealing with imaging experiments, a highly repeatable mechanical ventilation is required [159] and as of recently also custom-made devices have been available providing specific solutions to these requirements [160]. In our case we settled for the commercially available and widely used FlexiVent (SCIREQ Scientific Respiratory Equipment Inc.) which is a high-precision small animal ventilator combining basically all features of mechanical ventilation with measurements of respiratory mechanics such as the assessment of compliance or resistance. In the following we give a short introduction on the main features that were relevant for our experiments and a detailed description about the integration at the beamline.

The FlexiVent is a piston-driven ventilator that covers animal sizes (weights) from about 8 g to 10 kg. Depending on the piston module in use these can be easily adapted, whereas in our cases only module FX1 has been utilized (covering animals from about 8-30 g). Thereby, the common challenge in mechanical ventilation is to determine very precisely the air volume and air pressure being delivered to the lung in order to avoid barotrauma/volutrauma [161]. The FlexiVent does so by monitoring two pressures being essential for its functionality: the *cylinder pressure* p_{cyl} (measuring the pressure in the piston) and the airway-opening pressure p_{ao} (measuring the pressure in the exhaled air). From these measurements, the following

relationships can be established:

$$p_{\text{cyl}} > p_{\text{ao}} > p_{\text{tr}} \quad \text{and} \quad V_{\text{displ}} > V_{\text{tr}}, \quad (4.43)$$

where p_{tr} is the pressure at the endpoint of the endotracheal cannula [see Fig. 4.31(a) in Sec. 4.4.5], V_{displ} is the displaced volume by the piston and V_{tr} is the volume delivered to the animal's trachea. Thus, p_{tr} and V_{tr} are the only quantities that directly relate to the lung pressure and volume, but cannot be measured directly (i. e. *in situ*). Hence, FlexiVent employs an indirect measuring technique which is based on characterizing the ventilator compartment. For the user, this is only relevant insofar that two separate calibrations need to be performed before operating the ventilator. First, when starting the experiment, a so-called *static calibration* is necessary to calibrate the two pressure transducers against the atmospheric pressure. This is achieved with a standard calibrated laboratory manometer in combination with a syringe for applying an external air pressure to the FlexiVent (e. g. 30 cmH₂O), and it is repeated twice for both pressure transducers. The second calibration step, namely the *dynamic calibration*, is then conducted with both the cannula and ventilation tubes being attached to the FlexiVent (visible in Fig. 4.27). The dynamic calibration usually is only necessary for calibrating so-called pre-defined *perturbations*, which represent random pressure/volume waveforms used for pulmonary functional measurements or are applied in imaging experiments where stable pressure-plateaus are desirable. However, some built-in perturbations such as the “deep inflation” are also necessary for internally determining the “cannula resistance” which is needed for running standard ventilations. Finally, it should be noted that perturbations are performed with closed valves, meaning that no O₂/CO₂ gas exchange takes place. Therefore they can only be used for limited time intervals.

From the software side, the ventilator is controlled via a dedicated PC (connected with an Ethernet connection) and the FlexiWare software. The latter one is divided into three separate parts of which only the former two were relevant to us:

- (1) **Study Definition:** for starting all experiments by creating a new study, setting animals specifications and study groups (strain, age, etc.).
- (2) **Experimental session:** stores all experimental configurations (such as perturbations) and is the main control interface for starting the ventilation.
- (3) **Review & Reporting:** used for exporting the measurement data.

In practice, one actually only needs to define the different animals' weights in the beginning, while all other settings such as the desired perturbations and ventilation settings can be changed on-the-fly.

Physiological ventilation experiments

For its standard operation the FlexiVent has been designed in the sense that the animal is placed in a lying position very close to the ventilator. This would not have been possible at the

beamline where the animals need to be mounted in an upright position (as shown in Fig. 4.19) and in special sample holders. Additionally, in order to enable free (tomographic) rotation we needed to utilize extended tube lengths (about 40 cm). As a result to these altered conditions, the standard ventilation parameters are not necessarily valid anymore, which is why they had to be identified in a separate approach.

For doing so, two ventilation experiments (April 2013 and June 2013) were conducted at the Clinic of Neonatology of the University Hospital of Lausanne (CHUV) with the main purpose of investigating the upright animal position, extended tube lengths and the usage of specific (narrowed) cannulas in respect to the blood gas values of the animals. The setup is depicted in Fig. 4.25 and was chosen so to optimally reproduce the conditions that would later exist at the beamline (see Fig. 4.31).

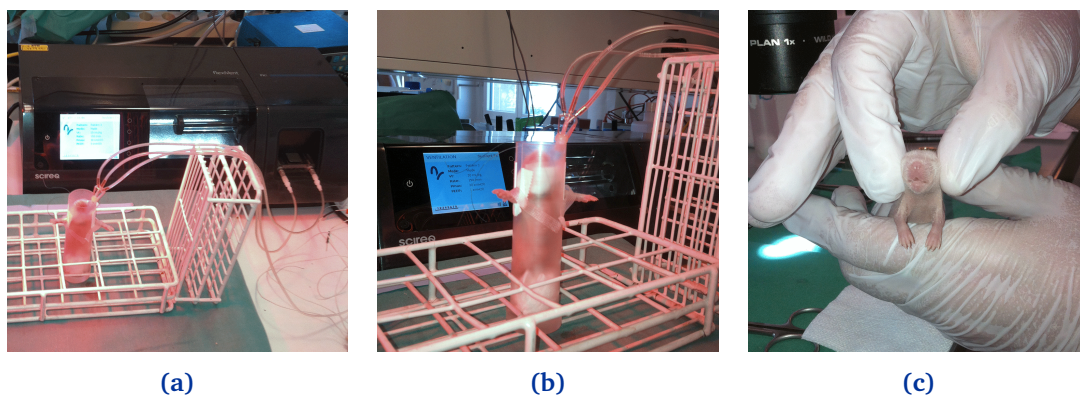


Figure 4.25. Experimental setup at the Clinic of Neonatology of the University Hospital of Lausanne (CHUV) for performing the ventilation experiments: (a) and (b) show the animal placed in the first version of the sample holder; in (c) an anesthetized newborn rat is shown having a significantly bigger head and bigger paws than a mouse of comparable size. These photos were crucial for designing the improved samples holders, shown in Fig. 4.24.

We used three litters of 5-7 days newborn rats and applied the same procedure to all animals. First, injection-based anesthesia based on a combination of Ketalan, Atropin and Prequillon (Acepromazin) was administered, followed by a tracheotomy. The animal was then connected to the FlexiVent, and mechanical ventilation was performed for about 30 min. During this time several perturbations were run in constant time intervals while monitoring the animal's ECG and rectal temperature in parallel. The animals were kept warm with a 150 W heating lamp. After finishing these processes, the animal was exsanguinated and blood gas measurements were performed (i-STAT 1 Analyzer 300-G, SN-345556). The complete procedure was repeated for all animals until an optimal set of ventilation parameters was found. After that, this setting was verified with another set of animals ($n = 3$).

We found that the quality of the ventilation process is significantly affected by the aforementioned modifications. The ideal ventilation parameters, represented by adequate blood gas values ($\text{pH} \approx 7.3$ and $p_{\text{CO}_2} \approx 65$), are summarized in Tab. 4.6, while the values are ex-

plained in the sketch of the ventilation curve in Fig. 4.26.

Table 4.6. Optimal ventilation settings yielding favorable blood gas values according to the right-side values. The breathing period τ is defined as: $\tau = 1/f$, with breathing frequency f .

Parameter	Value
inspiration time	0.076277 s
expiration time	0.22838 s
inflation time	0.095347 s
insp./exp. ratio	75.15 %
breathing frequency	150/min
volume	20 ml/kg

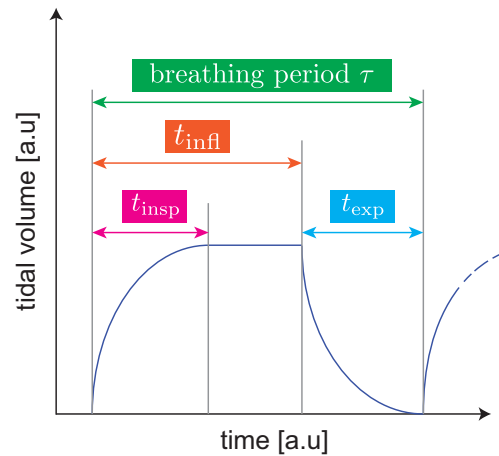


Figure 4.26. Ventilation curve as a function of time

A few more important aspects were found during this experiment. Firstly, the aforementioned two pressure transducers of the FlexiVent that are monitored continuously from within the FlexiWare software turned out to be extremely helpful in detecting failures happening during tracheotomy as well as other anomalies. For instance, if the cannula is misplaced or not closely attached to the trachea, this is immediately visible in the two curves. Similarly, if the anesthesia was not strong enough, spontaneous breaths would show up in the p_{ao} -curve. Secondly, we found that the ECG module of the FlexiVent was relatively unreliable in providing a solid ECG-signal which made it practically useless for our upcoming beamline experiments and necessitated the implementation of a dedicated ECG-device, described in the following section. Finally, the pure injection-based anesthesia proved to be relatively unreliable in terms of administering an appropriate dose. Namely, sometimes an animal needed twice the tabulated dose while others would die due to an overdose. This finding prompted us to switch to a combined injection-isoflurane anesthesia, explained in more detail in Sec. 4.4.5.

Other parameters such as the resistances R_T and R_S , which are suggested from the FlexiVent manual to be checked every time a calibration step is performed, did not play any significant role in our experiments.

Implementation at the beamline

For implementing the ventilator at the beamtime, another series of commissioning experiments (July to August 2013) were conducted to test the performance of the different TTL-trigger modes, their precisions, as well as to create appropriate perturbations for use in the *in vivo* experiments. For doing so, we designed a small lung phantom composed of a laboratory hand glove material (filled with sponge material) that was first used in combination with an oscil-

loscope (Tektronix TDS 2012/INS080) and later at the beamline in first imaging experiments.

The lung phantom as well as its corresponding tomographic slice are shown in Fig. 4.27. It is important to note that in Fig. 4.27(a) one tube is used for bringing the oxygenated air to the lungs, the other one for removing the CO₂-enriched air and the third one was plugged into the ECG device for particular kinds of measurements (see following section). The image in Fig. 4.27(b) was obtained at a constant pressure of 15 cmH₂O, which was used for simulating a breath-hold case for future tomographic lung imaging. As shown, the precision of the FlexiVent breath-hold pressure proved to be sufficient for obtaining motion-less tomographic reconstructions and was later measured with $\Delta p = \pm 0.1$ cmH₂O. In terms of beamline imple-

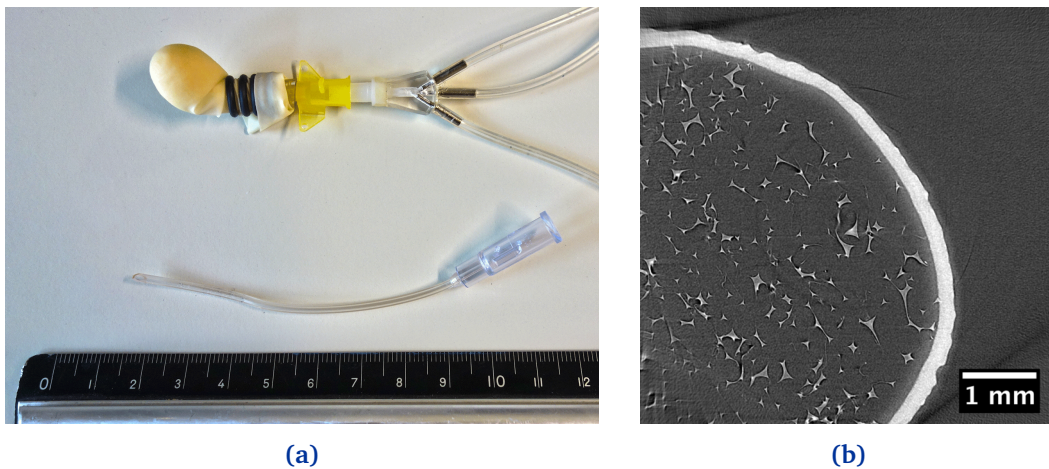


Figure 4.27. Lung phantom with a similar cannula that was used in the animal experiment (a). The original cannulas were much shorter, being about 1-2 cm. In (b) a tomographic slice of the lung phantom is shown that was obtained during the first imaging experiment.

mentation, the FlexiVent has two major limitations. It is unable to receive external triggers, and its software provides no API (application programming interface), which makes it impossible to integrate into the beamline in the same way as the rotation axis. Thus, for any experiment it has to be used as the “master” device that steers and/or launches all other components. On the other hand, it offers a wide range of TTL-triggering options and settings, which are summarized as follows:

- (1) **Continuous:** sends a continuous trigger signal when the ventilator is switched on.
- (2) **Synchronize with ventilation:** sends a continuous signal when ventilation is started.
- (3) **Synchronize with inspiration:** sends a “HIGH” trigger signal upon the start of the inspiration, which switches to a “LOW” signal at the end-expiration point. The start of the “HIGH” signal can be delayed by setting a *trigger delay* and the duration can be extended by setting a *release delay*. Both delay times achieved sub-millisecond precision, measured with the aforementioned oscilloscope.

- (4) **Synchronize with expiration:** functions similar as (3), with the difference that the trigger is fired when the piston begins to move back from the end-expiration point (t_{infl} in Fig. 4.26).
- (5) **Synchronize with perturbation:** fires a trigger when a perturbation starts, again with the possibility of defining a *trigger delay*. Here it is important to understand the following process: When a perturbation is started from within the software, the piston first moves to a defined starting point. Hereafter, the piston begins to move starting the actual perturbation, which is also the time point when this trigger is fired.
- (6) **Synchronize with perturbation preparation:** fires a trigger when the piston begins to move into the starting position, preparing for the actual perturbation.
- (7) **Synchronize with perturbation equilibrium:** fires the trigger in the same way as before, but ends the trigger just before starting the actual perturbation.
- (8) **Synchronize with perturbation and equilibrium:** is a combination of (5) and (7).

Following these tests, we identified two different acquisition modes that could be used for our future *in vivo* imaging experiments, namely a “breath-hold acquisition”, where a particular pressure is aligned and held during which the tomographic acquisition takes place. Alternatively, one could also use an “inspiration-triggered” acquisition mode, where each breath would be combined with the aforementioned “snap-and-step” mode of the rotation axis. As we will show later, due to the heart-induced motion artifacts, only the former one was used in the end. For this to work, long breath-hold perturbations needed to be created, which are not standardly included in the FlexiWare software. Those were created with the so-called “perturbation editor”, provided by the manufacturer of the ventilator.

4.4.4 ECG and oscilloscope

During the commissioning of the small animal ventilator it became clear that a dedicated electrocardiogram (ECG) device will need to be installed in order to perform reliable *in vivo* monitoring of the animals cardiac (life) activity. Moreover, after conducting the first *in vivo* imaging tests, we found that valuable CT reconstructions could only be obtained if the tomographic rotation angles were accurately known. As we explain later in Chapter 7, we applied a prospective heartbeat-triggered acquisition mode under constant rotation speed during a breath-hold phase where each heartbeat triggers a tomographic projection image. Thus, the main requirement from the ECG device was to have the possibility of firing TTL-triggers upon every registered heartbeat and to enable custom delays.

The acquired device (SA Instruments, Inc.), shown in Fig. 4.28, makes this possible, but also offers various other features that came in handy during the *in vivo* experiments. The device is controlled from a dedicated PC via serial connection, which in our case is the same PC where we are running the controls software for the small animal ventilator. With this, the PC serves as the main controls device for the animal’s life activity. The three electrodes



Figure 4.28. Front and rear view of the ECG device with all available connectors. The ECG electrodes, the rectal temperature measurement module as well as the respiration trigger are connected to the front. On the back, the ECG gating signal is available (“Gate”), and the serial connector for the PC controls software is plugged.

are connected to the animal with thin pins that are stuck under the skin of the three paws (2 front paws and one rear). Usually, ECG signals are obtained by putting the electrodes on the animal's paws directly (with electrode plates) and by using contact gel to improve signal quality, while our technique represents a quite invasive method for the animal. We tested both techniques during a short experiment at the Institute for Anatomy of the University of Bern (March 2014) and found that only one of the two is applicable when the animal is being moved (during image acquisition). Namely, the method with the pins yielded a much stronger and more reliable signal, particularly in those cases when the electrode cables are moved in respect to the animal (e.g. during tomographic rotation). Hence, we decided to adopt that method for the future, also following the fact that we were only dealing with terminal (acute) *in vivo* experiments where the animal is continuously kept under deep anesthesia and sacrificed in the end.

After connecting the pins to the animal, the ECG device then fires continuous TTL-triggers, which can be modified in many ways. Firstly, the ECG-trigger **delay time** serves the purpose of setting a delay time between the heartbeat signal and the time point when the device fires the trigger. This is particularly useful if one aims at imaging the lung during an ideally motionless heartbeat phase. For instance, the ECG device captures the QRS-complex (ventricular depolarization), which is followed by a rapid heart contraction. Ideally, one would aim at imaging the lung before the QRS impulse, which can be overcome by setting an appropriate delay (in our case between 100-200 ms). Another important value is the so-called **blanking time**, which defines a minimum heartbeat period for firing a TTL-trigger. Since the heartbeat is usually very irregular, this setting allows to ignore those heartbeats that occur *too early*. Finally, the **trigger length** represents another crucial quantity that has to be set very precisely in an imaging experiment. In our case we set this value according to the time needed to open the shutter and to acquire an image.

The prospective breath-hold gating acquisition is schematically depicted in Fig. 4.29. As it can be seen, the ECG is directly connected to two outputs via the Signal box: the millisecond shutter and the so-called “trigger exposure” of the camera. The schematic is explained as follows: When the image acquisition is started under a slow rotation, the “Aerotech PSO” signal

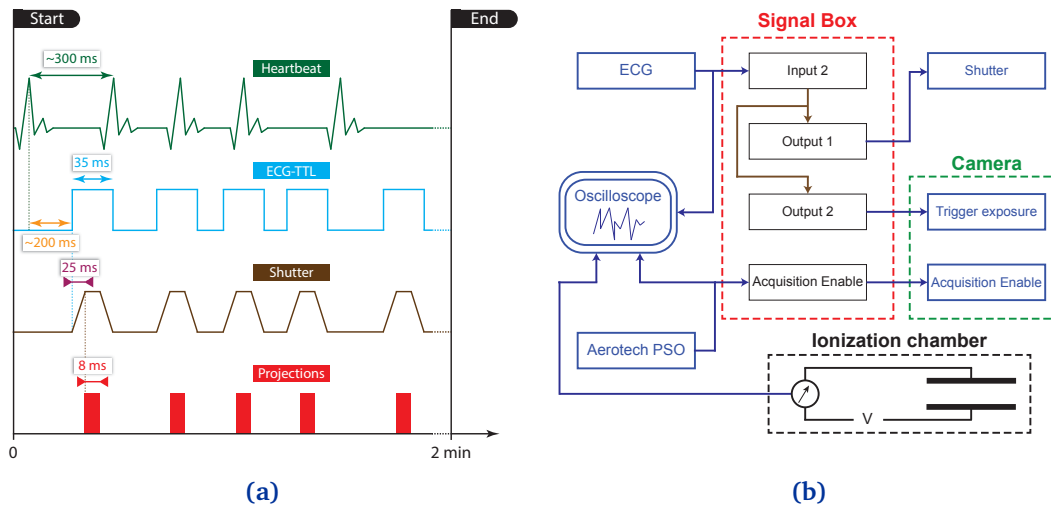


Figure 4.29. Complete TTL triggering schematic for the *in vivo* setup: **(a)** shows all delay times under a long breath-hold and isoflurane anaesthesia, assuming a heartbeat rate around 200 beats per minute (BPM), **blinking time** of ca. 200 ms, **shutter opening time** of 25 ms, **exposure time** of up to 8 ms, **ECG trigger length** of 35 ms **(b)** shows the necessary connections for the prospective heartbeat-triggered acquisition scheme. As visible, three signals are recorded with an oscilloscope, the ECG and Aerotech PSO for obtaining the projection angles and the ionisation chamber current for on-the-fly dose monitoring.

changes to “HIGH” and enables the “Camera acquisition”. From this moment on, every ECG-pulse triggers the “Exposure” in the detector (which is disabled in the case that the “Camera acquisition” is on “LOW”). At the same time, when the ECG fires a trigger, the millisecond-shutter is opened. The delay between milli-second shutter opening and the time point when the camera indeed acquires the image is set in the camera driver and accounts for the fact that the shutter opens with a precise 25 ms-delay.

In order to calculate the exact rotation angles for each projection, all signals are recorded with a laboratory oscilloscope along with the current signal from the ionization chamber for on-the-fly X-ray flux monitoring. The typical signals are shown in Fig. 4.30(a), while in Fig. 4.30(b) the typical rotation angle increments in an *in vivo* scan are compared to an ideal tomographic (equiangular) sampling. During tomographic acquisition the animal rotates constantly, while at each heartbeat a tomographic projection is acquired. The angular increments of these tomographic projections become bigger as the heartbeat rate becomes smaller. Despite this (almost) linear slow-down which happens during a long breath-hold, the strong irregularities in the heartbeat period are still visible and eventually contribute to the deterioration in final image quality unless they are corrected (shown in Chapter 7).

In Listing 4.1 the MATLAB code is shown, which is used to calculate the rotation angles from the two signals in Fig. 4.30(a). The calculated angles are then directly input into the tomographic reconstruction algorithm.

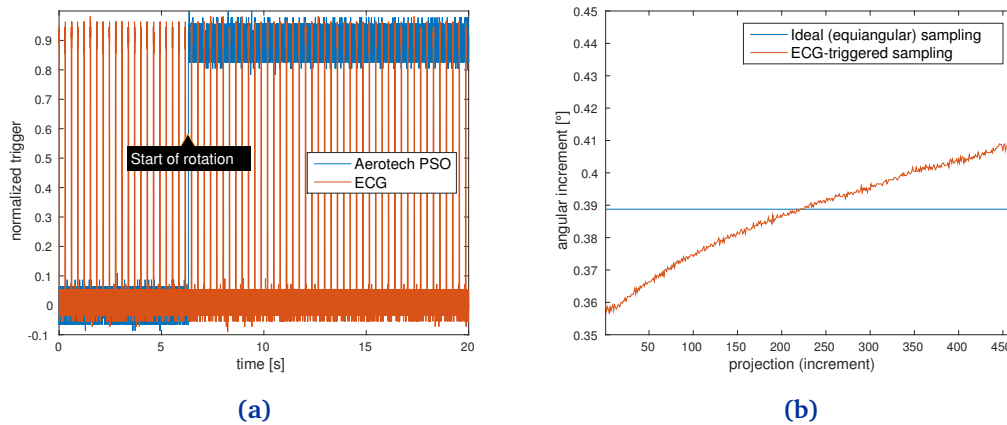


Figure 4.30. Recorded oscilloscope signal (a) and resulting (b) angular increments for each projection. As shown, the angular increments increase as the heartbeat rate decreases.

Listing 4.1. MATLAB script for calculating tomographic rotation angles from the oscilloscope signals. The TTL-threshold is set lower than the usual 5V because of the FPGA-based signal box which gives “high” signals in the range of 3.5V.

```

1 thresh = 2.5; % TTL-threshold
2
3 % (1) Load CSV-File into matrix a
4 a = csvread( csvfile, 21 );
5
6 time = a(:,1);
7 PSO = a(:,3);
8 ECG = a(:,2);
9
10 % (3) Get lengths
11 PSO_new = PSO( PSO > thresh );
12 length_PSO = length( PSO_new );
13 ECG_new = ECG( ECG > thresh );
14
15 % (4) Differential signal
16 ECG_diff = diff( ECG_new );
17 ECG_diff_pos = find( ECG_diff > thresh ); % peak positions
18
19 % (4) Calculate angles
20 angles = ( ECG_diff_pos./length_PSO ) .* 180;
21
22 % (5) Export angles to file
23 [...]

```

Finally, a couple of practical aspects have to be noted. When working with the pin-electrodes for monitoring the ECG, they have to be cleaned regularly in order to get a sufficient signal-to-noise ratio of the ECG signal.

The ECG device also provides the possibility to measure air pressure, which is useful in respiratory-triggered gating (e. g. in micro-CTs) where a cushion is usually placed under the animal. In our case, this feature was useful to identify motion-less heart-beat phases, e. g. when

connecting the third valve of the endotracheal cannula [see Fig. 4.27(a)] under a breath-hold phase to the respiratory input of the ECG (Fig. 4.28 left) one can directly observe the correlation between the electrical activity of the heart and the heart-induced pressure oscillation in the lung.

4.4.5 Animal preparation and anesthesia

From the findings of the (non-imaging) ventilation experiments described in Sec. 4.4.3, we concluded that the best solution would be a combined injection/isoflurane anesthesia protocol, having basically two major advantages: on the one hand, the dose of the injection-anesthesia can be chosen to be very low, as it is only required to put the animal to sleep while performing the tracheotomy; on the other hand, it is possible to keep the animal anesthetized for a very long time without repeating the injections. From the ventilator's point of view, being a piston-driven machine and thus not being compatible with compressed air, a dedicated isoflurane-influx/outflow solution had to be developed.

The final setup is sketched in Fig. 4.31 where the main focus was to establish a constant mixed air/isoflurane flow without increasing the imparted pressure on the FlexiVent ventilator, which would eventually alter its precision after being calibrated. This was achieved by an open-atmospheric flow system, which was designed in order to absorb the remaining isoflurane and thus prevent isoflurane-exposure to the human experimenters. In Fig. 4.31(a) also the final endotracheal cannula is depicted where the blue color (left tube) indicates the oxygenated air and the red color (right tube) the exhaled air from the animal. The air/isoflurane mixture, after being emitted from the FlexiVent streams through a ventilator before finally being absorbed in the isoflurane absorber. The only component missing in the sketch is the isoflurane blender (shown in Fig. 4.19 E). In Fig. 4.31(b) and Fig. 4.31(c) the animal is shown when mounted on

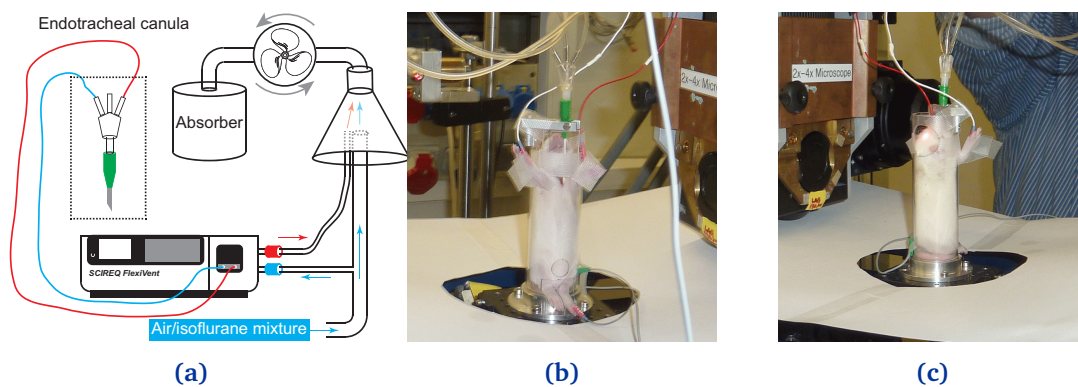


Figure 4.31. Sketch of the isoflurane-influx/outflow system (a), which was designed due to the fact that the ventilator only works in combination with atmospheric pressure. In (b) and (c) the animal positioning in the sample-holders during the experiment is shown.

the rotation stage prior to starting the image acquisition. Clearly visible are the endotracheal cannula (green), the holes in the sample holder that enable the recording of the ECG signal

from the paws of the animals, and finally [in Fig. 4.31(c)] the bright spot on the animal's head represents the (light) pinpoint from the visible-light laser used for alignment.

According to this setup we established an animal handling protocol that was subsequently used during all *in vivo* experiments. The detailed steps are summarized as follows:

- (1) First the animal is anesthetized with an injection of a mixture of xylazine and ketamine, which takes about 10 min to put the animal into deep sleep, while still free-breathing.
- (2) Subsequently a tracheotomy is performed, the animal is placed into the sample-holder [see Fig. 4.31(b) Fig. 4.31(c)] and the endotracheal canula is mounted and fixed.
- (3) The animal is then transferred to the beamline hutch, mounted on the sample manipulator and externally ventilated with a small animal's breathing device (FlexiVent) with a O₂/air-isoflurane mixture of about 2 – 3%. The body temperature is kept constant with a 150 W heating lamp (mounted about 40 cm distant to the animal), and the temperature is monitored rectally (with the ECG device). The explicit breathing parameters are summarized in Tab. 4.6.
- (4) At the same time the three paws of the animal are connected to the ECG-device with small pins, and the ECG-electrodes are mounted so that they don't interfere with the X-ray beam. Both the ECG and the animal-ventilation are monitored via a portable notebook (easily moved inside and outside the hutch).
- (5) The desired region of interest (ROI) is then aligned with a pre-aligned laser pointer that is placed so that it points to the middle of the ROI of the X-ray projection image. This alignment is cross-checked visually from various angles (0°, 90°, 180° and 270°), which suffices an estimated precision in ROI-alignment about 400 μm.
- (6) After this procedure is finished, the controls PC is moved outside, and the hutch is closed being ready for image acquisition.

With this protocol it takes about 30-40 minutes between the first injection anesthesia until the first images can be acquired. As will be explained later, a prospective heartbeat-triggered breath-hold acquisition scheme was applied for about 2 min. During this phase we usually observed a slight decrease in heartbeat frequency, usually by not more than 20 %. Followed by each breath-hold phase the animals again were ventilated regularly, and the heartbeat recovered rapidly, usually being in the range of 190 – 210 BPM in the isoflurane-anesthetized rats. According to this procedure the animals were kept stable and in deep sleep for several hours, while routinely a complete scan (i. e. when acquiring multiple lung pressure under multiple breath-holds) would take about two hours. During this time, however, we ensured to perform regular ventilation phases after each breath-hold. After the *in vivo* experiments had been terminated, the animals were administered an overdose of pentobarbital, while still being constantly ventilated and monitored in their ECG-activity. It took about 20-30 min before the ECG-signal had completely vanished, after which e. g. immediate (fresh) *ex vivo* images could be acquired.

Dose optimization approach to fast X-ray microtomography of the lung alveoli

The following chapter represents a reprinted manuscript published as: G. Lovric, S.F. Barré, J.C. Schittny, M. Roth-Kleiner, M. Stampanoni, and R. Mokso, *Journal of Applied Crystallography*, **46**(4), 856, 2013 [162].

5.1 ABSTRACT

A basic prerequisite for *in vivo* X-ray imaging of the lung is the exact determination of radiation dose. Achieving resolutions of the order of micrometers may become particularly challenging owing to increased dose, which in the worst case can be lethal for the imaged animal model. A framework for linking image quality to radiation dose in order to optimize experimental parameters in respect of dose reduction is presented. Our approach may find application for current and future *in vivo* studies to facilitate proper experiment planning and radiation risk assessment on the one hand and exploit imaging capabilities on the other.

5.2 INTRODUCTION

The development of high-speed time-resolved tomographic microscopy is of great interest for various three-dimensional *in vivo* studies. One important application is the study of lung dynamics, in particular lung inflation and deflation issues during physiological as well as mechanical ventilation, which is required, for example, after a premature birth or during a general anesthetic. Two hypotheses on the structural alterations in the gas-exchange area during breathing are still under debate: a heterogeneous distention pattern [163] of different lung areas and a homogeneous cyclic opening-and-collapse [164] of all alveoli.

In the recent past, lung imaging with small animal models has become an established tech-

nique at synchrotrons [165–167], priorly making rapid data acquisition and high-resolution X-ray imaging possible [168]. Kitchen et al. [169] performed phase-contrast X-ray imaging of mice and rabbits *in vivo* in two dimensions and developed a method for visualizing lung liquid clearance at birth [31, 170]. Bayat et al. [166] used xenon as a contrast agent and were able to measure and visualize gas distribution within the lungs in three dimensions, enabling further functional studies [171–173]. More recently, synchrotron-based tomographic microscopy has been utilized to study the distribution of gas flow throughout the airway tree in connection with altered lung motion an indicator for regional lung disease [174, 175].

So far, all studies were either performed in two dimensions only or suffered from low temporal and spatial resolution; high-resolution lung images in three dimensions, on the other hand, were successfully obtained only for static samples [23, 176–179]. Thus, *in vivo* X-ray tomography with micrometer spatial and sub-second temporal resolution remains a challenge, and many open questions in the study of lung physiology remain unanswered.

We describe our approach to image formation of biologically relevant features in the lung, aiming at optimal image quality in terms of contrast, spatial and temporal resolution and deposited radiation dose. In particular we show current limitations towards *in vivo* imaging at the micrometer scale.

5.3 MATERIALS AND METHODS

5.3.1 Image acquisition

The experiment was carried out at the X02DA TOMCAT beamline of the Swiss Light Source (SLS) at the Paul Scherrer Institute (Villigen, Switzerland). The experimental setup is depicted in Fig. 5.1: the X-ray beam, produced by a 2.9 T bending magnet on a 2.4 GeV storage ring (with ring current $I = 400$ mA, top-up mode), is monochromated with a double-multilayer monochromator and tuned to 21 keV. A sample-to-source distance of 25 m is used for pro-

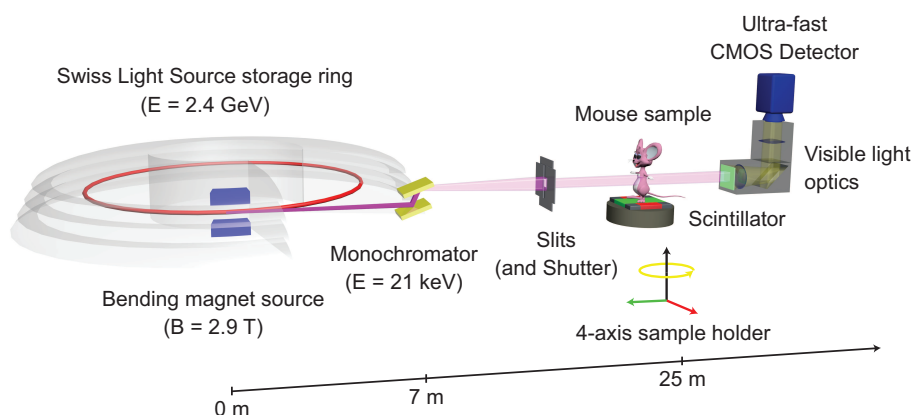


Figure 5.1. Experimental setup at the X02DA TOMCAT beamline.

ducing an X-ray beam with appropriate spatial coherence properties. We used a high-speed CMOS detector (PCO.Dimax) coupled to visible-light optics with $100\ \mu\text{m}$ and $20\ \mu\text{m}$ thick scintillators for medium and high spatial resolutions, respectively. The samples were probed with two different optics, yielding effective pixel sizes of $2.9\ \mu\text{m}$ and $1.1\ \mu\text{m}$, respectively. For these two optics the field of view was adjusted with horizontal and vertical slits, located just before the sample and producing beam sizes of $5.8 \times 2.7\ \text{mm}^2$ and $2.2 \times 2.2\ \text{mm}^2$, respectively. The sample-to-detector distance z was varied in the range 24-300 mm to allow for the variation of the Fresnel interference pattern for image quality optimization purposes. Raw images were acquired with exposure times ranging from 2 to 13 ms and 901 tomographic projections.

The measurements were performed *ex vivo* on mice aged 37 d ($n = 3$ / Balb-C, central animal facility of the University of Bern) that were sacrificed before the experiment. The mice were killed with an overdose of a combination of Acepromazine, Xylazin and Ketamin. They were then placed in an upright position into a 2.5 cm-diameter falcon tube. All parts of the animal experiments were approved and supervised by the Swiss Agency for the Environment, Forest and Landscape, and the Veterinary Service of the Canton of Bern.

5.3.2 Post-processing

The aforementioned setup facilitates propagation-based phase contrast, represented by interference fringes on the tissue interfaces in the recorded digital projection images. Prior to further analysis, each projection was corrected with the respective dark and flat-field image. In a second step, single-image phase and intensity extraction were applied to all projections [65]. In a third step, the computed tomography (CT) reconstruction was conducted with the *gridrec* algorithm [71], enabling fast reconstructions of large data sets. Finally, the CT reconstructions obtained from phase-retrieved images and absorption images were fused in the Fourier domain in order to correct for the high-pass characteristics of the Paganin algorithm [180]. The complete post-processing flowchart is depicted in Fig. 5.2.

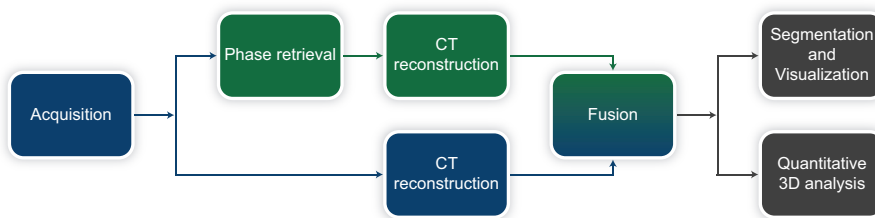


Figure 5.2. Flowchart of the post-processing pipeline. After image acquisition, the CT-reconstructed volumes obtained from absorption and phase-retrieved images are fused in the Fourier domain. Afterwards, further analysis (segmentation, visualization etc.) can be applied.

5.3.3 Image analysis

The reconstructed tomographic slices were examined in view of contrast-to-noise ratio (CNR) and resolution. For the CNR following formula was used:

$$\text{CNR} = 2 \left(\frac{|S_{\text{obj}} - S_{\text{bg}}|}{\sigma_{\text{obj}} + \sigma_{\text{bg}}} \right), \quad (5.1)$$

where S_i represent mean pixel values and σ_i standard deviations of a manually defined object and background region, respectively. One has to consider, however, that the object (i. e. lung tissue) consists of blood vessels and erythrocytes which have different densities and may lead to distorted contrast levels. Under the present imaging scheme, this effect is negligible.

The resolution was determined by a criterion based upon Fourier analysis [181]. Considering a test image, the resolution was obtained by taking a line profile and calculating its power spectral density (PSD). The PSD converges towards a value that can be defined as the noise baseline. Taking the value of the PSD at the noise baseline twice and matching it to the respective spatial frequency yields the resolution. This can be made more robust and fully automated if one operates on the mean PSD, obtained from many line profiles. The only necessary condition for this method requires the highest spatial frequency of the image to be lower than the Nyquist frequency of the line profile. Since the smallest features of the lung are at least of the order of tens of pixels, this condition was fulfilled for both optics of our setup.

Additionally, the results were cross-checked with another method by which the resolution is derived from a line profile taken along an edge in the image. The line profile is then fitted with an error function by means of a least-squares fit, and the resolution is determined from the slope of the function.

In Fig. 5.3 the test image with the defined object and background regions, the line profile, the line profile along the edge, and the calculated PSD are shown. The image in Fig. 5.3(a) was constructed from a region near the center of the original tomographic slice in order to reduce the radial dependency of the resolution originating from the tomographic reconstruction. The resolution x_{res} is calculated by

$$x_{\text{res}} = p_{\text{size}} \times \frac{x_n}{k_{\text{res}}}, \quad (5.2)$$

where p_{size} is the pixel size of the detector, x_n the number of pixels for the taken line profile and k_{res} the spatial frequency obtained from the resolution criterion in Fig. 5.3(d).

5.3.4 Dose calculations

The X-ray radiation dose was assessed in two steps by theoretical and experimental means. First, the theoretical flux F was calculated with the TOMCAT beamline parameters [114] and the following formula [42]:

$$\frac{dF}{d\phi} = 2.46 \times 10^{23} E_e^2 [\text{GeV}] I [\text{A}] G_1 \left(\frac{\omega}{\omega_c} \right), \quad (5.3)$$

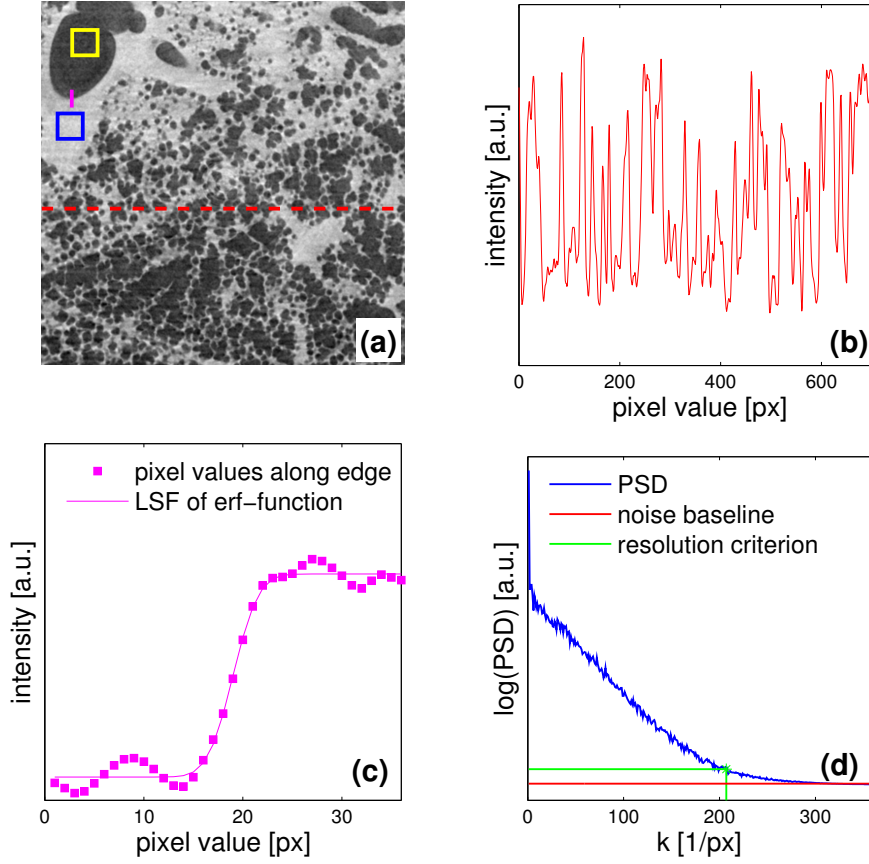


Figure 5.3. (a) A tomographic slice of a lung for the $2.9\ \mu\text{m}$ -pixel-size optics. Regions for calculating CNR are defined by the rectangles, the red dashed line indicates the input for the line-profile plot in (b) and the solid magenta line indicates the edge line plot in (c). (d) Mean PSD from many line plots with the calculated noise base line and the respective resolution criterion.

with electron energy E_e , ring current I and

$$G_1(y) = y \int_y^{\infty} K_{5/3}(y') dy', \quad (5.4)$$

where ω_c is the critical frequency of the bending-magnet radiation, ω the emitted photons frequency and $K_{5/3}$ represents the modified Bessel function of the second kind. In Eq. (5.3) the flux is given in practical units [$\text{photons s}^{-1} \text{mrad}^{-1} (0.1\% \text{ bandwidth})^{-1}$]. Thus it has to be further corrected in order to include bandwidth and reflectivity of the monochromator as well as all optical elements that further reduce the theoretical flux. In a second step, the absorbed dose [182] of a 2.5 cm water column was calculated from NIST mass attenuation coefficients (<http://physics.nist.gov/PhysRefData/XrayMassCoef/ComTab/water.html>). The

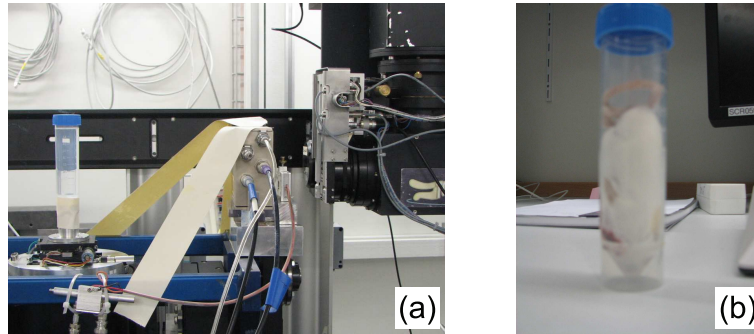


Figure 5.4. Dose and flux measuring setup. (a) Water column with reference ionization chamber and a silicon pin diode (placed behind the ionization chamber). (b) Frozen mouse sample.

X-ray flux was determined experimentally with a calibrated silicon pin diode [134] and a frozen mouse sample in connection with a 2.5 cm water column to verify that the modeling with water is appropriate. Images from the setup are depicted in Fig. 5.4.

5.4 RESULTS

Lung images were reconstructed from tomographic projections taken at five different propagation distances. Figure 5.5 shows the calculated CNR and resolution for each distance and for different weighting factors for the absorption images in the fusion algorithm. The bracket values denote resolutions obtained from the edge-fitting method. As expected, for the transport-of-intensity-based phase retrieval approach in the near-field region the optimal propagation distance is near the value of $p_{\text{size}}^2/\lambda[\text{m}]$, where p_{size} is the pixel size and λ is the wavelength. We show that fine tuning this distance can significantly affect the CNR. By applying the fusion algorithm [180], it is possible to increase the resolution further, but at a cost of CNR. This can be used for adjusting the resolution of the reconstructed image. It has been reported elsewhere [183, 184] that phase-contrast images of lungs exhibit better contrast and especially less noise than pure absorption images. We addressed this issue by evaluating the degree of “segmentability” in a tomographic scan. In Fig. 5.6 the two images and the respective binary images obtained by thresholding are plotted. The total scan time was 5.4 s, and the CNR for the absorption and phase-retrieved images were 1.8 and 15.0, respectively, which makes up a difference of approximately one order of magnitude. However, the segmentation from the absorption images shows small artefacts originating from the higher noise level. We further found that a CNR of ~ 2 is currently the lower limit for a successful segmentation and in some cases necessitates further processing (e. g. filtering). This limit was verified by visual inspection. Finally, CNR and the X-ray radiation dose were calculated as functions of the total scan time of a tomographic scan, as shown in Fig. 5.7. The values for CNR obtained from

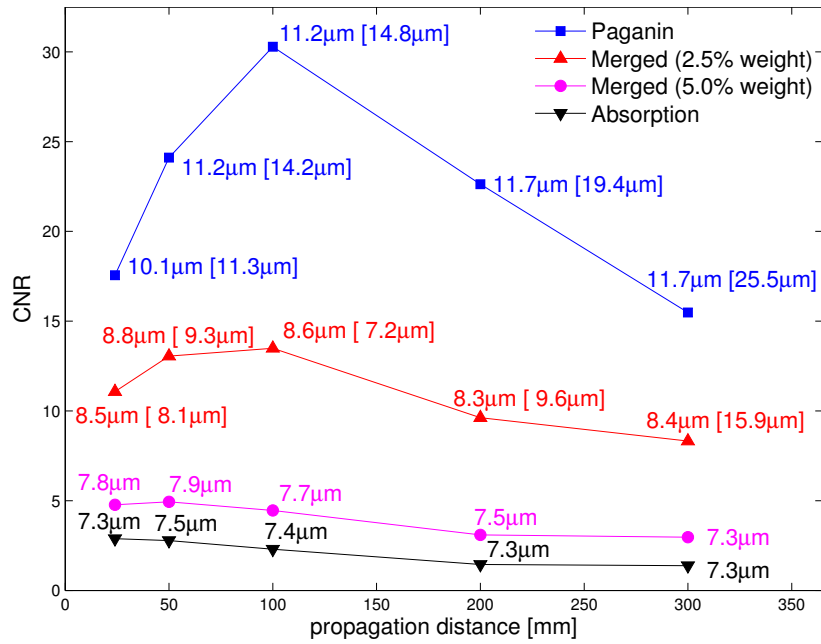


Figure 5.5. Contrast-to-noise ratio (CNR) as a function of sample-to-detector (propagation) distance and the weighting of the absorption image in the fusion algorithm. The values were calculated for the $2.9\ \mu\text{m}$ -pixel-size optics and 11.7 s total scan time. The bracket denote resolutions obtained from the edge-fitting method.

experimental data were fitted and extrapolated using the following function:

$$f(t) = a[1 - \exp(-b \cdot t)], \quad (5.5)$$

where a, b represent arbitrary parameters for the nonlinear fit and t the total scan time. The function derives from the fact that the CNR will be zero if the sample is not exposed to X-rays ($t = 0$). Thus its origin is at zero. The upper value of CNR is limited by the mean pixel values represented by the density values of the biological material and their standard deviations which are inherent to the acquisition scheme. CNR will therefore converge to a saturation value in the tomographic reconstruction.

5.5 DISCUSSION

The optimization of CNR in respect to the deposited radiation dose is crucial in low-dose experiments. In particular, we found that the application of the one-shot phase-retrieval algorithm [65] increased CNR by almost a factor of ten compared with the pure absorption-contrast images. However the spatial resolution decreased, as shown in Fig. 5.5. It is also evident that tuning the propagation distance can affect CNR by a factor of two under the given conditions.

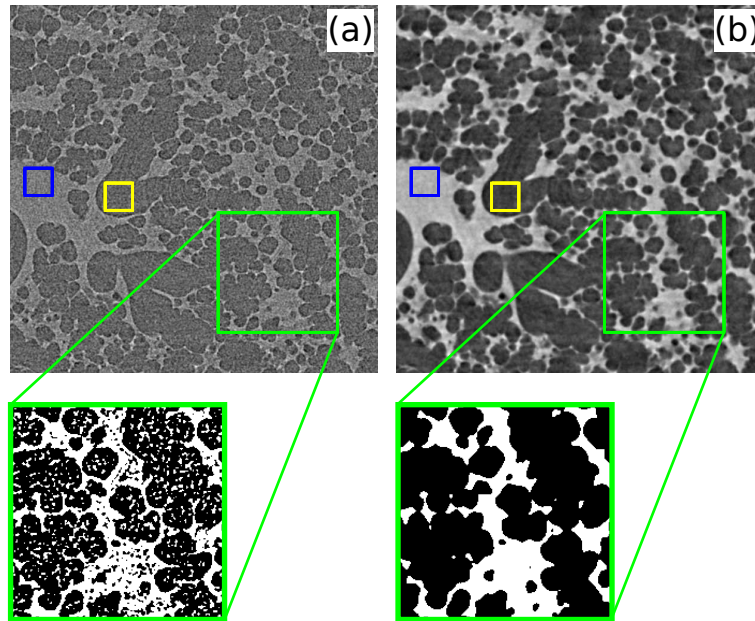


Figure 5.6. Comparison of tomographic slices before and after thresholding obtained from pure absorption-contrast (a) and phase-retrieved projection images (b). For both images the total scan time was 5.4 s. The small rectangles denote the regions for calculating the CNR.

These results indicate that the optimal propagation distance, represented by a trade-off between CNR and resolution, and fusion parameters are particularly important and should be considered before the experiment. Furthermore, we found that the resolutions obtained from the two different criteria are not consistent for larger propagation distances, and the robustness of the edge-fitting method in general was bad. This can be explained as follows: by increasing the propagation distance the edge enhancement becomes more pronounced and the Fourier resolution criterion detects edge artefacts as “features”, whereas the edge fitting gives a poorer result. Thus, the Fourier resolution criterion has to be handled with care for larger propagation distances.

For the radiation dose we found that the $1.1\ \mu\text{m}$ -pixel optics (numerical aperture: 0.4) yielded a lower dose than the $2.9\ \mu\text{m}$ -pixel optics (numerical aperture: 0.2) for the same CNR values. The main reason for this result is the fact that images for the two optics were not acquired under the same experimental conditions, i. e. optimized propagation distance etc. Apart from that, one also has to regard the efficiencies of the different optics. Finally, another reason is the fact that images from both optics were reconstructed from local tomographic projections. Since we calculated the total dose in the irradiated volume, the smaller field-of-view means lower energy deposition for the same volume. Obviously, the dose rate in the lungs will be higher for the $1.1\ \mu\text{m}$ -pixel optics.

The model function from Eq. (5.5) for extrapolating CNR as a function of the total scan time still needs to be verified with the *gridrec* algorithm [71]. However, taking the range of interest that we analyzed, a similar fit (e. g. linear) would only cause negligible errors. From

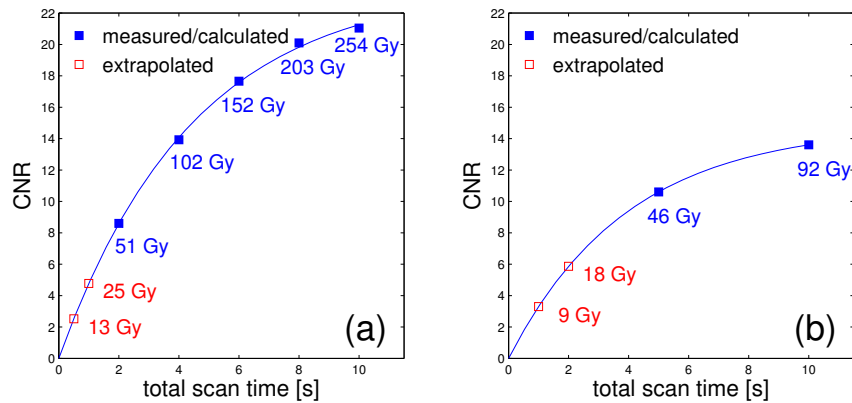


Figure 5.7. CNR as a function of total scan time per tomographic scan for the two different optics in use: (a) Optics with $2.9 \mu\text{m}$ effective pixel size. (b) Optics with $1.1 \mu\text{m}$ pixel size.

the results in Figs. 5.6 and 5.7 we further hypothesize that under the given conditions the lowest achievable dose for obtaining the necessary CNR is 10 and 5 Gy, respectively.

5.6 CONCLUSION

We have developed a framework for optimizing experimental parameters in medium-dose experiments, which is particularly important for current efforts in developing microtomographic *in vivo* X-ray imaging to study lung physiology at the micrometer scale. Thanks to the fast phase-retrieval and CT reconstruction algorithms, it is possible to apply the optimization steps on-the-fly (or even in real time) as an initial part of a beamline experiment.

We showed that the lowest achievable dose at the moment is in the range of 5-10 Gy per tomographic scan at a total scan time of approximately 0.5 s and approximate resolutions between $4\text{-}10 \mu\text{m}$, producing images with an approximate CNR of 2. Our results indicate that *in vivo* tomography at the micrometer scale and sub-second temporal resolution should be feasible, but will necessitate further adjustments.

5.7 ACKNOWLEDGEMENTS

We thank Gordan Mikuljan for his great support in setting up the experiment at the beamline. This study was supported by the National Competence Center in Biomedical Imaging (NC-CBI), Grant Nr. 1126.0076, and Swiss National Science Foundation (SNF), Grant Nr. CR2312-135550.

Quantitative analysis of intact lungs at the alveolar and acinar scale

The following chapter represents a manuscript currently in preparation for publication by following authors: G. Lovric, I. Vogiatzis Oikonomidis, J.C. Schittny, M. Roth-Kleiner, R. Mokso, and M. Stampanoni.

6.1 ABSTRACT

With the advent of highly brilliant third-generation synchrotron X-ray sources *in vivo* imaging of biological samples has recently reached micrometer spatial and sub-second temporal resolutions. Analyzing high-resolution 3D biological structures such as lung tissue, however, still poses a great challenge due to its complexity and hierarchical branching scheme. In this work we demonstrate the application of quantitative tools for morphological and topological analyses applied to high-resolution 3D lung image data, inflated at different pressure levels. We show how the tools might be used for a detailed description of lung inflation patterns, providing deeper insight into lungs physiology and opening a whole new range of applications. We present indications for a heterogeneous distension pattern and discuss first quantitative evidence of tissue over-extension upon higher peak-inspiratory pressures.

6.2 INTRODUCTION

Nowadays established techniques that utilize synchrotron-based X-ray microtomography cover a wide range of fields, including biology [185, 186], materials science [187, 188], soft condensed matter physics [189], geoscience [190–192], paleontology [193, 194] as well as other related disciplines. Recent advances in instrumentation, in particular due to the continuous improvements made in spatial and temporal resolutions, have significantly increased the importance of time-resolved studies, making *in vivo* imaging at the micrometer scale and in 3D a reality [195, 196]. Current efforts go straight in the direction of developing imaging sys-

tems with high spatial, temporal and density resolutions in a dose efficient manner that will facilitate further dynamic four-dimensional studies [197].

At the same time synchrotron-based lung imaging techniques with small animals (rats, mice, rabbits) have been established in various studies and provided matchless insights into some of the most interesting questions in lung physiology and development [23, 31, 198]. Broadly speaking, three complementary approaches have been pursued: (i) dynamic *in vivo* studies in 2D and at pixel sizes in orders of tens of micrometers for investigating lung liquid clearance phenomena, effects of positive end-expiratory pressures (PEEP) and improved ventilation strategies [25, 26, 167], with recent advances towards 3D [175]; (ii) *in vivo* imaging in 3D at lower resolutions [172, 184] has been applied to study various alterations to regional gas distributions in the lung, such as the effect of PEEP [199], tidal volume [200] or the heterogeneity introduced by particular disease models [171]; and (iii) high-resolution 3D imaging of fixed lung samples has been routinely used for characterizing in high detail various aspects of individual rat lung acini and their developmental stages [13, 177, 201]. We have recently shown that tomographic *in vivo* imaging of the lung at the micrometer scale is feasible [162], and with the recent advances in fast X-ray tomographic microscopy the next step towards time-resolved studies is at hand [197]. Despite these experimental developments, little has been done to introduce novel concepts into the quantitative analysis of high-resolution 3D lung images. The standard structural analysis of the lung is still mostly based on stereology, which appears unsuitable for handling high-throughput data and for establishing an automated (computer-guided) process [202, 203].

From a pure post-processing point of view, lung tissue comprises a binary structure of air and tissue, analogous e. g. to the one of solidified alloy materials [204, 205]. During lung development, the continuous optimization process of increasing gas-exchange surface in accordance with lung volume growth results in a very complex hierarchical structure with a huge air-to-tissue surface area [14, 21]. Hence, two intrinsic quantities are affected for the most part, the air-to-tissue surface area with its shape and the air volume within the lung. To investigate small structural changes in lung tissue at the micrometer scale, it is thus necessary to assess these quantities in 3D and at very high resolution, posing requirements for both experimental realization as well as post-processing from segmentation to quantification. While the detailed air recruitment mechanism is still under debate, a full quantitative characterization of lung tissue could bring new facts to light, supporting either of the two currently discussed hypotheses: (i) a heterogeneous distention pattern of different lung areas [163] or (ii) a homogeneous cyclic opening-and-collapse of all alveoli [164].

In this work we present a full route to quantitative analysis of high-resolution 3D lung image data, starting from the image acquisition scheme, how it particularly affects the segmentation and by making the link to quantitative 3D characterization of lung tissue. We introduce a modified local structural thickness analysis for assessing volumetric changes at various scales. For topological analyses of the air-to-tissue surface in the lung, we apply the theory from differential geometry to calculate localized surface curvatures. Although both techniques originate from various studies in materials science, we show for the first time their adaptation to lung tissue. Since our methods are solely based on open-source tools/algorithms, they can

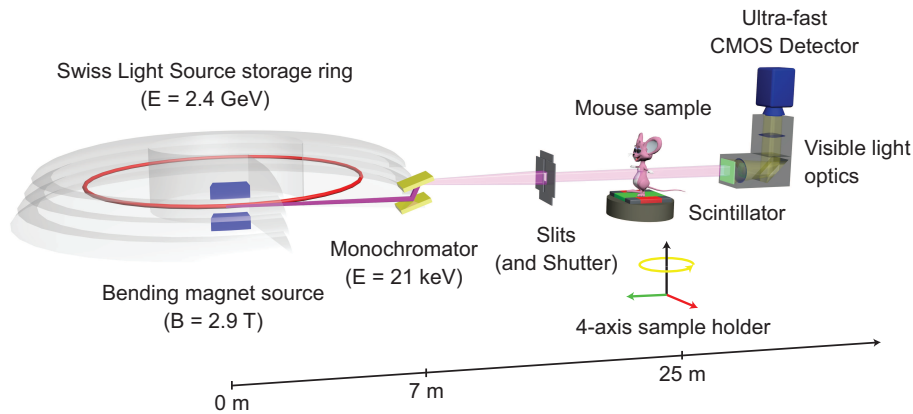


Figure 6.1. Experimental setup at the X02DA TOMCAT beamline.

easily be expanded and applied to equivalent studies in other disciplines.

6.3 MATERIALS AND METHODS

6.3.1 Image acquisition

The detailed experimental setup has been reported elsewhere (Chapter 5 and Reference 162, respectively). In short, the experiment was carried out at the X02DA TOMCAT beamline of the Swiss Light Source (SLS) at the Paul Scherrer Institute (Villigen, Switzerland). The experimental setup is depicted in Fig. 6.1: the X-ray beam, produced by a 2.9 T bending magnet on a 2.4 GeV storage ring (with ring current $I = 400$ mA, top-up mode), is monochromatized with a double-multilayer monochromator and tuned to 21 keV. A sample-to-source distance of 25 m is used for producing an X-ray beam with appropriate spatial coherence properties. We used a high-speed CMOS detector (PCO.Dimax) coupled to visible-light optics with a $150\ \mu\text{m}$ and $20\ \mu\text{m}$ thick scintillator for medium and high spatial resolutions, respectively. The samples were probed with two different optics, yielding effective pixel sizes of $2.9 \times 2.9\ \mu\text{m}^2$ and $1.1 \times 1.1\ \mu\text{m}^2$, respectively. For these two optics the field of view was adjusted with horizontal and vertical slits, located just before the sample, and producing beam sizes of $5.8 \times 2.7\ \text{mm}^2$ and $2.2 \times 2.2\ \text{mm}^2$, respectively. The sample to detector distance z was set to 100 mm, yielding an optimal trade-off between contrast-to-noise ratio and resolution at the respective experimental settings [162]. All scans were performed with 5 ms single-projection exposure times and 901 tomographic projections, giving total scan times in the range of 5 s per volume.

6.3.2 Animal preparation

The measurements were performed *ex vivo* on adult mice ($n = 2$ / Balb-C, central animal facility of the University of Bern) that were sacrificed before the experiment. The mice were anesthetized with an overdose of a combination of Acepromazine, Xylazine, and Ketamin. Sub-

sequently a tracheotomy was performed and the animal was placed, together with the endotracheal cannula, in an upright position into a custom-made sample holder. Afterwards the animal was sacrificed with an overdose of pentobarbital in order to prevent moving artifacts caused by the heart beat. Different pressures (10 cmH₂O, 20 cmH₂O and 30 cmH₂O) were then set into the animal's lung using a small-animal ventilator (SCIREQ FlexiVent), and for each pressure level a tomographic scan was performed. Images were taken no longer than 30 min after the lethal injection to preserve more or less *in vivo* conditions. All parts of the animal experiments were approved and supervised by the Swiss Agency for the Environment, Forest and Landscape and the Veterinary Service of the Canton of Bern.

6.3.3 Post-processing

The aforementioned setup facilitates propagation-based phase-contrast images, which were input to the single-image phase and intensity extraction algorithm by Paganin et al. [65] and subsequently CT-reconstructed with the *gridrec* algorithm [71]. However, this acquisition scheme – coupled with the low-exposure and low-number-of-projections setting – produces CT reconstructions with various artifacts that make an automatic segmentation impossible. The reason is that the single-image phase retrieval enhances edge-blurring, leading to an overall decrease in resolution as well as to a reduction of visibility of very thin structures [162]. Although this effect can be overcome by using a simple fusion algorithm that combines the phase-retrieved images with the absorption ones to yield enhanced edge contrast, it reduces the signal-to-noise ratio in the reconstructed images and thus makes an automatic segmentation more challenging [180]. Therefore, in the present work we have chosen a different post-processing approach. We first discuss the aforementioned artifacts present in the images before describing our segmentation method in detail.

As shown in Fig. 6.2, the most dominant effect causes different regions in the lung to be segmented by varying degrees, while other effects are not immediately obvious. For instance, in Fig. 6.2(a) the thin septal walls that separate single alveoli produce only a slightly stronger signal than the surrounding background. Further on, the region-of-interest (local) tomography introduces a superimposed gradient in the grayscale images resulting in different foreground (lung tissue) and background (air) gray values for different regions in the tomographic slices [206], leading to the fact that in Fig. 6.2(b) the septa are not correctly recognized for the two regions. Finally, the differentiation of foreground and background is strongly dependent on the inspected lung region itself (not shown here), leading to an additional per-slice variation of background illumination gradients and tomographic slice histograms. Thus, in the best case numerous steps are necessary for obtaining the binary segmented images of lung tissue and air which in return serve as a basis for further quantitative analysis. For addressing all the above issues we have developed a semi-automatic technique that is applicable to any comparable problem in image segmentation. The method is automatized almost to the full extent, but requires user interaction in one single step in order to decide which segmentation result is sufficient for further data processing.

The detailed post-processing flowchart is depicted in Fig. 6.3 and the processing steps can

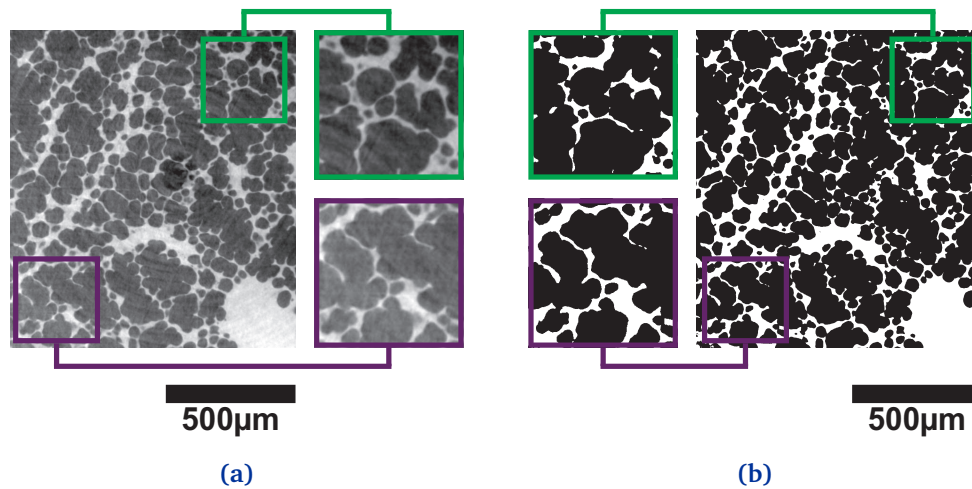


Figure 6.2. Result of automatic threshold segmentation: **(a)** Original tomographic slice; **(b)** binary image after automatic Otsu segmentation. The background illumination gradient produces different segmentation results for the two regions in the tomographic slice.

be summarized as follows:

- (1) First [Fig. 6.3 (A)], the datasets at different peak-inspiratory pressures are registered manually with each other to compensate for shifts in the sample position and the irregular up-scaling upon inflation. The used registration method has been discussed shortly in Sec. 3.5. As a result, we obtain cropped gray-value images of regions of interest of the lung tissue, which are related to each other under a Euclidean transformation.
- (2) In the next step [Fig. 6.3 (B)], background illumination correction is applied to correct the gradient arising from the region-of-interest (local) tomography artifact. This represents a common problem in image processing, and various morphological operations have been suggested, each adapted to particular problems [207]. In our case we assume that the background is a linear gradient and we perform a so-called erosion (with a disk-shaped structure element of 20 px). Without going into further details, the step can be thought of as finding the minimal values in each pixel's surrounding and then “filtering” the whole image so that at the end of the process only these values remain (e. g. similar to a non-linear “minimum filter”). In theory, the background gradient is then clearly visible, but also strongly structure-dependent. For this reason, all extreme values are removed from the histogram creating a so-called “masked” image. Subsequently a plane is fitted onto the masked image and in the last step subtracted from the original one.
- (3) Automatic Otsu segmentation [208] is applied [Fig. 6.3 (D)] and the optimal gray value is stored for latter usage.
- (4) In parallel [Fig. 6.3 (C)], a so-called “ridged image” is created by means of so-called line-shaped profiles, originally introduced by Babin et al. [209]. The idea is motivated

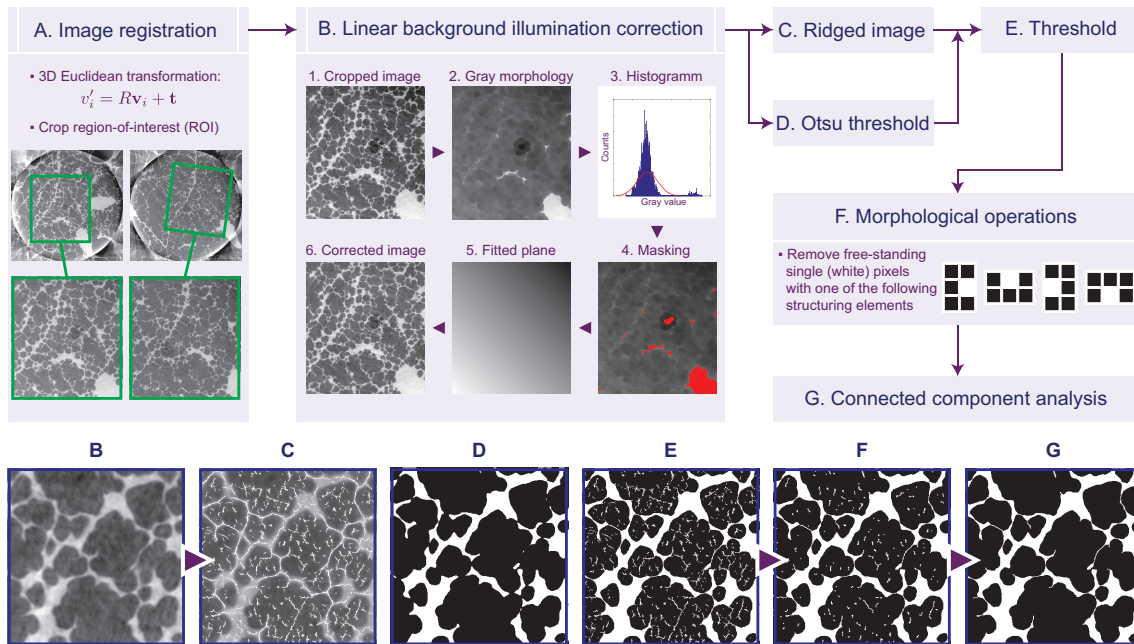


Figure 6.3. Complete segmentation flowchart from image registration to final binary segmentation of the high-resolution lung data. Image registration (A) is conducted by calculating a rotation matrix R and a translation vector t and by transforming all image voxels; in (B) the cropped tomographic slices are subtracted with linear gradient images (B.5); the ridged image (C) is obtained by means of line-shaped profiles; the images are thresholded (E) with the Otsu-value (D); finally the morphological operations (F) and the connected component analysis (G) remove noise artifacts. The result is best visible by comparing image D to image G.

by the fact that in the original image thin septa are visible by eye as they slightly differ from the background, but their signal is too weak to be recovered during an automatic (global) segmentation step. If we now take a line profile through the image and extract all local maxima from this line profile, in theory we should be able to recover each septa. In practice, this step is the only one that requires user interaction, as the user has to decide the margin under which the septa will be discriminated from the background. In our algorithm we enable the discrimination of septa by defining a minimal/maximal thickness, minimal gray-value and minimal gray-value margin in respect to the background. The line profiles are conducted in four directions in the image: 0° , 45° , 90° and 135° . Whenever a septa is detected, the respective pixel value in the original image is set to the brightest value, making sure that from now the (alleged) septa will be always detected as tissue. However, as seen in Fig. 6.3 (C), due to noise in the background, new features are added as well.

- (5) In the next step [Fig. 6.3 (E)], binary threshold is conducted by using the Otsu parameter from (3).

- (6) Morphological operations [Fig. 6.3 (F)] are applied to remove free-standing pixels, since (4) has produced (dependent on the explicit conditions) a significant amount of artifacts. Here we use four manually-defined simple structuring elements that are based on the following assumption: a single free-standing pixel *always* represents an artifact because septa (being very thin and sometimes occupying only single pixels) are always connected with other lung tissue.
- (7) Finally [Fig. 6.3 (G)], a connected component analysis is conducted in 3D to remove artifacts that are thicker than single pixels and that were not removed during the previous steps. After this step the final binary segmented image is used for further processing.

6.3.4 Local thickness analysis

The volumetric change of alveolar structures upon inflating the lung with increasing peak-inspiratory pressures in intact animals has been measured by different means so far, either by manual counting [210] or by detecting changes in the power spectral density of lungs speckle images [211]. These measures, however, provide only limited insight, namely at lungs peripheral areas, or by giving only global volume changes without insight into the detailed processes (i. e. no direct observations). In Fig. 6.4, only a small part of a lung's CT slice is illustrated to show how lung tissue stretches at two different pressures. Our aim in the following is to quantify these volumetric changes in 3D. Similar tasks are usually performed in various other

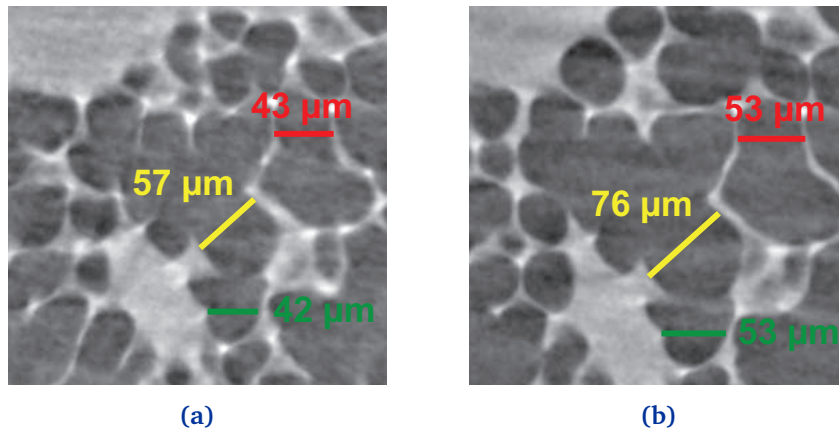


Figure 6.4. Manual measure of air “thickness” on a 2D tomographic slice at two different peak-inspiratory pressures: (a) for 5 cmH₂O; (b) for 10 cmH₂O.

studies, such as bone [212] or materials science [213], for which a so-called thickness map analysis has been developed by Hildebrand and Rüegsegger [214]. The local thickness τ can then be defined as follows:

$$\tau(\mathbf{p}) = 2 \times \max(\{r | \mathbf{p} \in \text{sph}(\mathbf{x}, r) \subseteq \Omega, \mathbf{x} \in \Omega\}), \quad (6.1)$$

where \mathbf{p} is an arbitrary point of a set Ω , a set $\Omega \subset \mathbf{R}^3$ defining the structure under study, $\text{sph}(\mathbf{x}, r)$ is a sphere with center \mathbf{x} and radius r . Simply, τ gives the maximum diameter of the spheres that fit inside an arbitrarily chosen object. If applied in our case, in order to get the diameter of the airspaces we define the air volume as the “object”.

The detailed calculation steps are as follows: at first, the Euclidean distance map is calculated, and redundant points that do not give any structural information are deleted to create a ridge (or skeleton) of the distance map. Afterwards, the ridge is scanned in order to find the largest possible sphere that the ridge belongs to. Finally, a cleanup-step is applied to the surface voxels by replacing their local thickness with the average of the neighboring non-background voxels in order to correct errors originating from the background/foreground interface [215]. The result is used to calculate *how many* structures of a certain size exist in the 3D image data. Dividing the number of voxels of a specific thickness value by the corresponding volume of a sphere with the same diameter should result in the “amount” of these structures. As a validation step, tests were performed on phantom data of randomly positioned spheres of arbitrary sizes. An overestimation was observed for spheres of up to 60 voxels in diameter due to finite-volume effects (“staircase approximation”). The same tests were performed on cylindrical phantoms. In all cases the error behavior was the same. As a result, we implemented a simple correction factor so that the thickness-map values give the values of the corresponding local volumes.

6.3.5 Curvature analysis

The second part of the quantitative analysis was conducted on the air-to-tissue interfaces in the lung. While the local thickness gives a pure local volumetric representation, it does not provide information on the topological properties of the material. For conducting these analyses, the theory of differential geometry comes in handy, as it enables to apply established topological measurements on surfaces. From a computational point of view surfaces are represented by (polygonal) meshes and, contrary to pure pixel data, these have the advantage of storing more properties for a 3D volume, such as surface normals, surface facet areas and so forth [216]. Before describing our analysis pipeline in more detail, we first give a short overview on the curvature analysis in general.

The surface curvature has been studied extensively in the field of material science, in particular with alloy structures, where it represents an important factor providing indication of local variations in surface energy [204] or gives the direction of diffusion-driven flux [205]. In biological materials such as plants structure curvature has been found to be genetically controlled [217], thus indicating the biophysical perspectives of this quantity. Recently, the potential in medical image analysis has been recognized, but the full application is still on the way [216, 218].

By calculating the eigenvalues of the shape operator on all surface points (vertices), we obtain the minimum and maximum curvatures (also called principal curvatures) per vertex, κ_1 and κ_2 , which are linked with the mean curvature H and the Gaussian curvature K in the

following way:

$$\kappa_1 = H - \sqrt{H^2 - K} \quad (6.2)$$

$$\kappa_2 = H + \sqrt{H^2 - K}. \quad (6.3)$$

Thus, both the Gaussian and the mean curvatures can be expressed by the principal curvatures as well:

$$H = \frac{\kappa_1 + \kappa_2}{2} \quad (6.4)$$

$$K = \kappa_1 \cdot \kappa_2 \quad (6.5)$$

In addition we define now so-called ISD (interface shape distribution) plots, which are two-dimensional probability density functions in dependence on the two principal curvatures. An example of such an ISD-plot is shown in Fig. 6.5, and we can immediately identify four regions within the plot. As we will show later, most of the lungs interfaces belong to “Region 1”, i. e. the positive elliptic region, while others present saddle surfaces, and “Region 4” is the negative elliptic one. The whole processing pipeline is depicted in Fig. 6.6 and explained as follows:

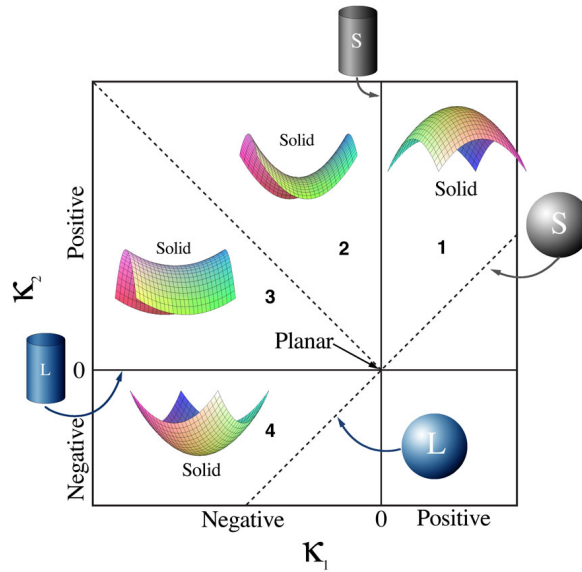


Figure 6.5. Interface shape distributions (ISD-plot) explanation, adapted with permission from J.L. Fife [205]. It represents a 2D probability density in dependence on the the minimum curvature κ_1 and the maximum one κ_2 for each vertex on the mesh.

- (1) Starting from the 3D segmented data the air-to-tissue surface mesh is first created with the so-called marching-cubes algorithm, implemented in VTK [219]. The produced triangulated mesh, depending on the original data size, has then about 30 millions of vertices.

- (2) High-frequency noise originating from discrete data is then removed by Laplacian smoothing [220], implemented in the open-source MEPP platform [221]. The noise occurs due to sharp borders of single pixels.
- (3) The principle curvatures are then calculated on the smoothed surface mesh from a curvature estimator algorithm based on normal cycles [222], also implemented in [221]. Here we only note that according to the theory of normal cycles one can define a radius of a vertex when calculating the principal curvatures. This aspect is used later on and explained in more detail.
- (4) Finally the data is further processed to create either 3D renderings according to the principal curvatures or calculate 2D probability densities, the so-called ISD plots. For the latter ones we apply the kernel density estimator introduced by Duong [223].

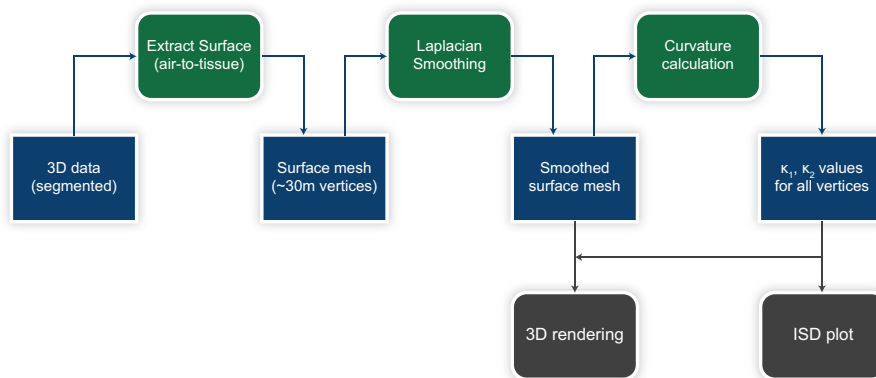


Figure 6.6. Processing flowchart for the curvature analysis. From the segmented volume the surface is first extracted [219], creating a surface mesh of about 30 million vertices. Subsequently Laplacian smoothing [220] is applied to reduce high-frequency noise, and curvature calculation is performed [222] to extract the two principal curvatures for all vertices. These are then used to create the ISD-plots and the 3D renderings.

6.4 RESULTS

6.4.1 Image formation

Two *ex vivo* animals were imaged with two different optics to evaluate the level to which biologically relevant features can be identified and extracted (segmented). In both cases the exposure times per projection were tuned to 5 ms with a total of 901 tomographic projections. The comparison between the $2.9\ \mu\text{m}$ -pixel-size and $1.1\ \mu\text{m}$ -pixel-size optics is plotted in Fig. 6.7 for a $0.8 \times 0.8\ \text{mm}^2$ field of view. As it can be seen in Fig. 6.7(a), with the lower-resolution optics the thin walls between the alveoli (septa) are still visible, but are completely

lost in the segmentation step [Fig. 6.7(b)]. With the high-resolution optics, the visibility of the septa is significantly enhanced and can be recovered in the binary segmented image [as shown in Fig. 6.7(d)] by applying our segmentation technique. However, small artifacts are introduced when conducting the “ridged” image step in the segmentation method (step C in Fig. 6.3), which is indicated with the red arrows in the segmented image.

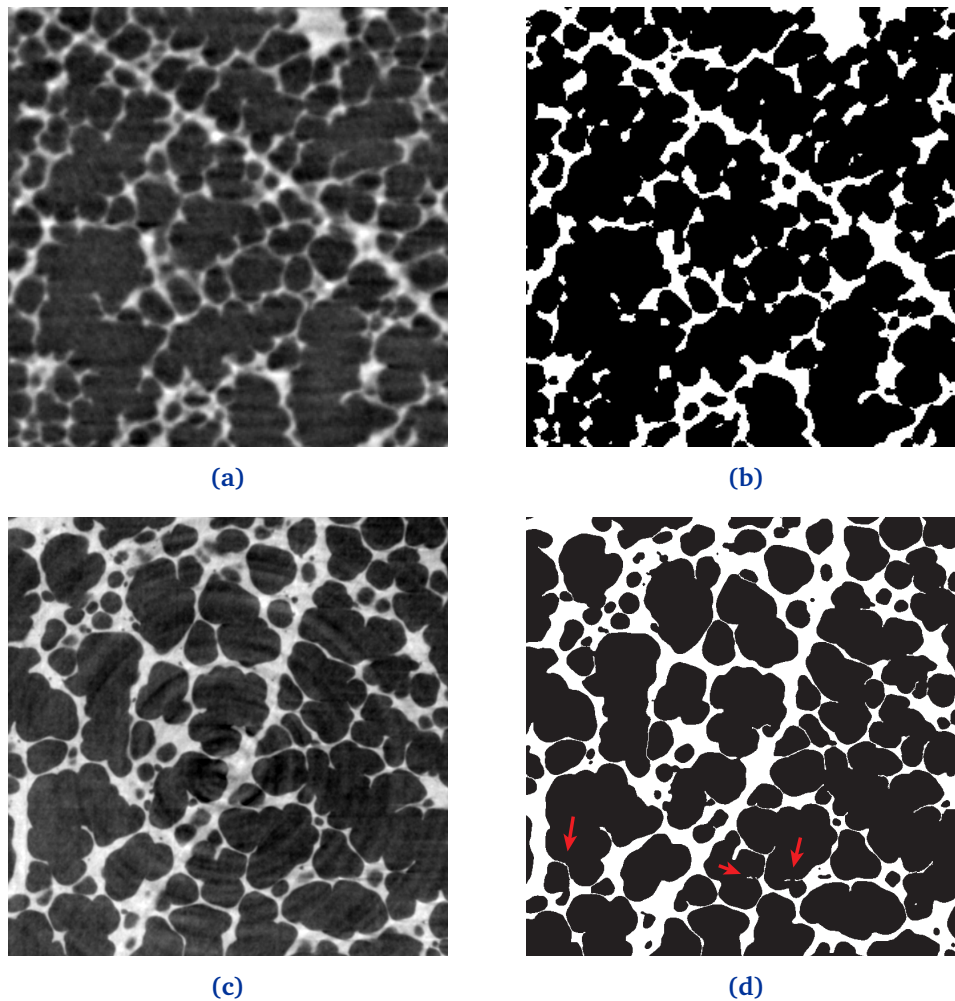


Figure 6.7. Comparison between the low-resolution and high-resolution optics for a 0.8×0.8 mm² field of view: (a) shows the tomographic slice of the $2.9 \mu\text{m}$ -pixel-size optics; (b) the corresponding binary segmented image with visible holes between single alveoli; (c) shows the tomographic slice of the $1.1 \mu\text{m}$ -pixel-size optics; and (d) shows its corresponding segmented image. The red arrows display artifacts introduced by the segmentation.

In both of the aforementioned quantitative analyses techniques the artifacts introduced by the segmentation technique play only a marginal role. On the one hand, for the thickness analysis, the complete missing of septa (i. e. if the segmentation technique from Sec. 6.3.3 is not applied) causes the air volume to appear larger, which corresponds to a particular uncertainty

in identifying single alveolar spaces. The additional introduction of single-pixel artifacts, however, causes only a negligible deviation of the computed local volumes. On the other hand, for the curvature analysis, the additional artifact-structures are easily removed after the curvatures have been calculated, as they represent very sharp surfaces. Alveolar walls, however, despite being thin are still connected with neighboring lung tissue and hence represent smooth surfaces with mostly homogeneous curvatures.

From these results we can already state that a curvature analysis has only limited validity on the wrongly segmented volume, as most of the relevant (septal) surfaces vanished. For this reason, the curvature analysis is only applied to the image data obtained with the high-resolution optics.

6.4.2 Thickness maps results

The results from the thickness map analysis, overlaid on the original data, are shown in 2D for small regions of interest in Fig. 6.8, where the colors are chosen according to structural diameters. As it can be seen, with increasing pressure, there is an increase of orange-to-yellow structures corresponding to structural diameters of approximately $70\ \mu\text{m}$ and a decrease of red structures, corresponding to structural diameter of about $40\ \mu\text{m}$.

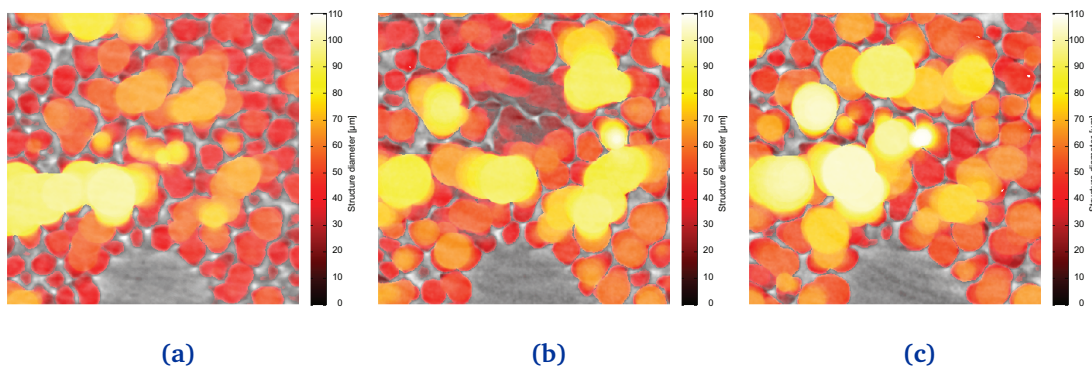


Figure 6.8. Structure diameters obtained by thickness map calculation for three different peak-inspiratory pressures: **(a)** $10\ \text{cmH}_2\text{O}$; **(b)** $20\ \text{cmH}_2\text{O}$; **(c)** $30\ \text{cmH}_2\text{O}$.

In Fig. 6.9 the probability density functions (PDF) of the thickness maps are plotted in dependence on the structure diameters for the two different optics. Again, we observe a shift from small diameters (around $40\ \mu\text{m}$) at a peak-inspiratory pressure of $10\ \text{cmH}_2\text{O}$ towards bigger diameters (around $70\ \mu\text{m}$) with increasing pressure. This trend is observable at both magnifications, and there appears to be no significant change in the calculated local thickness distributions. The plots have been limited to structural thicknesses of about $170\ \mu\text{m}$. This is due to the fact that big volumes can significantly alter the results when the lungs inflate as they move out of the region of interest, which is why they have been disregarded in the present representation. It should also be noted that the PDF for the higher magnification optics is more sensitive to small changes of local thicknesses, which is why the curve is more noisy

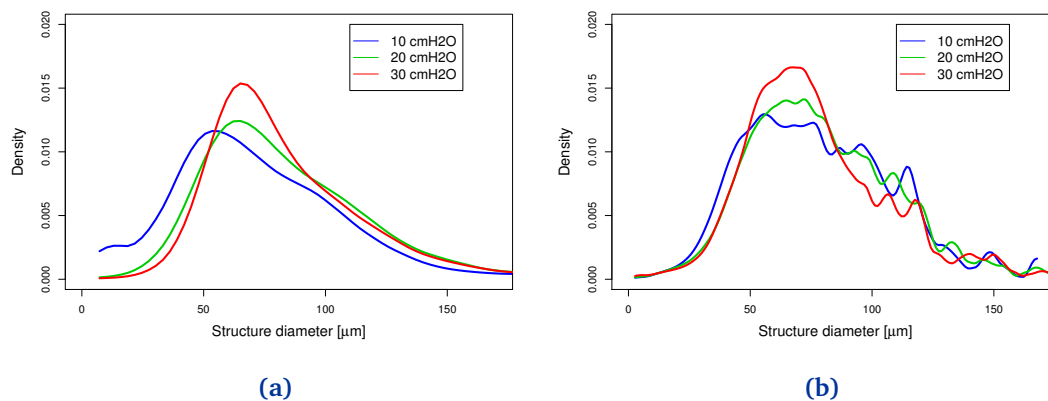


Figure 6.9. Probability density functions (PDF) of the local thicknesses for the two different optics: **(a)** shows the thickness-map PDF for the 2.9 μm -pixel-size optics; **(b)** shows the one for the 1.1 μm -pixel-size optics.

[Fig. 6.9(b)] than the one of the lower-magnifying optics in Fig. 6.9(a). Since the scale is in micrometer, the lower-resolution optics has a uncertainty of at least 3 μm due to its pixel size.

In Tab. 6.1, the volumetric distributions at four different scales (20 – 40 μm , 40 – 60 μm , 60 – 80 μm and 80-rest μm) are summarized, showing the same trends in a quantitative manner: with increasing peak-inspiratory pressure the volumetric increase happens at *Scale 3* with a simultaneous decrease of *Scale 1*.

Table 6.1. Volumetric distributions of the thicknesses at different scales and magnifications. The results are obtained by integrating the PDF-s from Fig. 6.9 according to the corresponding scales.

Pressure	Scale 1 (20 – 40 μm)	Scale 2 (40 – 60 μm)	Scale 3 (60 – 80 μm)	Scale 4 (80 – ... μm)
10 cmH ₂ O (2.9 μm)	8.6%	19.1%	17.0%	41.0%
20 cmH ₂ O (2.9 μm)	3.8%	16.1%	20.3%	50.2%
30 cmH ₂ O (2.9 μm)	2.2%	15.9%	24.8%	47.3%
10 cmH ₂ O (1.1 μm)	7.6%	21.7%	22.4%	43.4%
20 cmH ₂ O (1.1 μm)	5.4%	20.1%	25.5%	44.3%
30 cmH ₂ O (1.1 μm)	5.1%	22.2%	29.6%	38.0%

Finally, in Fig. 6.10 we show 3D representations of the thickness maps for the three different pressures and the two optics. In the low-resolution optics (bigger field-of view) the big airways have been excluded by being transparent (visible by the holes). The line through the center represents an interlobar septum, and it appears that the upper lobe increases more in volume than the lower one, following the color representation. This is noticeable through the

fact that the upper lobe adopts a more “reddish” color with higher inflation pressure. In both the high- and low-resolution cases, a slight heterogeneous pattern is visible.

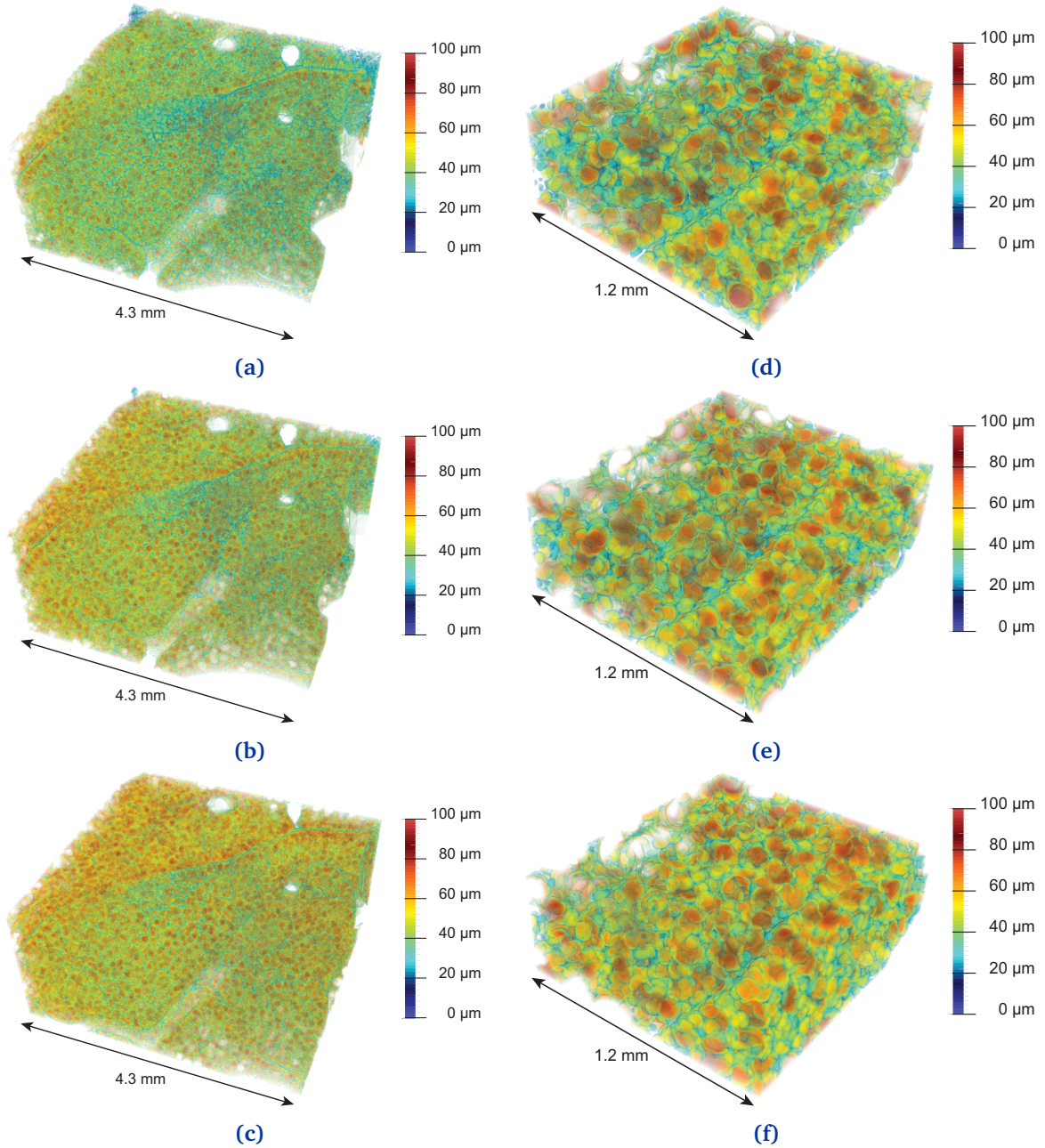


Figure 6.10. Visualization of the thickness maps in 3D: (a),(b) and (c) show the 10, 20 and 30 cmH₂O pressures for the 2.9 μm-pixel-size optics; (d),(e) and (f) show the ones for the 1.1 μm-pixel-size optics.

6.4.3 Curvature results

The interface shape distributions (ISD) for the three different pressures are plotted in Fig. 6.11, providing a map of the internal shape of the air-to-tissue surface in the lung. The plots can be thought as follows: According to the ISD definition in Fig. 6.6 the color representation corresponds to the probability of finding a certain surface shape within the lung. As expected, the highest density lies in “Region 1” and indicates that lungs are largely elliptically shaped. This complies very well to the ideal shape of alveoli, which can be thought of as small spherical (or rather elliptical) “sacs”. When increasing the pressure, at first we observe a transformation from a diverse to a more uniform distribution of curvatures on the surface [from Fig. 6.11(a) to Fig. 6.11(b)]. This is visible with the emergence of the bright (red) peak, but after increasing the pressure to 30 cmH₂O [Fig. 6.11(c)] this trend seems to invert again. In fact, the distribution slightly spreads into “Region 2” and “Region 3” (visible by the magenta blue tail going towards the left side). In total, however, the highest-density peak moves towards smaller principal curvatures (as indicated by the arrow). This is slightly visible by the move of the upper “blue-violet tail” towards the center.

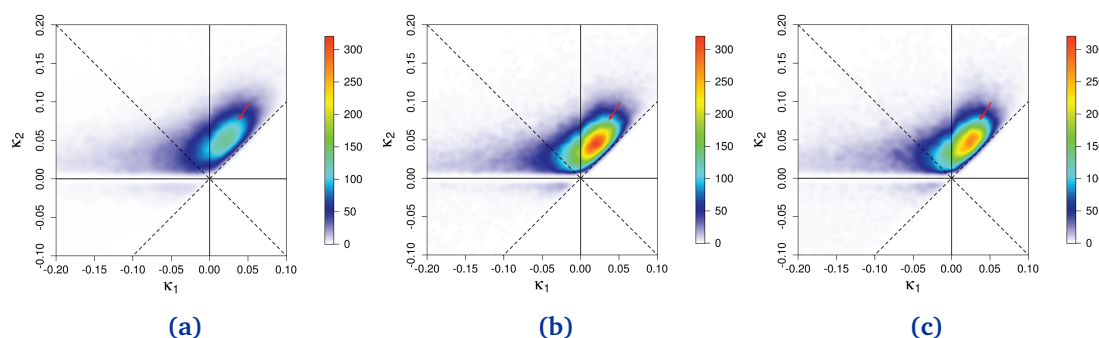


Figure 6.11. Interface shape distributions for the free different pressures: (a) 10 cmH₂O; (b) 20 cmH₂O; (c) 30 cmH₂O.

To better clarify these results, we plot both the Gaussian and the mean curvatures for the different pressures in Fig. 6.12. The Gaussian curvature is best illustrated by a flat surface such as an expanding disk that grows isotropically [217]: if the expansion is uniform (i. e. the overall shape remains the same) it will have zero Gaussian curvature; if the marginal regions grow slower than the central ones, the disk will exhibit a parabolic shape and the Gaussian curvature will be positive; and if the central region grows slower than the marginal ones, the disk will buckle and form a shape with a wavy edge (e. g. a saddle surface), rendering a negative Gaussian curvature. In our case, we observe an increase around zero, indicating that the existing surfaces within the lung *only* become more flat, as can be seen in Fig. 6.12(a). The mean curvature on the other hand indicates the aforementioned trend towards smaller principle curvatures in “Region 1”, however develops a peak at 0 with increasing pressure.

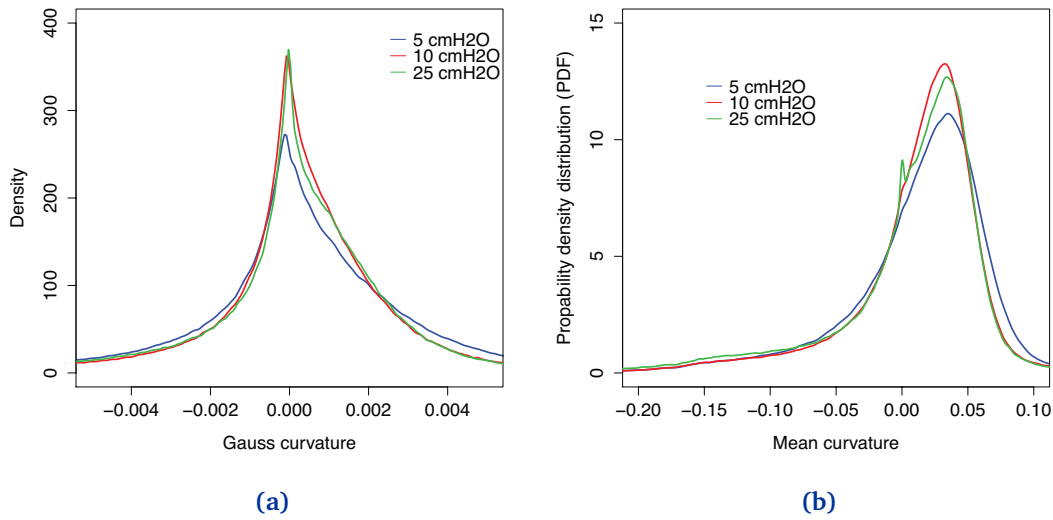


Figure 6.12. Probability density functions (PDF) of Gaussian **(a)** and mean **(b)** curvatures.

6.5 DISCUSSION

From the results of the thickness maps we identify structural diameters of 60–80 μm to increase in density when increasing the peak-inspiratory pressure in the lung. The results are comparable at both scales, meaning for both the low-resolution and the high-resolution optics and might indicate that the existing structures (20 – 40 μm) increase their volume, which is why they vanish with higher peak-inspiratory pressures. On the 3D scale, it appears that one lung lobe, when inflated to 30 cmH₂O has a higher mean local thickness than the other [visible for instance in the upper part in Fig. 6.10(c)]. Thus, a certain inter-lobar heterogeneity is visible, giving rise to the hypothesis that the inflation follows a distension pattern. This is supported by the effect that no “new” structures are visible at higher pressures and in general the probability density function of the thicknesses obeys the same distribution.

The findings from the curvature analysis are complementary, but do not follow this interpretation completely. Namely, on the one hand we found that lungs are mostly described by elliptical shapes ($\kappa_1, \kappa_2 > 0$), which poses the question whether it is possible to identify alveolar surfaces by a pure curvature analysis, which we discuss below. On the other hand, with increasing pressure it is clearly visible that the elliptical surfaces grow in diameter, which is best seen by looking at the positive mean curvature values in Fig. 6.12(b). Despite the small difference between 20 and 30 cmH₂O, all PDF-s follow the same trend in this region. However, there is a rising peak at mean curvature zero, which is not obvious from other observations.

The Gaussian curvature clearly suggests that all surfaces are becoming more flat towards higher pressures, which would not be the case if new alveoli were recruited. In terms of lung anatomy, Gaussian curvature can also be interpreted as follows: in the case of a broad distri-

bution we have saddle-surfaces (free septal edges), sharp edges (alveolar mouths), spherical shapes and so on. If the distribution becomes sharper around zero it means that there is a trend in all these surfaces towards a more flat shape, which obviously can only be the case for alveoli.

We also addressed the question whether a curvature analysis is enough to uniquely identify alveolar surfaces within the lung. For this, the four regions of the ISD-plot (Fig. 6.5) are visualized in 3D in Fig. 6.13(a). As it can be seen, the red surfaces (corresponding to “Region 1”)

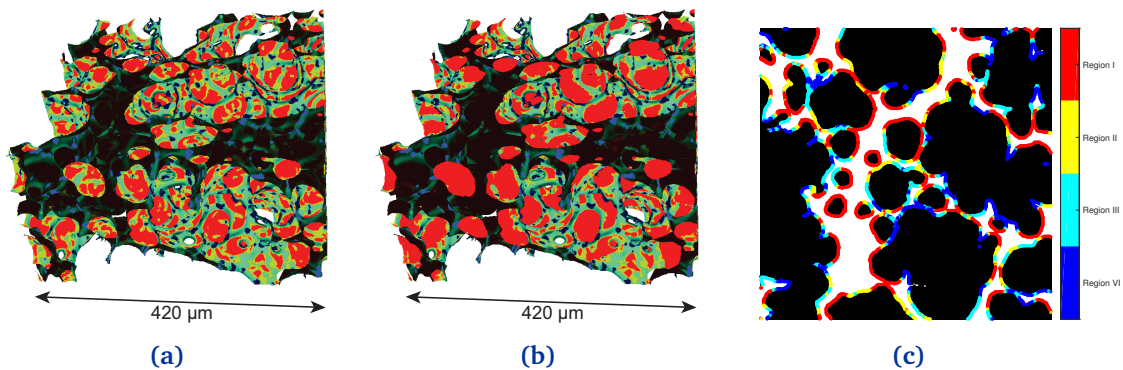


Figure 6.13. 3D visualization of the four regions from the ISD-plot with different geodesic radius: (a) depicts the calculation with radius $R = 3.5$ and (b) with $R = 15$. In (c) a 2D slice is shown from (b).

are indeed shown to lie on alveolar surfaces, however there are small surface areas that have different shape (non-elliptical) in between. This corresponds, in fact, to previous findings in lung anatomy indicating that alveoli hardly have a pure spherical/elliptical shape [15]. However, we can make use of a simple assumption by applying the normal cycle algorithm for calculating curvatures. Namely, if we set a big geodesic radius at each surface vertex small areas lying in the middle of the alveoli which do not have a strict spherical surface will be interpreted as spherical due to their surroundings. This fact is illustrated in Fig. 6.14: first (on the left) side the curvatures are mimicked to be calculated with small geodesic radii; then, once the geodesic radius increases, small deviations in the alveolar surface area are still recognized as being part of an alveolus. The result is plotted in Fig. 6.13(b) and in Fig. 6.13(c) the 2D slice is shown.

Finally we shortly discuss the very small difference between 20 cmH₂O and 30 cmH₂O. The change in the ISD plot in Fig. 6.11(c) suggests that despite the higher pressure a significant amount of elliptical surfaces is reduced. This could be interpreted as a possible over-stretching of lung tissue, previously only obtained through simulations [224] and could be explained as follows: at physiological lung pressures the lung maintains an elastic distension pattern; however, if the pressure is increased significantly the overstretching could cause significant deviations to the ideal shape of the alveoli. We close the discussion by showing such an example obtained with a different dataset, depicted in Fig. 6.15.

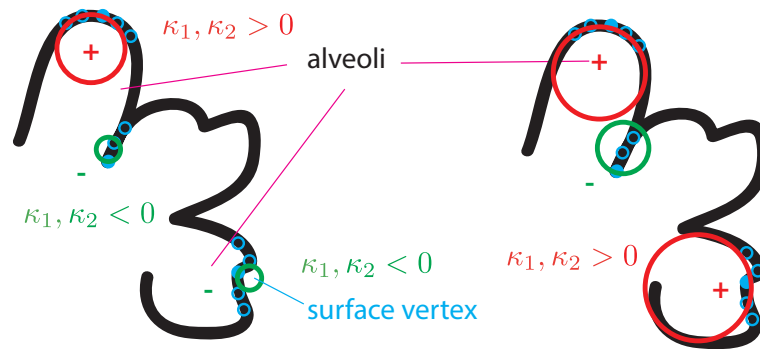


Figure 6.14. Sketch for depicting how small areas within the alveoli can be “forced” to be recognized as alveolar area, despite having a different shape. On the left side, the red circle (corresponding to the geodesic radius) identifies an elliptical shape, while the green one identifies a negative elliptical shape. If the geodesic radius is increased the vertex area in the lower left alveoli will be recognized as belonging to the alveolar surface.

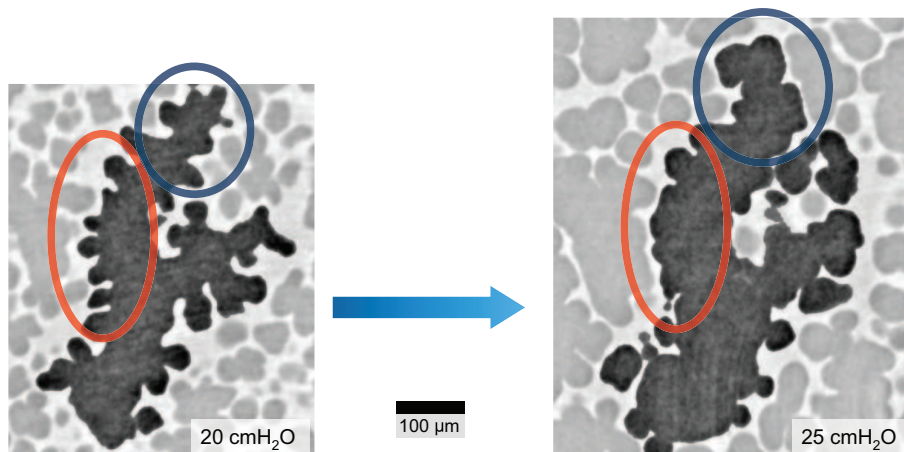


Figure 6.15. Significant alteration in alveolar surface shape when increasing the pressure from 20 cmH₂O to 25H₂O, possibly meaning a tissue overstretching.

6.6 CONCLUSION

We have presented a technique for the fast acquisition of 3D lung image data from intact *ex vivo* animals, followed by a detailed post-processing scheme ranging from segmentation to quantitative analysis. In doing so we applied two established quantitative measures to characterize fresh lung tissue at high resolutions and in 3D, in particular the thickness map and curvature analysis, which to the best of our knowledge represents the first evaluation of lung data of this kind. Hence, our post-processing and evaluation technique can serve as a complete toolbox for characterizing and analyzing lung data at that scale. Applied to the lung samples, we found first indications for a heterogeneous intra-lobar and inter-lobar distension

pattern, although still only observed *ex vivo*. Our results with fresh intact *ex vivo* animals indicate that no new alveoli are recruited upon lung inflation, but certain evidence of tissue over-extension is found. Finally, we showed first indicative results showing that the curvature analysis might serve as a tool for automatically identifying alveolar surfaces in high-resolution 3D lung image data. Finally, since our tools are completely based on open-source algorithms, they can easily be expanded and applied to other materials and studies.

6.7 ACKNOWLEDGEMENTS

We would like to acknowledge F. Arcadu, D. Pelt, S.F. Barre and G. Mikuljan for their help at the experiment, M. Kagias, K. Mader and J. Fife for fruitful discussions. This study was supported by the National Competence Center in Biomedical Imaging (NCCBI), grant No. 1126.0076, and the Swiss National Science Foundation (SNF), grant No. CR23I2-135550 with partial contribution from grant No. 153468.

Tomographic *in vivo* study of lung physiology at the micrometer scale

The following chapter represents a manuscript currently in preparation for publication by following authors: G. Lovric, F. Arcadu, I. Vogiatzis Oikonomidis, J.C. Schittny, M. Roth-Kleiner, R. Mokso, and M. Stampanoni.

7.1 ABSTRACT

Recent advances in synchrotron-based X-ray imaging techniques proved to reach micrometer resolutions and thus opened completely new insights into micrometer-scale biology. However, combining high spatial with temporal resolution, especially considering radiation dose, still remains a challenging task. Moreover, currently established methods in 3D lung imaging have been unsuccessful in answering still open questions in lung physiology. We demonstrate for the first time *in vivo* tomographic imaging of lungs with pixel sizes down to a micrometer and show first insights into high-resolution lung physiology. We identify temporal resolution as the main current limitation towards μm -resolution *in vivo* tomography, observe strong differences in lung tissue thicknesses between *in vivo* and *ex vivo* lung tissue and find for the first time direct evidence supporting a heterogeneous distension pattern at the level of alveoli, rather than the often-hypothesized alveolar recruitment.

7.2 INTRODUCTION

For various *in vivo* studies third-generation synchrotrons have proved to be valuable instruments, providing high sensitivity to soft tissue by highly coherent X-rays combined with sufficient flux. Ever since, *in vivo* techniques have covered a wide range of studies, such as bone microarchitecture [36, 225], microvasculature [226, 227], brain tumors [228], and in the recent past the area of respiratory physiology in insects and vertebrates [167, 172, 229–231]. More recently, several remarkable techniques have paved the road towards micrometer-scale

in vivo imaging: Moosmann et al. [195] utilized X-ray phase-contrast microtomography to examine the course of embryonic development in *Xenopus laevis*; dos Santos Rolo et al. [232] developed X-ray cine-tomography to study millimeter-sized samples such as fast-moving weevils; and finally 4D *in vivo* X-ray microscopy with projection-guided gating was introduced for revealing the mechanics of the blowfly flight motor at 150 Hz [233, 234]. However, within the scope of lung dynamics studies in mammals, no significant progress has been reported up to date and two hypotheses on the structural alterations in the gas-exchange area during breathing are still under debate: (i) a heterogeneous distention pattern [163] of different lung areas or (ii) a homogeneous cyclic opening-and-collapse [164] of all alveoli.

Most *in vivo* imaging studies on lungs are nowadays routinely performed in micro-CTs with anaesthetized free-breathing or mechanically ventilated small animal models, where commonly a prospective [235] or a retrospective [236] respiratory gating technique is applied. Despite recent improvements in dose efficiency, where pixel sizes in the order of $100 \times 100 \mu\text{m}^2$ and at dose rates in the range of 250 mGy to approximately 2 Gy (for full 4D-datasets) were reported [237], the techniques remain unsuitable for resolving single alveoli.

At synchrotrons, K-edge subtraction (KES) imaging was suggested by Bayat et al. [166] and subsequently applied to measure absolute regional lung volumes [238], bronchial kinetics [239] and airway function [172]. The pixel sizes reached down to about $50 \times 50 \mu\text{m}^2$, while the total dose amounted up to 10 Gy [200]. With the advent of single-shot phase retrieval methods Lewis et al. [167] utilized propagation-based phase-contrast imaging to dynamically identify and locate airway liquid in newborn rabbit pups. Subsequently, quantitative functional and anatomical imaging of lung ventilation was realized at even smaller pixel sizes (about $20 \times 20 \mu\text{m}^2$) and lower dose rates [240, 241], which became possible after recognizing that lungs produce a speckle pattern that can be exploited to significantly increase feature visibility [169]. Later on, the techniques were expanded to 3D by making use of particle image velocimetry (PIV) [174, 175]. Alternatively, the Fourier space signature of the speckle pattern was found to provide certain evidence of alveolar recruitment [242, 243] which, however, was neither verified nor falsified so far due to the lack of direct imaging methods. In parallel, Sera et al. [244] conducted high-resolution 4D lung imaging with intact (freshly sacrificed) mice at $11.8 \times 11.8 \mu\text{m}^2$ pixel sizes and under quasi-static inflation, being able to quantify diameters and lengths of smaller airways. In a later work they proposed a combined ECG and airway pressure synchronization that would enable 4D lung imaging with pixel sizes down to $12 \times 12 \mu\text{m}^2$ [184], but they concluded that the technique was unable to image alveolar kinematics [245]. The latest *in vivo* approach in the form of tracking X-ray microscopy was suggested by Chang et al. [210], who tracked sizes of single alveoli during inspiration and expiration, however being limited to single alveolar ducts or regions of interest located close to an edge of the lung. Thus, all aforementioned *in vivo* techniques so far were unsuitable for providing isotropic alveolar resolution in 3D, and the initially posed biological questions about how lungs inflate and deflate at a microscopic level still remain unanswered [16].

In the underlying paper we address these questions by introducing prospective heartbeat-gated synchrotron-based micro-CT where we adapt our previously suggested dose-optimized setup [162] to the *in vivo* case and employ a consistent triggering technique, coupled with the

subsequent CT-reconstruction. We present the first realization of *in vivo* lung tomography at pixel sizes down to $1.1 \times 1.1 \mu\text{m}^2$ and describe ventilation patterns at different lung pressures. Furthermore, we show the current limitations, discuss strategies for further improvements and for the first time show a direct comparison between *in vivo* and *ex vivo* lung tissue at the micrometer scale.

7.3 MATERIALS AND METHODS

7.3.1 Animal preparation

We used 9-days old newborn rats ($n = 3$, Wistar Bern, central animal facility of the University of Bern) for the experiments, whereas the detailed procedure in terms of animal preparation and anesthesia is described in detail in Sec. 4.4.5. The same protocol was applied to all animals and is summarized with the following three points:

- (1) **Intubation:** First, the animal is anesthetized with an injection of a mixture of xylazine and ketamine, which takes about 10 min to put the animal into deep sleep, while still free-breathing. Subsequently the animal is intubated by performing a tracheotomy and placed into the sample-holder. The endotracheal canula is mounted and fixed on the sample-holder [as shown in Fig. 7.2(b)] to remain rigid during the following tomographic image acquisition (sample rotation).
- (2) ***In vivo* imaging:** The animal (together with the sample-holder) is then transferred to the beamline hutch, mounted on the sample manipulator stage and externally ventilated with a small animal's breathing device (FlexiVent, SCIREQ Inc.) with an O_2 /air-isoflurane mixture of about 2 – 3%. By doing so, a ventilation protocol summarized in Tab. 4.6 in Sec. 4.4.3 is applied which was previously adjusted to yield positive blood gas values (in terms of CO_2 levels) while using a minimally invasive ventilation pattern. The body temperature is kept constant with a heating lamp and monitored rectally prior to starting the image acquisition. At the same time the three paws of the animal are connected to the ECG-device with small pins, and the ECG-electrodes are mounted so that they don't interfere with the X-ray beam. Both the cardiac activity and the animal's ventilation are monitored via a portable notebook. The desired region of interest (ROI) is aligned visually with a pre-aligned laser pointer that is placed in a way that it points to the center of the ROI of the X-ray projection image. The controls PC is then moved outside the beamline hutch, after which the first scan can be started.
- (3) **Postmortem imaging:** After the *in vivo* image acquisition is finished, the animal is administered an overdose of pentobarbital, while still being constantly ventilated and monitored in its ECG-activity. Following the injection, it takes about 20 – 30 min before the ECG-signal is completely gone, after which the first *ex vivo* images are then acquired.

With the described protocol it took about 30 – 40 minutes from the first injection anesthesia to the first acquired images and the whole imaging experiment required approximately

two hours per animal. As described in the following, the tomographic image acquisition was directly triggered by inducing a breath-hold with a particular pressure in the ventilated animal. After each breath-hold phase the animals were normally ventilated for about 10 min in order to recover from the long breath-hold.

7.3.2 Image acquisition and reconstruction

The experimental setup has been based on our previously developed protocol (Chapter 5 and Reference 162, respectively). The experiment was carried out at the X02DA TOMCAT beamline of the Swiss Light Source (SLS) at the Paul Scherrer Institute (Villigen, Switzerland), for which the setup is schematically depicted in Fig. 7.1: the X-ray beam, produced by a 2.9 T bending magnet on a 2.4 GeV storage ring (with ring current $I = 400$ mA, top-up mode), is monochromatized with a double-multilayer monochromator and tuned to 21 keV. A sample-to-source distance of 25 m is used for producing an X-ray beam with appropriate spatial coherence properties. We used a high-speed CMOS detector (PCO.Dimax) coupled to visible-light optics with a 150 μm and a 20 μm thick scintillator for medium and high spatial resolutions, respectively. The samples were probed with two different optics, yielding effective pixel sizes of $2.9 \times 2.9 \mu\text{m}^2$ and $1.1 \times 1.1 \mu\text{m}^2$, respectively. For these two optics the field of view was adjusted with horizontal and vertical slits, located just before the sample, and producing beam sizes of $5.8 \times 2.7 \text{ mm}^2$ and $2.2 \times 2.2 \text{ mm}^2$, respectively. The sample to detector distance z was set to 100 mm, yielding an optimal trade-off between contrast-to-noise ratio and resolution at the respective experimental settings [162].

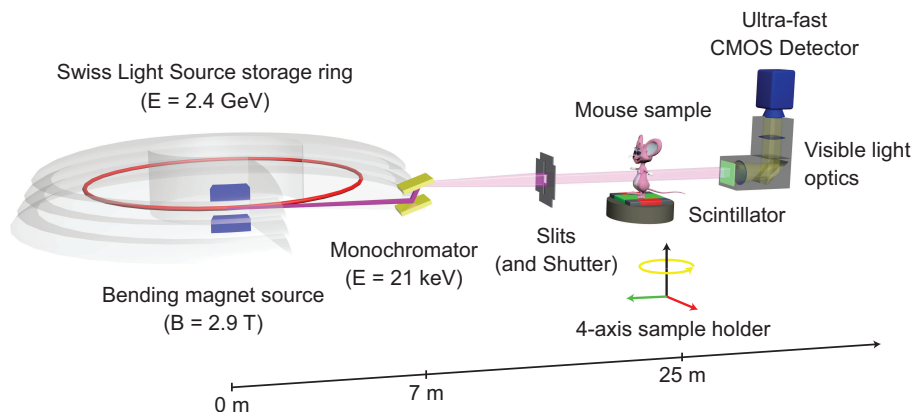


Figure 7.1. Experimental setup at the TOMCAT beamline

Unlike the *ex vivo* case, where the image acquisition is started immediately after inducing a breath-hold in the imaged animal and finished within a few seconds (see Sec. 6), the image acquisition protocol needed to be refined when dealing with *in vivo* samples. Namely, we found that the animal's heartbeat typically induces pressure oscillations in the lung (coupled with small displacements of the whole surrounding tissue) that make a CT reconstruction impossible. To overcome this problem we developed a so-called *prospective heartbeat-triggered*

gating technique with the aim to image the animal's lung at different lung pressures but at identical heartbeat phases. This means that each projection image had to be triggered by a heartbeat with an accurately adjusted delay.

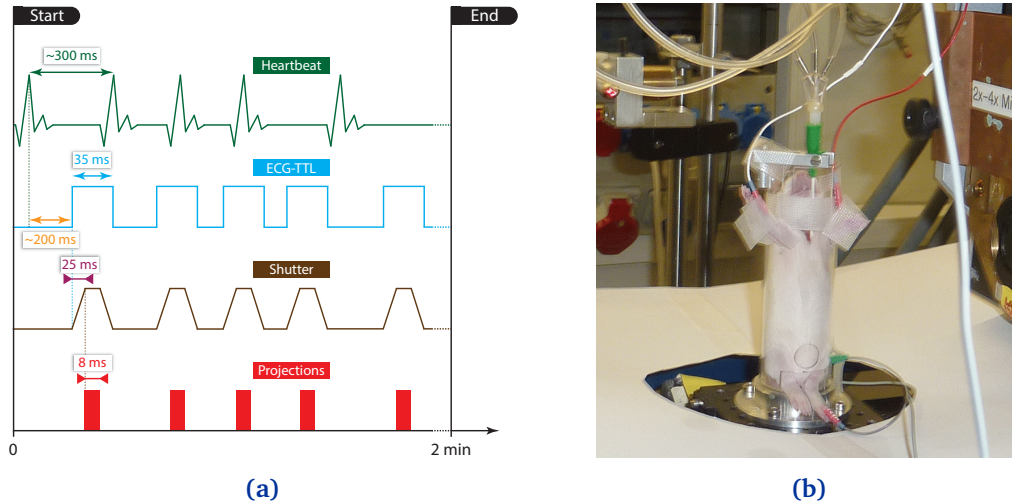


Figure 7.2. Schematic view of the image acquisition process: (a) shows the triggering scheme of the image acquisition and (b) shows the animal as it is mounted in the sample holder during the experiment.

The novel image acquisition protocol is schematically described in Fig. 7.2(a) and explained as follows:

- (1) After the animal is placed onto the rotation stage, following the animal preparation procedure [as described above in Sec. 7.3.1 and shown in Fig. 7.2(b)], the ECG-signal is continuously monitored. From the ECG device (SA Instruments, Inc.) a particular delay is set (e. g. 200 ms) after which the ECG device fires TTL-signals of a certain duration (e. g. 35 ms) after every heartbeat.
- (2) The TTL-signals directly trigger the X-ray shutter opening (and closing), which delays by 25 ms due to its internal mechanics.
- (3) In parallel, every TTL-signal from the ECG also triggers the camera exposure. The camera, however, after receiving the TTL-signal acquires an image only after a pre-defined delay which is adjusted corresponding to the shutter opening delay (25 ms, as stated above).
- (4) Shortly before starting the scan, the total scan time t_{scan} is calculated in dependency on the actual heartbeat rate and the desired number of projections:

$$t_{\text{scan}} [\text{s}] = \frac{60 \times n_{\text{proj}}}{f_{\text{HB}} [\text{BPM}]}, \quad (7.1)$$

where n_{proj} is the number of projection and f_{HB} is the heartbeat frequency given in “beats per minute”. Afterwards, the rotation speed is adjusted in accordance to the total scan time.

- (5) All the described triggering connections become effective and the actual image acquisition is started when a breath-hold phase is induced in the animal’s lung, after which the rotation axis begins to rotate slowly. During the subsequent constant 180° -rotation a tomographic image is then acquired each time the ECG detects a heartbeat.

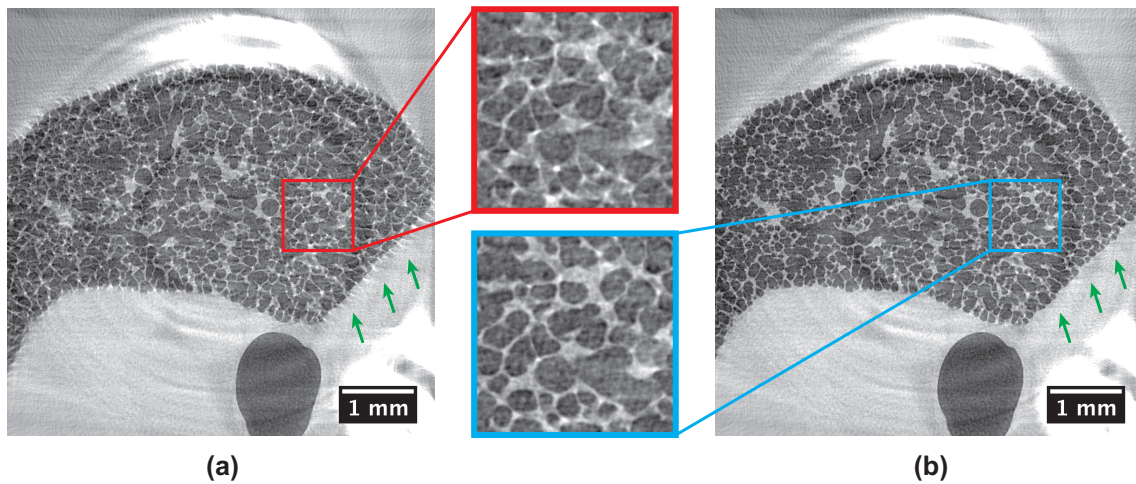


Figure 7.3. Comparison of a CT-reconstructed tomographic slice of an *in vivo* lung scan with assumed equiangular sampling (a) and explicit tomographic angle reconstruction (b). The latter is obtained from the recorded ECG signal, as discussed in Sec. 4.4.4. The number of projections was 461 at a pixel size of $2.9 \times 2.9 \mu\text{m}^2$.

With these settings the total scan time is in the range of 90 – 140 s with a total number of 400 – 450 projections, while the single-exposure times for each projection were set to 3 ms for the $2.9 \mu\text{m}$ -pixel-size and to 5 ms for the $1.1 \mu\text{m}$ -pixel-size optics, respectively. The associated entrance doses were 334 mGy and 557 mGy for the 3 ms and 5 ms exposure times, respectively. Since during the breath-hold phases the animals usually exhibit very irregular heartbeats, the detector is caused to acquire images also very irregularly. As a consequence, the tomographic projections are not sampled in an equiangular way, which in the case of standard tomographic reconstructions would produce significant artifacts. This problem can be overcome, however, if the explicit angle of every tomographic projection is saved and utilized in the CT-reconstruction step (e. g. during back projection). For this reason, we recorded all signals with a laboratory oscilloscope by which, following a simple post-processing procedure (described in detail in Sec. 4.4.4), every tomographic projection image was later assigned its explicit tomographic angle. After doing so, the tomographic projections are then phase-retrieved [65] and reconstructed with the gridrec algorithm by using the calculated angles [71]. The result can be seen in Fig. 7.3, where a comparison between a tomographic reconstruction *with* and *without* explicit recording of tomographic angles is shown.

7.4 RESULTS

In the following we present all results affiliated with our proposed prospective heartbeat-triggered gating technique. In the second part we present the biological findings that were made possible by high-resolution *in vivo* imaging.

7.4.1 Influence of heart-induced motion

As previously discussed, the heartbeat has a huge influence on the lung motion that becomes effective when imaging lungs at high resolution. This effect is best visible in Fig. 7.4 where a tomographic slice of a rat's lung is shown during a breath-hold phase, but under arbitrary motion of the heart. For this reason we employed a heartbeat-triggered gating technique to image the lung at identical phases of the heartbeat. However, this approach like any other gating technique relies heavily on the assumption that the movement is repeatable (“periodic”) and linear (with reproducible amplitudes), which we found not always to be the case in lungs.

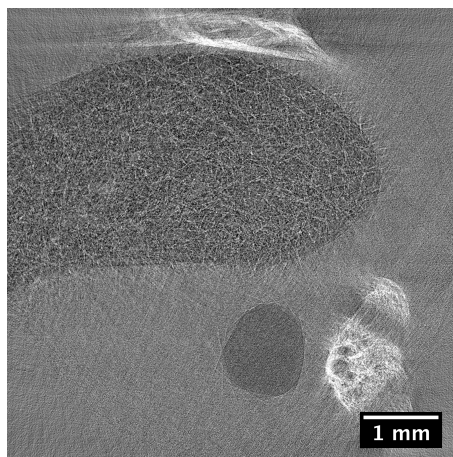


Figure 7.4. Tomographic slice of a rat's lung at a pixel size of $2.9 \times 2.9 \mu\text{m}^2$ and during a breath-hold phase without heartbeat-triggered gating. The heartbeat-induced motion artifacts in the lung are clearly visible.

In particular, we found that acquiring tomographic images of the lung immediately after the ECG impulse admittedly improves the quality of the lung images (compared to Fig. 7.4), but still introduces a significant amount of motion artifacts. This can be explained by closely looking at the QRS complex, i. e. the actual signal curve captured by the ECG device. Therein, the TTL-signal is triggered by a so-called R wave, which physiologically is followed by strong motion of the cardiac muscle (i. e. aortic valve opening). We therefore identified the phase shortly before the QRS complex to be as close as possible to a stationary phase of the heart, which is why we aimed to image the lung during this short period of time. This was achieved by setting a delay time in the ECG device between the R wave (i. e. the time when the ECG

device registers the heartbeat) and the actual TTL-impulse coming from the ECG device that triggers the imaging acquisition [i. e. the shutter opening etc. as shown in Fig. 7.2(a)]. Additionally, a so-called blanking time was set in order to ignore spontaneous heart beats that would occur earlier than the delay time. In Fig. 7.5 tomographic slices for three different delay times between 100 ms and 200 ms are shown. It is slightly visible that a delay time of 200 ms [in Fig. 7.5(a)] leads to a more blurry image than the other two.

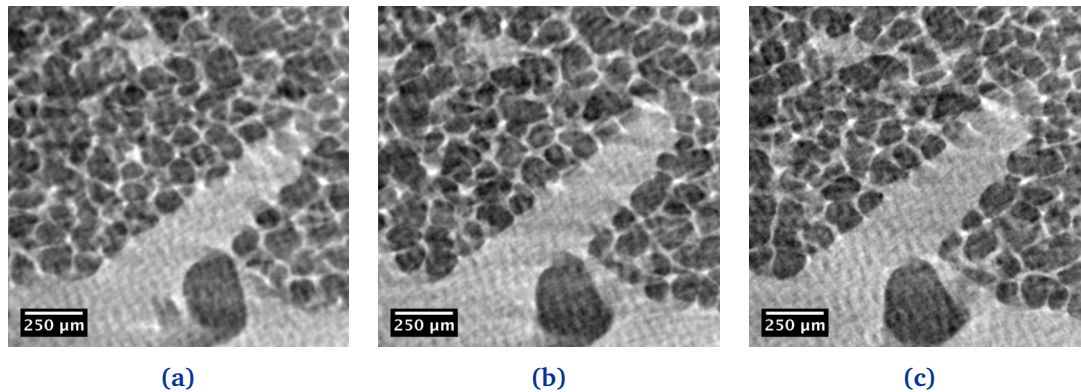


Figure 7.5. Various ECG-trigger delays for the $1.1\ \mu\text{m}$ -pixel-size-optic: **(a)** 200 ms; **(b)** 150 ms; **(c)** 100 ms.

To fully evaluate the performance of the proposed imaging technique we compared tomographic slices of each of the two different optics during an *in vivo* and an *ex vivo* tomographic acquisition. As mentioned in the previous section, this was achieved by administering an overdose of pentobarbital to the animal at the end of the *in vivo* scans and by acquiring images under the *ex vivo* condition thereafter. The comparisons are shown in Fig. 7.6 for the $2.9\ \mu\text{m}$ -pixel-size optics and in Fig. 7.7 for the $1.1\ \mu\text{m}$ -pixel-size optics. As it can be seen, for the $2.9\ \mu\text{m}$ -pixel-size optics the obtained image quality for both the *in vivo* and *ex vivo* samples yielded comparable results, meaning that the triggering technique is capable of producing motionless projection images and hence CT-reconstructions. For the $1.1\ \mu\text{m}$ -pixel-size optics, however, the difference was quite significant, namely in the sense that the *in vivo* samples showed increased blurring artifacts that can be associated with motions being present in the lung tissue.

In Figs. 7.6 and 7.7 the arrows indicate regions that can almost be matched completely with each other, while the red arrows (and green dots in Fig. 7.7) also show areas where the lung tissue thicknesses exhibit significant differences between the *in vivo* and the *ex vivo* case. In the images the red arrows point at different thicknesses of a (bigger) blood vessel and the green dots indicate different thicknesses in septa and connective lung tissue. Additionally, in nearly all cases when comparing the *in vivo* to the *ex vivo* data we observed a shrinking of the lung tissue, meaning that features that were observed *in vivo* appeared smaller during the subsequent *ex vivo* scans. This can be seen e. g. in Fig. 7.6 where the big airways appear to have bigger diameters in the *in vivo* case [Fig. 7.6(a)] despite setting a higher pressure in the postmortem scans [$35\ \text{cmH}_2\text{O}$ in Fig. 7.6(b)]. We discuss the biological relevance of this

effect later on, but note at this point that the main reason for this can be explained by the stiffer tissue in the *ex vivo* animal (i. e. emerging postmortem rigidity), where even a higher pressure is not able to inflate the lung as in the *in vivo* case.

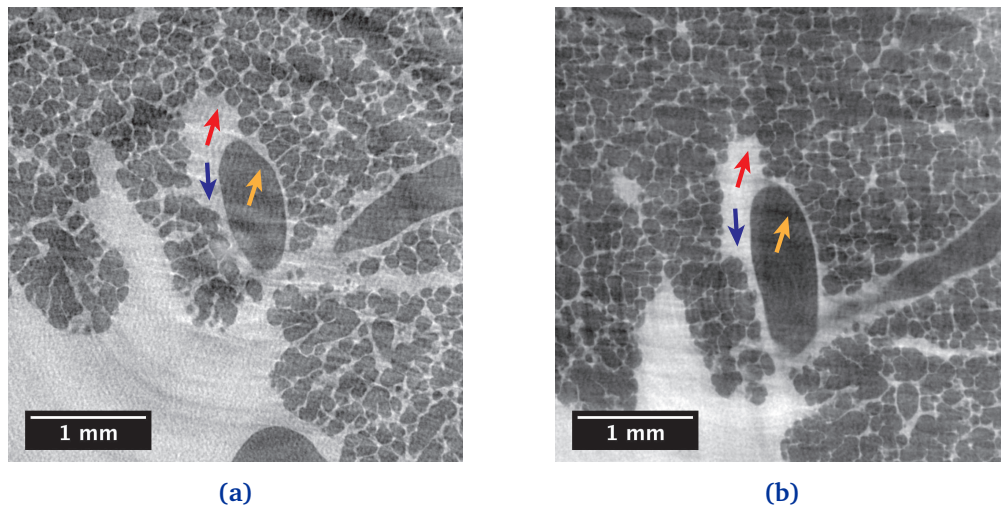


Figure 7.6. Comparison of tomographic slices acquired (a) *in vivo* at 15 cmH₂O peak-inspiratory pressure and (b) *ex vivo* at 35 cmH₂O for the 2.9 μm-pixel-size optics. The arrows indicate regions that can be matched unambiguously. The red arrows indicate the strong differences in lung tissue thickness between the *in vivo* and the *ex vivo* case.

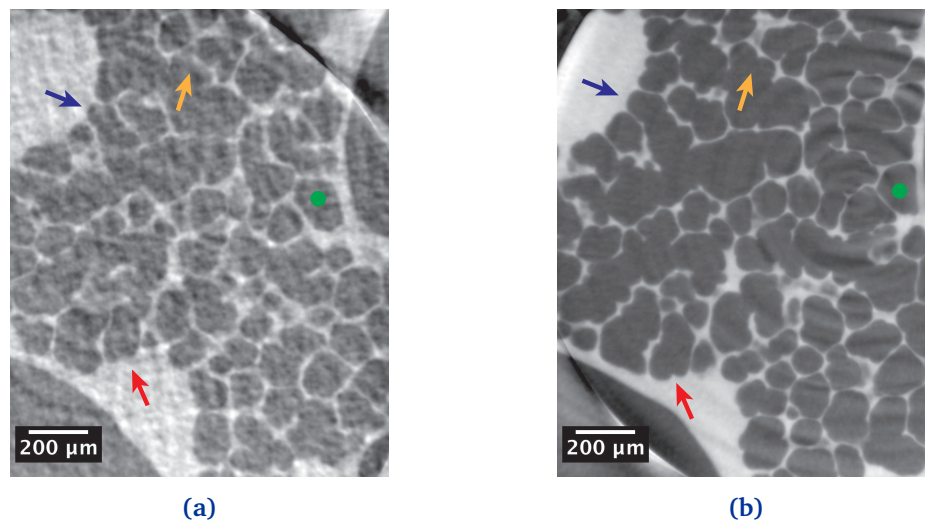


Figure 7.7. Comparison of (a) *in vivo* and (b) *ex vivo* tomographic slices for the 1.1 μm-pixel-size optics at 15 cmH₂O peak-inspiratory pressure. The arrows indicate regions that can be matched unambiguously, while the green circle shows the strong difference in septal thickness between the *in vivo* and the *ex vivo* case. Again, the red arrows additionally indicate the significant differences in lung tissue thickness.

7.4.2 Ventilation patterns at different pressures

The above results on the image quality evaluation yielded two consequences for our further analysis. On the one hand, the obtained images were not eligible for a(n) (semi-)automatic segmentation of the lung tissue. For the $2.9\ \mu\text{m}$ -pixel-size optics the *in vivo* and the *ex vivo* lung images showed comparable results, but we know from before that the segmentation results at this resolution are only partially correct (see Chapter 6). The $1.1\ \mu\text{m}$ -pixel-size optics in theory provides enough resolution to resolve both alveoli and septa, but due to motion artifacts in the *in vivo* case, the spatial resolution from the *ex vivo* scans could not be achieved. On the other hand, for both optics the lung structure (alveoli and septa) was sufficiently well resolved for a qualitative evaluation, which is why we chose a visual inspection approach of the high-resolution *in vivo* lung data to investigate the structural ventilation patterns.

As a first step, we analyzed whole tomographic slices, as shown for the $2.9\ \mu\text{m}$ -pixel-size optics in Fig. 7.8. As already outlined in detail in Chapter 6 for the *ex vivo* case, by closely looking at the images, an inter-lobar heterogeneous distension pattern is visible, where e. g. a strongly inflating area is indicated by the orange line, while other regions of the lung exhibited a slight intra-lobar stretch heterogeneity. Like before, the green arrows indicate alveolar sacs that can be matched almost completely at the different pressures and the respective regions. However, the red arrows indicate regions that appear to contain an increased number of alveoli with increasing peak-inspiratory pressures. At first appearance, this would let us suspect that additional alveoli are *recruited* when comparing the $5\ \text{cmH}_2\text{O}$ pressure to the $15\ \text{cmH}_2\text{O}$ one. Upon further inspection, however, we found the reason to arise from the fact that alveoli being located deeper in the volume are just moved into the inspected region (i. e. the displayed tomographic slice) upon inflation.

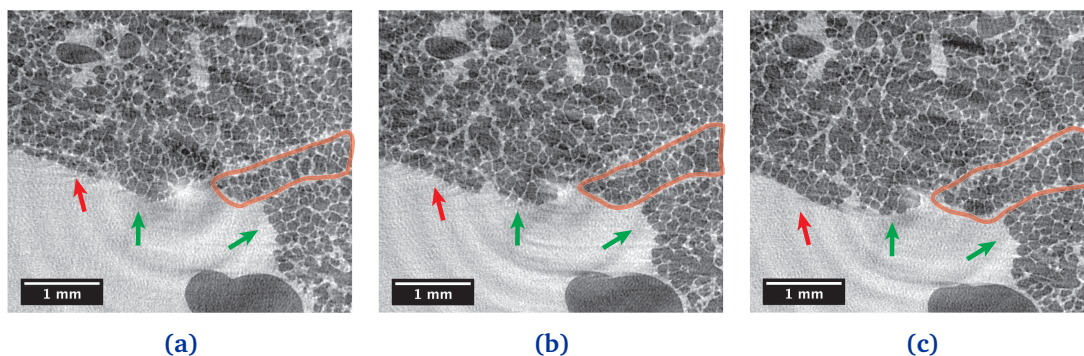


Figure 7.8. Tomographic slices of rats lungs at different breath-hold peak-inspiratory pressures: (a) $5\ \text{cmH}_2\text{O}$; (b) $10\ \text{cmH}_2\text{O}$; (c) $15\ \text{cmH}_2\text{O}$. The marked area (with the orange line) indicates the region of biggest stretching (approximate change in the central diameter of the tubular shape: from $350\ \mu\text{m}$ to $450\ \mu\text{m}$), the green arrows indicate regions that are very little changed upon inflation, while the red arrows show a region where an increased number of alveolar structures appears, which however originate from “deeper” slices.

Due to this fact, the next approach was to focus on very small regions within the 3D lung

image data in order to match identical alveolar structures at different pressures.

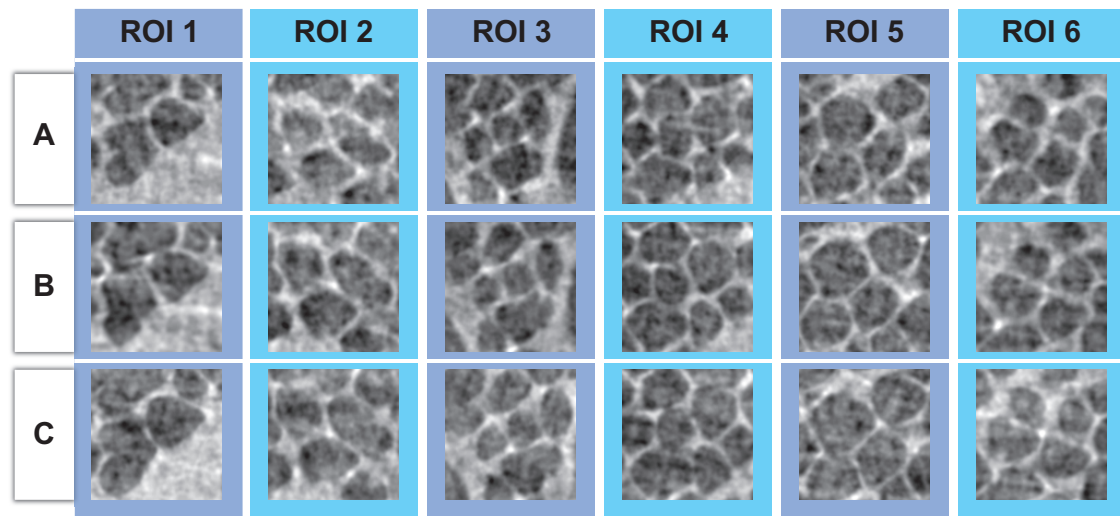


Figure 7.9. Small ROI-s for different breath-hold peak-inspiratory pressures with the $2.9\ \mu\text{m}$ -pixel-size optics: **A** = $5\ \text{cmH}_2\text{O}$, **B** = $10\ \text{cmH}_2\text{O}$, **C** = $15\ \text{cmH}_2\text{O}$. As it can be seen, the structural shapes are maintained upon inflation, only increasing their volume.

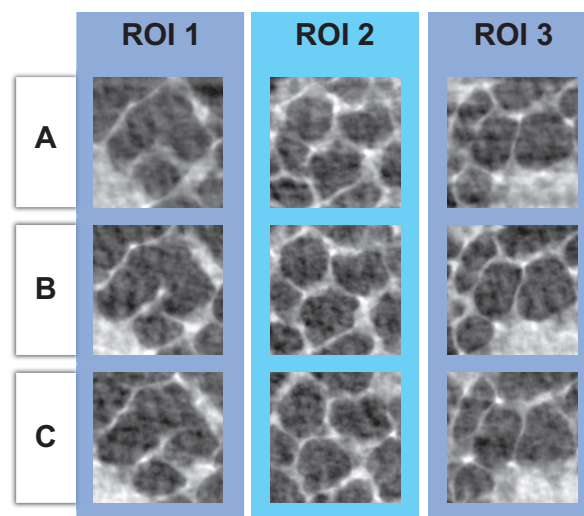


Figure 7.10. Small ROI-s for different breath-hold peak-inspiratory pressures with the $1.1\ \mu\text{m}$ -pixel-size optics: **A** = $5\ \text{cmH}_2\text{O}$, **B** = $10\ \text{cmH}_2\text{O}$, **C** = $15\ \text{cmH}_2\text{O}$. As it can be seen, the structural shapes are maintained upon inflation, only increasing their volume.

This is shown in Fig. 7.9 for animal A with the $2.9\ \mu\text{m}$ -pixel-size optics and in Fig. 7.10 for animal B with the $1.1\ \mu\text{m}$ -pixel-size optics. The regions of interest (ROI-s) were chosen in an arbitrary manner (i. e. by random statistical sampling) at different depths and positions within the 3D volume obtained at $5\ \text{cmH}_2\text{O}$ peak-inspiratory pressure. Subsequently, the re-

gions where matched manually for the higher pressures. As it can be seen in all images, the alveolar structures exhibited a more or less regular and isotropic up-scaling with increasing pressures despite small deviations in their structural shape. Similar behavior was observed in all inspected regions and, in particular, no evidence for alveolar recruitment was found, meaning that for all the small ROI-s that we considered the number of alveolar structures remained constant.

Finally, by analyzing the small ROI-s in Figs. 7.9 and 7.10, our observations from before were confirmed in the sense that the same amount of (biological) information was visible with both optics. Despite the three-fold smaller pixel size of the 1.1 μm -pixel-size optics, the *detail resolution* remained the same due to heart-induced motion artifacts. For the complete series of inflating lung images, the total absorbed doses for the two optics at a total of 450 tomographic projections were obtained from a simplified mouse model and yielded 93.3 Gy for the 2.9 μm -pixel-size and 58.8 Gy for the 1.1 μm -pixel-size optics. As discussed in detail in Sec. 4.3, the total absorbed dose represents a mean value of radiation dose, calculated from the total deposited energy (of the absorbed X-ray photons) in a given volume, which was the same under all conditions. Due to the smaller field of view of the 1.1 μm -pixel-size optics, and despite the higher single-projection exposures, consequently less photons are absorbed in the same volume during (local) tomographic acquisition. Naturally, this is not the case for localized lung doses, where the absorbed doses scale with the single-exposure entrance doses and therefore are higher in the case of the 1.1 μm -pixel-size optics (due to the longer exposure times). A further treatment of local organ doses would, however, necessitate a more complicated dose model and thus is beyond the scope of the present study. This aspect is shortly discussed in the final remarks in Chapter 8.

7.5 DISCUSSION

The heartbeat-triggered gating technique brought us to two essential findings regarding *in vivo* high-resolution 3D imaging of the lung. On the one hand, short exposure times (for single projections) in the order of milliseconds were necessary to obtain CT-reconstructed lung image data with alveolar resolution and without motion artifacts. The total absorbed doses of less than 100 Gy, which were necessary to obtain 3D lung images at three different pressures, are in addition well suited for terminal (acute) *in vivo* experiments where no immediate effects from the radiation on the lung structure are expected [144]. Following that, the shortest scan time for a complete tomographic scan is then given by Eq. (7.1) and typically was in the order of 2 min, while the exact number of projections varied depending on how constant the heartbeat remained during breath-hold. On the other hand, the timing of the single-projection exposure within the heartbeat cycle seems to be decisive. Thus, upon starting the experiment, one of the most crucial points is the correct choice of the ECG delay, namely the delay between “catching” the heartbeat with the ECG device and the time point when a tomographic projection is acquired. The fact that the single-projection exposure time of 3 – 5 ms represents only a very small fraction of a typical heartbeat period (i. e. 1 – 2% of the time interval) lets us further

come to the conclusion that the heartbeat-induced lung movement occurs in a highly non-linear way, namely that it propagates in different regions of the lung at different speeds. Thus, we hypothesize that an improvement in temporal resolution (i. e. shorter single-projection exposure times) will lead to CT-reconstructions with less motion artifacts, but at the same time the optimization of the exposure-timing within the heartbeat period will remain a crucial part.

From the 3D lung image data that was acquired at different peak-irspiratory pressures and by inspecting single tomographic slices, we observed a strongly heterogeneous inter-lobar and slightly heterogeneous intra-lobar distension pattern. As a consequence, it was impossible to match all lung regions within one tomographic slice as the alveolar structures stretch differently within the respective lung region and by different amounts depending on the spatial direction. In the areas where apparently new alveoli were recruited, it was found that those in fact only originated from deeper regions within the sample and that they did not increase their population. In all cases the structural shape of alveolar structures was maintained with increasing pressure and only an increase in volume was observed. The fact that we didn't find any evidence for alveolar recruitment leads directly to the question whether alveolar recruitment could still be observed elsewhere in the sample. However, our results let us conclude that even this being the case, its contribution to total lung inflation is expected to be marginal for the investigated pressure range of 5 – 15 cmH₂O.

In analyzing this result we have to take into account several other aspects. Firstly, data was acquired under quasi-static inflation, i. e. under a breath-hold phase, and at relatively low pressures in order to avoid possible over-extension of the lungs. Thus, our observations are not necessarily valid for a real dynamic case of a free-breathing animal. The quasi-static inflation on the other hand, despite being non-physiological, can be directly associated with so-called pressure-volume loops. In clinics, these represent a common recruitment technique and encompass a slow inflation to TLC (total lung capacity) and subsequently a slow deflation to FRC (functional residual capacity). They are commonly used for capturing volume-dependent non-linearities and thus commonly referred to as “recruitment”. Since in our case, where this condition was approximately emulated, we were unable to observe recruitment at an alveolar scale, the obvious question remains whether recruitment may appear in fact on acinar levels instead. Although this question remains highly speculative, from our findings (and under the investigated conditions) we can at least rule out the possibility that it happens on the level of alveoli.

Finally, we need to explain more fully the terminology of *tissue thickness*, which we used above when comparing the *in vivo* lung tissue with the *ex vivo* one. To be more exact, our proposed method for high-resolution phase-contrast imaging of the lung yields roughly two phases in gray levels in the CT-reconstructed lung images (apart from the highly absorbing bones): *air* and so-called *connective lung tissue*. The latter one is mainly composed of various membranous septa (e. g. interalveolar or lobar), blood vessels, surfactant and/or other liquids. In theory, these have different densities which, however, under the proposed acquisition scheme is hardly distinguishable in the obtained images. Hence, the observed difference in lung tissue thickness cannot be unambiguously accounted for and might be explained by a halted blood circulation in the *ex vivo* animal, but it remains open whether it is also correlated

with a redistribution of surfactant, possibly occurring after the animal's death. This last point, as well as the fact that we observed a slight shrinking of the lung tissue combined with an increase of tissue stiffness in the postmortem scans, highlights the need for *in vivo* techniques when carrying out conclusive physiological studies.

7.6 CONCLUSION

We have developed an animal preparation, anesthetic and handling protocol combined with a prospective heartbeat-triggered gating technique for the tomographic *in vivo* imaging of lungs at the level of single alveoli and at dose rates permitting terminal experiments. We have shown that short exposure times in the order of milliseconds combined with accurate trigger delays are necessary to enable functional analyses of lung inflation patterns with pixel sizes down to $1.1 \times 1.1 \mu\text{m}^2$. To the best of our knowledge our technique represents an improvement in spatial resolution by at least a factor of four compared to previous studies, which we believe will pave the road for future functional studies.

For the case of quasi-static breath-hold inflation we have observed a heterogeneous inter-lobar and intra-lobar distension pattern and by random sampling of small regions within the lung we have found no evidence for alveolar recruitment in the range of 5 – 15 cmH₂O peak-inspiratory pressure. In fact, lungs with increasing peak-inspiratory pressures appear to behave like an elastic distension pattern. Finally, strong differences between *in vivo* and *ex vivo* lung tissue were observed. In particular, we have shown that an increased tissue stiffness and shrinking of the lung takes place already shortly after the animal's death. Our findings thus strongly suggest that *in vivo* experimental conditions are preferred before being able to draw in-depth physiological conclusions from lung imaging experiments.

7.7 ACKNOWLEDGEMENTS

We would like to acknowledge D. Pelt and G. Mikuljan for their help at the experiment as well as Ruud B. van Heeswijk for fruitful discussions in preparation of the experiment. This study was supported by the National Competence Center in Biomedical Imaging (NCCBI), grant No. 1126.0076, and the Swiss National Science Foundation (SNF), grant No. CR23I2-135550 with partial contribution from grant No. 153468.

Summary

8.1 CONCLUSION

The underlying thesis was devoted to the development and realization of *in vivo* tomographic microscopy for the study of lung physiology by covering a variety of accompanying aspects. Having pursued the aim of conceiving a fully performant *in vivo* endstation with its first successful application to micrometer-scale tomography required a truly interdisciplinary approach across different fields and disciplines. In order to fully conclude the results from the present thesis, we will approach it from different directions.

The question of feasibility

Is in vivo lung tomography at the micrometer scale actually possible?

The project was initialized by in-depth characterizations of the on-site conditions. In first attempts to measure the X-ray source size, being the most fundamental quantity in coherent X-ray imaging, we encountered that the existing methods for doing so were not optimal and in our case were even unable to produce useful results. As a consequence we developed a robust tool for photon source geometry measurements using the fractional Talbot effect (summarized in Sec. 4.2) and characterized for the first time the coherence properties of the TOMCAT beamline under the settings of all three different monochromators. The results indicated that from the perspective of ideal X-ray phase-contrast performance, various X-ray energy ranges could be chosen for imaging lungs, which in the end was crucial for defining the X-ray energy of about 21 keV for the final *in vivo* setup.

Likewise, from the outset of the project, the aspect of X-ray radiation dose represented a crucial but unanswered question. In conjunction with it, there was no clear indication what image quality could be reached with what amount of radiation dose and how one would define the ultimate limit. Moreover, absolute X-ray photon fluxes at the TOMCAT beamline had only been measured tentatively up to that time and without explicit knowledge of the uncertainty.

As a consequence, this aspect has been treated in detail by developing a dose optimization approach to fast X-ray microtomography (see Chapter 5) with the accompanying theoretical follow-up treatment in Sec. 4.3. After having performed these studies, we basically concluded that *in vivo* tomography at the micrometer scale is possible under acute (terminal) experimental conditions, providing lung tomograms with acceptable image quality and approximate total absorbed doses of about 5-10 Gy. Complementary literature study in the field of radiation therapy supported this conclusion stating that no acute damage would affect the morphology of lungs during such an experiment. Finally, an absolute flux measurement system has been designed and commissioned to facilitate future on-line dose monitoring at the beamline.

In another effort to optimize image quality, a simple method was developed to analyze flat-field fluctuations present in the beam-profile (see Sec. 4.1). Although the investigation was inconclusive in the sense of identifying and ideally removing the vibration source, it can be a helpful tool in future attempts to do so.

The question of applicability

How do we do it?

The fact that at the beginning of the project there had been no expertise available for *in vivo* lung imaging and up to that date no *in vivo* experiments had ever been performed at the TOMCAT beamline, indicated in no uncertain terms that the complete animal handling protocol and experimental setup would have to be built from the ground up. After having conducted the first experiments with *ex vivo* animals, more and more requirements towards an ideal *in vivo* endstation could be formulated and following an iterative and step-wise approach the final construction proved to be successful. It is the hope of the author of the present thesis that the main findings in how to construct an *in vivo* endstation in all its details (presented in Sec. 4.4) will be of particular interest and use for other groups pursuing to establish similar studies.

The question of usefulness

What is the benefit?

After having had acquired the first high-resolution (still *ex vivo*) 3D lung image data that would potentially be possible to obtain in still-to-come *in vivo* measurements, the immediate question was how one could use these data to obtain better insight into lung physiology. In Chapter 6 this question is addressed by introducing two quantitative measures and investigating their applicability to lungs. For the *ex vivo* case and by looking at lungs at different inflated pressures, we characterize feature sizes of about 70 μm to grow in size when inflating lungs, while the overall air-to-tissue surface shape seems to be quite constant. The methods represent a first attempt to quantitative 3D lung image data analysis, and it should be possible to easily expand them to other areas or lungs under varying conditions. Besides, a simple new dedicated algorithm to improve segmentation of lung image data has been introduced.

***In vivo* and back to the origin: The biology**

What do we find?

Our first realization of a prospective heartbeat-triggered acquisition scheme to perform *in vivo* lung tomography at the micrometer scale was only possible thanks to all other previous developments described in the thesis. With this technique we were able to realize a four-fold improvement in spatial resolution compared to other related techniques and with an estimated total absorbed dose of about 100 Gray for the complete imaging of three quasi-static lung pressures, whereas it is appropriate to say that the dose could be reduced further. Of biological relevance is the fact that the initial results do not provide any proof for alveolar recruitment. Moreover, we found certain evidence for a heterogeneous distension pattern. On the other hand, for the first time a direct comparison between *in vivo* and *ex vivo* lung tissue at the micrometer scale was given.

8.2 PERSPECTIVES

The idea of the following section is to shortly summarize possible perspectives for future developments that emerged throughout the underlying project.

Novel acquisition scheme

Imaging lungs at high resolutions requires precise triggering with the heartbeat. This would represent no real problem in imaging, provided that the heartbeat would be regular and constant over time. However, that is not the case, which makes the use of a more advanced acquisition mode very hard. For instance, in order to resolve high-resolution lung features one would always need to perform tomography during some kind of breath-hold phase and “wait” to get a trigger signal from the heart impulse. An alternative approach which became apparent during our experiments would be to use a pacemaker in order to synchronize the heart with image acquisition. In case this worked, one would be able to resolve a true (dynamic) breathing phase and potentially even think of imaging a free-breathing animal model.

Dosimetry

In the present thesis the dose was calculated by simplified means, either by utilizing the skin entrance dose or the total absorbed dose. In the sense of future developments, a more precise way to do so would be through Monte Carlo simulations, which could provide detailed dose distributions. Preliminary work has been done e. g. by Peter [246], producing accurate dose distribution calculations for the two optics in use (as shown in Fig. 8.1). Particularly, if in the future the image acquisition could be optimized further, facilitating the use of a longitudinal animal (imaging) model, the approach of calculating dose distributions would be particularly important.

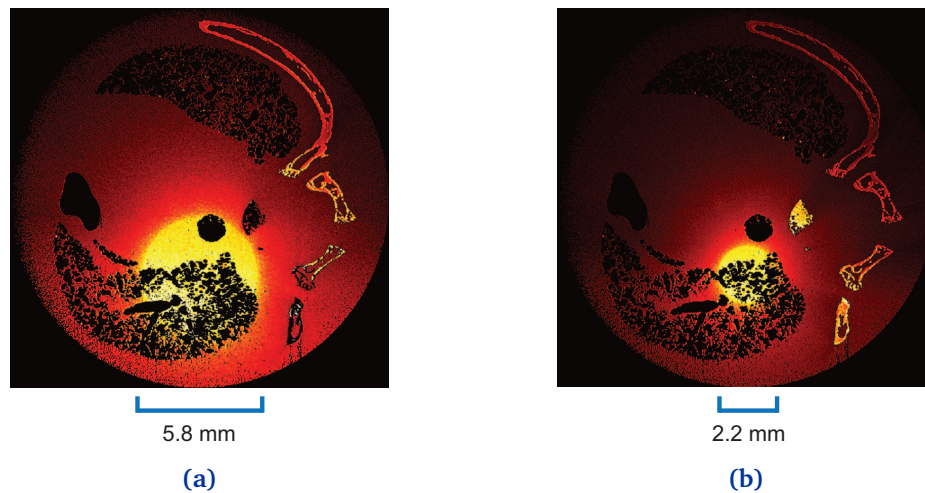


Figure 8.1. Monte Carlo calculations of dose distributions in the rat lungs, according to the two field of views in use: **(a)** $2.9\ \mu\text{m}$ -pixel-size optics; **(b)** $1.1\ \mu\text{m}$ -pixel-size optics. The plots have been reproduced with permission from S. Peter.

Improved CT reconstructions

Novel (iterative) CT algorithms are constantly being developed. In the course of the present project, a short collaboration was established to investigate the applicability of the NN-FBP [247] (neural network filtered backprojection) algorithm to lung tissue.

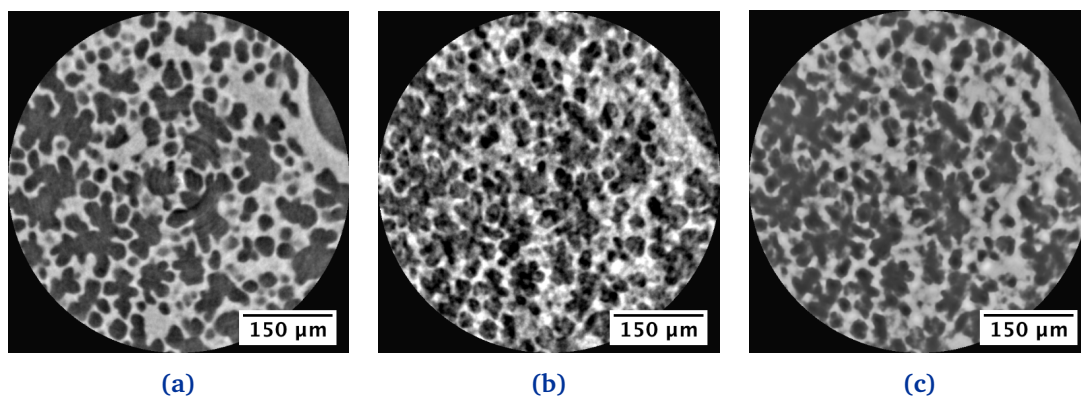


Figure 8.2. Application of NN-FBP with a reduced number of projections: **(a)** 900 projections (FBP reconstruction); **(b)** 300 projections (FBP); **(c)** 300 projections (NN-FBP). The images have been reproduced with permission from D. Pelt.

Its principle is described as follows: When performing filtered backprojection, a correct choice of the filter can potentially improve the quality of CT-reconstructions. In the NN-FBP approach the filter is composed by a neural-network-based training on “similar” datasets. Two kinds of results were obtained for the lung data acquired in our experiments: in Fig. 8.2 the

application of NN-FBP is shown to yield improved reconstruction image quality compared to the standard FBP under a reduced number of projections and in Fig. 8.3 NN-FBP is applied to improve the contrast (and thus segmentability) in noisy data.

As a general note, the approach appears particularly interesting as the training can happen on similar datasets. For future studies it could play a potential role to reduce radiation dose.

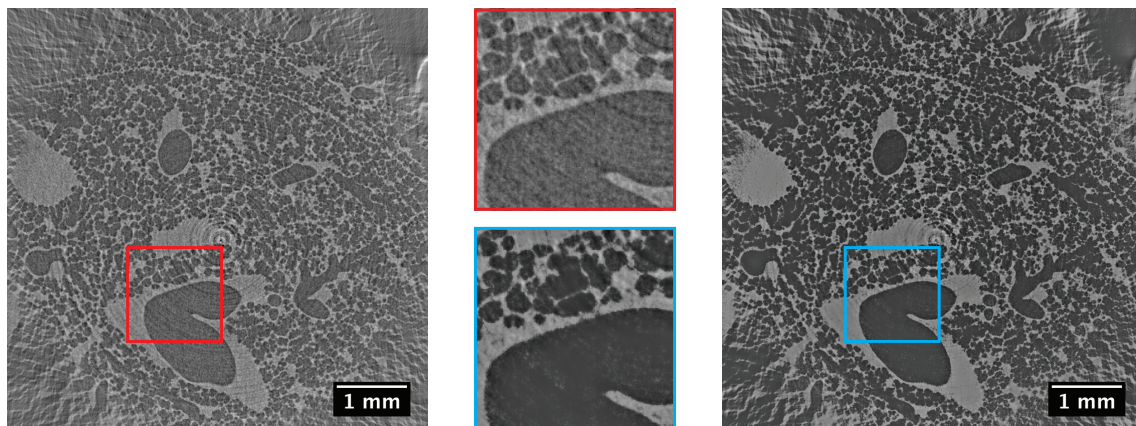


Figure 8.3. Application of NN-FBP in a noisy image. The left image shows a tomographic slice (reconstructed with FBP from 900 projections), and the right image shows the same dataset reconstructed with NN-FBP. The images have been reproduced with permission from D. Pelt.

Bibliography

- [1] S. E. Weinberger, B. A. Cockrill, and J. Mandel. *Principles of Pulmonary Medicine*. Saunders Elsevier, 2nd edition, 2008.
- [2] E. Bancalari. *The Newborn Lung: Neonatology Questions and Controversies*. Saunders, 1st edition, 2008.
- [3] D. Wulfsohn, J. Knust, M. Ochs, J. R. Nyengaard, and H. J. G. Gundersen. Stereological estimation of the total number of ventilatory units in mice lungs. *Journal of Microscopy* **238**, 75, 2010.
- [4] Patrick J. Lynch, medical illustrator. Bronchial anatomy. http://commons.wikimedia.org/wiki/File:Bronchial_anatomy.jpg#/media/File:Bronchial_anatomy.jpg, 2015. [Online; accessed 14-April-2015].
- [5] K. Horsfield. Diameters, generations, and orders of branches in the bronchial tree. *Journal of Applied Physiology* **68**, 457, 1990.
- [6] E. R. Weibel. Fractal geometry: a design principle for living organisms. *The American Journal of Physiology* **261**, L361, 1991.
- [7] D. M. Hyde, N. K. Tyler, L. F. Putney, P. Singh, and H. J. G. Gundersen. Total number and mean size of alveoli in mammalian lung estimated using fractionator sampling and unbiased estimates of the Euler characteristic of alveolar openings. *The Anatomical Record Part A: Discoveries in molecular, cellular, and evolutionary biology* **277**, 216, 2004.
- [8] J. C. Schittny. Strukturelle Entwicklung – von der Anlage zur adulten Lunge. In E. von Mutius, M. Gappa, E. Eber, and U. Frey, editors, *Pädiatrische Pneumologie*, pages 3–16. Springer, 3rd edition, 2014.
- [9] M. Ochs, J. R. Nyengaard, A. Jung, L. Knudsen, M. Voigt, T. Wahlers, J. Richter, and H. J. G. Gundersen. The number of alveoli in the human lung. *American Journal of Respiratory and Critical Care Medicine* **169**, 120, 2004.
- [10] M. Rodriguez, S. Bur, A. Favre, and E. R. Weibel. Pulmonary Acinus: Geometry and Morphometry of the Peripheral Airway System in Rat and Rabbit. *The American Journal of Anatomy* **180**, 143, 1987.
- [11] H. Itoh, M. Nishino, and H. Hatabu. Architecture of the Lung. *Journal of Thoracic Imaging* **19**, 221, 2004.

- [12] P. Gehr, M. Bachofen, and E. R. Weibel. The normal human lung: ultrastructure and morphometric estimation of diffusion capacity. *Respiration Physiology* **32**, 121, 1978.
- [13] S. F. Barre, D. Haberthur, M. Stampanoni, and J. C. Schittny. Efficient estimation of the total number of acini in adult rat lung. *Physiological Reports* **2**, e12063, 2014.
- [14] E. R. Weibel. What makes a good lung? *Swiss Medical Weekly* **139**, 375, 2009.
- [15] J. D. Escolar and A. Escolar. Lung hysteresis: a morphological view. *Histology and Histopathology* **19**, 159, 2004.
- [16] G. C. Smaldone and W. Mitzner. Viewpoint: Unresolved mysteries. *Journal of Applied Physiology* **113**, 1945, 2012.
- [17] D. S. Faffe and W. A. Zin. Lung parenchymal mechanics in health and disease. *Physiological Reviews* **89**, 759, 2009.
- [18] M. Roth-Kleiner and M. Post. Similarities and dissimilarities of branching and septation during lung development. *Pediatric Pulmonology* **40**, 113, 2005.
- [19] D. R. Chang, D. Martinez Alanis, R. K. Miller, H. Ji, H. Akiyama, P. D. McCrea, and J. Chen. Lung epithelial branching program antagonizes alveolar differentiation. *Proceedings of the National Academy of Sciences* **110**, 18042, 2013.
- [20] J. C. Schittny and P. H. Burri. Development and growth of the lung. In A. Fishman, J. Elias, J. Fishman, M. Grippi, R. Senior, and A. Pack, editors, *Fishman's Pulmonary Diseases and Disorders*, chapter 5, pages 91–114. McGraw-Hill Professional, 4th edition, 2008.
- [21] R. J. Metzger, O. D. Klein, G. R. Martin, and M. A. Krasnow. The branching programme of mouse lung development. *Nature* **453**, 745, 2008.
- [22] K. Bauer, A. Rudert, and C. Brucker. Three-Dimensional Flow Patterns in the Upper Human Airways. *Journal of Biomechanical Engineering* **134**, 071006, 2012.
- [23] J. C. Schittny, S. I. Mund, and M. Stampanoni. Evidence and structural mechanism for late lung alveolarization. *American Journal of Physiology - Lung Cellular and Molecular Physiology* **294**, L246, 2008.
- [24] M. J. Herring, L. F. Putney, G. Wyatt, W. E. Finkbeiner, and D. M. Hyde. Growth of alveoli during postnatal development in humans based on stereological estimation. *American Journal of Physiology - Lung Cellular and Molecular Physiology* **307**, L338, 2014.
- [25] M. L. Siew, A. B. te Pas, M. J. Wallace, M. J. Kitchen, R. A. Lewis, A. Fouras, C. J. Morley, P. G. Davis, N. Yagi, K. Uesugi, and S. B. Hooper. Positive end-expiratory pressure enhances development of a functional residual capacity in preterm rabbits ventilated from birth. *Journal of Applied Physiology* **106**, 1487, 2009.

- [26] A. B. te Pas, M. Siew, M. J. Wallace, M. J. Kitchen, A. Fouras, R. A. Lewis, N. Yagi, K. Uesugi, S. Donath, P. G. Davis, C. J. Morley, and S. B. Hooper. Establishing functional residual capacity at birth: the effect of sustained inflation and positive end-expiratory pressure in a preterm rabbit model. *Pediatric Research* **65**, 537, 2009.
- [27] P. Thunqvist, P. Gustafsson, M. Norman, M. Wickman, and J. Hallberg. Lung function at 6 and 18 Months After Preterm Birth in Relation to Severity of Bronchopulmonary Dysplasia. *Pediatric Pulmonology* **50**, 978, 2015.
- [28] B. J. Smith, K. A. Grant, and J. H. T. Bates. Linking the Development of Ventilator-Induced Injury to Mechanical Function in the Lung. *Annals of Biomedical Engineering* **41**, 527, 2013.
- [29] J. H. Bates and B. Smith. Assessing the Progression of Ventilator-Induced Lung Injury in Mice. *IEEE Transactions on Biomedical Engineering* **60**, 3449, 2013.
- [30] J. L. Carroll. Developmental plasticity in respiratory control. *Journal of Applied Physiology* **94**, 375, 2003.
- [31] S. B. Hooper, M. J. Kitchen, M. L. Siew, R. A. Lewis, A. Fouras, A. B te Pas, K. K. Siu, N. Yagi, K. Uesugi, and M. J. Wallace. Imaging Lung Aeration and Lung Liquid Clearance At Birth Using Phase Contrast X-Ray Imaging. *Clinical and Experimental Pharmacology and Physiology* **36**, 117, 2009.
- [32] M. L. Siew, A. B. te Pas, M. J. Wallace, M. J. Kitchen, M. S. Islam, R. A. Lewis, A. Fouras, C. J. Morley, P. G. Davis, N. Yagi, K. Uesugi, and S. B. Hooper. Surfactant increases the uniformity of lung aeration at birth in ventilated preterm rabbits. *Pediatric Research* **70**, 50, 2011.
- [33] R. R. Mercer and J. D. Crapo. Three-dimensional reconstruction of the rat acinus. *Journal of Applied Physiology* **63**, 785, 1987.
- [34] F. Kiessling and B. J. Pichler. *Small Animal Imaging: Basics and Practical Guide*. Springer, 2010.
- [35] E. M. van Rikxoort and B. van Ginneken. Automated segmentation of pulmonary structures in thoracic computed tomography scans: a review. *Physics in Medicine and Biology* **58**, R187, 2013.
- [36] S. Bayat, L. Apostol, E. Boller, T. Brochard, and F. Peyrin. In vivo imaging of bone micro-architecture in mice with 3D synchrotron radiation micro-tomography. *Nuclear Instruments and Methods in Physics Research Section A* **548**, 247, 2005.
- [37] A. Compton and S. Allison. *X-rays in Theory and Experiment*. Van Nostrand, 2nd edition, 1935.

- [38] J. Baruchel, J.-L. Hodeau, M. S. Lehmann, J.-R. Regnard, and C. Schlenker, editors. *Neutron and Synchrotron Radiation for Condensed Matter Studies*. Springer Berlin Heidelberg, 1994.
- [39] D. Attwood. *Soft X-Rays and Extreme Ultraviolet Radiation: Principles and Applications*. Cambridge University Press, 2007.
- [40] J. Als-Nielsen and D. McMorrow. *Elements of Modern X-ray Physics*. Wiley, 2nd edition, 2011.
- [41] W. C. Röntgen. Über eine neue Art von Strahlen. *Annalen der Physik* **300**, 12, 1895.
- [42] K.-J. Kim. Optical and power characteristics of synchrotron radiation sources. *Optical Engineering* **34**, 342, 1995.
- [43] K.-J. Kim. Brightness, coherence and propagation characteristics of synchrotron radiation. *Nuclear Instruments and Methods in Physics Research A* **246**, 71, 1986.
- [44] S. L. Hulbert and J. M. Weber. Flux and brightness calculations for various synchrotron radiation sources. *Nuclear Instruments and Methods in Physics Research A* **319**, 25, 1992.
- [45] M. J. Berger, J. H. Hubbell, S. M. Seltzer, J. Chang, J. S. Coursey, R. Sukumar, D. S. Zucker, and K. Olsen. XCOM: Photon Cross Section Database (version 1.5), 2010.
- [46] R. James. *The Optical Principles of the Diffraction of X-rays*. The Crystalline state - Vol II. G. Bell and Sons, 1962.
- [47] O. Klein and Y. Nishina. ON THE SCATTERING OF RADIATION BY FREE ELECTRONS ACCORDING TO DIRAC'S NEW RELATIVISTIC QUANTUM DYNAMICS. In *The Oskar Klein Memorial Lectures*, volume 853, pages 113–129. World Scientific, 1994.
- [48] L. Mandel and E. Wolf. *Optical Coherence and Quantum Optics*. Cambridge University Press, 1995.
- [49] J. P. Guigay. Fourier transform analysis of Fresnel diffraction patterns and in-line holograms. *Optik* **49**, 121, 1977.
- [50] A. Pogany, D. Gao, and S. W. Wilkins. Contrast and resolution in imaging with a micro-focus x-ray source. *Review Of Scientific Instruments* **68**, 2774, 1997.
- [51] M. Langer, P. Cloetens, J.-P. Guigay, and F. Peyrin. Quantitative comparison of direct phase retrieval algorithms in in-line phase tomography. *Medical Physics* **35**, 4556, 2008.
- [52] K. A. Nugent. Coherent methods in the X-ray sciences. *Advances in Physics* **59**, 158, 2009.
- [53] P. Cloetens, R. Barrett, J. Baruchel, J.-P. Guigay, and M. Schlenker. Phase objects in synchrotron radiation hard x-ray imaging. *Journal of Physics D: Applied Physics* **29**, 133, 1996.

- [54] X. Wu and H. Liu. Clarification of aspects in in-line phase-sensitive x-ray imaging. *Medical Physics* **34**, 737, 2007.
- [55] S. W. Wilkins, Y. I. Nesterets, T. E. Gureyev, S. C. Mayo, A. Pogany, and A. W. Stevenson. On the evolution and relative merits of hard X-ray phase-contrast imaging methods. *Philosophical Transactions of the Royal Society A* **372**, 20130021, 2014.
- [56] P. Cloetens, W. Ludwig, J. Baruchel, D. Van Dyck, J. Van Landuyt, J. Guigay, and M. Schlenker. Holotomography: Quantitative phase tomography with micrometer resolution using hard synchrotron radiation x rays. *Applied Physics Letters* **75**, 2912, 1999.
- [57] J. P. Guigay, M. Langer, R. Boistel, and P. Cloetens. Mixed transfer function and transport of intensity approach for phase retrieval in the Fresnel region. *Optics letters* **32**, 1617, 2007.
- [58] S. Zabler, P. Cloetens, J.-P. Guigay, J. Baruchel, and M. Schlenker. Optimization of phase contrast imaging using hard x rays. *Review of Scientific Instruments* **76**, 073705, 2005.
- [59] M. Reed Teague. Deterministic phase retrieval: a Green's function solution. *Journal of the Optical Society of America* **73**, 1434, 1983.
- [60] K. A. Nugent, T. E. Gureyev, D. F. Cookson, D. Paganin, and Z. Barnea. Quantitative Phase Imaging Using Hard X Rays. *Physical Review Letters* **77**, 2961, 1996.
- [61] A. Bravin, P. Coan, and P. Suortti. X-ray phase-contrast imaging: from pre-clinical applications towards clinics. *Physics in Medicine and Biology* **58**, R1, 2013.
- [62] T. E. Gureyev, A. Roberts, and K. A. Nugent. Partially coherent fields, the transport-of-intensity equation, and phase uniqueness. *Journal of the Optical Society of America A* **12**, 1942, 1995.
- [63] T. E. Gureyev and S. W. Wilkins. On x-ray phase imaging with a point source. *Journal of the Optical Society of America A* **15**, 579, 1998.
- [64] T. Gureyev, S. Mayo, S. Wilkins, D. Paganin, and A. W. Stevenson. Quantitative In-Line Phase-Contrast Imaging with Multienergy X Rays. *Physical Review Letters* **86**, 5827, 2001.
- [65] D. Paganin, S. C. Mayo, T. E. Gureyev, P. R. Miller, and S. W. Wilkins. Simultaneous phase and amplitude extraction from a single defocused image of a homogeneous object. *Journal of Microscopy* **206**, 33, 2002.
- [66] A. C. Kak and M. Slaney. *Principles of Computerized Tomographic Imaging*. IEEE Press, 1988.
- [67] T. Farquhar, A. Chatziioannou, G. Chinn, M. Dahlbom, and E. Hoffman. An investigation of filter choice for filtered back-projection reconstruction in PET. *IEEE Transactions on Nuclear Science* **45**, 1133, 1998.

- [68] J. D. O'Sullivan. A Fast Sinc Function Gridding Algorithm for Fourier Inversion in Computer Tomography. *IEEE Transactions on Medical Imaging* **4**, 200, 1985.
- [69] J. I. Jackson, C. H. Meyer, D. G. Nishimura, and A. Macovski. Selection of a convolution function for Fourier inversion using gridding. *IEEE Transactions on Medical Imaging* **10**, 473, 1991.
- [70] B. A. Dowd. Developments in synchrotron x-ray computed microtomography at the National Synchrotron Light Source. In *Proceedings of SPIE*, volume 3772, pages 224–236. SPIE, 1999.
- [71] F. Marone and M. Stampanoni. Regridding reconstruction algorithm for real-time tomographic imaging. *Journal of Synchrotron Radiation* **19**, 1, 2012.
- [72] C. Hintermüller, F. Marone, A. Isenegger, and M. Stampanoni. Image processing pipeline for synchrotron-radiation-based tomographic microscopy. *Journal of Synchrotron Radiation* **17**, 550, 2010.
- [73] A. Kyrieleis, V. Titarenko, M. Ibison, T. Connolley, and P. J. Withers. Region-of-interest tomography using filtered backprojection: Assessing the practical limits. *Journal of Microscopy* **241**, 69, 2010.
- [74] E. A. Rashed and H. Kudo. Towards high-resolution synchrotron radiation imaging with statistical iterative reconstruction. *Journal of Synchrotron Radiation* **20**, 1, 2012.
- [75] B. Münch, P. Trtik, F. Marone, and M. Stampanoni. Stripe and ring artifact removal with combined wavelet—Fourier filtering. *Optics Express* **17**, 8567, 2009.
- [76] T. M. Deserno. *Biomedical Image Processing*. Springer, 2010.
- [77] J. Fischer and A. del Río. A fast method for applying rigid transformations to volume data. In *WSCG SHORT Communcation papers proceedings*, volume 12. UNION Agency — Science Press, 2004.
- [78] J. Ohser and K. Schladitz. *3D Images of Materials Structures: Processing and Analysis*. Wiley-VCH, 2009.
- [79] A. Rack, T. Weitkamp, I. Zanette, C. Morawe, A. Vivo Rommeveaux, P. Tafforeau, P. Cloetens, E. Ziegler, T. Rack, A. Cecilia, P. Vagovič, E. Harmann, R. Dietsch, and H. Riesemeier. Coherence preservation and beam flatness of a single-bounce multilayer monochromator (beamline ID19—ESRF). *Nuclear Instruments and Methods in Physics Research A* **649**, 123, 2011.
- [80] C. Homann, T. Hohage, J. Hagemann, A.-L. Robisch, and T. Salditt. Validity of the empty-beam correction in near-field imaging. *Physical Review A* **91**, 2015.

- [81] O. Bunk, F. Pfeiffer, M. Stampanoni, B. D. Patterson, C. Schulze-Briese, and C. David. X-ray beam-position monitoring in the sub-micrometre and sub-second regime. *Journal of Synchrotron Radiation* **12**, 795, 2005.
- [82] W. Burger and M. J. Burge. *Digitale Bildverarbeitung*. Springer, 2nd edition, 2006.
- [83] F. Nicoud, G. Castellazzi, P. J. Lesniewski, and J. C. Thomas. Fast template tracking in video sequences. *Review of Scientific Instruments* **82**, 105110, 2011.
- [84] J. P. Lewis. Fast Template Matching. In *Vission Interface*, volume 95, pages 120–123. Canadian Image Processing and Pattern Recognition Society, 1995.
- [85] G. Lovric, P. Oberta, I. Mohacsi, M. Stampanoni, and R. Mokso. A robust tool for photon source geometry measurements using the fractional Talbot effect. *Optics Express* **22**, 2745, 2014.
- [86] I. A. Vartanyants and A. Singer. Coherence properties of hard x-ray synchrotron sources and x-ray free-electron lasers. *New Journal of Physics* **12**, 035004, 2010.
- [87] S. Dierker, R. Pindak, R. Fleming, I. Robinson, and L. Berman. X-Ray Photon Correlation Spectroscopy Study of Brownian Motion of Gold Colloids in Glycerol. *Physical Review Letters* **75**, 449, 1995.
- [88] I. Robinson, J. Libbert, I. Vartanyants, J. Pitney, D. Smilgies, D. Abernathy, and G. Grübel. Coherent x-ray diffraction imaging of silicon oxide growth. *Physical Review B* **60**, 9965, 1999.
- [89] S. Roy, D. Parks, K. A. Seu, R. Su, J. J. Turner, W. Chao, E. H. Anderson, S. Cabrini, and S. D. Kevan. Lensless X-ray imaging in reflection geometry. *Nature Photonics* **5**, 243, 2011.
- [90] A. Momose, T. Takeda, Y. Itai, and K. Hirano. Phase-contrast X-ray computed tomography for observing biological soft tissues. *Nature Medicine* **2**, 473, 1996.
- [91] C. David, B. Nohammer, H. H. Solak, and E. Ziegler. Differential x-ray phase contrast imaging using a shearing interferometer. *Applied Physics Letters* **81**, 3287, 2002.
- [92] M. Dierolf, A. Menzel, P. Thibault, P. Schneider, C. M. Kewish, R. Wepf, O. Bunk, and F. Pfeiffer. Ptychographic X-ray computed tomography at the nanoscale. *Nature* **467**, 436, 2010.
- [93] B. Abbey, L. W. Whitehead, H. M. Quiney, D. J. Vine, G. A. Cadenazzi, C. A. Henderson, K. A. Nugent, E. Balaur, C. T. Putkunz, A. G. Peele, G. J. Williams, and I. McNulty. Lensless imaging using broadband X-ray sources. *Nature Photonics* **5**, 420, 2011.
- [94] P. Modregger, F. Scattarella, B. Pinzer, C. David, R. Bellotti, and M. Stampanoni. Imaging the Ultrasmall-Angle X-Ray Scattering Distribution with Grating Interferometry. *Physical Review Letters* **108**, 2, 2012.

- [95] M. Born and E. Wolf. *Principles of Optics: Electromagnetic Theory of Propagation, Interference and Diffraction of Light*. Cambridge University Press, 7th edition, 1999.
- [96] V. Kohn, I. Snigireva, and A. Snigirev. Direct measurement of transverse coherence length of hard X rays from interference fringes. *Physical Review Letters* **85**, 2745, 2000.
- [97] D. Paterson, B. Allman, P. McMahon, J. Lin, N. Moldovan, K. Nugent, I. McNulty, C. Chantler, C. Retsch, and T. Irving. Spatial coherence measurement of X-ray undulator radiation. *Optics Communications* **195**, 79, 2001.
- [98] B. J. Thompson and E. Wolf. Two-beam interference with partially coherent light. *Journal of the Optical Society of America* **47**, 895, 1957.
- [99] C. Chang, P. Naulleau, E. Anderson, and D. Attwood. Spatial coherence characterization of undulator radiation. *Optics Communications* **182**, 25, 2000.
- [100] W. Leitenberger, S. Kuznetsov, and A. Snigirev. Interferometric measurements with hard X-rays using a double slit. *Optics Communications* **191**, 91, 2001.
- [101] T. Panzner, W. Leitenberger, J. Grenzer, Y. Bodenthin, T. Geue, U. Pietsch, and H. Möhwald. Coherence experiments at the energy-dispersive reflectometry beamline at BESSY II. *Journal of Physics D: Applied Physics* **36**, A93, 2003.
- [102] W. Leitenberger, H. Wendrock, L. Bischoff, and T. Weitkamp. Pinhole interferometry with coherent hard X-rays. *Journal of Synchrotron Radiation* **11**, 190, 2004.
- [103] M. Yabashi, K. Tamasaku, and T. Ishikawa. Characterization of the Transverse Coherence of Hard Synchrotron Radiation by Intensity Interferometry. *Physical Review Letters* **87**, 140801, 2001.
- [104] F. Pfeiffer, O. Bunk, C. Schulze-Briese, A. Diaz, T. Weitkamp, C. David, J. F. van der Veen, I. Vartanyants, and I. K. Robinson. Shearing Interferometer for Quantifying the Coherence of Hard X-Ray Beams. *Physical Review Letters* **94**, 164801, 2005.
- [105] K. S. Morgan, S. C. Irvine, Y. Suzuki, K. Uesugi, A. Takeuchi, D. M. Paganin, and K. K. Siu. Measurement of hard X-ray coherence in the presence of a rotating random-phase-screen diffuser. *Optics Communications* **283**, 216, 2010.
- [106] J. J. A. Lin, D. Paterson, A. G. Peele, P. J. McMahon, C. T. Chantler, K. A. Nugent, B. Lai, N. Moldovan, Z. Cai, D. C. Mancini, and I. McNulty. Measurement of the Spatial Coherence Function of Undulator Radiation using a Phase Mask. *Physical Review Letters* **90**, 074801, 2003.
- [107] I. A. Vartanyants, A. Singer, A. P. Mancuso, O. M. Yefanov, A. Sakdinawat, Y. Liu, E. Bang, G. J. Williams, G. Cadenazzi, B. Abbey, H. Sinn, D. Attwood, K. A. Nugent, E. Weckert, T. Wang, D. Zhu, B. Wu, C. Graves, A. Scherz, J. J. Turner, W. F. Schlotter, M. Messerschmidt, J. Lüning, Y. Acremann, P. Heimann, D. C. Mancini, V. Joshi, J. Krzywinski,

- R. Soufli, M. Fernandez-Perea, S. Hau-Riege, A. G. Peele, Y. Feng, O. Krupin, S. Moeller, and W. Wurth. Coherence Properties of Individual Femtosecond Pulses of an X-Ray Free-Electron Laser. *Physical Review Letters* **107**, 144801, 2011.
- [108] P. Cloetens, J. P. Guigay, C. De Martino, J. Baruchel, and M. Schlenker. Fractional Talbot imaging of phase gratings with hard x rays. *Optics Letters* **22**, 1059, 1997.
- [109] J.-P. Guigay, S. Zabler, P. Cloetens, C. David, R. Mokso, and M. Schlenker. The partial Talbot effect and its use in measuring the coherence of synchrotron X-rays. *Journal of Synchrotron Radiation* **11**, 476, 2004.
- [110] T. Weitkamp, B. Nohammer, A. Diaz, C. David, and E. Ziegler. X-ray wavefront analysis and optics characterization with a grating interferometer. *Applied Physics Letters* **86**, 054101, 2005.
- [111] A. Diaz, C. Mocuta, J. Stangl, M. Keplinger, T. Weitkamp, F. Pfeiffer, C. David, T. H. Metzger, and G. Bauer. Coherence and wavefront characterization of Si-111 monochromators using double-grating interferometry. *Journal of Synchrotron Radiation* **17**, 299, 2010.
- [112] A. Rack, T. Weitkamp, M. Riotte, D. Grigoriev, T. Rack, L. Helfen, T. Baumbach, R. Dietsch, T. Holz, M. Krämer, F. Siewert, M. Meduna, P. Cloetens, and E. Ziegler. Comparative study of multilayers used in monochromators for synchrotron-based coherent hard X-ray imaging. *Journal of Synchrotron Radiation* **17**, 496, 2010.
- [113] A. Yaroshenko, M. Bech, G. Potdevin, A. Malecki, T. Biernath, J. Wolf, A. Tapfer, M. Schüttler, J. Meiser, D. Kunka, M. Amberger, J. Mohr, and F. Pfeiffer. Non-binary phase gratings for x-ray imaging with a compact Talbot interferometer. *Optics Express* **22**, 547, 2014.
- [114] M. Stampanoni, A. Groso, A. Isenegger, G. Mikuljan, Q. Chen, A. Bertrand, S. Henein, R. Betemps, U. Frommherz, P. Böhler, D. Meister, M. Lange, and R. Abela. Trends in synchrotron-based tomographic imaging: the SLS experience. In *Proceedings of SPIE*, volume 6318, pages 63180M–1–14. SPIE, 2006.
- [115] J. W. Goodman. *Introduction to Fourier Optics*. McGraw-Hill Companies, 2nd edition, 1996.
- [116] P. Cloetens. *Contribution to Phase Contrast Imaging , Reconstruction and Tomography with Hard Synchrotron Radiation: Principles , Implementation and Applications*. Phd thesis, Vrije Universiteit Brussel, 1999.
- [117] T. Weitkamp, C. David, C. Kottler, O. Bunk, and F. Pfeiffer. Tomography with grating interferometers at low-brilliance sources. In *Proceedings of SPIE*, volume 6318, pages 63180S–1–10. SPIE, 2006.

- [118] R. Kluender, F. Masiello, P. van Vaerenbergh, and J. Härtwig. Measurement of the spatial coherence of synchrotron beams using the Talbot effect. *Physica Status Solidi A* **206**, 1842, 2009.
- [119] W. H. Southwell. Validity of the Fresnel approximation in the near field. *Journal of the Optical Society of America* **71**, 7, 1981.
- [120] G. Lovric. Source size calculator. <http://www.psi.ch/sls/tomcat/>, 2013. [Online; accessed 26-February-2016].
- [121] S. Gorelick, J. Vila-Comamala, V. A. Guzenko, R. Barrett, M. Salomé, and C. David. High-efficiency Fresnel zone plates for hard X-rays by 100 keV e-beam lithography and electroplating. *Journal of Synchrotron Radiation* **18**, 442, 2011.
- [122] S. Yasin, D. Hasko, and H. Ahmed. Comparison of MIBK/IPA and water/IPA as PMMA developers for electron beam nanolithography. *Microelectronic Engineering* **61-62**, 745, 2002.
- [123] J. M. Boone, J. A. Brink, S. Edyvean, W. Huda, W. Leitz, C. H. McCollough, M. F. McNitt-Gray, P. Dawson, P. L. M. Deluca, S. M. Seltzer, J. A. Brunberg, G. W. Burkett, R. L. Dixon, J. Geleijns, J. P. McGahan, S. E. McKenney, N. J. Pelc, J. H. Siewerdsen, J. A. Seibert, H. Winer-Muram, and S. Wootton-Gorges. Radiation dose and image-quality assessment in computed tomography. *Journal of the ICRU* **12**, 9, 2012.
- [124] R. Taschereau, P. L. Chow, and A. F. Chatziioannou. Monte Carlo simulations of dose from microCT imaging procedures in a realistic mouse phantom. *Medical Physics* **33**, 216, 2006.
- [125] A. Bitar, A. Lisbona, P. Thedrez, C. Sai Maurel, D. Le Forestier, J. Barbet, and M. Bardies. A voxel-based mouse for internal dose calculations using Monte Carlo simulations (MCNP). *Physics in Medicine and Biology* **52**, 1013, 2007.
- [126] S. K. Carlson, K. L. Classic, C. E. Bender, and S. J. Russell. Small animal absorbed radiation dose from serial micro-computed tomography imaging. *Molecular Imaging and Biology* **9**, 78, 2007.
- [127] A. Rose. A Unified Approach to the Performance of Photographic Film, Television Pickup Tubes, and the Human Eye. *Journal of the Society of Motion Picture Engineers* **47**, 273, 1946.
- [128] R. Hegerl and W. Hoppe. Influence of Electron Noise on Three-dimensional Image Reconstruction. *Zeitschrift für Naturforschung A* **31**, 1717, 1976.
- [129] B. F. McEwen, K. H. Downing, and R. M. Glaeser. The relevance of dose-fractionation in tomography of radiation-sensitive specimens. *Ultramicroscopy* **60**, 357, 1995.

- [130] J. H. Hubbell and S. M. Seltzer. Tables of X-ray Mass Attenuation Coefficients and Mass Energy-Absorption Coefficients from 1 keV to 20 MeV for Elements $Z = 1$ to 92 and 48 Additional Substances of Dosimetric Interest, 1996.
- [131] C. Hoeschen, D. Regulla, H. Schlattl, N. Petoussi-Henss, W. B. Li, and M. Zankl. How do we measure dose and estimate risk? In *Proc. SPIE*, volume 7961, page 79612F, 2011.
- [132] M. R. Howells, A. P. Hitchcock, and C. J. Jacobsen. Introduction: Special issue on radiation damage. *Journal of Electron Spectroscopy and Related Phenomena* **170**, 1, 2009.
- [133] E. Kuznetsova. *Dosimetry for Synchrotron-based X-Ray Tomographic Microscopy*. Semester thesis, ETH Zürich, 2012.
- [134] R. L. Owen, J. M. Holton, C. Schulze-Briese, and E. F. Garman. Determination of X-ray flux using silicon pin diodes. *Journal of Synchrotron Radiation* **16**, 143, 2009.
- [135] J. Wang, C. Morin, L. Li, A. P. Hitchcock, A. Scholl, and A. Doran. Radiation damage in soft X-ray microscopy. *Journal of Electron Spectroscopy and Related Phenomena* **170**, 25, 2009.
- [136] K. S. Paithankar and E. F. Garman. Know your dose: RADDOSE. *Acta Crystallographica Section D: Biological Crystallography* **66**, 381, 2010.
- [137] H. D. Barth, E. A. Zimmermann, E. Schaible, S. Y. Tang, T. Alliston, and R. O. Ritchie. Characterization of the effects of x-ray irradiation on the hierarchical structure and mechanical properties of human cortical bone. *Biomaterials* **32**, 8892, 2011.
- [138] R. Boistel, N. Pollet, J.-Y. Y. Tinevez, P. Cloetens, and M. Schlenker. Irradiation damage to frog inner ear during synchrotron radiation tomographic investigation. *Journal of Electron Spectroscopy and Related Phenomena* **170**, 37, 2009.
- [139] M. R. Howells, T. Beetz, H. N. Chapman, C. Cui, J. M. Holton, C. J. Jacobsen, J. Kirz, E. Lima, S. Marchesini, H. Miao, D. Sayre, D. A. Shapiro, J. C. H. Spence, and D. Starodub. An assessment of the resolution limitation due to radiation-damage in X-ray diffraction microscopy. *Journal of Electron Spectroscopy and Related Phenomena* **170**, 4, 2009.
- [140] E. Jassem and J. Jassem. Functional evaluation of postradiation lung injury. *Reports of Practical Oncology* **1**, 96, 1996.
- [141] Y. Seppenwoolde and J. V. Lebesque. Partial irradiation of the lung. *Seminars in Radiation Oncology* **11**, 247, 2001.
- [142] V. A. Semenenko, R. C. Molthen, C. Li, N. V. Morrow, R. Li, S. N. Ghosh, M. M. Medhora, and X. A. Li. Irradiation of varying volumes of rat lung to same mean lung dose: a little to a lot or a lot to a little? *International Journal of Radiation, Oncology, Biology, Physics* **71**, 838, 2008.

- [143] L. B. Marks, X. Yu, Z. Vujaskovic, W. Small, R. Folz, and M. S. Anscher. Radiation-induced lung injury. *Seminars in Radiation Oncology* **13**, 333, 2003.
- [144] Z.-Y. Hong, S. H. Eun, K. Park, W. H. Choi, J. I. Lee, E.-J. Lee, J. M. Lee, M. D. Story, and J. Cho. Development of a small animal model to simulate clinical stereotactic body radiotherapy-induced central and peripheral lung injuries. *Journal of Radiation Research* **55**, 648, 2014.
- [145] Z. Vujaskovic, L. B. Marks, and M. S. Anscher. The physical parameters and molecular events associated with radiation-induced lung toxicity. *Seminars in Radiation Oncology* **10**, 296, 2000.
- [146] A. Novakova-Jiresova, P. van Luijk, H. van Goor, H. H. Kampinga, and R. P. Coppes. Pulmonary radiation injury: identification of risk factors associated with regional hypersensitivity. *Cancer Research* **65**, 3568, 2005.
- [147] Q.-s. Pang, P. Wang, J. Wang, W. Wang, J. Wang, and Z.-y. Yuan. Basic research of the relationship between irradiation dose and volume in radiation-induced pulmonary injury. *Chinese Medical Journal* **122**, 1929, 2009.
- [148] T. Kawase, E. Kunieda, H. M. Deloar, S. Seki, A. Sugawara, T. Tsunoo, E. N. Ogawa, A. Ishizaka, K. Kameyama, A. Takeda, and A. Kubo. Experimental stereotactic irradiation of normal rabbit lung: computed tomographic analysis of radiation injury and the histopathological features. *Radiation Medicine* **25**, 453, 2007.
- [149] C. Almeida, D. Nagarajan, J. Tian, S. W. Leal, K. Wheeler, M. Munley, W. Blackstock, and W. Zhao. The role of alveolar epithelium in radiation-induced lung injury. *PLoS ONE* **8**, e53628, 2013.
- [150] T. Kron, L. Duggan, T. Smith, A. Rosenfeld, M. Butson, G. Kaplan, S. Howlett, and K. Hyodo. Dose response of various radiation detectors to synchrotron radiation. *Physics in Medicine and Biology* **43**, 3235, 1998.
- [151] N. Nariyama. Ion recombination in parallel-plate free-air ionization chambers for synchrotron radiation. *Physics in Medicine and Biology* **51**, 5199, 2006.
- [152] A. K. Bakshi, S. Chatterjee, T. Palani Selvam, and B. S. Dhabekar. Study on the response of thermoluminescent dosimeters to synchrotron radiation: experimental method and Monte Carlo calculations. *Radiation Protection Dosimetry* **140**, 137, 2010.
- [153] M. Krumrey, M. Gerlach, M. Hoffmann, and P. Müller. Thin Transmission Photodiodes as Monitor Detectors in the X-ray Range. *AIP Conference Proceedings* **879**, 1145, 2007.
- [154] M. Gerlach, M. Krumrey, L. Cibik, P. Müller, H. Rabus, and G. Ulm. Cryogenic radiometry in the hard x-ray range. *Metrologia* **45**, 577, 2008.

- [155] M. Stampanoni, R. Mokso, F. Marone, J. Vila-Comamala, S. Gorelick, P. Trtik, K. Jefimovs, and C. David. Phase-contrast tomography at the nanoscale using hard x rays. *Physical Review B* **81**, 1, 2010.
- [156] EPICS group. Experimental physics and industrial control system. <http://www.aps.anl.gov/epics/>, 2015.
- [157] M. Donnelley, D. Parsons, K. Morgan, K. Siu, and K. K. W. Siu. Animals In Synchrotrons: Overcoming Challenges For High-Resolution, Live, Small-Animal Imaging. *AIP Conference Proceedings, MASR 2010* **1266**, 30, 2010.
- [158] Toon-boom design studio. Toon mice, two cartoon mouse characters. http://artist-3d.com/free_3d_models/dnm/model_disp.php?uid=924, 2007. [Online; accessed 26-January-2016].
- [159] R. E. Jacob and W. J. Lamm. Stable Small Animal Ventilation for Dynamic Lung Imaging to Support Computational Fluid Dynamics Models. *PLoS ONE* **6**, e27577, 2011.
- [160] M. J. Kitchen, A. Habib, A. Fouras, S. Dubsky, R. A. Lewis, M. J. Wallace, and S. B. Hooper. A new design for high stability pressure-controlled ventilation for small animal lung imaging. *Journal of Instrumentation* **5**, T02002, 2010.
- [161] J.-D. Ricard, D. Dreyfuss, and G. Saumon. Ventilator-induced lung injury. *European Respiratory Journal* **22**, 2s, 2003.
- [162] G. Lovric, S. F. Barré, J. C. Schittny, M. Roth-Kleiner, M. Stampanoni, and R. Mokso. Dose optimization approach to fast X-ray microtomography of the lung alveoli. *Journal of Applied Crystallography* **46**, 856, 2013.
- [163] M. Mertens, A. Tabuchi, S. Meissner, A. Krueger, K. Schirrmann, U. Kertzscher, A. R. Pries, A. S. Slutsky, E. Koch, and W. M. Kuebler. Alveolar dynamics in acute lung injury: heterogeneous distension rather than cyclic opening and collapse. *Critical Care Medicine* **37**, 2604, 2009.
- [164] S. P. Albert, J. DiRocco, G. B. Allen, J. H. T. Bates, R. Lafollette, B. D. Kubiak, J. Fischer, S. Maroney, and G. F. Nieman. The role of time and pressure on alveolar recruitment. *Journal of Applied Physiology* **106**, 757, 2009.
- [165] N. Yagi, Y. Suzuki, K. Umetani, Y. Kohmura, and K. Yamasaki. Refraction-enhanced x-ray imaging of mouse lung using synchrotron radiation source. *Medical Physics* **26**, 2190, 1999.
- [166] S. Bayat, G. Le Duc, L. Porra, G. Berruyer, C. Nemoz, S. Monfraix, S. Fiedler, W. Thomlinson, P. Suortti, C. G. Standertskjöld-Nordenstam, and A. R. Sovijärvi. Quantitative functional lung imaging with synchrotron radiation using inhaled xenon as contrast agent. *Physics in Medicine and Biology* **46**, 3287, 2001.

- [167] R. A. Lewis, N. Yagi, M. J. Kitchen, M. J. Morgan, D. Paganin, K. K. W. Siu, K. Pavlov, I. Williams, K. Uesugi, M. J. Wallace, C. J. Hall, J. Whitley, and S. B. Hooper. Dynamic imaging of the lungs using x-ray phase contrast. *Physics in Medicine and Biology* **50**, 5031, 2005.
- [168] B. P. Flannery, H. W. Deckman, W. G. Roberge, and K. L. D'Amico. Three-Dimensional X-ray Microtomography. *Science* **237**, 1439, 1987.
- [169] M. J. Kitchen, D. Paganin, R. A. Lewis, N. Yagi, K. Uesugi, and S. T. Mudie. On the origin of speckle in x-ray phase contrast images of lung tissue. *Physics in Medicine and Biology* **49**, 4335, 2004.
- [170] M. J. Kitchen, R. A. Lewis, N. Yagi, K. Uesugi, D. Paganin, S. B. Hooper, G. Adams, S. Jureczek, J. Singh, C. R. Christensen, A. P. Hufton, C. J. Hall, K. C. Cheung, and K. M. Pavlov. Phase contrast X-ray imaging of mice and rabbit lungs: a comparative study. *The British Journal of Radiology* **78**, 1018, 2005.
- [171] H. Suhonen, L. Porra, S. Bayat, A. R. A. Sovijärvi, and P. Suortti. Simultaneous in vivo synchrotron radiation computed tomography of regional ventilation and blood volume in rabbit lung using combined K-edge and temporal subtraction. *Physics in Medicine and Biology* **53**, 775, 2008.
- [172] S. Bayat, L. Porra, H. Suhonen, T. Janosi, S. Strengell, W. Habre, F. Petak, Z. Hantos, P. Suortti, and A. Sovijärvi. Imaging of lung function using synchrotron radiation computed tomography: what's new? *European Journal of Radiology* **68**, S78, 2008.
- [173] S. Bayat, L. Porra, H. Suhonen, P. Suortti, and A. R. A. Sovijärvi. Paradoxical conducting airway responses and heterogeneous regional ventilation after histamine inhalation in rabbit studied by synchrotron radiation CT. *Journal of Applied Physiology* **106**, 1949, 2009.
- [174] A. Fouras, B. J. Allison, M. J. Kitchen, S. Dubsky, J. Nguyen, K. Hourigan, K. K. W. Siu, R. A. Lewis, M. J. Wallace, and S. B. Hooper. Altered lung motion is a sensitive indicator of regional lung disease. *Annals of Biomedical Engineering* **40**, 1160, 2012.
- [175] S. Dubsky, S. B. Hooper, K. K. W. Siu, and A. Fouras. Synchrotron-based dynamic computed tomography of tissue motion for regional lung function measurement. *Journal of the Royal Society, Interface* **9**, 2213, 2012.
- [176] H. S. Yong, E.-Y. Kang, Y. K. Kim, O. H. Woo, B. K. Shin, C. H. Oh, J. H. Je, H. Han, and J. S. Seo. Phase contrast microradiography of mouse lung using synchrotron X-ray: correlation with optical microscopy. *Yonsei Medical Journal* **50**, 422, 2009.
- [177] D. Haberthür, C. Hintermüller, F. Marone, J. C. Schittny, and M. Stampanoni. Radiation dose optimized lateral expansion of the field of view in synchrotron radiation X-ray tomographic microscopy. *Journal of Synchrotron Radiation* **17**, 590, 2010.

- [178] R. Mokso, F. Marone, D. Haberthür, J. C. Schittny, G. Mikuljan, A. Isenegger, and M. Stampanoni. Following Dynamic Processes by X-ray Tomographic Microscopy with Sub-second Temporal Resolution. In *AIP Conference Proceedings, XRM 2010*, pages 38–41, 2011.
- [179] L. Zhang, D. Li, and S. Luo. Non-invasive microstructure and morphology investigation of the mouse lung: qualitative description and quantitative measurement. *PLoS ONE* **6**, e17400, 2011.
- [180] S. Irvine, R. Mokso, P. Modregger, Z. Wang, F. Marone, and M. Stampanoni. Simple merging technique for improving resolution in qualitative single image phase contrast tomography. *Optics Express* **22**, 27257, 2014.
- [181] P. Modregger, D. Lübbert, P. Schäfer, and R. Köhler. Spatial resolution in Bragg-magnified X-ray images as determined by Fourier analysis. *Physica Status Solidi A* **204**, 2746, 2007.
- [182] V. E. Asadchikov, a. V. Buzmakov, D. a. Zolotov, R. a. Senin, and a. S. Geranin. Laboratory X-ray microtomographs with the use of monochromatic radiation. *Crystallography Reports* **55**, 158, 2010.
- [183] R. A. Lewis. Medical phase contrast x-ray imaging: current status and future prospects. *Physics in Medicine and Biology* **49**, 3573, 2004.
- [184] T. Sera, H. Yokota, K. Fujisaki, K. Fukasaku, H. Tachibana, K. Uesugi, N. Yagi, and R. Himeno. Development of high-resolution 4D in vivo-CT for visualization of cardiac and respiratory deformations of small animals. *Physics in Medicine and Biology* **53**, 4285, 2008.
- [185] J. U. Hammel, M. V. Filatov, J. Herzen, F. Beckmann, J. A. Kaandorp, and M. Nickel. The non-hierarchical, non-uniformly branching topology of a leuconoid sponge aquiferous system revealed by 3D reconstruction and morphometrics using corrosion casting and X-ray microtomography. *Acta Zoologica* **93**, 160, 2012.
- [186] B. Bayerlein, P. Zaslansky, Y. Dauphin, A. Rack, P. Fratzl, and I. Zlotnikov. Self-similar mesostructure evolution of the growing mollusc shell reminiscent of thermodynamically driven grain growth. *Nature Materials* **13**, 1102, 2014.
- [187] J. Lachambre, E. Maire, J. Adrien, and D. Choqueuse. In situ observation of syntactic foams under hydrostatic pressure using X-ray tomography. *Acta Materialia* **61**, 4035, 2013.
- [188] H. A. Bale, A. Haboub, A. A. MacDowell, J. R. Nasiatka, D. Y. Parkinson, B. N. Cox, D. B. Marshall, and R. O. Ritchie. Real-time quantitative imaging of failure events in materials under load at temperatures above 1,600 °C. *Nature Materials* **12**, 40, 2013.
- [189] K. Mader, R. Mokso, C. Raufaste, B. Dollet, S. Santucci, J. Lambert, and M. Stampanoni. Quantitative 3D characterization of cellular materials: Segmentation and morphology

- of foam. *Colloids and Surfaces A: Physicochemical and Engineering Aspects* **415**, 230, 2012.
- [190] D. R. Baker, F. Brun, C. O'Shaughnessy, L. Mancini, J. L. Fife, and M. Rivers. A four-dimensional X-ray tomographic microscopy study of bubble growth in basaltic foam. *Nature Communications* **3**, 1135, 2012.
- [191] F. Fuisseis, X. Xiao, C. Schrank, and F. De Carlo. A brief guide to synchrotron radiation-based microtomography in (structural) geology and rock mechanics. *Journal of Structural Geology* **65**, 1, 2014.
- [192] K. M. Kareh, P. D. Lee, R. C. Atwood, T. Connolley, and C. M. Gourlay. Revealing the micromechanisms behind semi-solid metal deformation with time-resolved X-ray tomography. *Nature Communications* **5**, 4464, 2014.
- [193] S. E. Pierce, P. E. Ahlberg, J. R. Hutchinson, J. L. Molnar, S. Sanchez, P. Tafforeau, and J. A. Clack. Vertebral architecture in the earliest stem tetrapods. *Nature* **494**, 226, 2013.
- [194] D. J. E. Murdock, X.-P. Dong, J. E. Repetski, F. Marone, M. Stampanoni, and P. C. J. Donoghue. The origin of conodonts and of vertebrate mineralized skeletons. *Nature* **502**, 546, 2013.
- [195] J. Moosmann, A. Ershov, V. Altapova, T. Baumbach, M. S. Prasad, C. LaBonne, X. Xiao, J. Kashef, and R. Hofmann. X-ray phase-contrast in vivo microtomography probes new aspects of *Xenopus* gastrulation. *Nature* **497**, 374, 2013.
- [196] S. M. Walker, D. A. Schwyn, R. Mokso, M. Wicklein, T. Müller, M. Doube, M. Stampanoni, H. G. Krapp, and G. K. Taylor. In Vivo Time-Resolved Microtomography Reveals the Mechanics of the Blowfly Flight Motor. *PLoS Biology* **12**, e1001823, 2014.
- [197] R. Mokso, F. Marone, S. Irvine, M. Nyvlt, D. Schwyn, K. Mader, G. K. Taylor, H. G. Krapp, M. Skeren, and M. Stampanoni. Advantages of phase retrieval for fast x-ray tomographic microscopy. *Journal of Physics D: Applied Physics* **46**, 494004, 2013.
- [198] J. F. Adam, S. Bayat, L. Porra, H. Elleaume, F. Estève, and P. Suortti. Quantitative functional imaging and kinetic studies with high-Z contrast agents using synchrotron radiation computed tomography. *Clinical and Experimental Pharmacology and Physiology* **36**, 95, 2009.
- [199] L. Porra, H. Suhonen, P. Suortti, A. R. A. Sovijärvi, and S. Bayat. Effect of positive end-expiratory pressure on regional ventilation distribution during bronchoconstriction in rabbit studied by synchrotron radiation imaging. *Critical Care Medicine* **39**, 1731, 2011.
- [200] L. Porra, S. Monfraix, G. Berruyer, G. Le Duc, C. Nemoz, W. Thomlinson, P. Suortti, a. R. a. Sovijärvi, and S. Bayat. Effect of tidal volume on distribution of ventilation assessed by synchrotron radiation CT in rabbit. *Journal of Applied Physiology* **96**, 1899, 2004.

- [201] D. M. Vasilescu, Z. Gao, P. K. Saha, L. Yin, G. Wang, B. Haefeli-Bleuer, M. Ochs, E. R. Weibel, and E. A. Hoffman. Assessment of morphometry of pulmonary acini in mouse lungs by nondestructive imaging using multiscale microcomputed tomography. *Proceedings of the National Academy of Sciences* **109**, 17105, 2012.
- [202] K. Miyamoto. Particle Number and Sizes Estimated from Sections - A History of Stereology. In R. Takaki, editor, *Research of Pattern Formation*, chapter 8, pages 507–516. KTK Scientific Publishers, 1994.
- [203] D. M. Vasilescu, C. Klinge, L. Knudsen, L. Yin, G. Wang, E. R. Weibel, M. Ochs, and E. A. Hoffman. Stereological assessment of mouse lung parenchyma via nondestructive, multiscale micro-CT imaging validated by light microscopic histology. *Journal of Applied Physiology* **114**, 716, 2013.
- [204] N. C. W. Kuijpers, J. Tirel, D. N. Hanlon, and S. Van der Zwaag. Quantification of the evolution of the 3D intermetallic structure in a 6005A aluminium alloy during a homogenisation treatment. *Materials Characterization* **48**, 379, 2002.
- [205] J. Fife and P. Voorhees. The morphological evolution of equiaxed dendritic microstructures during coarsening. *Acta Materialia* **57**, 2418, 2009.
- [206] X. Xiao, F. De Carlo, and S. Stock. Practical error estimation in zoom-in and truncated tomography reconstructions. *Review of Scientific Instruments* **78**, 063705, 2007.
- [207] G. Wang, Y. Wang, H. Li, X. Chen, H. Lu, Y. Ma, C. Peng, Y. Wang, and L. Tang. Morphological Background Detection and Illumination Normalization of Text Image with Poor Lighting. *PLoS ONE* **9**, e110991, 2014.
- [208] N. Otsu. A threshold selection method from gray-level histograms. *Automatica* **11**, 23, 1975.
- [209] D. Babin, A. Pižurica, J. De Vylder, E. Vansteenkiste, and W. Philips. Brain blood vessel segmentation using line-shaped profiles. *Physics in Medicine and Biology* **58**, 8041, 2013.
- [210] S. Chang, N. Kwon, B. M. Weon, J. Kim, C. K. Rhee, H. S. Choi, Y. Kohmura, M. Yamamoto, T. Ishikawa, and J. H. Je. Tracking X-ray microscopy for alveolar dynamics in live intact mice. *Scientific Reports* **3**, 1304, 2013.
- [211] A. F. T. Leong, D. M. Paganin, S. B. Hooper, M. L. Siew, and M. J. Kitchen. Measurement of absolute regional lung air volumes from near-field x-ray speckles. *Optics Express* **21**, 27905, 2013.
- [212] Y. Liu, D. Jin, C. Li, K. F. Janz, T. L. Burns, J. C. Torner, S. M. Levy, and P. K. Saha. A robust algorithm for thickness computation at low resolution and its application to in Vivo trabecular bone CT imaging. *IEEE Transactions on Biomedical Engineering* **61**, 2057, 2014.

- [213] H. Tran, P. Doumalin, C. Delisee, J. C. Dupre, J. Malvestio, and A. Germaneau. 3D mechanical analysis of low-density wood-based fiberboards by X-ray microcomputed tomography and Digital Volume Correlation. *Journal of Materials Science* **48**, 3198, 2013.
- [214] T. Hildebrand and P. Rügsegger. A new method for the model-independent assessment of thickness in three-dimensional images. *Journal of Microscopy* **185**, 67, 1997.
- [215] J. Schindelin, I. Arganda-Carreras, E. Frise, V. Kaynig, M. Longair, T. Pietzsch, S. Preibisch, C. Rueden, S. Saalfeld, B. Schmid, J.-Y. Tinevez, D. J. White, V. Hartenstein, K. Eliceiri, P. Tomancak, and A. Cardona. Fiji: an open-source platform for biological-image analysis. *Nature Methods* **9**, 676, 2012.
- [216] J. A. Levine, R. R. Paulsen, and Y. Zhang. Mesh Processing in Medical-Image Analysis – a Tutorial. *IEEE Computer Graphics and Applications* **32**, 22, 2012.
- [217] U. Nath, B. C. W. Crawford, R. Carpenter, and E. Coen. Genetic control of surface curvature. *Science* **299**, 1404, 2003.
- [218] N. Kang, M. W. Lee, and T. Rhee. Simulating Liver Deformation during Respiration Using Sparse Local Features. *IEEE Computer Graphics and Applications* **32**, 29, 2012.
- [219] W. Schroeder, K. Martin, and B. Lorensen. *Visualization Toolkit: An Object-Oriented Approach to 3D Graphics*. Kitware, 4th edition, 2006.
- [220] G. Taubin. Geometric Signal Processing on Polygonal Meshes. In S. Coquillart and D. Duke, editors, *STAR Proceedings of Eurographics*, 2000.
- [221] G. Lavoué, M. Tola, F. Dupont, and G. Lavou. MEPP - 3D mesh processing platform. In P. Richard, M. Kraus, R. S. Laramée, and J. Braz, editors, *Proceedings of the International Conference on Computer Graphics Theory and Applications (GRAPP 2012)*, pages 206–210. INSTICC Press, 2012.
- [222] D. Cohen-Steiner and J.-M. Morvan. Restricted delaunay triangulations and normal cycle. *Proceedings of the 19th conference on Computational geometry - SCG '03* page 312, 2003.
- [223] T. Duong. ks: Kernel Density Estimation and Kernel Discriminant Analysis for Multivariate Data in R. *Journal Of Statistical Software* **21**, 1, 2007.
- [224] S. M. K. Rausch, D. Haberthür, M. Stampanoni, J. C. Schittny, and W. A. Wall. Local Strain Distribution in Real Three-Dimensional Alveolar Geometries. *Annals of Biomedical Engineering* **39**, 2835, 2011.
- [225] I. V. Pratt, G. Belev, N. Zhu, L. D. Chapman, and D. M. L. Cooper. *In vivo* imaging of rat cortical bone porosity by synchrotron phase contrast micro computed tomography. *Physics in Medicine and Biology* **60**, 211, 2015.

- [226] J.-F. Adam, C. Nemoz, A. Bravin, S. Fiedler, S. Bayat, S. Monfraix, G. Berruyer, A. M. Charvet, J.-F. Le Bas, H. Elleaume, and F. Estève. High-resolution blood-brain barrier permeability and blood volume imaging using quantitative synchrotron radiation computed tomography: study on an F98 rat brain glioma. *Journal of Cerebral Blood Flow & Metabolism* **25**, 145, 2005.
- [227] B. Wang, B. Zhang, H. Huo, T. Wang, Q. Wang, Y. Wu, L. Xiao, Y. Ren, and L. Zhang. Detection of microvasculature alterations by synchrotron radiation in murine with delayed jellyfish envenomation syndrome. *Toxicon* **81**, 48, 2014.
- [228] A. Astolfo, E. Schültke, R. H. Menk, R. D. Kirch, B. H. J. Juurlink, C. Hall, L. A. Harsan, M. Stebel, D. Barbeta, G. Tromba, and F. Arfelli. In vivo visualization of gold-loaded cells in mice using x-ray computed tomography. *Nanomedicine: Nanotechnology, Biology, and Medicine* **9**, 284, 2013.
- [229] M. W. Westneat, O. Betz, R. W. Blob, K. Fezzaa, W. J. Cooper, and W.-K. Lee. Tracheal Respiration in Insects Visualized with Synchrotron X-ray Imaging. *Science* **299**, 558, 2003.
- [230] A. Kaiser, C. J. Klok, J. J. Socha, W.-K. Lee, M. C. Quinlan, and J. F. Harrison. Increase in tracheal investment with beetle size supports hypothesis of oxygen limitation on insect gigantism. *Proceedings of the National Academy of Sciences* **104**, 13198, 2007.
- [231] M. W. Westneat, J. J. Socha, and W.-K. Lee. Advances in Biological Structure, Function, and Physiology Using Synchrotron X-ray Imaging. *Annual Review of Physiology* **70**, 119, 2008.
- [232] T. dos Santos Rolo, A. Ershov, T. van de Kamp, and T. Baumbach. In vivo X-ray cinematography for tracking morphological dynamics. *Proceedings of the National Academy of Sciences* **111**, 3921, 2014.
- [233] D. A. Schwyn, R. Mokso, S. M. Walker, M. Doube, M. Wicklein, G. K. Taylor, M. Stamparoni, and H. G. Krapp. High-Speed X-ray Imaging on the Fly. *Synchrotron Radiation News* **26**, 4, 2013.
- [234] R. Mokso, D. A. Schwyn, S. M. Walker, M. Doube, M. Wicklein, T. Müller, M. Stamparoni, G. K. Taylor, and H. G. Krapp. Four-dimensional in vivo X-ray microscopy with projection-guided gating. *Scientific Reports* **5**, 8727, 2015.
- [235] N. L. Ford, H. N. Nikolov, C. J. D. Norley, M. M. Thornton, P. J. Foster, M. Drangova, and D. W. Holdsworth. Prospective respiratory-gated micro-CT of free breathing rodents. *Medical Physics* **32**, 2888, 2005.
- [236] N. L. Ford, A. R. Wheatley, D. W. Holdsworth, and M. Drangova. Optimization of a retrospective technique for respiratory-gated high speed micro-CT of free-breathing rodents. *Physics in Medicine and Biology* **52**, 5749, 2007.

- [237] S. Sawall, F. Bergner, R. Lapp, M. Mronz, M. Karolczak, A. Hess, and M. Kachelrieß. Low-dose cardio-respiratory phase-correlated cone-beam micro-CT of small animals. *Medical Physics* **38**, 1416, 2011.
- [238] S. Monfraix, S. Bayat, L. Porra, G. Berruyer, C. Nemoz, W. Thomlinson, P. Suortti, and A. R. a. Sovijärvi. Quantitative measurement of regional lung gas volume by synchrotron radiation computed tomography. *Physics in Medicine and Biology* **50**, 1, 2005.
- [239] S. Bayat, L. Porra, H. Suhonen, C. Nemoz, P. Suortti, and A. R. a. Sovijärvi. Differences in the time course of proximal and distal airway response to inhaled histamine studied by synchrotron radiation CT. *Journal of Applied Physiology* **100**, 1964, 2006.
- [240] S. B. Hooper, M. J. Kitchen, M. J. Wallace, N. Yagi, K. Uesugi, M. J. Morgan, C. Hall, K. K. W. Siu, I. M. Williams, M. Siew, S. C. Irvine, K. Pavlov, and R. a. Lewis. Imaging lung aeration and lung liquid clearance at birth. *The FASEB Journal* **21**, 3329, 2007.
- [241] M. J. Kitchen, R. A. Lewis, M. J. Morgan, M. J. Wallace, M. L. Siew, K. K. W. Siu, A. Habib, A. Fouras, N. Yagi, K. Uesugi, and S. B. Hooper. Dynamic measures of regional lung air volume using phase contrast x-ray imaging. *Physics in Medicine and Biology* **53**, 6065, 2008.
- [242] A. F. T. Leong, A. Fouras, M. S. Islam, M. J. Wallace, S. B. Hooper, and M. J. Kitchen. High spatiotemporal resolution measurement of regional lung air volumes from 2D phase contrast x-ray images. *Medical Physics* **40**, 041909, 2013.
- [243] A. F. T. Leong, G. A. Buckley, D. M. Paganin, S. B. Hooper, M. J. Wallace, and M. J. Kitchen. Real-time measurement of alveolar size and population using phase contrast x-ray imaging. *Biomedical Optics Express* **5**, 4024, 2014.
- [244] T. Sera, K. Uesugi, and N. Yagi. Localized morphometric deformations of small airways and alveoli in intact mouse lungs under quasi-static inflation. *Respiratory Physiology & Neurobiology* **147**, 51, 2005.
- [245] T. Sera, H. Yokota, G. Tanaka, K. Uesugi, N. Yagi, and R. C. Schroter. Murine pulmonary acinar mechanics during quasi-static inflation using synchrotron refraction-enhanced computed tomography. *Journal of Applied Physiology* **115**, 219, 2013.
- [246] S. Peter. *Implementation of a Monte Carlo model for dose calculations at TOMCAT beamline*. Master thesis, ETH Zürich, 2012.
- [247] D. M. Pelt and K. J. Batenburg. Fast tomographic reconstruction from limited data using artificial neural networks. *IEEE Transactions on Image Processing* **22**, 5238, 2013.

Curriculum vitae

■ ■ EDUCATION

- 2011 to 2015 **Doctorate in Biomedical Engineering**, Dr. sc. ETH Zurich
ETH Zurich, Zürich (Switzerland)
Paul Scherrer Institute, Villigen (Switzerland)
- PhD thesis: *In vivo study of lung physiology with dynamic synchrotron-based tomographic microscopy*
 - └ Doctoral advisor: Prof. Dr. Marco Stampanoni
 - └ Supervisor: Dr. Rajmund Mokso
- 2008 to 2010 **Master in Technical Physics**, MSc. (Dipl.-Ing.)
Graz University of Technology, Graz (Austria)
- Half-year research visit at *Hubei University, Wuhan (PR China)*
 - Master thesis: *Numerical Investigation of Strongly Correlated Electron and Electron-Phonon Systems*
 - └ Supervisor: Univ.-Prof. Dr. rer. nat. Enrico Arrigoni
- 2004 to 2008 **Bachelor in Technical Physics**, BSc.
Graz University of Technology, Graz (Austria)
- Bachelor thesis: *Fouriertransformationen*
 - └ Supervisor: Ao. Univ.-Prof. Dr. techn. Heinrich Sormann
- 1996 to 2004 **Grammar school (language focus)**, Matura
Bundesgymnasium Dreihackengasse, Graz (Austria)
- Scholarly paper: *Die Entstehung der Republik Kroatien - historische und biographische Bruchlinien* ("Fachbereichsarbeit")
 - └ Supervisor: Prof. Franz-Christian Weber
- 1992 to 1996 **Primary school**
Volksschule Karl Morre, Graz (Austria)

■■ CONFERENCES AND ABSTRACTS

- [G. Lovric](#), R. Mokso, F. Arcadu, I. Vogiatzis Oikonomidis, J. C. Schittny, M. Roth-Kleiner and M. Stampanoni *Tomographic in-vivo study of lung physiology at the micrometer scale*, MASR 2015, Grenoble & Villard de Lans, France, 2015. **└ Oral presentation**
- [G. Lovric](#), D. Schwyn, S. Walker, I. Oikonomidis Vogiatzis, J. C. Schittny, M. Roth-Kleiner, M. Stampanoni and R. Mokso, *Tomographic in-vivo respiration studies at the micrometer scale*, XRM 2014, Melbourne, Australia, 2014. **└ Invited plenary oral presentation**
- [G. Lovric](#), P. Oberta, I. Mohacsi, M. Stampanoni and R. Mokso, *A robust tool for photon source geometry measurements using the fractional Talbot effect*, XRM 2014, Melbourne, Australia, 2014. **└ Poster presentation**
- [G. Lovric](#), F. Arcadu, D. Schwyn, S. Walker, J. C. Schittny, M. Roth-Kleiner, M. Stampanoni and R. Mokso, *Tomographic in-vivo respiration studies at the micrometer scale*, XTOP 2014, Villard de Lans (Grenoble), France, 2014. **└ Oral presentation**
- [G. Lovric](#), P. Oberta, I. Mohacsi, M. Stampanoni and R. Mokso, *A robust tool for photon source geometry measurements using the fractional Talbot effect*, XTOP 2014, Villard de Lans (Grenoble), France, 2014. **└ Poster presentation**
- [G. Lovric](#), R. Mokso, J.C. Schittny, M. Roth-Kleiner and M. Stampanoni, *Towards microtomographic in vivo imaging*, ICTMS 2013, Gent, Belgium, 2013. **└ Plenary oral presentation**
- [G. Lovric](#), R. Mokso, J. C. Schittny, S. F. Barré, M. Stampanoni and [M. Roth-Kleiner](#), *High resolution X-ray tomographic microscopy to study ventilation induced morphological changes at alveolar level*, PAS meeting 2013, Washington DC, USA, 2013. **└ Poster presentation**
- [G. Lovric](#), R. Mokso, S. F. Barré, M. Roth-Kleiner, M. Stampanoni and J. C. Schittny, *Dose Optimization Approach To Fast X-Ray Microtomography Of The Lung Alveoli*, ATS International Conference 2013, Philadelphia, USA, 2013. **└ Poster presentation**
- [G. Lovric](#), R. Mokso, J.C. Schittny, M. Roth-Kleiner and M. Stampanoni, *Development of microtomographic in vivo imaging to study lung dynamics at the micrometer scale*, XTOP 2012, St. Petersburg, Russia, 2012. **└ Oral presentation**
- [G. Lovric](#), R. Mokso, D. Habarthur, J.C. Schittny, M. Roth-Kleiner and M. Stampanoni, *Development of microtomographic in vivo imaging to study lung dynamics at the TOM-CAT beamline*, SRI 2012, Lyon, France, 2012. **└ Poster presentation**
- [G. Lovric](#), R. Mokso, J.C. Schittny, M. Roth-Kleiner and M. Stampanoni, *In-vivo study of lung physiology with sub-second x-ray tomographic microscopy*, Second Joint Users Meeting @ PSI (JUM@P), PSI Villigen, Switzerland, 2011. **└ Poster presentation**

■ ■ SELECTED PUBLICATIONS

- G. Lovric, S. F. Barré, J. C. Schittny, M. Roth-Kleiner, M. Stampanoni, and R. Mokso. *Dose optimization approach to fast X-ray microtomography of the lung alveoli*. *Journal of Applied Crystallography*, **46**(4), 856–860, June 2013.
- G. Lovric, P. Oberta, I. Mohacsi, M. Stampanoni, and R. Mokso. *A robust tool for photon source geometry measurements using the fractional Talbot effect*. *Optics Express*, **22**(3), 2745, January 2014.

■ ■ COLLABORATIONS

- **University of Bern**
Institute of Anatomy, 3012 Bern, Switzerland
- **Centre hospitalier universitaire vaudois (CHUV)**
Clinic of Neonatology, 1011 Lausanne, Switzerland
- **Paul Scherrer Institute** (cross-departmental collaboration)
Laboratory for Micro- and Nanotechnology, 5232 Villigen, Switzerland
- **Academy of Sciences of the Czech Republic**
Institute of Physics, 18221 Prague, Czech Republic
- **Rigaku**
Rigaku Innovative Technologies Europe s.r.o., 14221 Prague, Czech Republic
- **Centrum Wiskunde & Informatica (CWI)**
Scientific Computing group, 1098 XG Amsterdam, The Netherlands
- **Delft University of Technology**
Department of Imaging Science & Technology, 2628 CJ Delft, The Netherlands
- **Czech Technical University in Prague**
Department of Physical Electronics, 11519 Prague, Czech Republic
- **Center for BioMedical Imaging (CIBM)**
CardioVascular MR Center, 1011 Lausanne, Switzerland